

UNIVERSITY OF MISKOLC

MIKOVINY SÁMUEL DOCTORAL SCHOOL OF EARTH SCIENCES

Head of doctoral school

Prof. Dr. Péter Szűcs

Professor

**Flow Profile Control in Hydraulic Fractured Wells –
Foundation of a New Geothermal Energy Production
Technology**

Ph.D. Thesis

AUTHOR:

Patrik Pusztai

MS in Petroleum Engineering

Master of Business Administration

ADVISORS:

Dr. Anita Jobbik

Senior Research Fellow

Dr. Krisztián Mátyás Baracza

Director, Senior Research Fellow

Miskolc, 2023

TABLE OF CONTENT

1	SUMMARY.....	XIII
2	ÖSSZEFOGLALÁS	XIV
3	INTRODUCTION & TOPIC RELEVANCE	1
3.1	Research purpose & research conducted	1
4	ENERGY OUTLOOK.....	4
5	GEOHERMAL ENERGY	9
5.1	Geothermal Energy Utilization	11
5.1.1	Direct Geothermal Energy Utilization	11
5.1.2	Indirect Geothermal Energy Utilization.....	12
5.2	Geothermal Resources	14
5.2.1	Hydrothermal resources.....	14
5.2.2	Hot Dry Rock resources.....	16
5.2.3	Magma resources	17
5.2.4	Geopressured resources	18
5.3	Enhanced Geothermal Systems (EGS).....	19
5.3.1	Thermal stimulation	20
5.3.2	Chemical stimulation.....	20
5.3.3	Hydromechanical stimulation	22
5.3.3.1	Massive water injection treatments.....	22
5.3.3.2	Hydraulic-proppant treatment	23
5.3.3.3	Multistage treatment	25
6	NEW EGS TECHNOLOGY	26
6.1	Intuition.....	26
6.2	Fundamental Considerations	29
6.3	Finite Element Simulation	30
6.3.1	Fracture geometry	30
6.3.1.1	Applied geometry.....	33

6.3.2	Meshing.....	35
6.3.2.1	Meshing quality.....	37
6.3.3	Applied physics.....	41
6.3.3.1	Boundary conditions.....	42
6.3.3.2	Transport equations.....	44
6.3.3.3	Steady-state simulation.....	45
6.3.3.4	Transient simulation.....	48
6.3.4	Validation of the model.....	49
6.3.5	Reducing simulation time.....	52
7	PROPPANT MEASUREMENTS AND ANALYSIS.....	55
7.1	Measurements.....	56
7.1.1	Validation of the measurement.....	58
7.1.2	Mixed proppant measurement results.....	59
7.2	Theoretical Analysis.....	60
7.2.1	Derivation of a new theoretical model.....	62
7.2.1.1	Modified particle friction factor correlations.....	64
7.2.2	Comparisons of the models.....	70
7.2.2.1	Specific gravity measurement.....	70
7.2.2.2	New bulk density measurement.....	71
7.2.2.3	Proppant-pack porosity.....	73
7.2.2.4	Result of the comparison.....	74
7.3	Modified Particle Friction Factor Correlation.....	75
7.4	Conclusion on the proppant measurement and analysis.....	77
8	RESULTS.....	79
8.1	Optimization procedure.....	81
8.2	Results summary.....	84
9	SCIENTIFIC ACHIEVEMENTS.....	88
9.1	Thesis #1.....	88
9.2	Thesis #2.....	88

9.3	Thesis #3.....	89
9.4	Thesis #4.....	89
9.5	Thesis #5.....	90
10	ACKNOWLEDGEMENT.....	91
11	REFERENCES.....	92
12	THE AUTHOR'S MAIN SCIENTIFIC PUBLICATIONS	I
12.1	Publications.....	I
12.2	Conferences.....	II
13	ANNEXES.....	IV
14	LIST OF ANNEXES	LI

LIST OF FIGURES

Figure 3-1: Visual representation of the new approach	2
Figure 3-2: Results of the coupled model (left: flow profile reached by the steady-state simulation, right: temperature profile reached by the transient simulation)	3
Figure 4-1: Global total energy consumption by energy source, 1990 - 2018 (EIA, 2021a)	4
Figure 4-2: Projection of global primary energy consumption by energy source, 2020 - 2050 (EIA, 2021b).....	5
Figure 4-3: World's power generation projections in two year increment™ (IEA, 2008; IEA, 2010; IEA, 2012; IEA, 2014; IEA, 2016; IEA, 2018; IEA, 2020)	6
Figure 4-4: Installed global renewable energy capacity by technology, 2000 - 2016 (Ritchie and Roser, 2020)	7
Figure 4-5: Global LCOEs from newly commissioned, utility-scale renewable power generation technologies, 2010-2020 (IRENA, 2021)	8
Figure 5-1: Current and projected electricity generation from renewable resources in case of stated policy and sustainable development scenario (IEA, 2020)	10
Figure 5-2: Global direct and indirect geothermal power generation, 1995 – 2015 (IGA, 2021; Lund and Toth, 2021; REN, 2021).....	11
Figure 5-3: Global direct geothermal capacity by use, 1995 – 2020 (Lund and Toth, 2021)	12
Figure 5-4: Thermal power plant efficiency comparison (Zarrouk and Moon, 2014).....	13
Figure 5-5: Schematic figure of a typical hydrothermal geothermal source with its main elements (Barbier, 2002).....	16
Figure 5-6: Simplified surface and subsurface system of Hijiori site (Oikawa et al., 2021)	17
Figure 5-7: Schematic representation of the IDDP-1 well and reservoir with the “as-built” drawing of the well (Elders and Fridleifsson, 2010; Palsson et al., 2014)	18

Figure 5-8: Results of chemical treatment in selected geothermal fields (Portier et al., 2009)	21
Figure 5-9: Proppant concentration distribution and geometry of a hydraulic-proppant treatment (Sharma et al., 2018)	24
Figure 5-10: Multistage horizontal EGS concept with one injection and one production well (Li et al., 2016).....	25
Figure 6-1: Schematic illustration of the GeneSys Hannover project (http://www.genesys-hannover.de).....	27
Figure 6-2: Conceptual illustration of a hydraulically induced fracture with a grouted island (Danko et al., 2018)	28
Figure 6-3: Schematic representation of the different single-well EGS methods (left model offered by Genesys project (Kehrer et al., 2007), middle model offered by Danko et al. (2018), right model offered by the current study).....	29
Figure 6-4: Hydraulic fracture geometries (upper left side PKN model, upper right side KGD model, bottom side penny-shaped model) (Adachi et al., 2007)	32
Figure 6-5: 3-D fracture propagation models (Weijers and de Pater, 2019).....	32
Figure 6-6: Vertical fracture produced under stress conditions (Hubbert and Willis, 1957)	33
Figure 6-7: Schematic representation of the fracture with the two symmetry planes	34
Figure 6-8: Schematic representation of the fracture with the two symmetry planes	34
Figure 6-9: Basic cell types for meshing.....	36
Figure 6-10: Meshing of the 3D model	37
Figure 6-11: Orthogonal quality of the generated mesh	38
Figure 6-12: Skewness of the generated mesh	39
Figure 6-13: Aspect ratio of the generated mesh	39
Figure 6-14: Temperature profiles in case of the 3 scenarios (upper pictures on the X-Y plane; lower picture on the Z-X plane).....	41

Figure 6-15: Symmetry boundary conditions on the X-Y and Y-Z planes	42
Figure 6-16: Reservoir wall boundary condition	43
Figure 6-17: Defined inlet and outlet boundary conditions.....	43
Figure 6-18: Flow profiles (left with 60°C inlet temperature and right 180°C inlet temperature)	45
Figure 6-19: Sensitivity analysis for porosity and loss coefficient	47
Figure 6-20: Sensitivity analysis for transient timestep.....	49
Figure 6-21: Geometry of the validation model.....	50
Figure 6-22: Meshing of the validation model.....	50
Figure 6-23: Pressure profile of the validation model	51
Figure 6-24: Results of the validation.....	51
Figure 6-25: Simplified flowchart of an evolutionary algorithm (Covas and Gaspar-Cunha 2009)	53
Figure 6-26: Absolute deviation of the fitting optimization from the total simulation result at different simulation times in the case of each zone has 128 <i>Darcy</i> permeability	53
Figure 6-27: Result of the curve fitting to reduce simulation time	54
Figure 7-1: Schematic representation of the standard equipment used for permeability and conductivity measurements.....	56
Figure 7-2: Size distribution histograms in case of the applied proppants	57
Figure 7-3: Validation of the measurement accuracy on the 30/50 mesh proppant	58
Figure 7-4: Effect of mixing on permeability at different closing pressures	59
Figure 7-5: Fracture permeability values using Eq. 7-5 and Eq. 7-6 (transient zone is just a visualization)	62
Figure 7-6: Effective range of the different modified particle friction factor models using Eq. 7-13	68

Figure 7-7: Behavior of different modified particle friction factor models in Eq. 7-13	69
Figure 7-8: Specific gravity of the proppant-packs with the gross variance of the measurements	70
Figure 7-9: Schematic illustration of the crush test apparatus used during the bulk density measurements (not to scale).....	71
Figure 7-10: Bulk density measurement results at different proppant mixtures and at different closing pressures	72
Figure 7-11: Porosity values at different applied closing pressure in case of different mixtures	73
Figure 7-12: Comparison of the calculated and measured fracture permeability values in case of the different models	74
Figure 7-13: Comparison of the results obtained by the modified correlation to the measured fracture permeability values.....	76
Figure 7-14: Comparison of the present work to the measured fracture permeability values	77
Figure 7-15: Comparison of the measured and calculated fracture permeability values with the 30/50 mesh size proppant.....	78
Figure 8-1: Results of the simulations	79
Figure 8-2: Total power production with each model	80
Figure 8-3: Comparing the effect of initial temperature in the fracture	81
Figure 8-4: Response surface of the analyzed dataset	84
Figure 8-5: Temperature, pressure, and velocity profiles of the optimized new EGS method and the method offered by Danko et al. (2018)	86
Figure 8-6: Comparison of thermal energy production of the two EGS technology	87
Figure 13-1: Aerial view of Stillwater combined power plant (DiPippo, 2016c)	IV
Figure 13-2: Direct steam schematic example, with surface condenser (Phair, 2016).....	V

Figure 13-3: Flash plant schematic example, showing potential for second and third flash stages (Harvey and Wallace, 2016)	V
Figure 13-4: Total flow schematic example (Smith, 2016)	VI
Figure 13-5: Basic binary cycle schematic example with air-cooled condenser (Mines, 2016)	VI
Figure 13-6: Compound fossil-geothermal hybrid schematic example (DiPippo, 2016b)	VII
Figure 13-7: Hybrid (single flash – binary) geothermal power plant schematic example (Dincer and Ezzat, 2018)	VII
Figure 13-8: Flow profiles in a single-well EGS model with and without a flow control mechanism (Danko et al., 2018)	XII
Figure 13-9: Different zones of proppant concentrations in the fractures based on studies (upper left by Gui et al. (2013), upper right by Stopa et al. (2014), bottom left by Sharma et al. (2018), bottom right by Muther et al. (2020))	XIII
Figure 13-10: Heat profile after the simulation in the X-Y, X-Z, and Y-Z axis.....	XIV
Figure 13-11: Edge-sizing during the meshing procedure	XV
Figure 13-12: Average outlet pressure during the steady-state simulation	XVI
Figure 13-13: Residuals during steady-state simulation	XVI
Figure 13-14: Residuals during transient simulation.....	XVII
Figure 13-15: Velocity profile of the validation model	XVII
Figure 13-16: Validation results I.....	XVIII
Figure 13-17: Validation results II.....	XIX
Figure 13-18: Fitting results based on different simulation time in case the fracture permeability in the zones is 128 <i>Darcy</i> with the difference in the sum temperatures ($\sum\Delta T$) of the simulated and the fitted data	XX
Figure 13-19: Equipment used during the measurements	XXI

Figure 13-20: Technical data sheet of the 30/50 mesh proppant used during the measurements (2/1).....	XXII
Figure 13-21: Technical data sheet of the 30/50 mesh proppant used during the measurements (2/2).....	XXIII
Figure 13-22: Pentapyc 5200e device used for specific gravity measurements.....	XXIV
Figure 13-23: API RP 19C measurement device used for bulk density measurements	XXV
Figure 13-24: Occhio Zephyr ESR 2 equipment used during proppant size distribution, sphericity and roundness measurements	XXV
Figure 13-25: Roundness and sphericity values of the 30/50 and 16/32 mesh proppants	XXVI
Figure 13-26: Pure and mixed proppant samples – before measurement	XXVI
Figure 13-27: 16/32 mesh proppant – sample after measurement 2/1	XXVII
Figure 13-28: 16/32 mesh proppant – sample after measurement 2/2	XXVII
Figure 13-29: 80:20 mixture of 16/32:30/50 mesh proppants – sample after measurement 2/1	XXVIII
Figure 13-30: 80:20 mixture of 16/32:30/50 mesh proppants – sample after measurement 2/2	XXVIII
Figure 13-31: 60:40 mixture of 16/32:30/50 mesh proppants – sample after measurement 2/1	XXIX
Figure 13-32: 60:40 mixture of 16/32:30/50 mesh proppants – sample after measurement 2/2	XXIX
Figure 13-33: 40:60 mixture of 16/32:30/50 mesh proppants – sample after measurement 2/1	XXX
Figure 13-34: 40:60 mixture of 16/32:30/50 mesh proppants – sample after measurement 2/2	XXX
Figure 13-35: 20:80 mixture of 16/32:30/50 mesh proppants – sample after measurement 2/1	XXXI

Figure 13-36: 20:80 mixture of 16/32:30/50 mesh proppants – sample after measurement 2/2	XXXI
Figure 13-37: 30/50 mesh proppant – A sample after measurement 2/1	XXXII
Figure 13-38: 30/50 mesh proppant – A sample after measurement 2/2	XXXII
Figure 13-39: 30/50 mesh proppant – B sample after measurement 2/1	XXXIII
Figure 13-40: 30/50 mesh proppant – B sample after measurement 2/2	XXXIII
Figure 13-41: 30/50 mesh proppant – C sample after measurement 2/1	XXXIV
Figure 13-42: 30/50 mesh proppant – C sample after measurement 2/2	XXXIV
Figure 13-43: Permeability, conductivity and fracture width results in case of the 16/32 mesh proppant at different closing pressures	XXXV
Figure 13-44: Permeability, conductivity and fracture width results in case of the 80:20 m/m% mixture of 16/32 and 30/50 mesh proppant at different closing pressures	XXXVI
Figure 13-45: Permeability, conductivity and fracture width results in case of the 60:40 m/m% mixture of 16/32 and 30/50 mesh proppant at different closing pressures	XXXVII
Figure 13-46: Permeability, conductivity and fracture width results in case of the 40:60 m/m% mixture of 16/32 and 30/50 mesh proppant at different closing pressures	XXXVIII
Figure 13-47: Permeability, conductivity and fracture width results in case of the 20:80 m/m% mixture of 16/32 and 30/50 mesh proppant at different closing pressures	XXXIX
Figure 13-48: API RP 19C crush test apparatus used for bulk density measurements ...	XL
Figure 13-49: Bulk density measurement setup	XLI
Figure 13-50: Bulk density measurement results on the proppant-pack mixtures	XLII
Figure 13-51: Simulation results I	XLIII
Figure 13-52: Simulation results II	XLIV
Figure 13-53: Simulation results III	XLV
Figure 13-54: Simulation results IV.	XLVI

Figure 13-55: Simulation results V.	XLVII
Figure 13-56: Residuals of the RSA model I.	XLVIII
Figure 13-57: Residuals of the RSA model II.	XLVIII
Figure 13-58: Response surface of the porosity values.....	XLIX
Figure 13-59: Residuals of the porosity RSM.....	XLIX
Figure 13-60: Convergence of the Danko model.....	L
Figure 13-61: Convergence of pressure difference of the Danko model.....	L

LIST OF TABLES

Table 4-1: Main Renewable Energy Sources and Their Usage Form	7
Table 6-1: Dimensions of the geometry	35
Table 6-2: Mesh quality indicators (Shen, 2019).....	38
Table 6-3: Results of sensitivity analysis for the effect of aspect ratio.....	40
Table 7-1: Summary of the basic parameters of the proppants.....	56
Table 7-2: Statistical comparison of the permeability results on the 30/50 mesh proppant	59
Table 7-3: Boundary conditions during the measurements	64
Table 7-4: Modified particle friction factor correlations considered in this study	65
Table 8-1: Dataset for the RSA.....	82
Table 8-2: Result of the RSA model	83
Table 8-3: Optimized permeability arrangement and proppant mixture	85
Table 13-1: Chemical analysis of waters associated with vapor-dominated and liquid-dominated geothermal systems (2/1)	VIII
Table 13-2: Chemical analysis of waters associated with vapor-dominated and liquid-dominated geothermal systems (2/2)	IX
Table 13-3: Status of global Enhanced Geothermal Systems	X
Table 13-4: Results of chemical treatment in selected geothermal fields	XI
Table 13-5: Different multistage fracturing projects in deviated or horizontal wells	XII

1 SUMMARY

Currently, Enhanced Geothermal Systems do not play a significant role in the renewable energy mix. In the past few years, several advancements were reached but the forecasts clearly indicate that although geothermal energy production has a major potential its widespread utilization is not probable without a compelling technological enhancement.

The research conducted and presented in the Thesis developed a novel EGS technology and established its theoretical background. First, a new idea was presented where a single-well, hydraulically fractured EGS system is defined where the fracture is supported by proppant. The fracture was divided into 4 circular zones in which the proppant permeability, thus the fracture permeability could be arbitrarily determined. With this method the deficiencies of the currently investigated similar approaches can be avoided, namely the whole rock surface is available for heat transfer and the different permeability zone provide an opportunity to control the flow in the fracture. A 3-dimensional Finite Element Model was built for simulating the new model. As a state-of-the-art approach, the steady-state and transient simulation was coupled in the model that facilitated to decrease in the required computational capacity. The model was validated by several API standard measurement that was carried out by the Author.

The research showed that the fluid flow in the propped fracture can be controlled by creating circular zones with different permeability values. This result proved the concept and open the possibility to optimize the permeability arrangement in the fracture to reach the best heat recovery. For the optimization purpose, a modern approach was designed based on a Response Surface Method applying multivariate polynomial regression. After the optimization, it was shown that the proposed technology if designed well can provide around 20 times better heat recovery from a geothermal resource than other models.

The research demonstrated that by mixing two proppant-packs the optimized fracture permeability values can be reached. For this, the Author performed several measurements and developed a new relationship between the modified particle friction factor and the proppant-pack permeability. With this new relationship, a semi-analytical model could be defined where the two driving mechanisms during flow through porous media could be integrated. A new bulk density measurement was also elaborated with which the proppant-pack porosities could be identified under different applied closing pressure.

The outcome of the research is a new EGS technology that can facilitate further studies and advancement in the renewable energy industry.

2 ÖSSZEFOGLALÁS

Jelenleg az *Enhanced Geothermal Systems* technológiák nem játszanak jelentős szerepet a megújuló energiaforrások tekintetében. Az elmúlt néhány évben számos előrelépés történt e területen, mindazonáltal az előrejelzések egyértelműen azt mutatják, hogy bár a geotermikus energiatermelésben komoly potenciál rejlik, széleskörű hasznosítása nem valószínűsíthető jelentős technológiai áttörés hiányában.

A kutatómunka során lefolytatott és a Disszertációban bemutatott kutatások során egy újszerű EGS technológia került kifejlesztésre, és annak elméleti megalapozására került sor. Először egy új ötlet került bemutatásra, ahol egy egyszeres kútban, hidraulikus rétegrepesztéssel létrehozott EGS rendszer került meghatározásra, ahol a repedést proppanttal van kitámasztva. A repedést 4 körkörös zónára került felosztásra, amelyekben a proppant permeabilitása, így a repedés permeabilitása tetszőlegesen meghatározható volt. Ezzel a módszerrel elkerülhetőek a jelenleg vizsgált hasonló megközelítések hiányosságai, vagyis a teljes kőzetfelület rendelkezésre áll hőátadás szempontjából, és az eltérő permeabilitási zónák lehetővé teszik a repedésben az áramlás szabályozását. Az új modell szimulálására egy 3 dimenziós végeelem modell készült. Korszerű megközelítésként a steady-state és a tranziens szimulációt összekapcsolásra került a modellben, ami elősegítette a szükséges számítási kapacitás csökkentését. A modellt a Szerző több API szabvány méréssel is validálta.

A kutatás kimutatta, hogy a proppanttal kitámasztott repedésben a folyadékáramlás szabályozható különböző permeabilitású kör alakú zónák kialakításával. Ez az eredmény igazolta a koncepciót, és megnyitotta a lehetőséget a repedés permeabilitási elrendezésének optimalizálására a legjobb hőkinyerés elérése érdekében. Az optimalizálás érdekében egy modern megközelítés került megtervezésre, amely a többváltozós polinomiális regressziót alkalmazó válaszfelületi módszeren alapul. Az optimalizálás után bebizonyosodott, hogy a javasolt technológia jól megtervezve körülbelül 20-szor jobb hővisszanyerést biztosíthat egy geotermikus erőforrásból, mint más modellek.

A kutatás kimutatta, hogy két *proppant-pack* összekeverésével az optimalizált repedés permeabilitási értékek elérhetőek. Ehhez a Szerző több mérést is végzett, és egy új összefüggést dolgozott ki a módosított részecskesúrlódási tényező és a *proppant-pack* permeabilitás között. Ezzel az új kapcsolattal egy félanalitikus modell definiálható, ahol a porózus közegen való áramlás során a két hajtómechanizmus integrálható. Kidolgozásra került egy új térfogatsűrűség-mérés is, amellyel a *proppant-pack* lehet meghatározni különböző alkalmazott zárónyomás mellett.

A kutatás eredménye egy új EGS technológia, amely elősegítheti a további tanulmányokat és előrelépést a megújuló energiaiparban.

ADVISORY RECOMMENDATION

Patrik Pusztai, the Thesis's Author, was born in Miskolc in 1992. At the University of Miskolc, he completed his Earth Science Engineering (B.Sc.) and Petroleum Engineering (M.Sc.) degrees in 2015 and 2017, respectively with excellent results. After that, the Author started his Ph.D. studies at the Mikoviny Sámuel Doctoral School of Earth Sciences and began his research on hydraulic fracturing and flows in micro and nano pore-size porous media in the Research Institute of Applied Earth Sciences in 2017. The researches were part of the international project GINOP 2.3.2-15-2016-100010, " Development of enhanced engineering methods with the aim at utilization of subterranean energy resources." He concurrently studied MBA (Master of Business Administration), and in 2019 he earned a degree certificate with an outstanding rating.

Along with performing exceedingly well in the training requirements, he also got a head start on his research by focusing on a specific chapter and the benefits of his habit. His research on a variety of hydraulic fracturing and porous flows topics was presented in outstanding venues, such as conferences and contests held on a national and international level. His main scientific achievements are the followings:

- 2014. Takács Ernő Scientific Student Competition, Miskolc: „Makói Palagáz” **1. place**
- 2014. Conference of Scientific Students' Associations, Miskolc: „Hidraulikus Rétegrepszítés Optimalizálása Költséghatékony Szempontból” **2. place**
- 2015. XXXII. National Conference of Scientific Students' Associations, Budapest: „Hidraulikus Rétegrepszítés Optimalizálása Költséghatékony Szempontból” **3. place**
- 2016. Conference of Scientific Students' Associations, Miskolc: „Overview and Application of Shale Gas Flow Models through a Hungarian Ultra High Pressure High Temperature (UHPHT) Reservoir’s Core Samples” **2. place**
- 2017. XXXIII. National Conference of Scientific Students' Associations, Dunaújváros: : „Overview and Application of Shale Gas Flow Models through a Hungarian Ultra High Pressure High Temperature (UHPHT) Reservoir’s Core Samples” **1. place**
- 2017. Gold Academic Medallion
- 2016. – 2017. “New National Excellence Scholarship”
- 2015. – 2017. “MOL Academic Scholarship”
- 2017. – 2018. “Diákhitel Scholarship”
- 2017. – 2018. „MNB Ösztöndíj”

He took **1. place** in the MOL FRESHHH international contest in 2018 (5,000 competitors), showcasing his aptitude for successfully overcoming engineering, financial, and optimization difficulties along the whole petroleum value chain. This accomplishment demonstrated his ability to address complicated problems by skillfully fusing the analytical and pragmatic mindsets and as a result the biggest Hungarian Petroleum company offered him a full-time job.

In 2018, at the beginning of his Ph.D. studies, the Author decided to investigate the potential of propped hydraulic fracture in case of geothermal energy production further based on his previous research experience. Therefore, he marked the title of his research activity as the „Flow Profile Control in Hydraulic Fractured Wells – Foundation of a New Geothermal Energy Production Technology”. The significance of the selected topic is justified by the increasing role of renewable energy resources in the energy mix. Furthermore, the lack of a comprehensive investigation of the single-well geothermal systems in the international literature points out the unique nature of the topic. In light of the aforementioned, the subject is not only current but also pioneering from a theoretical and practical standpoint. The Author of this Thesis successfully utilized his petroleum engineering and modeling knowledge to develop and investigate a new EGS (Enhanced Geothermal System) technology. This type of interdisciplinary research is not very common in international practice, and the promising new results may affect the future role of the geothermal energy production. The Thesis is appropriately constructed and proves the candidate’s skills in scientific research and publication. Several of the novel methods and numerical models developed by the Author can be considered as new scientific achievements in the discipline of hydraulic fracturing and/or geothermal energy. The candidate has fulfilled the requirements for the Ph.D. degree. He is the author or co-author of several scientific articles in this topic. Furthermore, he held several conference presentations in the topic at different conferences.

Miskolc, August 25, 2023

Dr. Krisztián Mátyás Baracza

Director, Senior Research Fellow

3 INTRODUCTION & TOPIC RELEVANCE

As global energy consumption will increase significantly in the future and the potentially available hydrocarbon resources are finite and become more expensive and difficult to reach, the role of renewable energy resources will be more prominent. It is also promoted by intense environmental endeavors in the form of regulatory and social pressure. Geothermal energy resources have an immense potential, but today do not play a significant role in the renewable energy mix. It is mainly because the economics are highly dependent on the geological and regulatory environment and usually have a higher investment need, thus a longer pay-back time. Without technological innovation, it is unlikely that this energy carrier will play a vital function in the future.

Several different geological formation and technology is available to harvest the energy of the Earth crust. The precursor and inspiration of this research was the Enhanced Geothermal Systems (EGS). There is not a universally accepted definition of EGS, but in most cases it covers technologies that make a geothermal reservoir economically viable to harvest. In most cases these technologies involve one or more injection and production wells to be implemented. Later studies such as [Kehrer et al. \(2007\)](#) and [Danko et al. \(2018\)](#) offers EGS systems where the injection and production are integrated in one well, thus reducing the cost of the total investment. These methods although have some advantages also have some limitations that promotes further investigations in this area.

3.1 Research purpose & research conducted

The main goal of this study is to offer a novel EGS technology and elaborate on the essential theoretical background to facilitate further scientific research and tests in this area. The extensively employed hydraulic fracturing procedure in the oil and gas industry served as the foundation of this method. Although utilization of hydraulic fracturing technology for more efficient geothermal energy production is at the center of several current studies, with this new approach the energy production can be reached in a single well that potentially reduces the investment cost of the project. One of the unique ideas in this method is to create a more efficient flow profile (at the point of heat recovery) in the fracture by forming zones with different permeabilities in the fracture. In this way the surface that is available for heat recovery is not limited by any means and the flow can be optimized in the fracture to reach the maximum heat recovery from the system. It can be reached by a propping

agent, the so-called proppant. A conceptual representation of this new approach is illustrated in [Fig. 3-1](#), where only one side of the fracture's cross-section is represented.

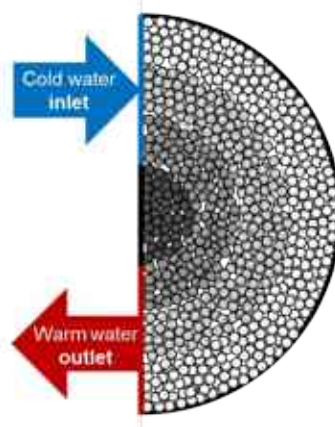


Figure 3-1: Visual representation of the new approach¹

The different concentric zones have different permeability values, thus providing a flow control mechanism in the fracture. In this thesis, a new semi-analytical approach is developed to reach arbitrary permeability values by mixing two distinct proppant packs together in different mass ratios. With this novel method, it can be determined in what mass percentage should two proppant-pack be mixed to provide the necessary permeability values under reservoir conditions.

During this EGS method, the obtained flow profile in the fracture can be described as a steady-state phenomenon, but in contrast, the heat recovery is constantly decreasing as the fluid draws the reservoir temperature down, so it is a transient phenomenon. This complex problem can be solved only numerically. The most popular approach in computational fluid dynamics is the Finite Element Method (FEM) because it uses the most stable numerical scheme ([Rapp, 2023](#)). For this reason, a FEM model was developed in this thesis where the computational domain is initially divided into discrete components so the describing differential equations can be solved numerically. Although the fracture often can be described in 2-dimension, in this special case where the heat recovery mainly takes place perpendicular to the fracture a 3-dimensional model had to be developed. In this research, a state-of-the-art, coupled steady-state – transient simulation was developed where the flow profile was reached by a steady-state simulation, and it coupled to the transient simulation where the heat recovery can be calculated. The results of the coupled model are illustrated in [Fig. 3-2](#).

¹ All the figures and tables are self-edited where it is not indicated otherwise.

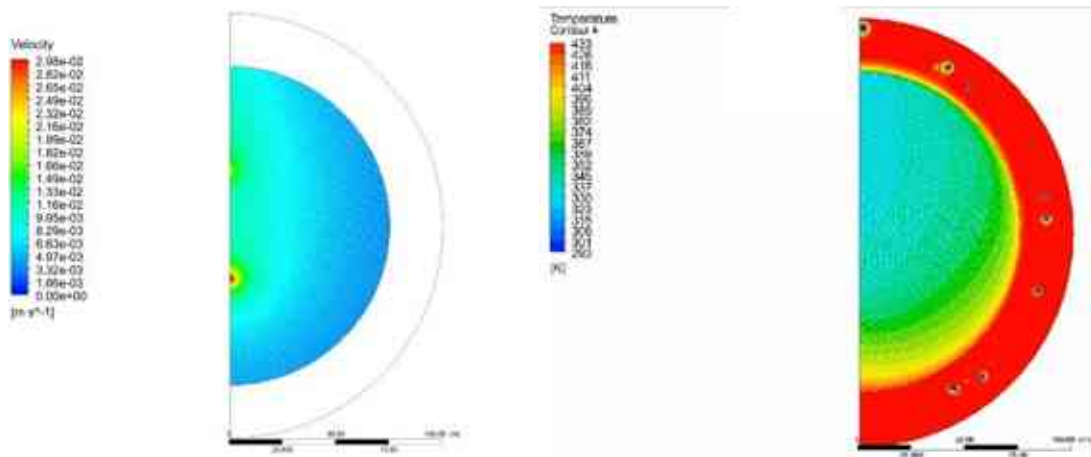


Figure 3-2: Results of the coupled model (left: flow profile reached by the steady-state simulation, right: temperature profile reached by the transient simulation)

After the numerical model was established the validation of the model was essential. For this purpose, several API standard measurements were performed and a new 3-dimensional model was built based on the apparatus. The measurements and the FEM results were compared.

The FEM simulation can require significant calculating capacities depending on the model and number of discrete elements. Since the dimensions of the fracture is several magnitudes smaller than the geothermal reservoir the developed model become robust and required several weeks to complete. To overcome this limitation an evolutionary algorithm-based optimization method was developed where the regression model resulted in a significant time reduction.

Numerous arrangements of the proppant-pack permeabilities can be reached in the fracture and all of them provide different thermal drawdown and production efficiency. To find the best arrangement of the zones (in the point of heat recovery) a response surface optimization method was developed with the integration of a multivariate polynomial regression.

The research techniques included all the conventional scientific techniques:

- literature review to identify perspectives,
- investigating analytical and numerical models to define research goals,
- semi-analytical model development to describe the phenomenon,
- numerical model development to represents transport phenomenon,
- performing laboratory experiments to validate the created numerical model
- utilize numerous optimization methods to make the most out of the models

4 ENERGY OUTLOOK

Before introducing the current study, it is important to have a basic knowledge about the energy mix and the role of renewable resources especially geothermal energy production.

Nowadays the renewable energy resources come into prominence as it is supported by social and regulatory background as well. The energy consumption in absolute term is increasing significantly meanwhile the energy mix is changing year by year. On [Fig. 4-1](#) the evolution of the primary energy consumption can be seen from 1990 to 2018.

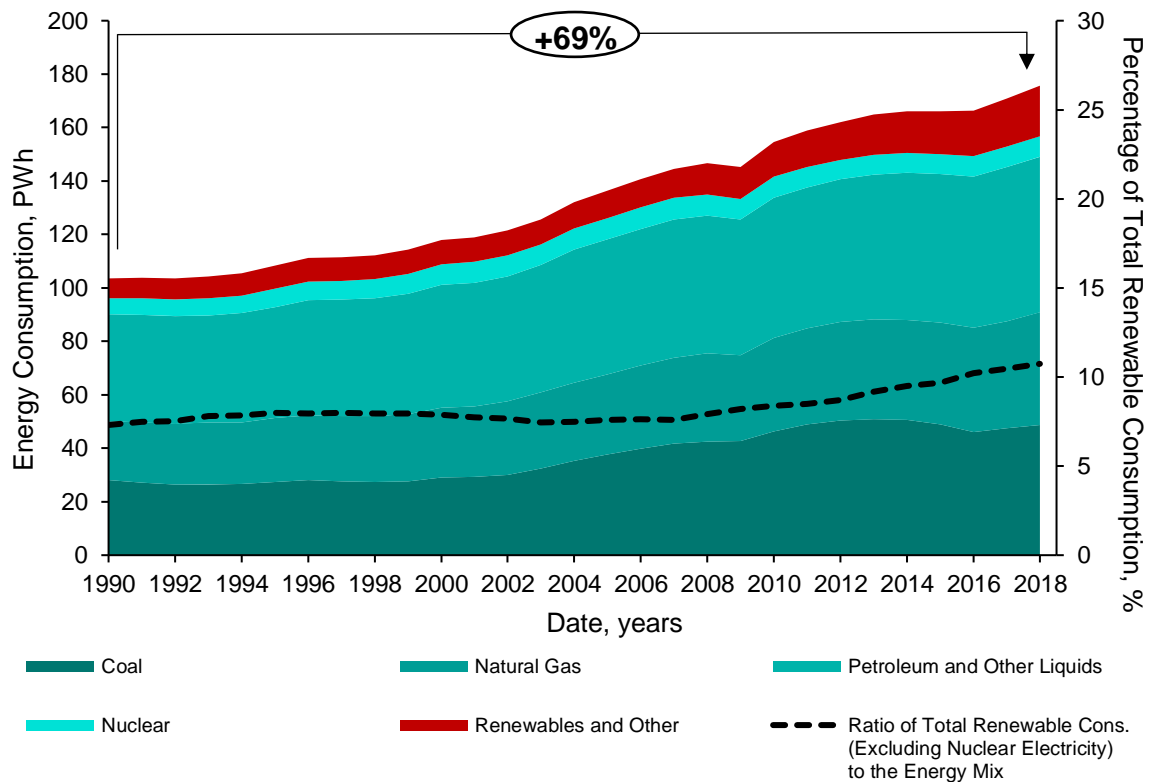


Figure 4-1: Global total energy consumption by energy source, 1990 - 2018 ([EIA, 2021a](#))

The vast majority of energy consumption come from fossil fuels as it has been in the past as well. In absolute term the total energy consumption of the world was around 100×10^{15} Wh in 1990 and its value increased by 69% till 2018. A slight increase can be identified in the ratio of renewable energy consumption to the total energy consumption and in 2018 the level of it reached around 11%. It is foreseen that the renewable energy sources will have a more dominant role in the upcoming years. In a conservative approach (absent significant changes in policy or technology) the ratio of renewable energy consumption in the total energy mix will have a value around 27% by 2050. The projection can be seen in the [Fig. 4-2](#).

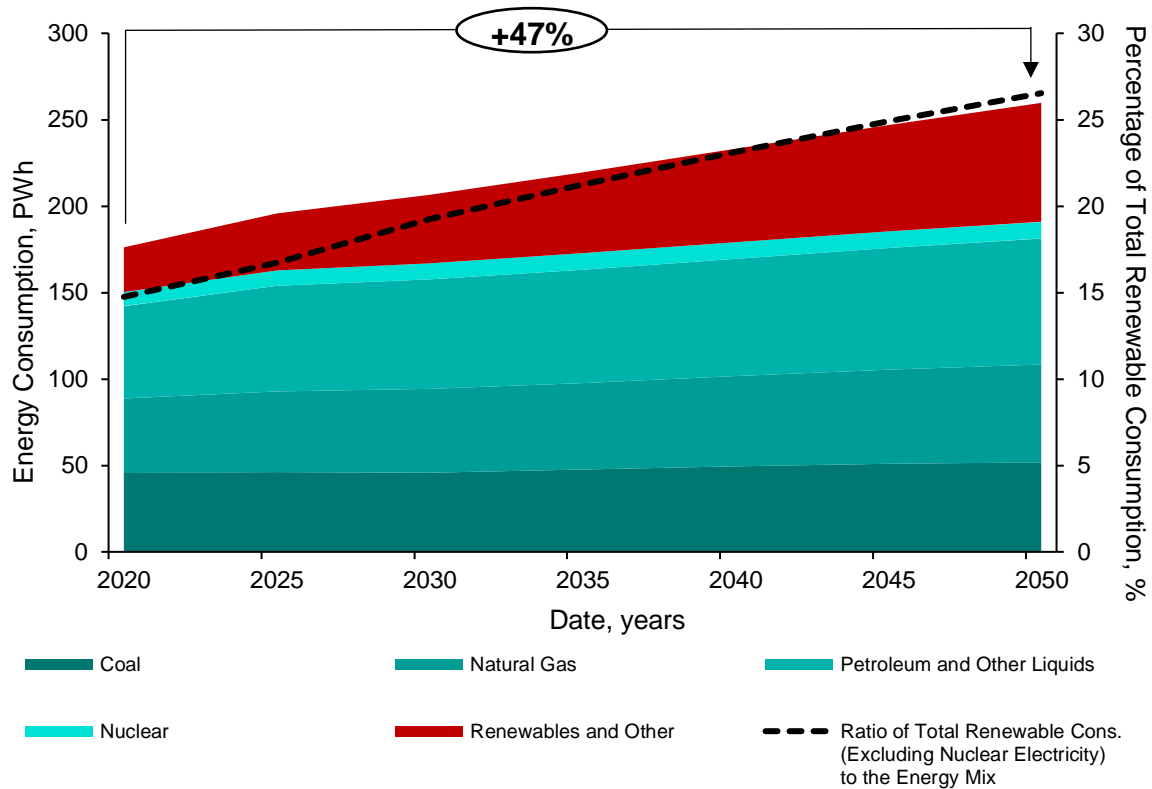


Figure 4-2: Projection of global primary energy consumption by energy source, 2020 - 2050 ([EIA, 2021b](#))

The forecast shows that the global energy consumption will increase nearly 50% over the next three decades. Although fossil fuels will remain the world’s largest energy source in 2050, the contribution of renewable energy sources will grow above 25%. In absolute term the total energy consumption will increase in the future but at a slower pace as in the past 20 years due to energy efficiency improvements both in the industrial and residential sector. Decreasing technology costs and supportive government policies can further promote the propagation of renewable energy sources leading to that the renewable energy sector is (and will be) the fastest-growing sector in the world. Also, an interesting result of the analysis is that the available projections in almost all consecutive years forecast higher and higher contribution of the renewable energy power generation. During the past 12 years the projected power generation for 2030 has been increased by 47%. This phenomenon can be seen in the [Fig. 4-3](#).

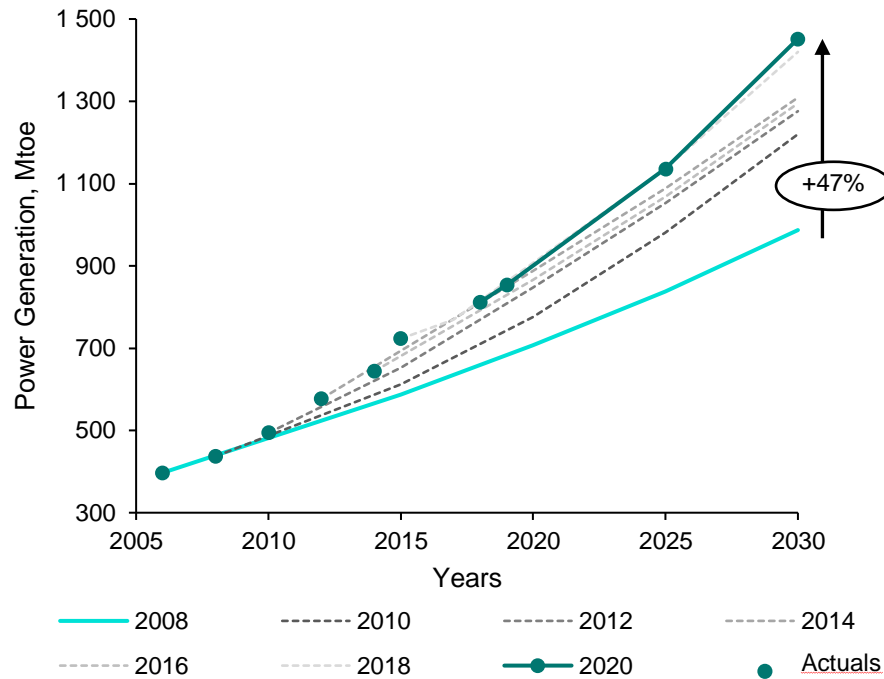


Figure 4-3: World's power generation projections in two year increment^{2,3,4,5} (IEA, 2008; IEA, 2010; IEA, 2012; IEA, 2014; IEA, 2016; IEA, 2018; IEA, 2020)

Renewable energy sources utilize variety of different types of energy sources. The main types of energy sources can be identified in the [Tab. 4-1](#). The common characteristics of all type of renewable energy sources is that they have a potential to provide energy with almost zero emissions of air pollutants and greenhouse gases and they are able to replenish themselves naturally. Despite the numerous advantages of renewable energy, several limitations exist. The main important shortcoming come from the fact that most of the energy sources are climate-dependent which results discontinuity in energy generation due to seasonal variations ([Owusu and Asumadu-Sarkodie, 2016](#)).

² 2008 data are for Reference Scenario, 2012-2018 data are for New Policies Scenario, 2020 data are for Stated Policies Scenario

³ „**Reference Scenario**, indicate what would happen if, among other things, there were to be no new energy-policy interventions by governments beyond those already adopted by mid-2008.” ([IEA, 2008](#))

⁴ “**New Policies Scenario** — takes account of the broad policy commitments and plans that have been announced by countries around the world, including the national pledges to reduce greenhouse-gas emissions and plans to phase out fossil-energy subsidies even where the measures to implement these commitments have yet to be identified or announced.” ([IEA, 2010](#))

⁵ “**Stated Policies Scenario** (STEPS) is based on today's policy settings and an assumption that the pandemic is brought under control in 2021. In this scenario, global GDP also returns to pre-crisis levels in 2021, and global energy demand in early 2023, but outcomes vary sharply by fuel. Renewables meet 90% of the strong growth in global electricity demand over the next two decades, led by continued high levels of solar PV deployment, but global coal use never gets back to previous levels. By 2040, coal's share in global energy demand dips below 20% for the first time in modern energy history.” ([IEA, 2020](#))

Table 4-1: Main Renewable Energy Sources and Their Usage Form

Energy Source	Energy Conversion and Usage Options
Hydropower	Power Generation
Modern Biomass	Heat and power generation, pyrolysis, gasification, digestion
Geothermal	Urban heating, power generation, hydrothermal, hot dry rock
Solar	Solar home system, solar dryers, solar cookers
Direct Solar	Photovoltaic, thermal power generation, water heaters
Wind	Power generation, wind generators, windmills, water pumps
Wave	Numerous designs
Tidal	Barrage, tidal stream

(Panwar et al., 2011)

Due to supportive regulatory and social background the installed capacities of different renewable resources have been increasing significantly from 2000. The hydropower has the most dominant role in the mix but other energy sources like wind and solar are utilized in an increasing rate as growing number of plants are installed. In Fig. 4-4 the installed total energy capacities can be identified in case of different sources. Hydropower contains wave and tidal energy utilization and solar contains direct solar utilization in the figure. Bioenergy includes traditional usage such as combustion of biomass and modern usage such as liquid biofuel production.

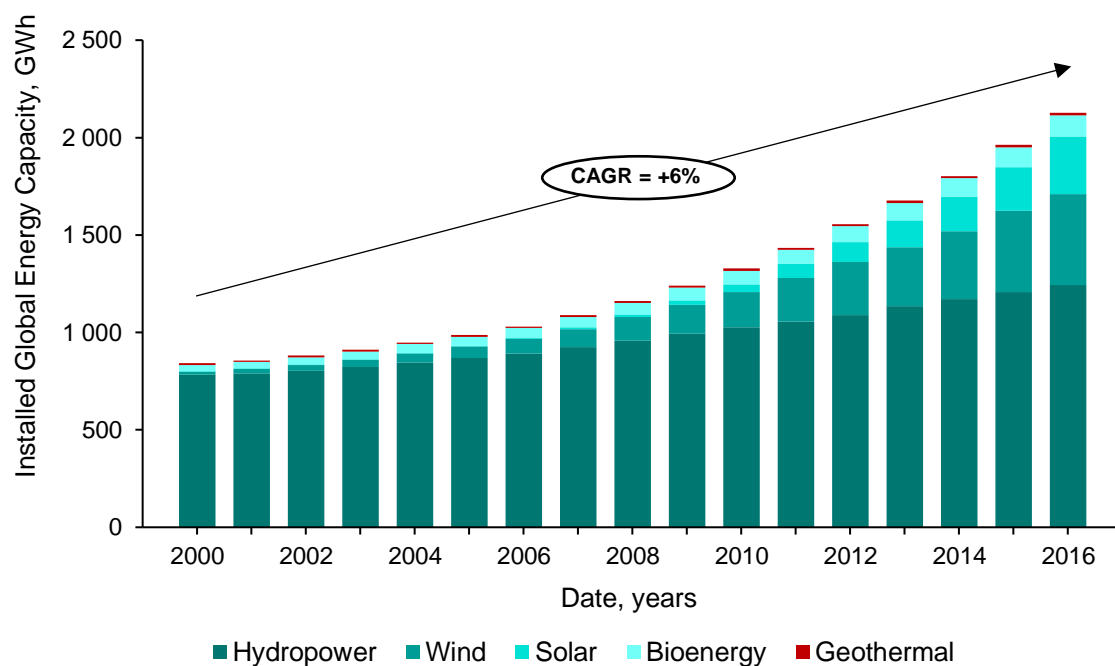


Figure 4-4: Installed global renewable energy capacity by technology, 2000 - 2016
(Ritchie and Roser, 2020)

Although one can see that the compound annual growth rate (CAGR) is +6% from 2000 to 2016 but the cumulative growth can be represented by an exponential curve rather.

There are dissimilarities among the different technologies as some of them can be connected to special local attributions and with it to different cost levels. It is necessary to investigate the levelized cost of energy (LCOE⁶) of each technology to get a clearer picture about the evolution and significance of these types of energy sources. [Fig. 4-5](#) shows the LCOE values of different technologies in 2010 and in 2020. Also, the diameter of the circles represents the size of the projects, with its center the value for the cost of each project on the Y-axis.

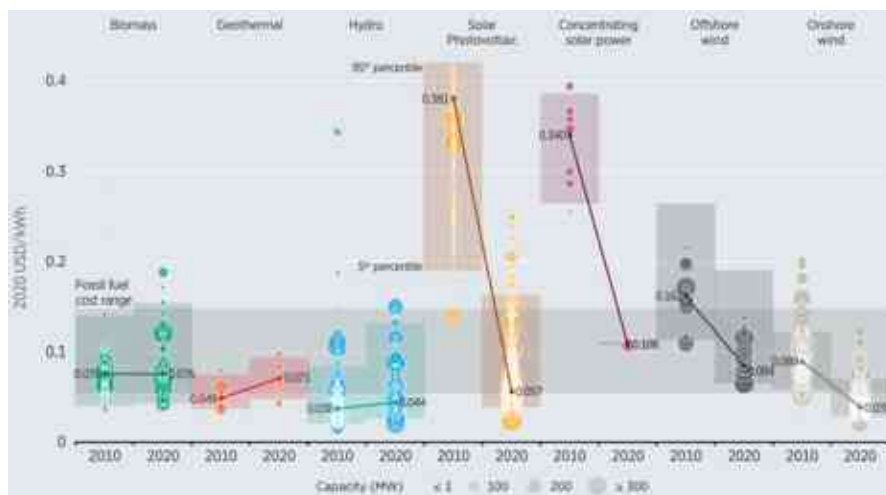


Figure 4-5: Global LCOEs from newly commissioned, utility-scale renewable power generation technologies, 2010-2020 ([IRENA, 2021](#))

Today, the unit costs of each renewable energy technologies are compatible with energy generated from fossil fuels. It can be identified that the unit costs significantly decreased in case of solar and wind technologies while stagnate or increased in case of other technologies. This lowering cost can be one of the most dominant triggers of the wide spreading of these technologies. In case of geothermal projects, the unit costs are one of the lowest but as the effectiveness of the technology is highly dependent on local nature the number and size of the projects are remained low in 2020. Number of projects increased significantly in case of biomass, hydro, solar and wind as renewable energy technologies are subsidized significantly in the past decade. It is worth to mention that the economic crisis caused by the COVID-19 in 2020 had a significant effect on industrial size projects.

⁶ “The LCOE metric provides an indication of the unit energy cost over the full life of a project, including capital, operating and financing costs.” ([Aldersey-Williams and Rubert, 2019](#))

5 GEOTHERMAL ENERGY

Geothermal energy is referred as the energy derived from the heat in the Earth interior ([Barbier, 1997](#)). The source of geothermal energy is the continuous heat energy flux flowing from the interior of the Earth to the surface ([Ismail, 2019](#)). It is usually described by the *geothermal gradient*, which comes from a combination of residual heat from planetary accretion (20%) and heat produced through radioactive decay of uranium, thorium, and potassium (80%) and its magnitude depends on the rate of heat production at depth, the dynamics of the system, and the conductivity of rocks ([Arndt, 2011](#)). The average geothermal gradient of the Earth (besides the anomalous volcanically active regions) is between 10 – 30 °C/km ([Banks, 2012](#)). [Beckers et al. \(2014\)](#) suggests a grouping method for the differentiation of geothermal resource grade, where low-grade is 30 °C/km, medium-grade is 50 °C/km and high-grade is 70 °C/km.

Geothermal energy is considered to be the only energy source that can supply power, independent of the climate ([Bronicki, 2016](#)). Geothermal energy as a renewable energy source was disputed by scientists as it is considered to be the only renewable that does not depend on sunlight; however, “it must be tapped slowly enough so as not to deplete the accessible reservoir of heat, and thus be truly renewable” ([Brown et al., 1990](#)). [Kozloff and Dower \(1993\)](#) pointed out that whether a resource can be considered as renewable depends on the time frame. It was suggested that if continuous production can be maintained, by today’s projection, at least for 300 years, then that fuel can be considered renewable since technical advances during that time will have rendered today’s perspective obsolete. In case of geothermal energy, the complete recovery of the reservoir temperature is typically less than 10 times the production period ([Mock et al., 1997](#)).

The geothermal potential of the Earth is vast. It is estimated that the energy stored at depth of 3 km is 43×10^6 EJ which is several magnitudes larger than the energy potential of all the fossil fuel combined ($\sim 36 \times 10^3$ EJ) ([Chandrasekharam and Bundschuh, 2008](#)). Unlike other conventional and renewable energy sources geothermal energy has distinct characterizations ([Ismail, 2011](#)):

- Available and stable always throughout the year
- Independent of weather conditions
- Has an inherent storage capacity

Besides these advantages it is also considered to be an environmentally friendly, clean energy source ([Chandrasekharam and Bundschuh, 2008](#)).

Although several benefits are associated to geothermal energy production, the utilization of it is low and all the different projections anticipate very moderate increase ([Fig. 5-1](#)). This phenomenon can be interpreted by different factors ([Kabeyi, 2019](#)):

- scarcity of exploitable sites (geological peculiarity),
- remote locations often far from load centers,
- undesirable gaseous emissions,
- expensive drilling (and success is not assured),
- funding and regulatory background,
- long gestation periods of between 5 and 10 years for conventional power plants.

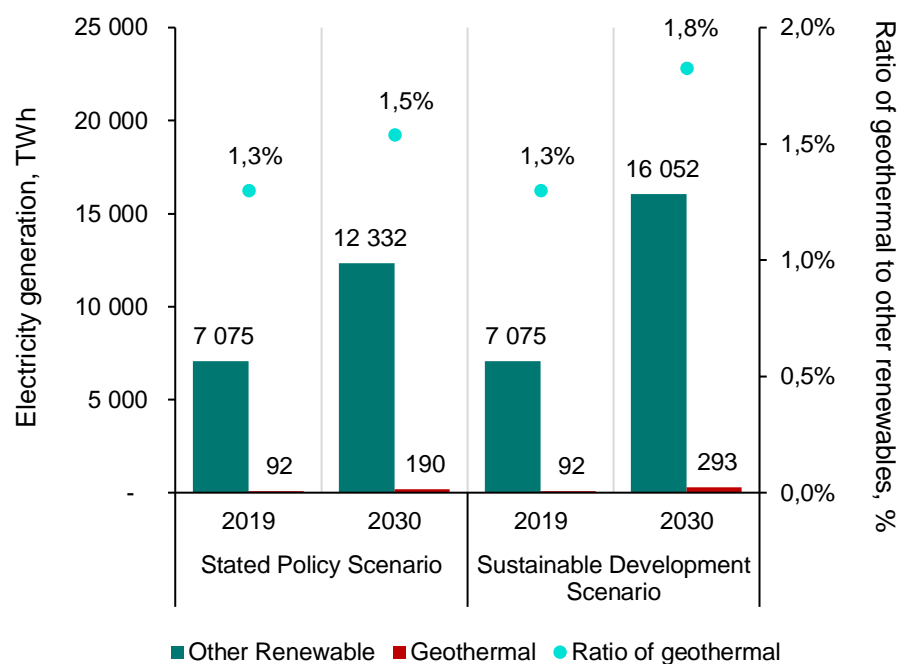


Figure 5-1: Current and projected electricity generation from renewable resources in case of stated policy and sustainable development scenario⁷ ([IEA, 2020](#))

It can be readily inferred that the role of geothermal energy in the renewable energy mix is and will be minimal unless the limiting factors can be resolved. A technological breakthrough in this field can facilitate the geothermal energy to reach yet untapped resources and have a more prominent role in the future.

⁷ “In the **Sustainable Development Scenario** (SDS), a surge in clean energy policies and investment puts the energy system on track to achieve sustainable energy objectives in full, including the Paris Agreement, energy access and air quality goals. The assumptions on public health and the economy are the same as in the STEPS.” ([IEA, 2020](#))

5.1 Geothermal Energy Utilization

The utilization of geothermal energy can be divided into the part used for electricity generation (indirect) and the part used for directly for heating purposes (direct). The direct and indirect power generation can be seen in the [Fig. 5-2](#) from 1995 to 2020, where data has been collected from several sources (direct power generation represented in 2020 is from data provided for end of 2019).

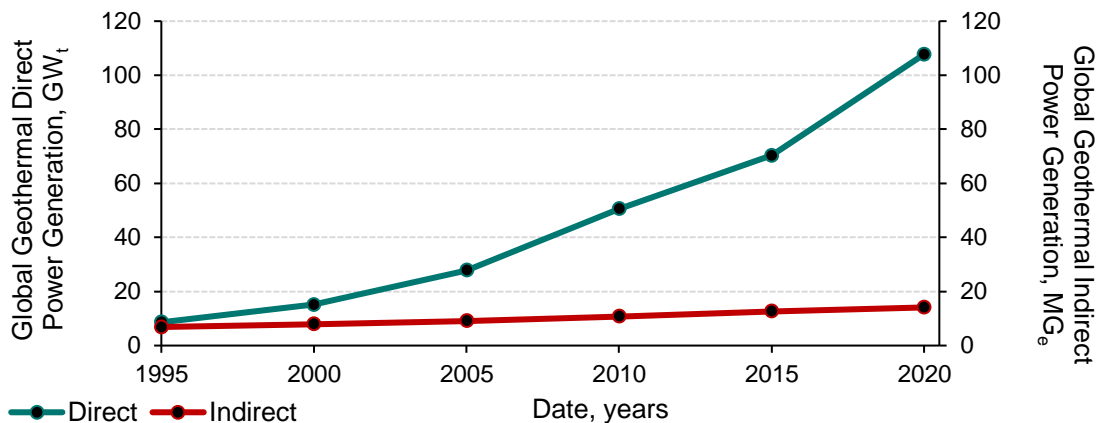


Figure 5-2: Global direct and indirect geothermal power generation, 1995 – 2015 ([IGA, 2021](#); [Lund and Toth, 2021](#); [REN, 2021](#))

The annual growth rate of direct geothermal power generation is around 11%, while the indirect geothermal power generation is 3%. In absolute terms at the end of 2019 the total global direct geothermal power generation reached more than 107.0 GW_t in contrast the electrical power generation reached only 14.1 GW_e .

5.1.1 Direct Geothermal Energy Utilization

Direct utilizations have a wide variety of end uses where the most common types are space heating, greenhouse, fish farming, bathing and industry ([Hammons, 2004](#)). Direct geothermal application can use both low temperature (from 10°C for soil warming) and high temperature (from 150°C for cement drying) resources and so these utilization method is much widespread in the world than electricity generation ([Hammons, 2004](#); [Mock et al., 1997](#)). The main direct applications in 2020 can be visualized in [Fig. 5-3](#), where others contain agricultural drying, cooling/snow melting, industrial uses, aquacultural pond heating and other minor usage like animal husbandry, spirulina cultivation, desalination, and sterilization of bottles. The most dominant contributor of the direct geothermal utilization is the geothermal heat pump, which accounts for 71.6% of the world installed capacity and the number of countries with such installations has more than doubled from 2000 to 2020 reaching 54 ([Lund and Toth, 2021](#)). The compound annual growth rate of the geothermal

heat pump capacity is +16.1%, while this value in case of the rest of the direct utilization technologies is +6.1%. It is worth to mention that the annual growth rate of geothermal direct utilization is exponential and so a linear line does not reflect the true potential of this sector.

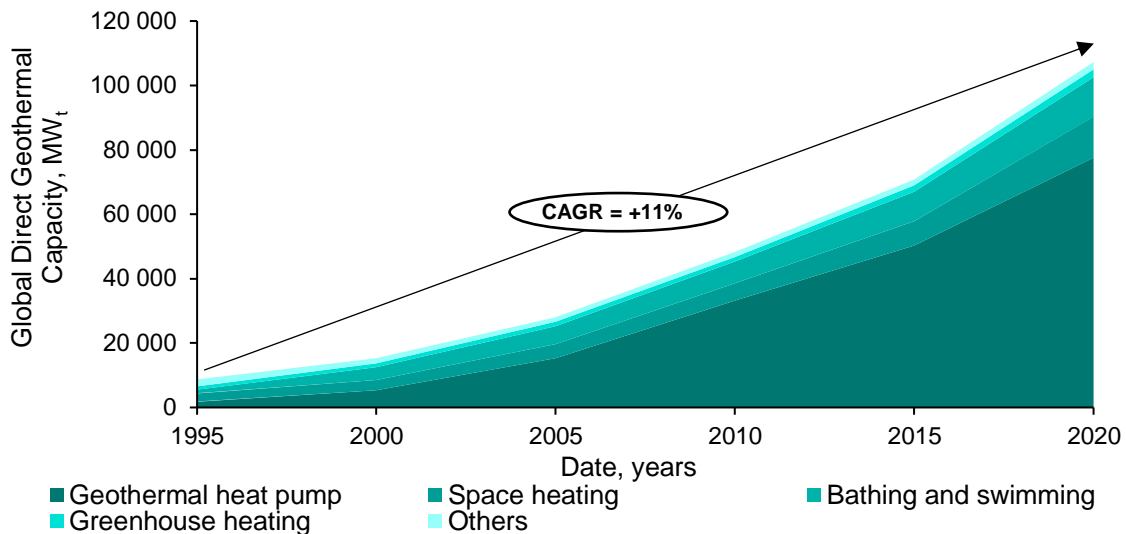


Figure 5-3: Global direct geothermal capacity by use, 1995 – 2020 ([Lund and Toth, 2021](#))

5.1.2 Indirect Geothermal Energy Utilization

Indirect geothermal energy utilization involves a power conversion technology that convert the thermal energy content of geothermal fluid into mechanical power to drive a generator and produce electricity ([Bronicki, 2016](#)). Several different technologies are available for this conversion ([DiPippo, 2016a](#); [Smith, 2016](#); [Dincer and Ezzat, 2018](#), [Fazal and Kamran, 2021](#)):

- **Direct steam** geothermal energy conversion systems (*dry steam* and *superheated steam* plants): The steam is produced directly from the underground reservoir to the power plant where it is directed into a turbine/generator unit. This was the first commercialized type of geothermal power plant.
- **Flash steam** geothermal energy conversion systems (*single-, double-, and triple-flash* and *combined-cycle* plants): This type of geothermal power generation is the most used technique worldwide, especially at higher temperatures (higher than 182°C). Mixture of hot water and steam is produced from the geothermal reservoir (as it flows upward the pressure decreases and some of the water boil to steam as well) and the mixture is flashed (up to several stages) and the steam is used to power a turbine/generator. As of 2018 the single and double flash stages are dominating the commercially available geothermal power plants with around two-third of installed geothermal power plant.

- **Total flow and other** systems involving two-phase expansion: As there is a considerable loss due to separation of the liquids the power output of the system can be improved by using an expander to expand the geothermal fluid mixture.
- **Binary** geothermal energy conversion systems (*basic Rankine, dual-pressure, and dual-fluid* cycles): Binary cycle power plants operate at lower temperatures water (about 107-182°C) and so this hot water is used to boil a working fluid which then turn the turbine/generator.
- **Combined and Hybrid** Geothermal Power Systems: These systems consist of either combination of different types of geothermal energy conversion systems or some type of geothermal plant combined with a plant using other different source of energy. One example can be seen in [Appendix A](#), which shows the aerial view of the Stillwater power plant in Nevada, USA where a photovoltaic (PV) power plant with a peak capacity of 26 MW was combined with a geothermal binary plant reaching the total installed capacity of 47.2 MW.

Schematic representations of the above-mentioned technologies can be seen in [Appendix B-G](#). These different technologies have been developed to reach higher efficiency of the plants as geothermal power plants have lower efficiency relative to other thermal power plants, such as coal, natural gas, oil and nuclear power stations. It can be seen on the [Fig. 5-4](#) those other types of power plants can reach efficiency between 30% and 40%, while geothermal power plants' average efficiency is slightly above 10%. This lower efficiency level can be described by several different factors: geothermal fluid energy loss (because it should led through several pieces of equipment); separating losses; non-condensable gas (NCG) content; heat loss from equipment; turbine and generator efficiency and power plant parasitic load (e.g. fans, pumps, and gas extraction system) ([Zarrouk and Moon, 2014](#)).

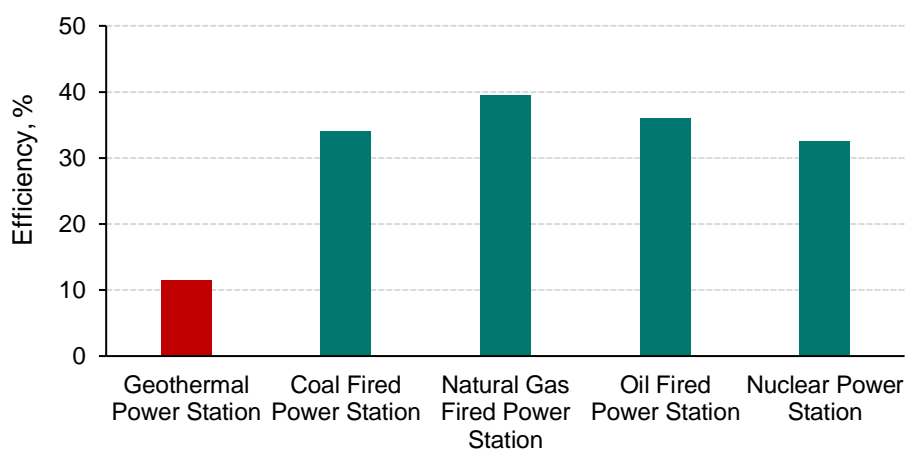


Figure 5-4: Thermal power plant efficiency comparison ([Zarrouk and Moon, 2014](#))

5.2 Geothermal Resources

The basic requirements for geothermal systems are listed below and each element can be also identified on [Fig. 5-5](#) ([Gupta and Roy, 2007a](#); [Barbier, 2002](#)):

1. Large source of heat
2. Reservoir to accumulate heat
3. Barrier to hold the accumulated heat
4. (Recharge area – in case of sources where natural fluid is supplied)

There are different geological conditions that could result in a variety of geothermal systems. However, based on common characteristics these can broadly classified in different groups ([Gupta and Roy, 2017a](#)). Four commonly used categories are described in the following subchapters.

5.2.1 Hydrothermal resources

Hydrothermal resources contain steam and/or high-temperature water and because of the convectively active, permeable reservoir the geothermal fluid can be produced spontaneously ([Mock et al., 1997](#)).

- **Vapor-dominated** systems contains water at high pressure and temperature more than 100 °C. When this water is produced to the surface the pressure is reduced and large quantities of steam is generated, thus producing a mixture of saturated steam and water. The ratio of steam to water varies from one site to another. Fields which provide superheated steam with no associated fluids are also known as *Dry Steam* fields ([Gupta and Roy, 2007a](#)). Vapor-dominated geothermal sources are less frequent, and they are usually exploited to produce electricity ([Mock et al. 1997](#)). Some of the best-known vapor-dominated geothermal fields are listed below:
 - The Geysers field in the United States with an installed capacity of ~1,590 MW in 2010 ([Brophy et al., 2010](#));
 - Cerro Prieto field in Mexico with an installed capacity of ~720 MW in 2007 ([Gupta and Roy, 2007b](#));
 - Larderello field in Italy with an installed capacity of ~550 MW ([Dincer and Ezzat, 2018](#)).
- **Liquid-dominated** resources are characterized by liquid water as the continuous pressure-controlling fluid phase ([Gupta and Roy, 2007a](#)). These types of sources are more frequent than vapor-dominated types. Fields containing low salinity water and reaching temperature up to 350 °C can be considered as high quality. Resources with

fluid temperatures ranging from 40°C to 300°C are being used commercially worldwide for generating electricity and/or providing process and residential heat ([Mock et al. 1997](#)). Some well known liquid-dominated geothermal fields are listed below:

- Wairakei field in New Zealand with an installed capacity of ~175 MW ([Thain and Carey, 2009](#));
 - Ahuachapan field in El Salvador with an installed capacity of ~95 MW ([Moya Rojas, 2016](#); [DiPippo, 2016c](#)).
- **Hybrid** resources can be found several places in their natural states as contained both vapor-dominated and liquid-dominated regions. In some cases, the field is liquid-dominated driven by an up flow of liquid and on the top of it there is a small vapor-dominated region because of the lower overburden pressure. Some examples are listed below:
 - Los Azufres field in Mexico with an installed capacity of ~270 MW ([Gutiérrez-Negrín et al., 2020](#));
 - Olkaria field in Kenya with an installed capacity of ~150 MW ([Axelsson et al., 2013](#)).

On the other hand, there are fields where the up flow is vapor-dominated, but a central steam “jet” pushes through a liquid layer ([Grant and Bixley, 2011](#)). An example for this:

- Patuha field in Indonesia with an installed capacity of 55 MW ([Ashat et al., 2019](#)).

During production the characteristic of the resource can be changed significantly as in case of a liquid-dominated resource during production the reservoir pressure is continuously depleting (without any fluid injection to the system) thus reaching the boiling point of the fluid and become more a vapor-dominated resource. This phenomenon was experienced at the Wairakei field in New Zealand ([Grant and Bixley, 2011](#)).

A general arrangement can be visualized on [Fig. 5-5](#). It should be noted that the fluid composition of different hydrothermal resources can significantly vary and thus, it should be taken into account in case of the exploitation of these resources. The main chemical composition of some geothermal fluids is collected in [Appendix H-I](#).

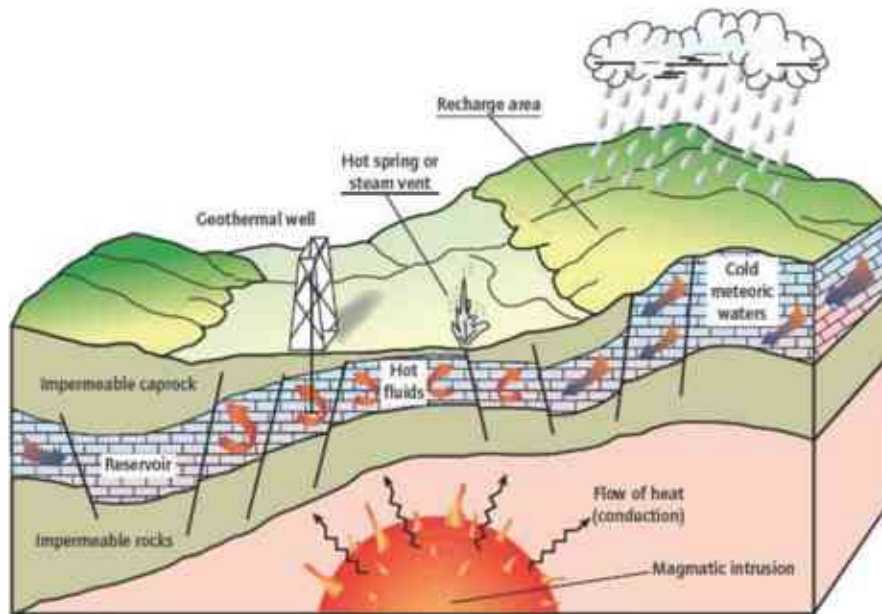


Figure 5-5: Schematic figure of a typical hydrothermal geothermal source with its main elements ([Barbier, 2002](#))

5.2.2 Hot Dry Rock resources

Hot Dry Rock (HDR) geothermal resources are those subsurface reservoirs where fluid is not naturally present ([Soelaiman, 2016](#)). In theory, these types of geothermal sources are available everywhere around the globe by drilling sufficiently deep wells ([Mock et al. 1997](#)). In practice the geothermal gradient, specific for the given area one of the key drivers for an economically viable field as greater geothermal gradient results shorter and so cheaper well drilling procedure. Usually, HDR geothermal resources are considered to have higher than average geothermal gradient, so the depth of the rock is shallow enough to be accessible (< 3 000 m) ([Salameh, 2014](#)). In case of a reservoir that have suitable porosity (matrix or fracture) it is technically possible to inject water into the rock and produce back the heated water with another well(s) ([Fanchi, 2010](#)). Often these types of reservoirs are tight, so an economical production rate cannot be achieved without the utilization of a formation intensification method, such as hydraulic or explosive fracturing ([Bronicki, 2003](#)). A practical arrangement can be visualized on [Fig. 5-6](#), where the simplified surface and subsurface structures can be seen at the Hijiori test site in Japan. If an enhancement method is applied to utilize the geothermal heat of the formation the term “EGS – Enhanced Geothermal System” is used ([Soelaiman, 2016](#)) (detailed in chapter [5.3](#)). It is often reached by the implementation of one or more injection wells (see in [Fig. 5-6](#)). In cases where natural water is present in open fractures or in rock matrix porosity in some extent, the geothermal source is often referred as *Hot Wet Rock* ([Mock et al., 1997](#)).

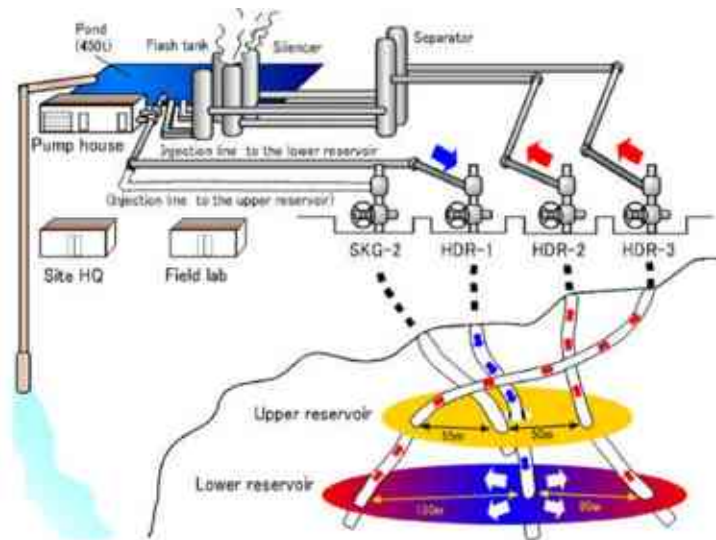


Figure 5-6: Simplified surface and subsurface system of Hijiori site ([Oikawa et al., 2021](#))

5.2.3 Magma resources

Magma resources (or molten rock) exploit the convective heat of the molten magma in the upper 10 km of the continental crust. In some cases, a portion of the convective heat is transferred to *hydrothermal* systems and this energy is available as conventional geothermal energy ([Hardee, 1981](#)). As this conventional energy represents a relatively small fraction of the total convective energy in the magma the utilization of the magma resources usually reached by the creation of a heat exchanger on the surface of the lava flow ([Kundu, 2017](#)). As these types of sources are rubbing the border of the current drilling and well completion technics only a few pilot plants exist. One example is the Iceland Deep Drilling Project (IDDP) that investigates the possibility of greatly increasing the energy resources of Iceland by producing deep, high-enthalpy, supercritical⁸ geothermal fluid. [Fridleifsson et al. \(2010\)](#) introduced that a geothermal production well that producing supercritical water can exceed the electricity generation potential compared to a traditional well by 10 times. The first well (out of the proposed three) was attempted to drill 4.5 km deep into a supercritical zone in the Krafla Geothermal Field but it had to be terminated at 2.1 km as >900 °C magma flowed into it. The well was completed to produce from the >500 °C zone thus it become the world's hottest producing geothermal well ([Elders et al., 2014](#); [Palsson et al., 2014](#)). The schematic representation of the reservoir and the well can be seen in [Fig. 5-7](#), where it can be identified that 3 attempts were initiated unsuccessfully to drill deeper by avoiding the intruded zone. In 2017 the drilling of IDDP-2 at Reykjanes

⁸ Supercritical: The critical point for pure water, where the distinction between liquid, vapor, and steam disappears, is at 374°C and 22.1 MPa ([Fridleifsson et al., 2020](#))

Peninsula in Iceland was finished at 4,659 meters depth. Although successful flow test has not been performed until the end of 2020, the project has already demonstrated that it is possible to drill a supercritical geothermal well, resulting that it is the deepest and hottest (estimated around 535 °C) drillhole so far sited on an active mid-ocean spreading center ([Fridleifsson et al., 2020](#)).

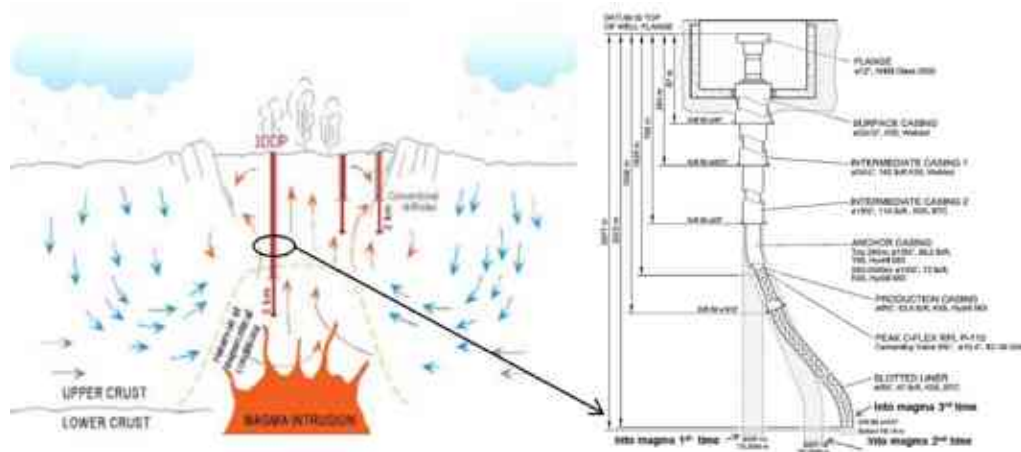


Figure 5-7: Schematic representation of the IDDP-1 well and reservoir with the “as-built” drawing of the well ([Elders and Fridleifsson, 2010](#); [Palsson et al., 2014](#))

5.2.4 Geopressured resources

Geopressured resources are constituted by a hydrothermal reservoir with a higher pore pressure than hydrostatic reference and containing dissolved gaseous hydrocarbon ([Santilano et al., 2019](#)). Usual depth of such reservoirs are 3-6 km and the usual temperature ranges are varying between 90 °C – 200 °C ([Bronicki, 2013](#)). These type of resource besides the thermal and hydraulic energy contains chemical energy as well. According to this, three types of energy can be exploited ([Santilano et al., 2019](#)):

- chemical energy from the combustion of hydrocarbons,
- thermal energy from hydrothermal fluids and
- kinetic energy from well-head overpressured regimes.

Because of the additional types of energy sources this resource can trigger the economic feasibility of projects. Many resources occur in on-shore and off-shore petroleum basins ([Mock et al., 1997](#)). Although the potential is assumed to be high, geopressured resources are still considered to be unconventional because of various technical problems (e.g., sustainability of the exploitation) ([Santilano et al., 2019](#)). Potential reservoirs can be found in the northern Gulf of Mexico and in Hungary ([Bronicki, 2013](#); [Árpási et al., 2000](#)).

5.3 Enhanced Geothermal Systems (EGS)

Electrical power generation from geothermal energy has traditionally associated with large reserves of hydrothermal resources. The steps are very similar to oil reserves: locate the reservoir, investigate whether it contains sufficient fluid, build a plant to extract the resource and when the resource depleted the process reach the end ([Olasolo et al., 2016](#)). Such hydrothermal systems ultimately depend on three factors ([Huenges, 2016](#); [Olasolo et al., 2016](#)):

- a) sufficient temperature of the reservoir,
- b) considerable amount of fluid in the reservoir
- c) production rate (at least 100 m³/h has to be achieved), so permeability of the reservoir.

While a reservoir with a sufficiently high temperature can be reached almost anywhere at sufficient depth, the economically interesting locations are restricted as the “b” and “c” factors are not always available in place ([Mondejar and Chamorro, 2017](#)). These limitations have forced scientists to seek alternative solutions to reduce dependency on naturally occurring geothermal reservoirs ([Olasolo et al., 2016](#)). Many of the hydrothermal and petrothermal⁹ systems can be exploited to an economic state by means of a so-called enhanced (or engineered) geothermal system (EGS) ([Huenges, 2016](#)). EGS systems are geothermal reservoirs in which technologies enable economic utilization of low permeability Hot Dry Rock resources or low permeability hydrothermal resources by improving the productivity (or injectivity) of a geothermal reservoir.¹⁰ As the concept of EGS is designed to make geothermal energy utilization feasible in most reservoir environments there is a huge untapped potential ([Bathia, 2014](#)). For example, the estimated, traditional geothermal potential of Taiwan is 989 MW_e, whereas that of EGS is approximately 31.8 GW_e ([Lu, 2018](#)).

EGS can be achieved by creating fluid connectivity through hydraulic, thermal, or chemical stimulation in the reservoir or applying advanced well configuration methods (sometimes combination of them are implemented ([Breede et al., 2013](#))) ([Huenges, 2016](#)). Formally, these EGS methods can be categorized based on their radius of impact. Chemical and thermal methods can improve the near wellbore region up to a distance of a few tens of meters, while hydraulic fracturing and advanced well configuration methods can improve the far field up to several hundreds of meters away from the borehole ([Huenges, 2016](#)). In

⁹ Petrothermal: Systems that are not bound to water-bearing formations in the subsurface ([Huenges, 2016](#))

¹⁰ There is no universally established definition of EGS, but the offered concept satisfies most of the EGS definitions available in the public domain ([Breede et al., 2013](#))

[Appendix J](#), several different EGS projects can be seen with additional information and also several under development and producing EGS projects are listed and detailed by Breede et al. ([Breede et al., 2013](#)). In the following subchapters each EGS methods are introduced briefly.

5.3.1 Thermal stimulation

It has been observed many times that the performance of geothermal injection wells improves over time and cold-water injection improves well permeability, which were caused by undeliberate thermal stimulation resulting that many wells that were initially unproductive became productive ([Rose et al., 2012](#)). Thermal stimulation is investigated sporadically in the literature, however it may constitute a key effect especially in geothermal wells, where temperature differences between the stimulating fluid and the formation is expected to be significant ([Peter-Borie et al., 2019](#)). Thermal stimulation can enhance the permeability of the near wellbore region (which may have been reduced by the drilling operation) or may open hydraulic connections to naturally permeable zones that were not intersected before ([Huenges, 2016](#)). Sudden introduction of cold fluid to the hot reservoir can cause localized stress concentration (because of the heterogeneous contraction of the minerals) and rock damage thus permeability improvement ([Doonechaly and Bruhn, 2018](#)). In connection to the outer stress field, fractures will be generated and the part of the rocks in the neighborhood of preferred fluid pathways will get a greater temperature decrease with cold fluid injection and thus preferred further opening ([Huenges, 2016](#)). This self-reinforcing effect either leads to reopening of existing, possibly sealed fractures, or creates new fractures ([Huenges, 2016](#)). These two phenomenon caused by the induced thermal stresses are also known as thermal shearing and thermal fracturing ([Peter-Borie et al., 2019](#); [Ghassemi et al., 2007](#)).¹¹ The shearing and fracturing takes place near the wellbore as the consequence of the rock cooling, so it is different from hydraulically induced fractures where the fractures are created or expanded by raising fluid pressure sufficiently (see in chapter [3.3.3](#)) ([Grant et al., 2013](#)).

5.3.2 Chemical stimulation

Specific chemicals are able to dissolve minerals from the formation during circulation that leads to an enhance flow performance near wellbore by means of utilizing mainly acids that react and remove mineral phases restricting fluid flow ([Huegens, 2016](#)). Chemical

¹¹ Main difference between fracturing and shearing that during fracturing new fractures are propagating from the borehole, while during shearing slip along pre-existed fractures are induced ([Gischig and Preisig, 2015](#))

stimulation techniques have been developing for more than 100 years in the oil and gas industry to improve well productivity ([Thomas and Morgenthaler, 2000](#)). Despite all the differences between petroleum and geothermal reservoirs the chemical stimulation has been taken over from the oil and gas industry. Two basic types of chemical stimulation techniques can be distinguished. *Matrix* stimulation in sandstones is performed to dissolve and/or disperse materials that reduce productivity/injectivity, while in carbonate formations the goal is to create new, unimpaird flow channels between the formation and the wellbore ([Portier et al., 2009](#)). Matrix stimulation is called matrix acidizing when the treating fluid is an acid. During matrix acidizing the chemical injection takes place at a lower pressure to prevent formation fracturing ([Hill and Schechter, 2000](#)). *Fracture* acidizing is very similar to a normal fracturing process (detailed in chapter [3.3.3](#)) with the main difference that instead of a propping agent the fracture is kept open with the help of the acidizing treatment as the acid etches the fracture faces ([Mack and Dowell, 2000](#)). Chemical stimulation has been proven to be efficient in the history. In [Fig. 5-8](#) the injectivity indexes of selected chemical stimulation processes can be seen. The results show that in each case the injectivity indexes improved with an average improvement of 365%, which indicates that this stimulation method has potential. The complete table can be found in [Appendix K](#).

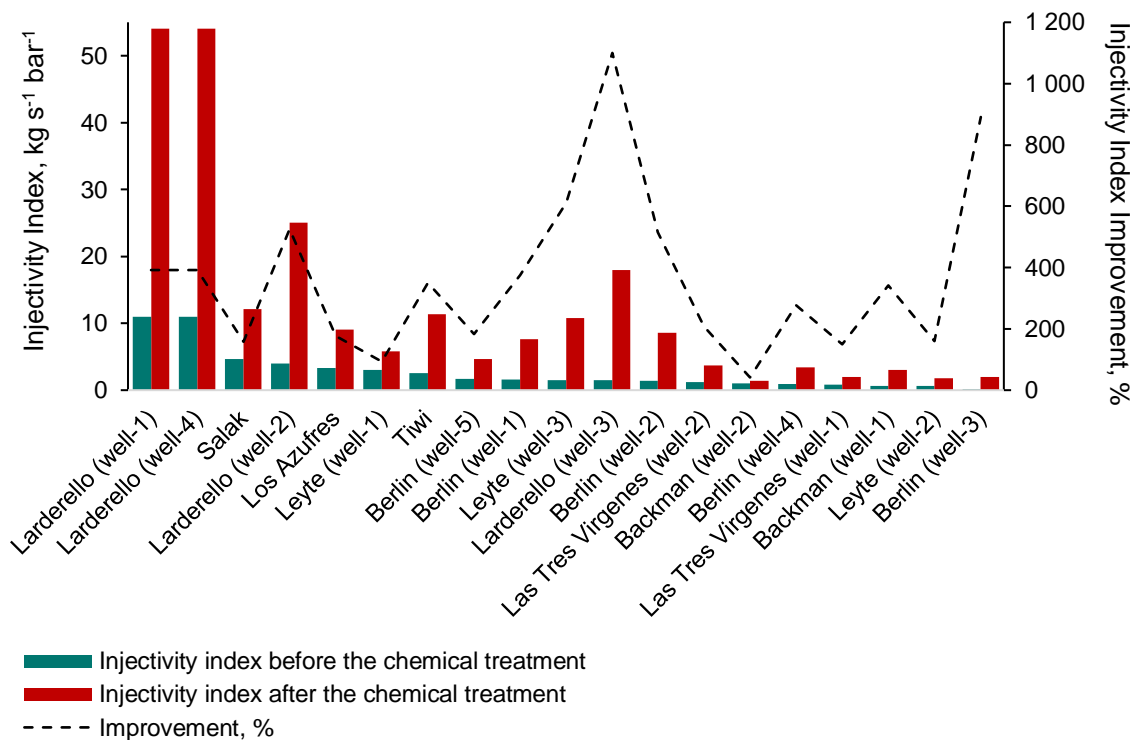


Figure 5-8: Results of chemical treatment in selected geothermal fields ([Portier et al., 2009](#))

The two most common acidizing agents are hydrochloric acid (HCl) and hydrofluoric acid (HF). Hydrochloric acid reacts with limestone to produce carbon dioxide (gas) and calcium chloride (salt that is soluble in water), which are later removed from the formation during production ([Robertson and Chilingarin, 1989](#)). After the successful limestone acidizing treatments¹², new treatments for sandstone reservoirs were developed by utilizing hydrofluoric acid besides HCl, as HF¹³ dissolves clay minerals and silica ([Portier et al., 2009](#)). Other substances can be also used during the process such as potassium chloride (KCl), NTA¹⁴, ammonium chloride (NH₄Cl) and sodium carbonate (Na₂CO₃).

In geothermal wells, during injection and production scaling can occur in the reservoir, which deteriorate the permeability ([Portier et al., 2009](#)). Scaling issues are mainly dependent on the dissolved minerals (most frequent observed minerals are sodium, chlorine, calcium, bicarbonate, potassium, silica and sulfate, plus heavy metals such as mercury, copper, lead, and zinc) ([Barbier, 2002](#)). Changes of pressure, temperature and pH in case of injection and production lead to deposition of hard inverse-solubility inorganic salts from the geothermal fluid ([Azari et al., 2020](#)). As scaling is probably anywhere during the production path, it can occur in the reservoir causing a significant reduction in the formation permeability ([Andritsos et al., 2002](#)). Chemical stimulation methods have been proven to be efficient to manage the scaling phenomenon.

5.3.3 Hydromechanical stimulation

In case of hydromechanical stimulation a pressurized liquid is used to enhance the performance of the geothermal well by fracturing it artificially. Three main treatments can be identified in this group.

5.3.3.1 Massive water injection treatments

Massive water injection treatment in the oil and gas industry (i.e., massive hydraulic fracturing or MHF) is a widely used formation stimulation technique that is usually applied in low permeability reservoirs (generally less than 0.1 md) to obtain an economical production rate ([Law and Spencer, 1993](#)). When the term and the technique was developed (in the 1970s) the treatment considered to be much larger than other treatments at that time ([King and Miskimins, 2020](#)). In the 1970s the treatment may involve the use of at least

¹² First recorded acid treatment was made on 10 August 1895, resulting oil and gas production enhancement of the well respectively by 300% and 400% ([Robertson and Chilingarin, 1989](#)).

¹³ Mixture of HCl and HF is often referred as mud acid in the literature ([Abdollahi and Shadizadeh, 2012](#))

¹⁴ NTA: nitrilotriacetic acid (C₆H₉NO₆)

50,000 to 500,000 gal treating fluid (mainly water), which would be considered small by today's standards ([Agarwal et al., 1979](#); [King and Miskimins, 2020](#)). The fracture induced with this method is usually long (in the range of a few 100 m) and narrow (in the range of a few 1 mm) ([Khasanov et al., 2009](#); [Huenges; 2016](#)). Generally, the fracture is prevented from closure by the injection of a granular material with high crush resistance, thus reaching a highly conductive channel ([Belyadi et al., 2019](#)). This granular propping agent, also called proppant, is composed of small particles made of solid material, typically sand, or man-made ceramic material ([Guo et al., 2017](#)).

Although, this hydraulic fracturing technology is widespread in the oil and gas industry, it is still in the trial-and-error phase for exploiting geothermal systems efficiently ([Huenges, 2016](#)). The main intent of this method in case of geothermal reservoirs is to enhance the permeability of the natural joint network by shearing or widening the naturally occurring fractures with massive water injection ([Adams and Rowe, 2013](#)). In this case as the created or enhanced fracture system has enormous size the technique was considered without the usage of proppants, since it seemed too costly or technically impractical to place proppant material over such large areas. However, most of the major EGS projects shows that instead of connecting the natural fractures, generally one large wing-crack is created by the stimulation process ([Jung, 2013](#)). This phenomenon can be a plausible explanation for the intense and strong induced seismicity as well as for the strong after-shocks observed at various EGS-locations, one example is: In December 2006 a massive fluid injection was performed in Basel, Switzerland for geothermal reservoir enhancement. The operation takes place at 5 km depth and last for 6 days. During the treatment approximately 13,000 microearthquakes were detected by borehole network and the largest of the induced earthquakes, which had a magnitude of ML 3.4, was strongly felt in the Basel area and led to the termination of the project ([Kraft and Deichmann, 2014](#)). Whether the shock was caused by the EGS project has been questioned, nonetheless the project has been terminated and the inhabitants were compensated ([Lu, 2018](#)).

5.3.3.2 Hydraulic-proppant treatment

Different types of hydraulic-proppant treatment can be applied in a wide range of formations with varying permeabilities ([Patel et al. 2014](#)). Comparing to massive water injection hydraulic-proppant treatment usually results shorter fracture length (about 50 - 100 m) and wider fracture aperture (up to 10 mm) ([Huenges, 2016](#)). In case of moderate and high permeability formations ($k > 1$ md) the main objective of the treatment is to bypass the near-wellbore damage, while in case of formations with low permeability ($k < 0.1$ md) the main

objective of the treatment is to actually stimulating the performance by creating an artificial, highly conductive flow path ([Smith and Hannah, 1996](#); [Speight, 2016](#)). This flow path is then prevented from closure by a granular material, so-called proppant. Many different proppants have been developed with various applications, sizes, types and shapes. [Liang et al. \(2016\)](#) has published a comprehensive review paper on different proppant technologies. Typically, the main sequence of the hydraulic-proppant treatment are as follows ([Speight, 2016](#)):

- a) *Acid stage*: acid solution is used to clear cement debris in the wellbore and provide an open conduit for other fracturing fluids;
- b) *Pad stage*: consists of slickwater¹⁵ solution to opens the formation and helps to facilitate the flow and placement of proppant material;
- c) *Prop sequence stage*: may consist of several different substages of water combined with proppant material in different concentration;
- d) *Flushing stage*: freshwater is used to sufficiently flush the excess proppant from the wellbore.

As the proppant usually pumped into the fracture with different concentrations (see in point “c” above) the final proppant concentration in the fracture varies, as it can be seen in [Fig. 5-9](#).

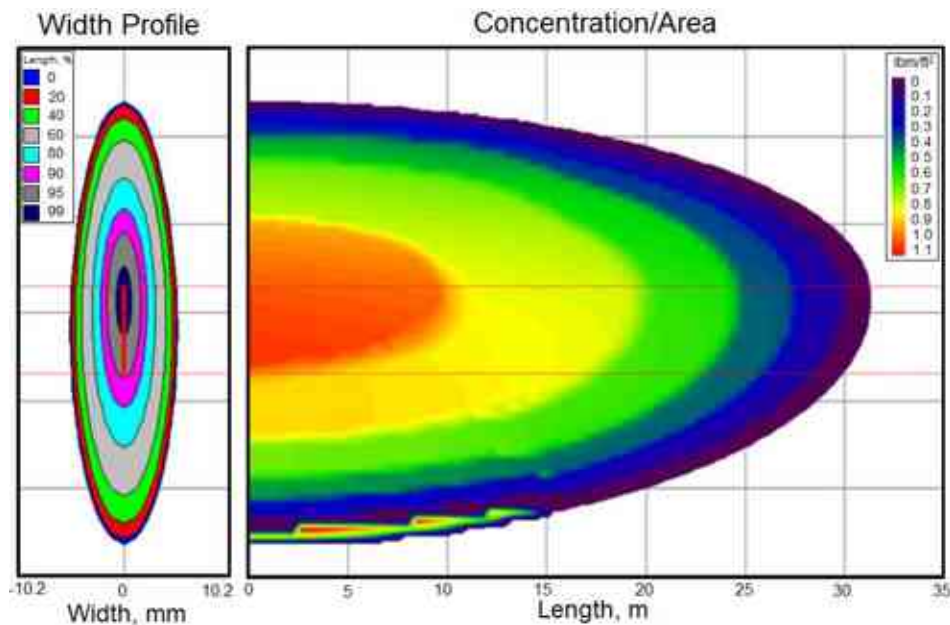


Figure 5-9: Proppant concentration distribution and geometry of a hydraulic-proppant treatment ([Sharma et al., 2018](#))

¹⁵ Slickwater is a routinely used fluid in hydraulic fracturing and mainly contains water with additional chemicals (such as friction-reducing agents and clay-stabilizers) ([An et al., 2020](#))

5.3.3.3 Multistage treatment

Currently, most the field and conceptual EGS projects are designed as a single-stage fracturing in nearly vertical wells with openhole completion ([Cao et al., 2016](#); [Bradford et al., 2016](#); [Lu, 2018](#); [Han et al., 2019](#)). This is mainly caused by the following points ([Han et al., 2019](#)):

- Horizontal drilling in rocks that have high temperature is technically challenging and costly;
- EGS methods mainly focuses on shear stimulation.

It is generally believed that the self-propping effect can improve the conductivity of natural fractures, however some studies revealed limitations to this conventional EGS design ([Dezayes et al., 2010](#); [Brown et al., 2012](#)). One of the major limitations is the determination whether the slipping fracture would be able to self-propping under in-situ stresses. It has been found that only some natural fractures provide strong conductivity and in addition, the flow usually tends to localize into highly conductive fractures around the wellbore, which reduce the overall heat efficiency of the system ([Han et al., 2019](#)).

The basic idea of multistage treatment is sectioning and stimulating individual parts of the well to achieve larger surface areas. Boreholes are usually deviated from vertical to intersect the maximum number of natural fissures ([Huenges, 2016](#)). Injection/production well can be sectioned by different completion methods and will be stimulated independently by water injection ([Salah et al., 2017](#)). A relatively new concept in this area is the combination of horizontal drilling method with the multistage fracking method, see in [Fig. 5-10](#). Multiple stages can increase the potential revenue of the project by more than an order of magnitude.

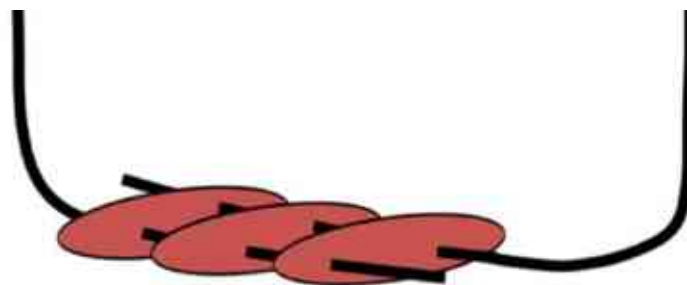


Figure 5-10: Multistage horizontal EGS concept with one injection and one production well ([Li et al., 2016](#))

Different vertical and horizontal multistage fracturing methods can be seen in the [Appendix L](#) with additional information.

6 NEW EGS TECHNOLOGY

As it can be seen from the chapter above there are several stimulation methods to exploit geothermal reservoirs more effectively. Although it is foreseen that geothermal energy production will not play a significant role in the future (compared to other technologies), technological advancement can change its role notably. One of the main limiting factors of geothermal energy utilization is the geological environment. Most projects seek a reservoir that contains steam and/or high-temperature water and has reasonably high permeability, so injection wells are not essential to exploit the resource economically. Although these conditions lower the investment cost of the project, they also limit the available areas. To overcome this, researchers developed enhanced methods (see chapter [5.3](#)) which have proven to be effective. Hydromechanical stimulation techniques provide a favorable alternative that can be used for a wide range of reservoir properties. Massive water injection has negative social and often regulatory discrimination and without the application of a propping agent, the open fracture cannot be assured. In the case of a multistage treatment, the technology is not yet mature enough to implement economically in a geothermal reservoir.

6.1 Intuition

To extend the applicable range of geothermal energy production technologies a new concept has been investigated in the previous decades. A so-called single-well EGS method provides an alternative solution for exploiting geothermal heat from even HDR formations without the need for injection well. To reach this, a closed loop system should be created where the production and injection wells are realized within the same well and the surface available for heat transfer is increased by a hydraulic fracture. This arrangement has been investigated by two independent research groups with a different approach.

[Kehrer et al. \(2007\)](#) introduced the concept of a demonstration project where a hydraulic fracture was created in a tight sediment at almost 4 km depth. The concept assumes that though the overall permeability of these formations is low, open flow paths (faults, fracture zones, or intersections of them) exist even at the investigated depths and that these paths can be accessed from a borehole by creating a hydraulically induced fracture. In this concept the application of a propping agent was eliminated as self-propping of the formation is assumed. The hot water produced will then be reinjected after use via the annulus in the same borehole into a permeable rock formation at more shallow depths. The schematic illustration of the concept can be seen in the [Fig. 6-1](#).

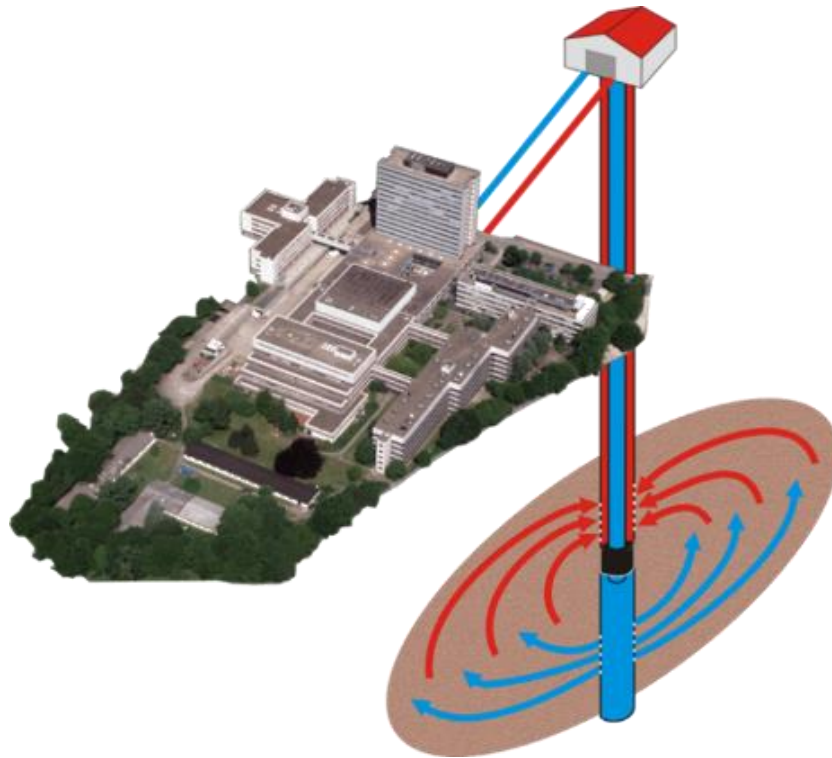


Figure 6-1: Schematic illustration of the GeneSys Hannover project (<http://www.genesys-hannover.de>)

The project goal was to supply the office and laboratory buildings of the GEOZENTRUM with geothermal heat. The project name became GeneSys Hannover and a single well was drilled in 2009 near Hannover and the hydraulic fracturing was performed successfully in 2011. Although after the production test in 2011 a drill hole closure occurred due to a chemical precipitated salt plug, the single-well EGS concept proved its legitimacy. The concept was further analyzed in the literature ([Orzol et al., 2004](#); [Orzol et al., 2005](#); [Tischner et al., 2010](#)).

[Danko et al. \(2018\)](#) introduced a conceptual study where a single hydraulic fracture was created, and the fluid was circulated in the fracture. The simulation showed that the surface of the fracture cannot be utilized efficiently without a flow control technique as the fluid flow is concentrated in the near-wellbore zone. To solve this issue, they offered a so-called “grouted area” or “grouted island” around the center of the fracture, which helps the fluid to flow to the edge area of the fracture and also helps to prevent the fracture from closing (the flow profiles can be visualized in [Appendix M](#)). The grouted island is a non-permeable zone and can be made by either cement or geopolymer. The conceptual illustration of the model can be visualized in the [Fig. 6-2](#).

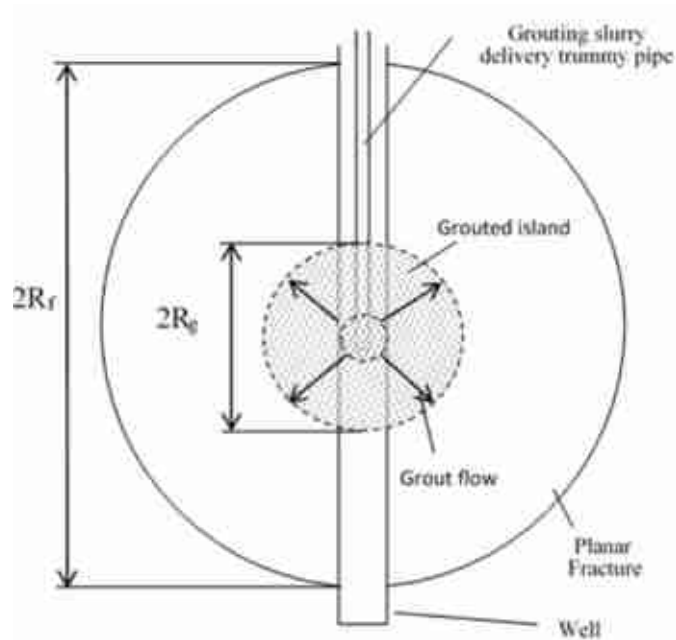


Figure 6-2: Conceptual illustration of a hydraulically induced fracture with a grouted island ([Danko et al., 2018](#))

This advanced concept shows that the power generation under 30 days of production can be significantly higher with this arrangement than in case of an open fracture. Later this concept was further studied by [Danko et al. \(2020\)](#) to strengthen its validity.

The above described two concepts proved that a single-well EGS concept can be efficient for geothermal heat recovery. First, a project initiated to validate that a connection can be created in a hydraulically fractured single-well between the production and injection sections. Second the concept was further developed by controlling the flow in the fracture for more effective heat recovery by implementing a non-permeable middle zone in the fracture. Although the concept offered by [Danko et al. \(2018\)](#) could be used to enhance the performance of a single-well EGS system, its practical considerations should be further analyzed (e.g., injecting the grouted island into the near wellbore zone, will the grouted island prevent the fracture from closure). Also, the grouted island concept limits the heat transfer surface area by around 10% ([Danko et al. 2018](#)).

To further improve the concepts a hydraulic-proppant treatment is offered to implement on a single-well EGS concept by this study. The hydraulic-proppant treatment has already proved in the oil and gas industry and the technology is mature. With this method, it can be assured that the fracture is kept open thus provides a highly conductive flow path and offers opportunity to control the flow in the fracture without the limitation aroused by the grouted island concept.

6.2 Fundamental Considerations

As it was mentioned in the previous subchapter, the validity of a single-well EGS concept has been proven by the Genesys project. [Danko et al. \(2018\)](#) showed that a single open fracture cannot be used efficiently to utilize the heated surface of the fracture as the fluid's mass flow is concentrated at the near wellbore zone and not evenly in the fracture. This results that the heat of the near wellbore zone will be drained rapidly and as the fluid flow is concentrated in this region the heat recovery will not be efficient. [Danko et al. \(2018\)](#) offered a flow control concept by implementing a non-permeable zone in the middle of the fracture which can alter the fluid flow further in the fracture thus providing a more evenly distributed flow profile. This method can be efficient based on simulations thus providing a slower thermal drawdown by around 10%. Although this concept was established by simulation, two drawbacks can be mentioned. One is that this concept has never been implemented in in-situ conditions during a pilot, which may highlight some technical limitations. The second is that the impermeable zone injected in the middle of the fracture reduces the convective surface by around 10%.

To overcome these limitations and offer a technically viable concept that does not reduce the surface area of the fracture, the implementation of a proppant treatment is proposed by this study. Applying proppants with different permeabilities in the fracture the fluid flow can be altered and controlled. By creating different zones, the mass flow in the fracture can be evenly distributed thus maximizing the heat recovery. The arrangements of the different methods can be visualized in [Fig. 6-3](#).

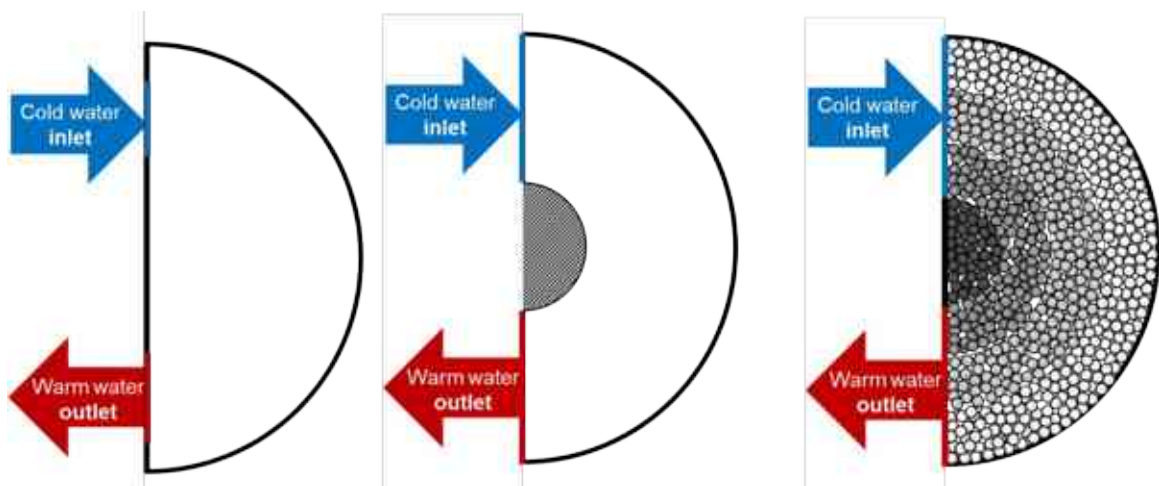


Figure 6-3: Schematic representation of the different single-well EGS methods (left model offered by Genesys project ([Kehrer et al., 2007](#)), middle model offered by [Danko et al. \(2018\)](#), right model offered by the current study)

The arrangement of different proppant zones in the fracture is a proven method in the oil and gas industry but has never been investigated for this purpose. In the industry it is most used to reach the best conductivity of the fracture to maximize the wells' productivity ([Mao et al., 2021](#)). Several literatures showed that the proppant concentration in the fracture is designed and created with different zones ([Gui et al., 2013](#); [Stopa et al., 2014](#); [Sharma et al., 2018](#); [Muther et al., 2020](#)) and some of the obtained arrangements can be visualized in [Appendix N](#).

Build on the experiences of the oil and gas industry the concept to create different permeability zones in the fracture (as shown is [Fig. 6-3](#)) can be a viable solution. Because of the complexity of the concept the fluid flow and the corresponding heat recovery could not be determined analytically thus a numerical simulation should be implemented. Although the fluid flow could be determined by a 2-dimensional model (similarly as [Danko et al. \(2018\)](#) proposed) the heat recovery from the reservoir is mainly taken place perpendicularly to the flow profile, so a 3-dimensional, finite element simulation should be created.

6.3 Finite Element Simulation

In this research, flow, and heat transmission in the fracture have been modeled using finite element method (FEM) with the ANSYS Software. FEM can be used to produce repeated solutions and can flexibly adapt to different physical problems which are governed by partial differential equations. The advantage of utilizing the finite element method is that it transforms the partial differential equation into a collection of simple algebraic equations and, for situations with time variations, into ordinary differential equations ([Kalra and Mashuq-un-Nabi, 2016](#)). Three steps are included in the FEM process:

- Pre-processing: establishing boundary requirements and creating the mesh
- Solution: the differential equations are solved on the mesh
- Post-processing: the results are visualized and can be further interpreted

6.3.1 Fracture geometry

Hydraulic fracture geometry is a complex function of several reservoir and operational properties ([Belyadi et al., 2019](#)):

- initial reservoir stress conditions (global and local),
- heterogeneous and anisotropic rock mechanical properties (Young's modulus and Poisson's ratio), permeability, porosity, natural fracture system

- injection rate, volume, and pressure.

Specific presumptions have been established in order to model this complex process while keeping the basic characteristics of hydraulic fracture geometry. For this reason, researchers initially assumed that the hydraulic fracturing procedure would take place in a homogenous and isotropic formation that result in a symmetric, bi-wing fracture from the point or line source of the injecting fluid. In these models the fracture half length and width are changing as function of time and pumped volume while the fracture height remains constant. Consequently, these models are referred to as 2-D models.

Two widely accepted 2-D fracture propagation models are usually used to describe hydraulic fracture in a vertical well, while one model was established to model hydraulic fracturing in radial direction. These models view hydraulic stimulation as a single planar fracture that propagates into the formation commencing at the wellbore.

The PKN model ([Perkins and Kern, 1961](#); [Nordgren, 1972](#)) assumes that the fracture width (w) is tied to the height (H) of the fracture, thus this model is applicable to describe long fractures of limited height and elliptical vertical cross-section.

The KGD model ([Khristianovic and Zheltov, 1955](#); [Geertsma and de Klerk, 1969](#); [Daneshy, 1973](#)) assumes that the fracture width is proportional to the length (l) of the fracture, thus this model is applicable to describe fractures in which the length/height aspect ratio is small.

The third model is used to simulate hydraulic fracture propagation in a radial direction, which is the so-called penny-shaped or radial fracture model. This model has found application in shallow formations where overburden stress became equal to minimum horizontal stress. In this case, the symmetric geometry was assumed to be at the point of line-injection source ([Belyadi et al., 2019](#)). The three models can be visualized in [Fig. 6-4](#).

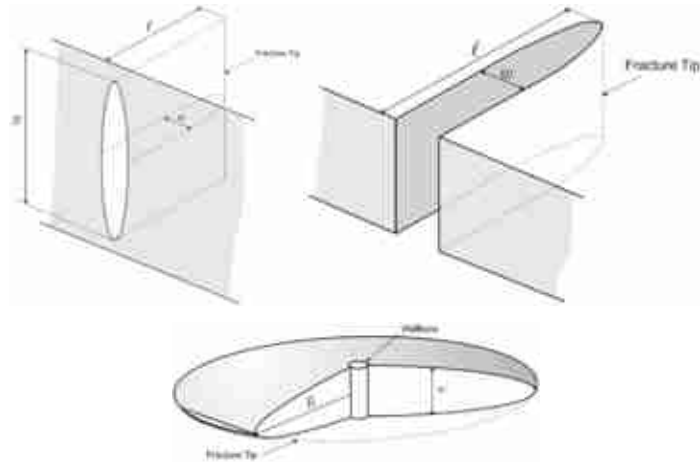


Figure 6-4: Hydraulic fracture geometries (upper left side PKN model, upper right side KGD model, bottom side penny-shaped model) ([Adachi et al., 2007](#))

While the constant height models made it possible to describe the fracture propagation during the fracturing process simpler, they also provide major constraints for the applicability of these models ([Weijers and de Pater, 2019](#)). To provide a more practical geometries the so called 3-D fracture models were developed mostly in the 1980s. As increasing computational power became available, simulations were increasingly employed to assess how fractures expanded in length, width and height over time for a formed fracture that propagates in a vertical plane. They can be broadly divided into three categories: pseudo 3-D models, parameterized 3-D models, and fully meshed 3-D models. The different 3-D models can be visualized in [Fig. 6-5](#).

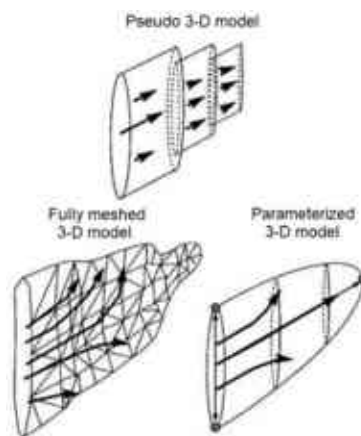


Figure 6-5: 3-D fracture propagation models ([Weijers and de Pater, 2019](#))

The above-described models have been created to analytically determine the fracture propagation during a hydraulic fracturing process. Although these models can be used to match the production data, they also have limitations. Determining the exact geometry of a given hydraulic fracture is a complex task. Several diagnostic tools are available to measure

the in-situ geometry of a hydraulic fracture: microseismic ([Warpiski et al., 2005](#); [Mayerhofer et al., 2006](#)), tiltmeter ([Wright et al., 1998](#)), well testing ([Cipolla and Mayerhofer, 1998](#)), radioactive tracers ([Scott et al., 2010](#)), chemical tracers ([Gardien et al., 1996](#); [Leong et al., 2015](#)), pressure interference ([Awada et al., 2015](#); [Seth et al., 2018](#); [Seth et al., 2019](#)) and water hammer measurements ([Carey et al., 2015](#)). Although these diagnostic tools can be useful, they can only provide an approximation of the real geometry of the fracture. To get an idea how a real fracture can look like after a treatment an experiment was conducted by [Hubbert and Willis \(1957\)](#). A picture taken to the experiment shows a vertical fracture created under stress conditions and can be visualized in [Fig. 6-6](#).

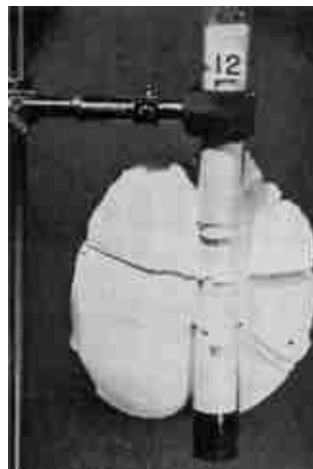


Figure 6-6: Vertical fracture produced under stress conditions ([Hubbert and Willis, 1957](#))

6.3.1.1 Applied geometry

Since the goal of this current study is to establish the theoretical background of a new EGS method and prove the concept by the means of simulation and laboratory measurements, a simple penny-shaped model has been used which assumes that the fracture has been created in a homogeneous and isotropic reservoir. This model provides practical simplicity (in the point of finite element simulation) and enables to compare the outcomes with the results obtained by the model of [Danko et al. \(2018\)](#).

As the geometry is symmetric in two planes it could be reduced to a quarter volume. The schematic representation of the geometry with the symmetry planes can be seen in the [Fig. 6-7](#), where the bluish area is the fracture in the brownish reservoir, and the grey planes are the symmetry planes.



Figure 6-7: Schematic representation of the fracture with the two symmetry planes

The 3D model was constructed with separated fracture zones to allow for the succeeding stages to have various properties (like porosity and permeability). The fracture was divided into 4 radial zones, which can be seen in [Fig. 6-8](#) as with bluish color¹⁶. To obtain better mesh quality the inner-most zone was constructed by a so-called O-grid method and in this way the highly skewed cells could be removed ([Tu et al. 2018](#)). Also, the outer zones were divided into four sections to be able to define different values of them as needed. The rock body is represented with brown color in the figure. The geometry is symmetric on the X-Y and Y-Z plane as described previously.

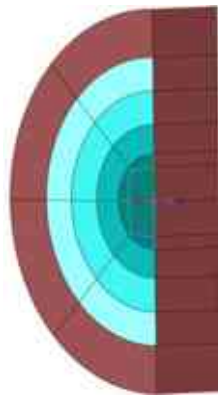


Figure 6-8: Schematic representation of the fracture with the two symmetry planes

The dimensions are represented in [Tab. 6-1](#). One can see that the width of the rock in the radial direction is smaller than in the axial direction and it can happen as during the heat transfer the rock only interact with the width of the fracture in the radial direction. It results

¹⁶ In the following chapters the different zones from darker blue to lighter blues are often referred as k_1 , k_2 , k_3 , and k_4 respectively indicating they can have different permeability values.

that the heat transfer is minimal in that direction and the radius of the rock body could be reduced. This phenomenon can be seen in [Appendix O](#).

Table 6-1: Dimensions of the geometry

Name	Value
Fracture width, m	0.02
Zone 1 diameter, m	25.0
Zone 2 diameter, m	40.0
Zone 3 diameter, m	57.5
Zone 4 diameter, m	75.0
Rock diameter, m	100.0
Rock width, m	50.1

In the model all the dimensions were parameterized to be able to modify the geometry easily and efficiently.

6.3.2 Meshing

Mesh generation is the process during which a continuous geometric shape is divided into discrete geometric and topological cells. This method is a discrete, local approximation of the entire shape, so it is necessary to generate a mesh that properly models the geometry and contains the smallest possible number of elements, thus reducing the number of calculation operations to be performed during the simulations. In terms of cell types, 2-dimensional and three-dimensional types are distinguished. 2-dimensional cells are typically triangular or square in shape. The 3-dimensional cell types are tetrahedron, hexahedron, prism (wedge), pyramid, and polyhedron. The properties of the geometry determine which type of cell will result in the best quality mesh, however, in industrial practice, the two most common types are the tetrahedron and hexahedron (in 3-dimensional cases) ([Alberich-Bayarri et al. 2007](#)). The different cell types can be visualized in [Fig. 6-9](#).

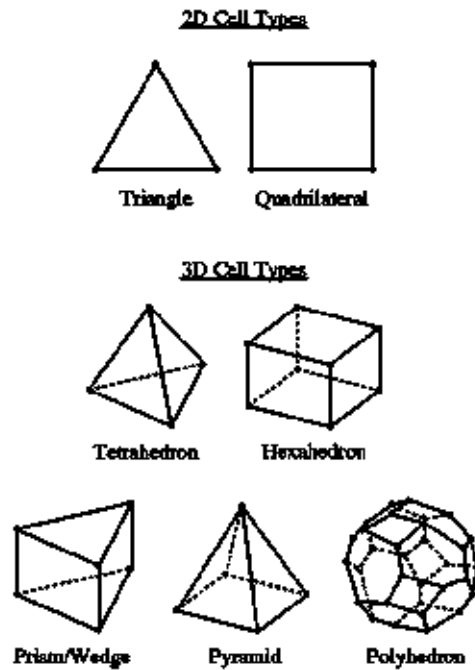


Figure 6-9: Basic cell types for meshing

In this study parametric meshing was done on the 3D model by hexahedrons and to generate higher quality, sweeping method¹⁷ was used also. The generated number of nodes is 2,930,192 and the number of elements is 2,869,600 which can be considered as a robust model and requires significant computing power. This result could be reached only by including sweep meshing method on the model, where at the connections of the zones the density of the meshing is greater. Semi-automated mesh generation was done with fixed meshing order. The meshing is illustrated in the [Fig. 6-10](#), where the model can be seen on the X-Y, Y-Z axis. The edge sizing can be seen in [Appendix P](#).

¹⁷ “The sweeping algorithm is a classical algorithm that can generate high quality hexahedral meshes for swept volumes.” ([Wu et al. 2017](#))

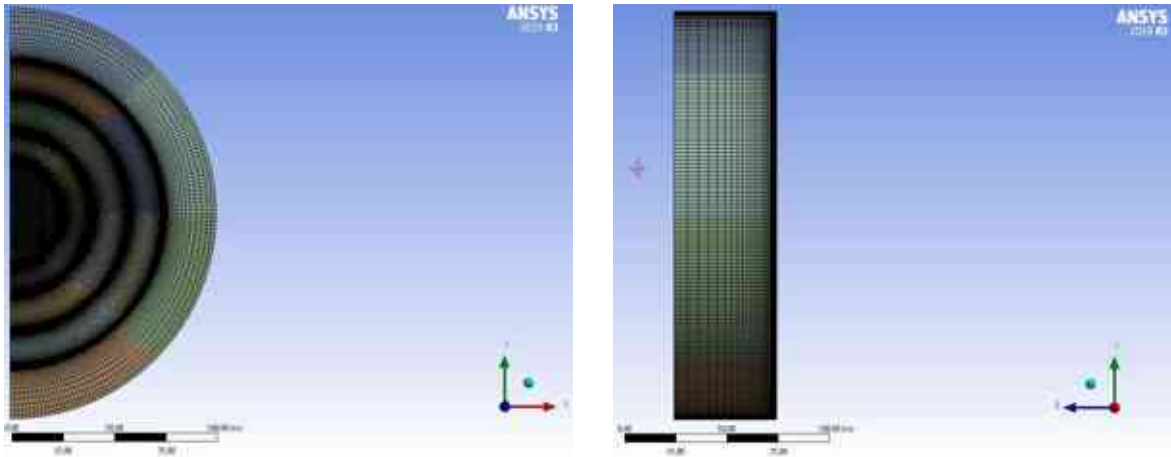


Figure 6-10: Meshing of the 3D model

Since the fracture is several magnitudes narrower than the rock body it results that several magnitude differences are present between the axial and radial sizes of the model. This difference results in mesh with a larger aspect ratio.

6.3.2.1 Meshing quality

Several metrics is available to define the quality of the meshing. In this part the generated mesh is evaluated based on 3 metrics: orthogonal quality, skewness, aspect ratio.

In the case of orthogonal quality, we examine how well the angles closed by the adjacent walls match compared to the angles considered optimal. The worst orthogonal quality is 0, while the best is 1 ([ANSYS, 2019](#)).

Skewness is defined differently for each cell type. In the case of hexahedrons, it can be defined as the worst normalized angle, among all 6 surfaces and vectors, which is defined at the center of gravity of the cell and the centers of the surfaces. In the case of tetrahedrons, it can be defined as the ratio of the areas of the elements compared to the area of an equilateral triangle (with a circle inscribed around the same triangle). In essence, it expresses how deformed our cell is compared to the idealized cell.

The aspect ratio can be defined as the ratio of the circle that can be written around the cell to the diameter of the circle that can be written in the cell. In essence, it tells us how flattened our cell is in one direction or another. Its value is most optimal if it is set to 1, and if it gets larger, it can cause problems during simulations (e.g., divergence). However, if the flow velocities and the problem permit, a much higher aspect ratio can provide adequate results.

[Tab. 6-2](#) shows the basic requirements for each quality test.

Table 6-2: Mesh quality indicators ([Shen, 2019](#))

Test	Best quality	Worst quality	Min. or max. acceptable value
Orthogonal quality	1	0	0.2
Skewness	0	1	0.9
Aspect ratio	0	1	N/A

In terms of orthogonal quality, the structured mesh of the model shows extremely good results. The value of the minimum orthogonal quality for the entire model was 0.841, which is well above expectations, while the average orthogonal value is 0.998, which indicates a very high-quality mesh. [Fig. 6-11](#) shows the distribution of certain orthogonal values in the model. One can see that the value close to 1 almost completely determines the quality of the generated mesh, and values smaller than that are hardly found in the model.

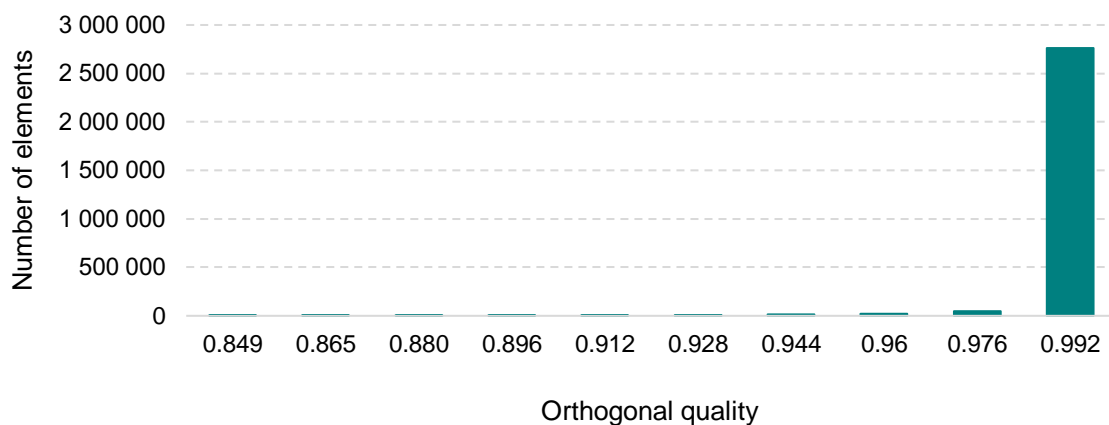


Figure 6-11: Orthogonal quality of the generated mesh

The evaluation of the skewness of the generated mesh also shows a similar result as in case of the orthogonal quality analysis, thus the quality of the generated mesh is adequate from this point of view. The maximum skewness value taken in the model is 0.369, which is well below the expected maximum value (0.9). The average value is 0.019, which predicts a well-structured mesh. [Fig. 6-12](#) shows the distribution of skewness values, where the ordinate of the graph is the element number, and the abscissa is the skewness value. One can see that 96.4% of all elements have lower than 0.1 skewness value.

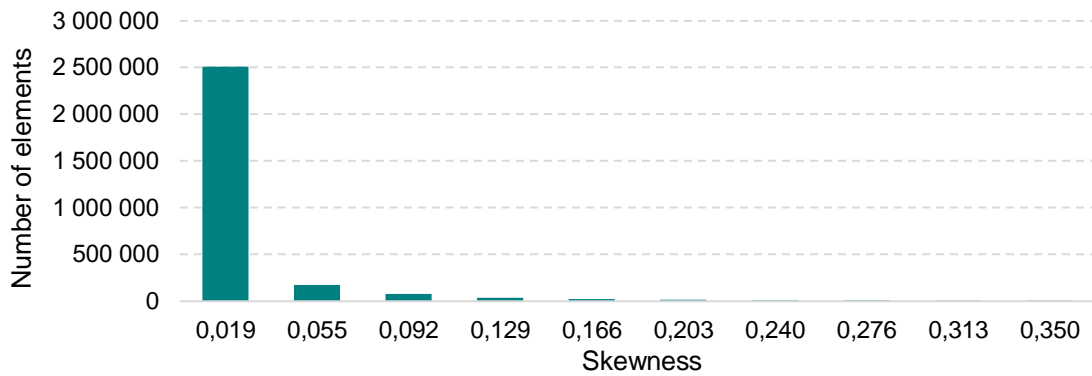


Figure 6-12: Skewness of the generated mesh

There is no maximum expected value for the aspect ratio value in the literature, as each problem defines a unique value. However, the upper limit of the finite element simulation software is typically a value between 10 and 100, while on the other hand, the CFX software used in the simulations can be used up to a value of 1,000. However, it is important to note here that higher aspect ratio values are also acceptable if there is no strong transverse gradient (boundary layer in the model). In the present case, slow flow velocities develop in the fracture, which make it possible to use a laminar flow model, thereby significantly easing the requirements for the aspect ratio of the mesh. This is favorable, as the use of long and narrow cells results the least number of elements, but also the best quality in terms of other indicators. The maximum aspect ratio for this model is 12,296 and the average value came out to be 519 after the mesh generation. 86% of the cells have the aspect ratio value below 616. This can be seen in [Fig. 6-13](#).

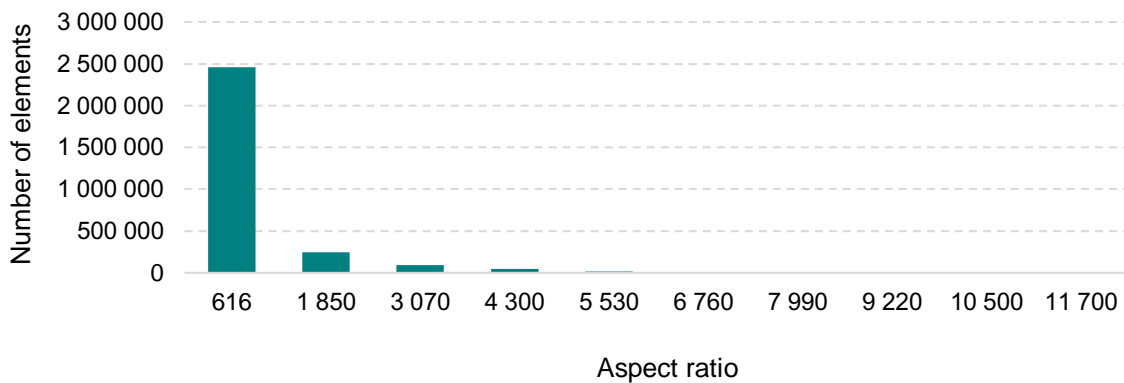


Figure 6-13: Aspect ratio of the generated mesh

These values can be considered high and further analysis is necessary to ascertain the applicability of the model as in the case of the present model, reducing this value would drastically increase the number of elements, making the model impossible to run in practice.

Three different models were run in the simulation with different element number and so different aspect ratio to evaluate the effect of the higher aspect ratios. The parameters and the results are shown in [Tab. 6-3](#) where the three different scenarios are represented with A, B, and C.

Table 6-3: Results of sensitivity analysis for the effect of aspect ratio

	Meshing metrics			Results	
	Nodes	Elements	Aspect ratio	Heat transfer, kW/m ²	Pressure difference, Pa
A	1,112,010	1,073,600	12,033	73.95	57.55
B	3,976,903	3,871,000	6,019	73.92	57.96
C	17,254,113	16,896,000	3,010	73.94	58.15

From the obtained results, it can be observed that in order to halve the value of the maximum aspect ratio, it is necessary to increase the number of elements on a much larger scale. In the case of a model containing nearly 17 million elements, the simulation time increases drastically which prevents the practical utilization of such model. The simulations did not provide a significant difference in the two results (transferred heat, pressure drop). The conclusion can be drawn from this that under the present conditions (geometric, fluid mechanics, and heat transfer) an aspect ratio of the order of 10,000 can also be used during the simulations. Thus, it can be stated that the aspect ratio has no significant effect on the modeled laminar flow, as well as on the heat transfer process and the developed model works properly. Regarding the temperature distributions, also no significant difference can be observed in the case of the individual models (A, B, C), which is illustrated in [Fig. 6-14](#). Based on this analysis the developed meshing of the model can be considered as a well-structured and practical model. [Fig. 6-14](#) illustrates the model offered by [Danko et al. \(2018\)](#) with the impermeable middle zone.

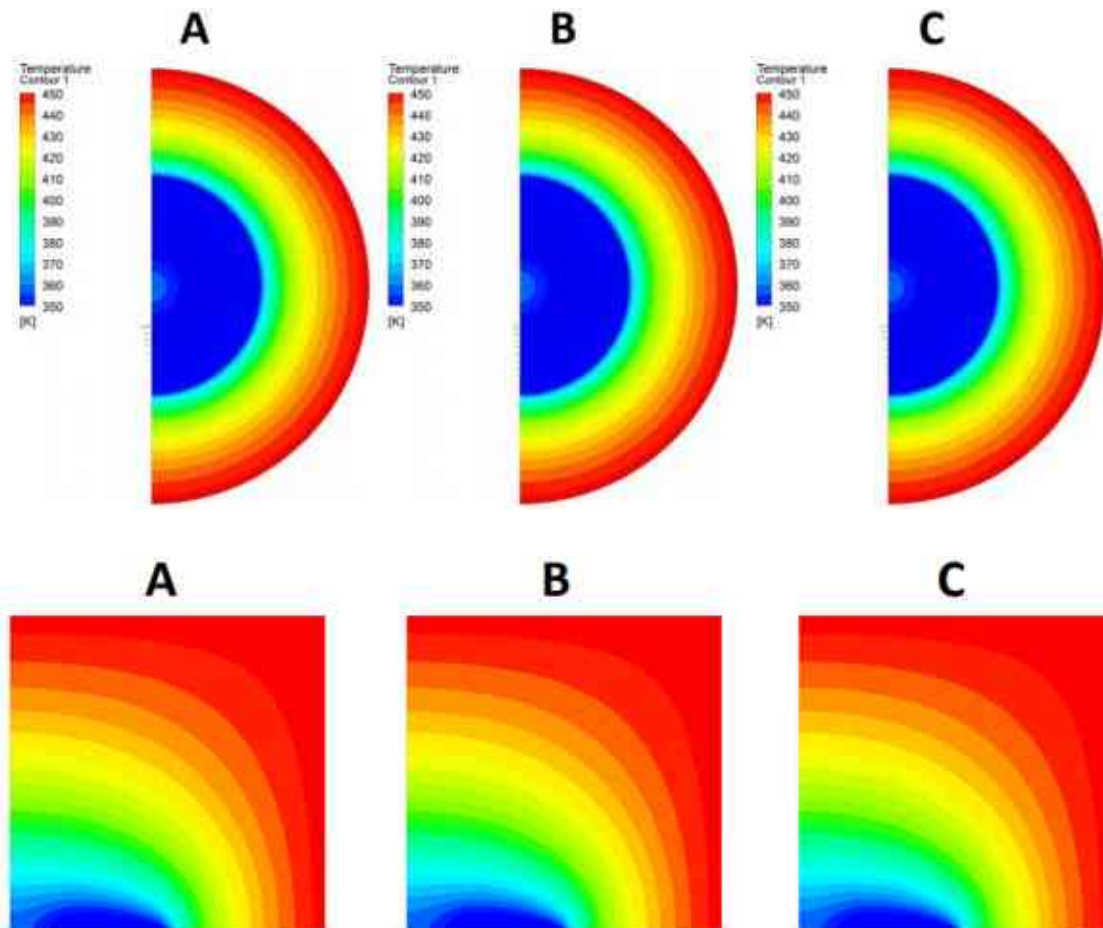


Figure 6-14: Temperature profiles in case of the 3 scenarios (upper pictures on the X-Y plane; lower picture on the Z-X plane)

6.3.3 Applied physics

The simulation was separated into two phases to reduce the running time. In the first part a steady-state simulation¹⁸ was done where only the fluid mechanics was applied and the energy equations, thus heat transfer were enabled. In the second part the flow profile was recorded and a transient simulation¹⁹ was done where the fluid mechanics equations were enabled and only the energy equations were solved.

¹⁸ “Steady state simulations, by definition, are those whose characteristics do not change with time and whose steady conditions are assumed to have been reached after a relatively long time interval. They therefore require no real time information to describe them. Many practical flows can be assumed to be steady after initial unsteady flow development, for example, after the start up of a rotating machine.” (ANSYS, 2011)

¹⁹ “Transient simulations require real time information to determine the time intervals at which the CFXSolver calculates the flow field. Transient behavior can be caused by the initially changing boundary conditions of the flow, as in start up, or it can be inherently related to the flow characteristics, so that a steady state condition is never reached, even when all other aspects of the flow conditions are unchanging. Many flows, particularly those driven by buoyancy, do not have a steady state solution, and may exhibit cyclic behavior.” (ANSYS, 2011)

6.3.3.1 Boundary conditions

In general, boundary conditions (BCs) are restrictions required to solve a boundary value problem. The definition of a boundary value problem is a differential equation (or system of differential equations) that must be solved in a domain where the boundary conditions are known. Compared to the "initial value problem," where conditions are only known for one extreme of the interval. Boundary value problems play a crucial role in many applications and phenomena, including solid mechanics, heat transfer, fluid mechanics, and acoustic diffusion. Initial value problems typically refer to difficulties to be solved in time, while they naturally exist in every problem based on a differential equation to be solved in space.

Symmetry conditions: As it was mentioned earlier the created geometry is symmetrical to the X-Y and Y-Z plane, so it was necessary to define boundary conditions on those surfaces. The defined boundary conditions of the symmetries are illustrated in [Fig. 6-15](#).

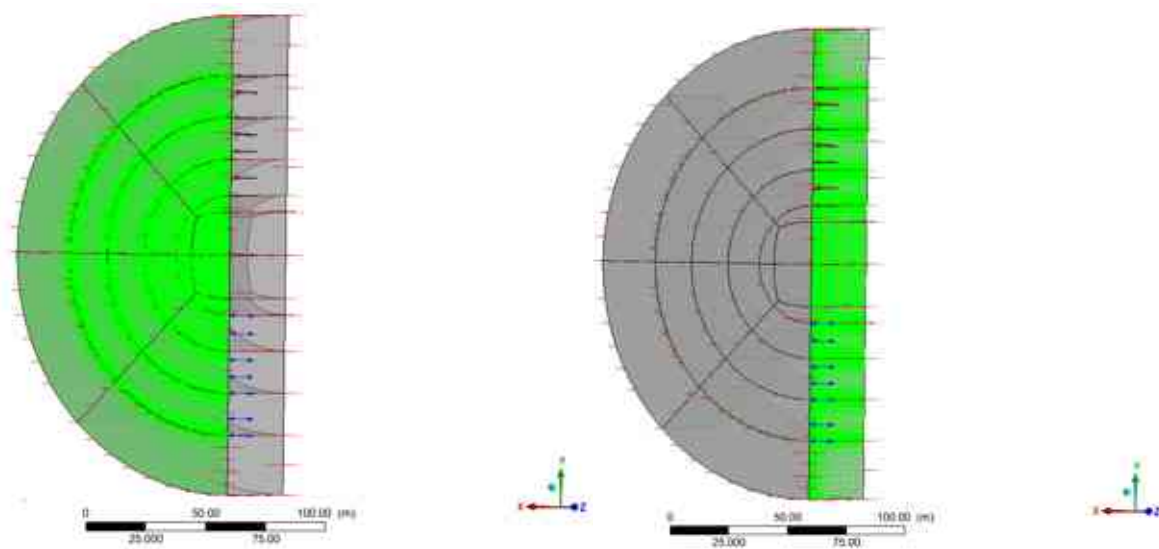


Figure 6-15: Symmetry boundary conditions on the X-Y and Y-Z planes

Rock wall condition: Since the reservoir can be interpreted as an infinite heat source the rock width was selected to be 50 meter and a boundary condition was necessary to be defined at the outer surface. In this way the heat transfer from the reservoir was established. The temperature on the outer rock surface was set to be 180 °C and can be visualized in [Fig. 6-16](#). Other parameters were also compulsory to define and for this reason the following parameters were set for the reservoir body, which was assumed to be a stationary, continuous solid body:

- Thermal conductivity: $\lambda = 3 \text{ W/mK}$
- Specific heat capacity: $c_p = 845 \text{ J/kgK}$

- Density: $\rho = 2,700 \text{ kg/m}^3$

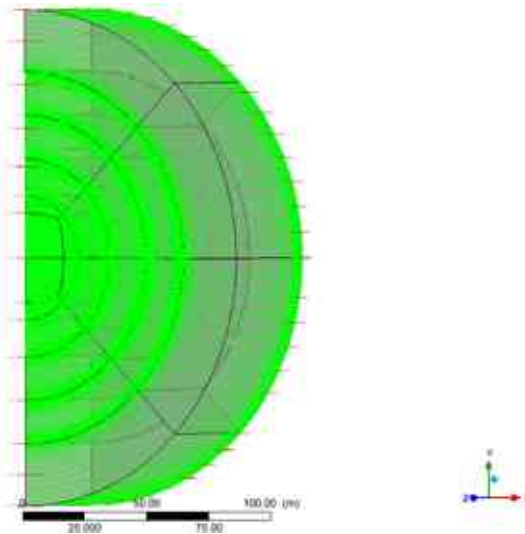


Figure 6-16: Reservoir wall boundary condition

Inlet and outlet boundary conditions: In case of the *inlet boundary condition* a subsonic flow regime was defined with predefined mass flow rate. A uniform mass influx is assumed to exist over the entire boundary as the flow direction is defined as normal to the boundary. During the simulations 9 t/h mass flow rate was assumed with the inlet temperature of 60 °C. Regarding the *outlet boundary condition* also a subsonic flow regime was defined with opening boundary condition type. The relative pressure was set to be 0 Pa and the flow direction assumed to be normal to boundary condition. In both boundary conditions the surfaces were chosen to be the outer 3 porous zones as indicated in [Fig. 6-17](#), where the black arrows represent the inlet boundary conditions and the blue arrows represent the outlet boundary conditions.

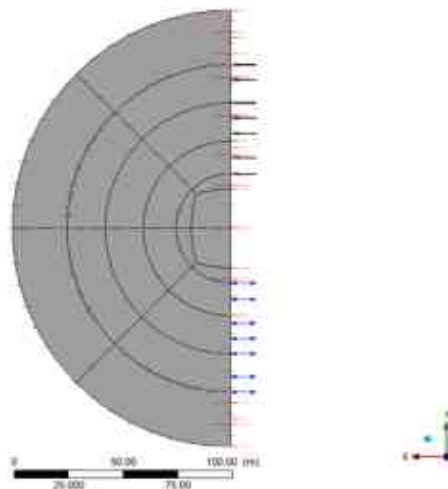


Figure 6-17: Defined inlet and outlet boundary conditions

6.3.3.2 Transport equations

There are three transport equations that describe the instantaneous equations of *mass*, *momentum*, and *energy* conservation. A flow field is characterized by balance in mass, momentum, and total energy described by the continuity equation, the Navier-Stokes equations, and the total energy equation and can be written respectively as follows in a stationary frame.

The Continuity Equation (mass) in fluid dynamics states that the local increase of density with time must be balanced by a divergence of the mass flux and expressed in [Eq. 6-1](#). With other words the rate at which mass enters a system is equal to the rate at which mass leaves the system plus the accumulation of mass within the system ([Pedlosky, 1987](#)).

$$\frac{\partial \rho}{\partial t} + \nabla \cdot (\rho U) = 0 \quad (6-1)$$

Where ρ is the density, t is the time, U is the flow velocity vector field.

The Momentum Equation states that the rate of change in linear momentum of a volume moving with a fluid is equal to the surface forces and the body forces acting on a fluid and expressed in a differential form as [Eq. 6-2](#).

$$\frac{\partial(\rho U)}{\partial t} + \nabla \cdot (\rho U \otimes U) = -\nabla p + \nabla \cdot \tau + S_M \quad (6-2)$$

where p is the static (thermodynamic) pressure, S_M is the momentum source, and the stress tensor, τ , is related to the strain rate by [Eq. 6-3](#)

$$\tau = \mu \left(\nabla U + (\nabla U)^T - \frac{2}{3} \delta \nabla \cdot U \right) \quad (6-3)$$

where μ is the dynamic viscosity, T is the static (thermodynamic) temperature, δ is the identity matrix or Kronecker Delta function. Complete [Eq. 6-2](#) with [Eq. 6-3](#) the more generally known form of the Momentum Equation can be expressed, as follows ([Eq. 6-4](#)):

$$\frac{\partial(\rho U)}{\partial t} + \nabla \cdot (\rho U \otimes U) = -\nabla p + \mu \left(\nabla U + (\nabla U)^T - \frac{2}{3} \delta \nabla \cdot U \right) + S_M \quad (6-4)$$

The Total Energy Equation states that the total energy of an isolated system remains constant, i.e., it is conserved over time and energy is not created or destroyed but is transformed from one form to another. It can be expressed as [Eq. 6-5](#) where the sum of the internal energy and kinetic energy is represented, as follows:

$$\frac{\partial(\rho h_{tot})}{\partial t} - \frac{\partial p}{\partial t} + \nabla \cdot (\rho U h_{tot}) = \nabla \cdot (\lambda \nabla T) + \nabla \cdot (U \cdot \tau) + U \cdot S_M + S_E \quad (6-5)$$

where λ is the thermal conductivity, h_{tot} is the total enthalpy, related to the static enthalpy $h(T,p)$ by [Eq. 6-6](#):

$$h_{tot} = h + \frac{1}{2} U^2 \quad (6-6)$$

The term $\nabla \cdot (U \cdot \tau)$ represents the work due to viscous stresses and is called the viscous work term. This models the internal heating by viscosity in the fluid and is negligible in most flows. The term $U \cdot S_M$ represents the work due to external momentum sources and is currently neglected.

6.3.3.3 Steady-state simulation

During the steady-state simulation the energy term was enabled to reduce the calculation time. The assumption that the heat transfer is negligible during the steady-state flow and does not influence the flow profile was confirmed by two separate simulations with 60°C and 180°C inlet temperature of the fluid. The obtained difference between the models the steady-state simulation after convergence was reached is illustrated in [Fig. 6-18](#).

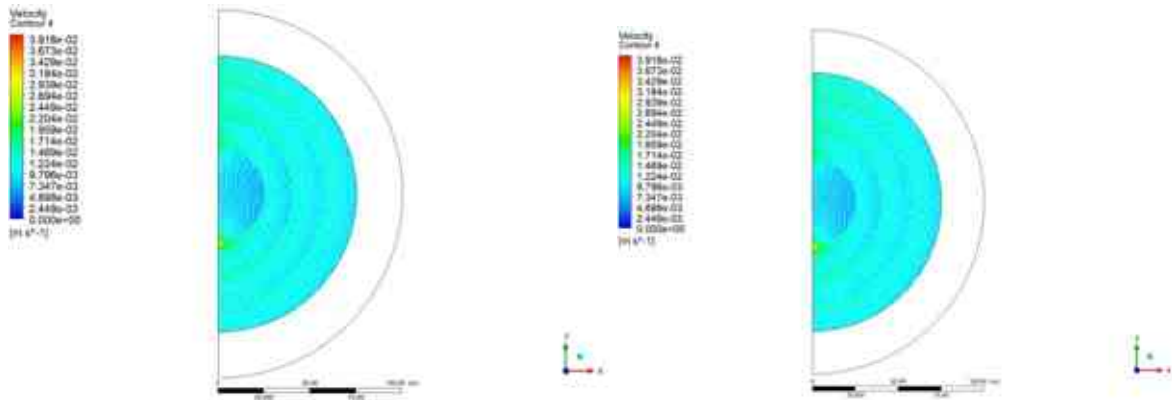


Figure 6-18: Flow profiles (left with 60°C inlet temperature and right 180°C inlet temperature)

The average outlet pressure was 82.20 Pa in case of the 60°C inlet temperature and 82.18 Pa in case of the 180°C inlet temperature, which can be considered neglectable. The pressure convergence during the simulation can be visualized in [Appendix Q](#), while the convergence of the root mean square normalized residuals of mass and momentum over the whole domain is illustrated in [Appendix R](#).

The fracture was depicted in the model as a porous domain containing one continuous fluid. The loss term and all other terms in the governing equations are modified by porosity. This formulation is therefore also known as the "full porous model" or the "true velocity formulation". This approach supports both solid models for the solid's thermal conductivity, for instance, and models for the domain's fluid-solid interaction.

The Navier-Stokes equations and the widely used Darcy's law for flows in porous regions are both simultaneously generalized in the "full porous model". The 'infinitesimal' control volumes and surfaces are expected to be substantial in relation to the interstitial spacing of the porous medium but relatively small in relation to the scales that you want to resolve when deriving the continuum equations. As a result, it is believed that the supplied control surfaces and cells have both solid and fluid regions.

The volume porosity, ϕ is the ratio of the volume and V' available for the fluid to flow and the physical volume V of the cell and it can be described by [Eq. 6-7](#).

$$V' = \phi V \quad (6-7)$$

It is assumed that the vector area available to flow, A' , through an infinitesimal planar control surface of vector area A is given by [Eq. 6-8](#) as follows:

$$A' = K \cdot A \quad (6-8)$$

where $K = (K^{ij})$ is a symmetric second rank tensor, called the area porosity tensor. Each term in the Continuity Equation ([Eq. 6-1](#)) and in the Momentum Equation ([Eq. 6-4](#)) should be multiplied by these ratios ([Eq. 6-7](#) or [Eq. 6-8](#)) to express those transport equations in cases where the flow is in a porous media. As the Energy Equation was disabled during the steady-state simulation its conversion is not necessary. In this scenario the Continuity Equation becomes [Eq. 6-9](#) and the Momentum Equation becomes [Eq. 6-10](#).

$$\frac{\partial}{\partial t} \phi \rho + \nabla \cdot (\rho K \cdot U) = 0 \quad (6-9)$$

$$\frac{\partial}{\partial t} (\phi \rho U) + \nabla \cdot (\rho (KU) \otimes U) = -\phi \nabla p + \nabla \cdot \left(\mu K \cdot \left(\nabla U + (\nabla U)^T - \frac{2}{3} \delta \nabla \cdot U \right) \right) + \phi S_M \quad (6-10)$$

In this case the isotropic loss model was used and the momentum loss through an isotropic region can be formulated using permeability and loss coefficients by [Eq. 6-11](#) as follows ([ANSYS, 2011](#)):

$$S_{M,x} = -\frac{\mu}{K_{perm}} U_x - K_{loss} \frac{\rho}{2} |U| U_x$$

$$S_{M,y} = -\frac{\mu}{K_{perm}} U_y - K_{loss} \frac{\rho}{2} |U| U_y \quad (6-11)$$

$$S_{M,z} = -\frac{\mu}{K_{perm}} U_z - K_{loss} \frac{\rho}{2} |U| U_z$$

where K_{perm} is the permeability and K_{loss} is the quadratic loss coefficient. The pressure gradient in the porous domain is influenced by this momentum source term, which results in a pressure drop proportionate to the fluid velocity across the porous domain ([Martínez et al., 2012](#)). The linear component of this source represents viscous losses, and the quadratic term represents inertial losses.

As the effect of loss coefficient is relevant in case of non-laminar flows the value of this term could be determined optionally. Also, the effect of porosity should not have major effect on the fluid dynamics of the model. To confirm these a sensitivity analysis was done. The essence of the sensitivity analysis was to run and evaluate several simulations with different porosity and loss coefficient values and see what the effect of these two parameters are on the pressure is drop. The results are illustrated in [Fig. 6-19](#).

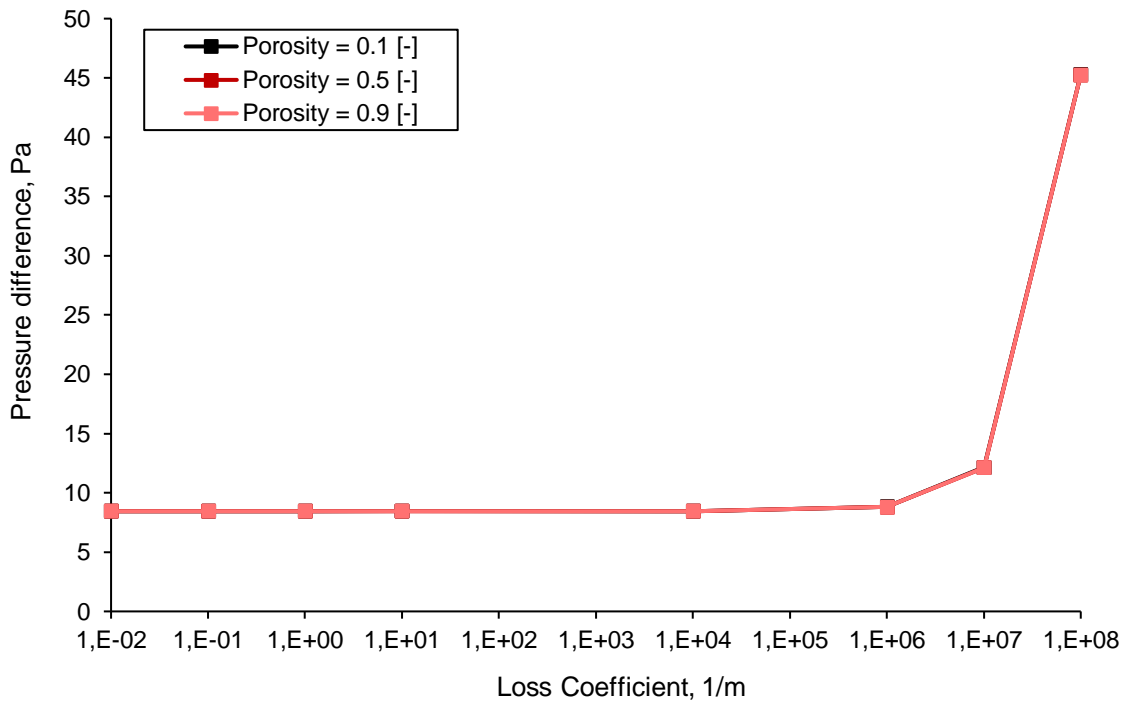


Figure 6-19: Sensitivity analysis for porosity and loss coefficient

It can be readily inferred that the effect of loss coefficient on the pressure difference is negligible until the value of 1,000,000 1/m. As low mass flow rates were selected to simulate laminar flows this value is lower than that and can be arbitrarily selected below this value. In case of porosity which was also an input during the simulation its value does not have significant effect on the pressure drop thus on the flow profile.

The result of the steady-state state simulation is a flow profile which is mainly determined by the permeability of each zone (an example can be seen in [Fig. 6-19](#)). This flow profile is then fixed and connected to the transient simulation where the energy equation is calculated across the meshed domain. In all simulation 6,000 timesteps were used for the iterations which was more than sufficient to reach a suitable convergence on the model.

6.3.3.4 Transient simulation

In case of low-speed flows an alternative form of the Energy Equation ([Eq. 6-5](#)), the so-called *Thermal Energy Equation* can be used. To derive it, an equation is needed to be defined for the mechanical energy, K ([Eq. 6-12](#)), which is then can be implemented into the Momentum Equation ([Eq. 6-2](#)) in the form of [Eq. 6-13](#) as the dot product of U .

$$K = \frac{1}{2} U^2 \quad (6-12)$$

$$\frac{\partial(\rho K)}{\partial t} + \nabla \cdot (\rho U K) = -U \cdot \nabla p + U \cdot (\nabla \cdot \tau) + U \cdot S_M \quad (6-13)$$

Subtracting [Eq. 6-13](#) from the Total Energy Equation ([Eq. 6-5](#)) yield the Thermal Energy Equation by [Eq. 6-14](#), as follows:

$$\frac{\partial(\rho h)}{\partial t} - \frac{\partial p}{\partial t} + \nabla \cdot (\rho U h) = \nabla \cdot (\lambda \nabla T) + U \cdot \nabla p + \tau : \nabla U + S_E \quad (6-14)$$

The term $\tau : \nabla U$ is called the viscous dissipation and always positive. This term is insignificant in most fluid flow and describes the internal heating by the fluid's viscosity.

During the transient simulation the mass and momentum equations were enabled to reduce the simulation capacity and only the energy equation was calculated and with this approach a relatively large timestep can be reached without damaging convergence. In this study 900 seconds was chosen to be the timestep during the simulation as it was proved to be sufficient by a sensitivity analysis. The result of the sensitivity analysis is illustrated in [Fig. 6-20](#).

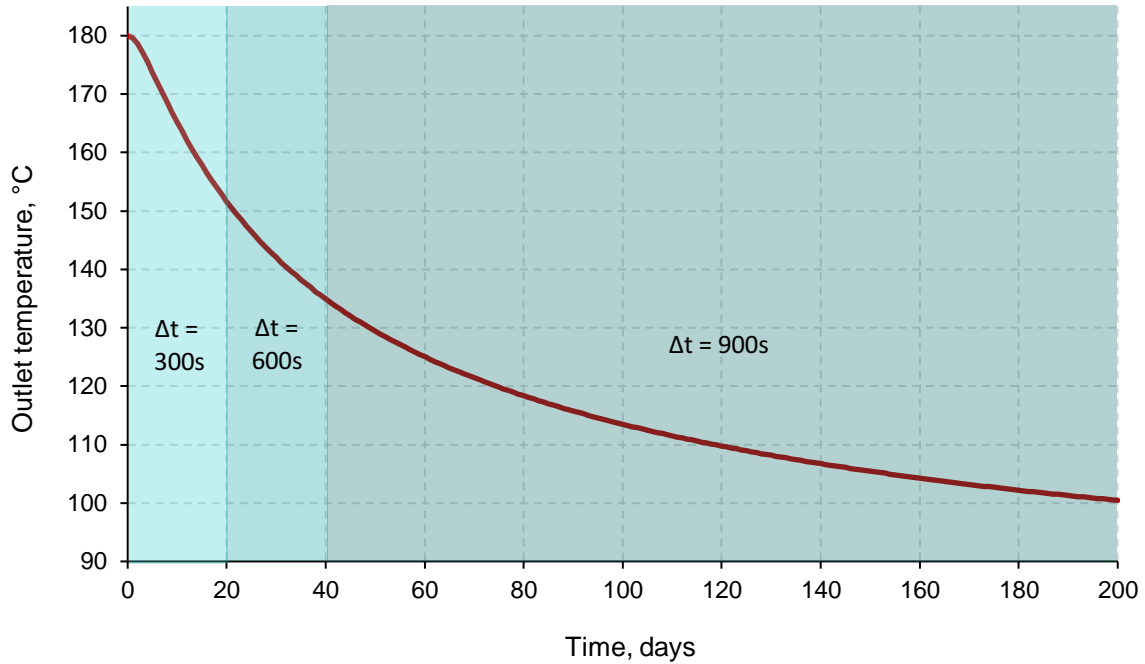


Figure 6-20: Sensitivity analysis for transient timestep

It can be readily inferred that the temperature curve in respect of time is continuous with all timestep which means that the convergence in case all timestep was adequate. Five coefficient loop iteration was selected during the transient simulation since the model converged properly with this approach as it can be seen in [Appendix S](#).

The goal of the simulations is to prove that the flow in the fracture, thus the heat production can be controlled and optimized with different proppant permeability values of each zone. The thermal power that can be reached is basically the area under the *Outlet temperature* vs *Time* (see in [Fig. 6-20](#)). The exact calculation can be seen in [Eq. 6-15](#), as follows:

$$Q = c_p m (T_{out} - T_{in}) \quad (6-15)$$

where Q is the thermal power, m is the mass flow rate. As c_p , m , T_{in} , are constant, during result comparisons only the sum of the outlet temperatures at each timesteps will be presented.

6.3.4 Validation of the model

Since all theoretical models needs to be validated with real observation the developed finite element simulation had to be tested as well. No exact equipment is available to measure the behavior of flow in propped fracture in this arrangement, although there are standard proppant measurement methods and equipment that can be utilized for this purpose. The

widely accepted and used API RP 19D ([API RP19D, 2008](#)) was used to validate the model and the measurement procedure is presented in [Chapter 7](#). Based on this standard measurement a 16/32 mesh sized proppant were tested. After that the geometry of the simulation was changed to match the measurement apparatus. The geometry is illustrated in [Fig. 6-21](#). The scone shape geometry is a porous domain as was applied during the fracture simulation and all other boundary conditions were assigned similarly as presented.

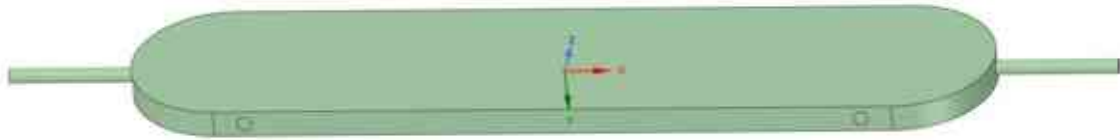


Figure 6-21: Geometry of the validation model

The meshing was done in the body with a different approach using tetrahedron method but focusing on the mesh quality to reach similar threshold values. The generated mesh can be visualized in [Fig. 6-22](#). The average orthogonal quality was 0.787, the average skewness of the model was 0.215, and the average aspect ratio was reached at 1.798. With this quality, it can be established that the meshing quality was suitable to reach proper convergence during the simulation.

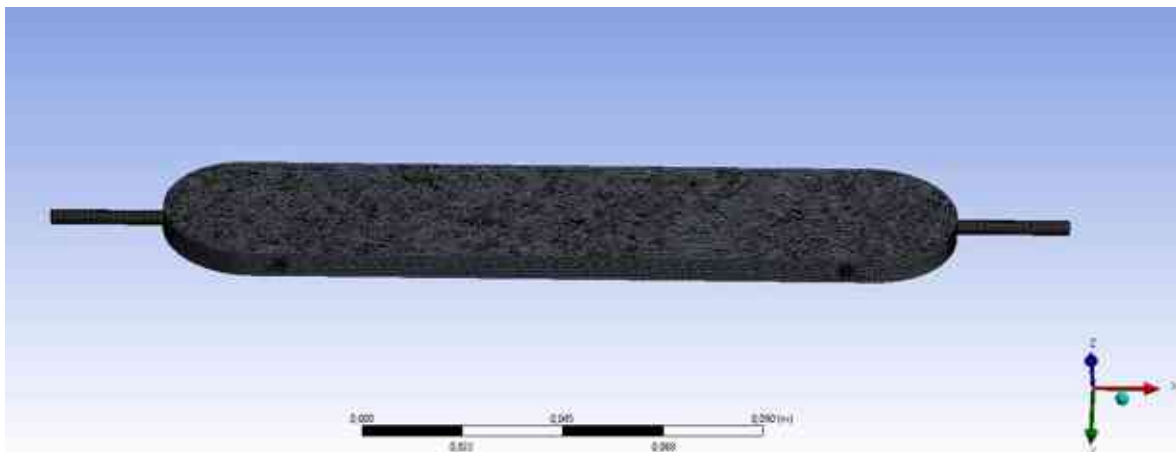


Figure 6-22: Meshing of the validation model

With this validation the behavior of the steady-state simulation was tested as the main purpose of the measurement procedure is to analyze the proppant conductivity which has an effect on the flow profile but the heat transfer phenomenon cannot be tested in this way. The pressure profile of the steady-state simulation is illustrated in [Fig. 6-23](#), while the velocity profile can be seen in [Appendix T](#).

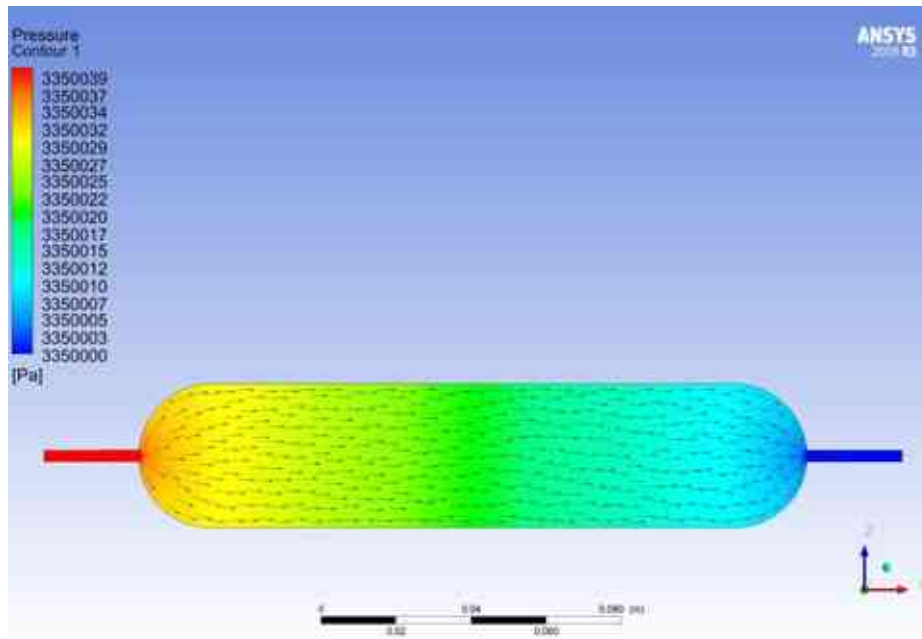


Figure 6-23: Pressure profile of the validation model

After the measurements and simulations, the result of the comparison confirms that the simulation describes reality efficiently. Detailed comparison can be seen in [Appendix U-V](#). The average variance is 0.41%, that can be considered a very efficient model and the results of the measurement and simulation can be seen in [Fig. 6-24](#).

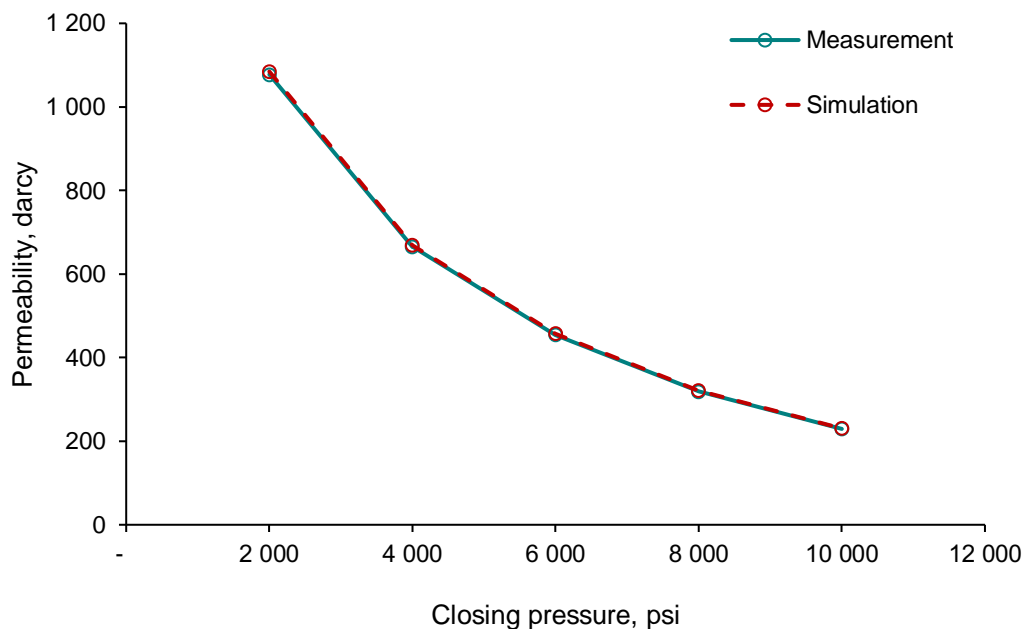


Figure 6-24: Results of the validation

6.3.5 Reducing simulation time

Based on the first simulations during which the transient interrupt condition was set to be at 100 °C, the average time required for one complete simulation was at least 20 days depending on the trend of the outlet temperature curve. As several measurements are required to have a comprehensive data set for the optimization of permeability arrangement, the simulation time had to be reduced. Since the outlet temperature and time curves can be described by a reciprocal function where the independent variable should be raised to the power and as the initial inlet temperature of the fluid is 60 °C it must be the convergence value. The basic equation can be seen in [Eq. 6-16](#).

$$f(x) = \left(\frac{a}{b+x}\right)^c + 60 \quad (6-16)$$

Where a , b , and c are the parameters and x is the independent variable. Using the simulation results it can be tested that how long simulation is necessary to approximate the final result efficiently by optimizing the parameters to reach the least *R-square* values. For the optimization purpose, the genetic or evolutionary algorithm was selected, which incorporates randomness and inheritance into the optimization process ([Wang et al. 2011](#)) and is based on evolutionary computing, whose main idea is formed from Darwin's theory of evolution ([Kazemi et al. 2020](#)). In essence, the algorithm creates an analogy between the optimization process and the natural selection of living organisms. In an iterative process, the genetic search enhances a population of artificial individuals, and the genetic information of the chromosomes (model variables) are randomly exchanged during the process ([Szabó and Dobróka 2017](#)). The steps of the optimization are illustrated in [Fig. 6-25](#).

The main steps can be described by the followings ([Covas and Gaspar-Cunha 2009](#); [Maad 2016](#)): (1) The calculations start with the random definition of all the individuals composing the population (population initialization step). (2) In the following evaluation step, the values of the criteria for each individual are determined from the data created by the modeling routine. (3) Once these are known, it is possible to determine the fitness of every individual (value F). (4) This is then followed by the reproduction step which is basically the cloning of an individual without modification to maintain high fitness in the next generation. (5) Then crossovers of the selected individuals are happened when the attributes of the parents are mixed. (6) The last basic operator is the mutation which provides an element of randomness in the individuals of the population. (7) Calculations finish when all individuals converge to the same solution, or when a prescribed number of generations have been explored.

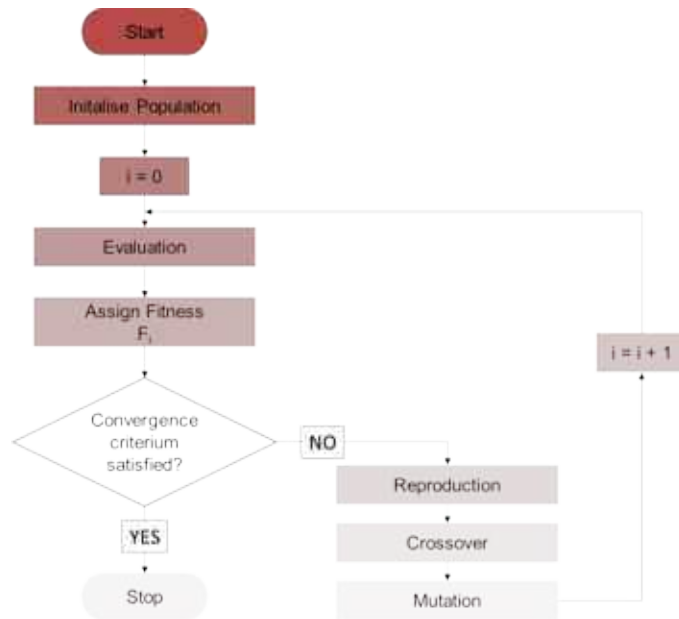


Figure 6-25: Simplified flowchart of an evolutionary algorithm ([Covas and Gaspar-Cunha 2009](#))

One result can be seen in [Fig. 6-26](#), where the permeability of the four different zones was set to be 128 Darcy. The optimizations of the fitting curves were done on the 10-, 20-, 30-, 60-, 90-, 120-, 150-, and 180-days data set and the results were compared to the total simulation data. The results show that the more simulation time is used the better fitting can be reached. Detailed illustration of the results can be found in [Appendix W](#).

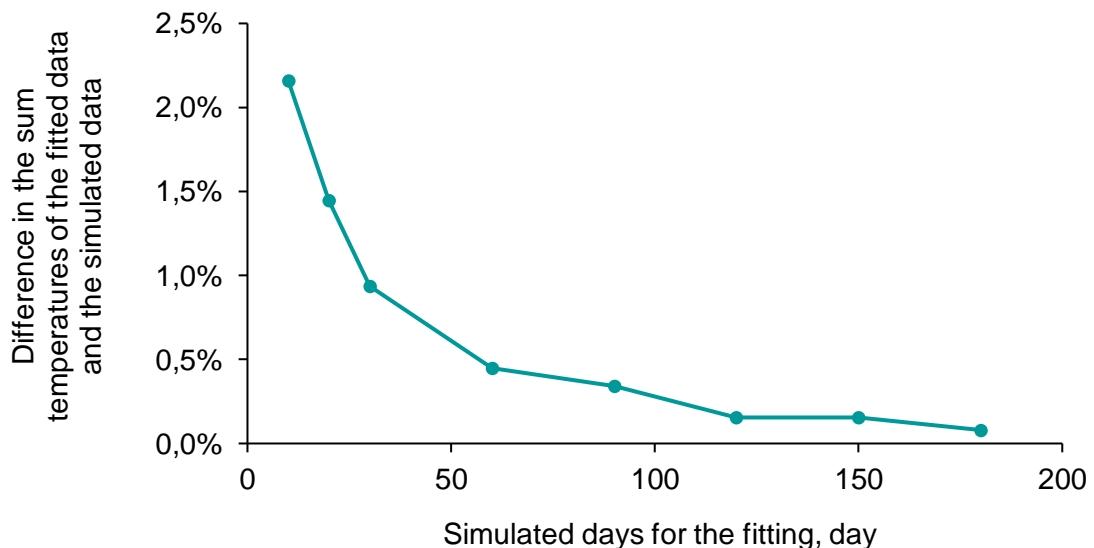


Figure 6-26: Absolute deviation of the fitting optimization from the total simulation result at different simulation times in the case of each zone has 128 Darcy permeability

To be able to identify the optimal simulation time where the remaining data can be calculated with the optimized function without compromising the accuracy, five full-time

simulations were run. Then the results were tested with the previously presented optimization method. The results are illustrated on [Fig. 6-27](#).

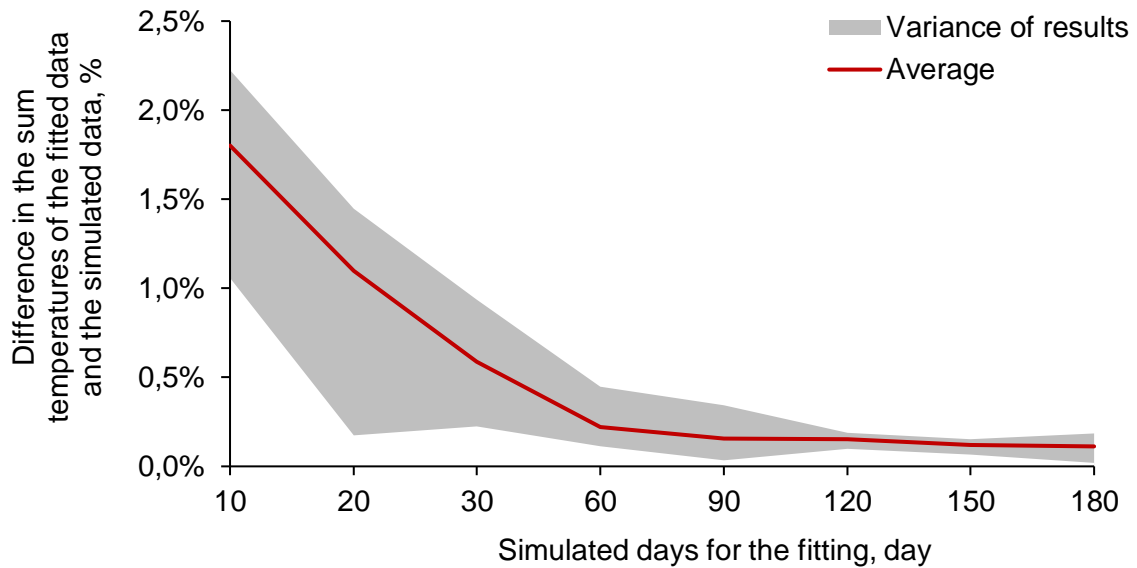


Figure 6-27: Result of the curve fitting to reduce simulation time

One can readily infer that a lower value of variance can be reached with more simulation time. In this study 90 days of simulation was set as with this interval the remaining curve can be forecasted with high certainty at lower than 0.5% variance. With this approach the simulation time could be reduced significantly, and the accuracy of the model was not severely compromised.

7 PROPPANT MEASUREMENTS AND ANALYSIS

As it is mentioned, the basic principle of the new method for flow profile control is to create several propped zones in the fracture with different permeability values. With an optimization tool the most effective arrangement can be reached in point of heat recovery. One approach could be the application of different types and/or mesh size proppants in the fracture. Depending on the optimization result the exact values cannot be reached in all zones as all proppants have assigned permeability values which are available in their technical data sheet. A new method should be developed to reach a wide range of fracture permeability values under the reservoir conditions.

The new suggested method is to mix proppants with different particle size distribution. It can be seen intuitively that mixing smaller sized proppants into a larger sized proppant pack will reduce the permeability of the pack as the smaller diameter proppants will occupy smaller volumes that previously was available for fluid flow. This phenomenon has been proven by the literature but since the main objective in the oil and gas industry is to improve the conductivity of fractures this topic is sporadically analyzed previously ([McDaniel and Willingham 1978](#); [Schmidt et al., 2014](#)). To be able to establish the connection between mixed proppant pack's properties and the final conductivity values several measurements were performed.

There are two different, widely accepted measurement methods in the industry to determine the fracture permeability and conductivity of proppant-packs. The first standardized measurement method was introduced by the American Petroleum Institute in 1989 under the code of API RP 61 and with the name "Recommended Practices for Evaluating Short Term Proppant-pack Conductivity" ([API RP 61, 1989](#)). As the measurement method has high uncertainty, a modified approach and new equipment began to spread in the industry ([Penny, 1987](#)). In the upcoming years, this modified approach became the standard procedure in the industry, then the International Organization for Standardization adopted the method in 2008 under the code DIN EN ISO 13503-5 ([ISO 13503-5, 2006](#)). Later the American Petroleum Institute also adapted under the code API RP 19D and with the name "Recommended Practice for Measuring the Long-term Conductivity of Proppants" ([API RP 19D, 2008](#)). It is worth mentioning that significant variances can be observed between measurements under the same conditions. On average, the variance between the measurements is $\pm 20\%$, but as high as 80% variance also can be found ([Richard et al., 2019](#); [Anderson, 2013](#)). This phenomenon can be interpreted with different factors, but mainly the proppant size distribution and the initial and loaded proppant arrangement

influence the behavior in which cases creating the same conditions is impractical (Liang et al., 2015). One can see that the API RP 19D measurement requires around two weeks to complete, which makes it impractical to measure several samples for analysis.

7.1 Measurements

Based on the API RP 19D, eight measurements have been performed on the standardized equipment on two different proppants and their different mass percentage mixtures to determine the proppant-pack permeabilities under different closing pressures. A schematic illustration of the standard measurement equipment can be found in the Fig. 7-1, while a photo taken on the equipment can be seen in the Appendix X.

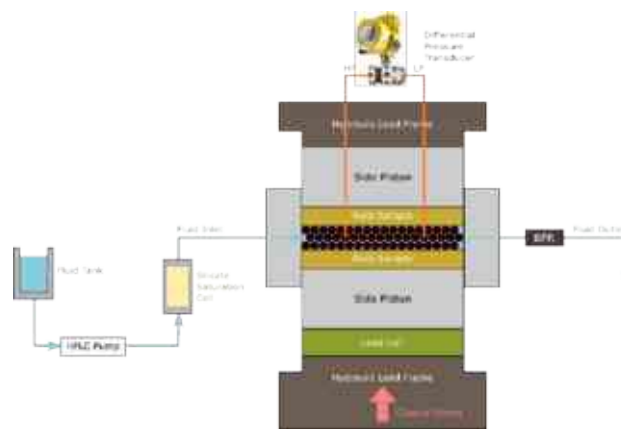


Figure 7-1: Schematic representation of the standard equipment used for permeability and conductivity measurements

The proppants were spherical ceramic balls, but their size distribution and other parameters differed. The proppant with a smaller median particle diameter is a 30/50 mesh sized light-weight ceramic proppant (technical datasheet can be seen in the Appendix Y-Z), while the proppant with larger median particle size is a 16/32 mesh ceramic proppant with higher crush resistance (no technical datasheet was available). The basic parameters of the two proppants are detailed in Tab. 7-1.

Table 7-1: Summary of the basic parameters of the proppants

Parameters	Technical data sheet, 30/50 mesh	Measured, 30/50 mesh	Measured, 16/32 mesh
Specific gravity, -	2.71	2.67	3.01
Bulk density (at 0 psi), g/cm ³	1.56 ²⁰	1.51	1.74
Median particle diameter, μm	473	470	907
Roundness, -	0.9	0.83	0.80
Sphericity, -	0.9	0.84	0.85

²⁰ Data was not specified for mesh diameter in the technical data sheet.

The specific gravity was measured by a Pentapyc 5200e device (see in [Appendix AA](#)) which operates on the principle of gas displacement, and the bulk density at atmospheric pressure was determined by the [API RP 19C \(2008\)](#) standard measurement method and device (see in [Appendix AB](#)). Instead of the methods recommended in the API RP 19C standard, a more modern measurement approach was used to measure the proppants' size distribution, roundness, and sphericity. For this purpose, an Occhio Zephyr ESR 2 equipment was used (see in [Appendix AC](#)) that measured more than 30,000 randomly selected proppant particles in the 30/50 mesh sample and more than 16,000 particles in the case of the 16/32 mesh sample. The equipment uses image analysis by a double telecentric lens which constantly analyzes the gravity-free falling particles. This equipment is a suitable and compact replacement for typical sieve analysis processes, as it can autonomously analyze particles between 30 μm and 3 cm. It can be seen that the proppant particles are not perfectly rounded and spherical which may have an effect on the models' behavior (results can be seen in [Appendix AD](#)). The histogram of the size distribution measurement results can be seen in [Fig. 7-2](#). One can observe that there is only minimal overlap between the size ranges of the two proppants, which serves the purpose of perceiving the changes in permeability and conductivity effectively due to mixing.

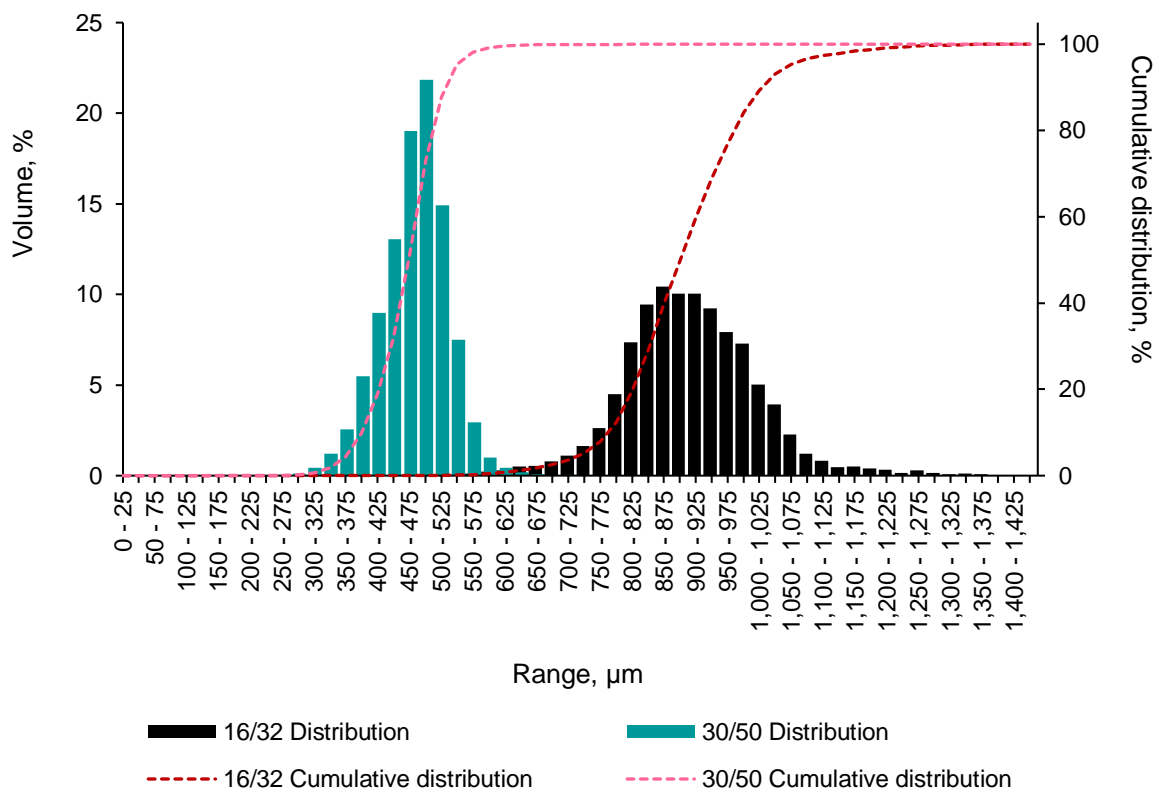


Figure 7-2: Size distribution histograms in case of the applied proppants

7.1.1 Validation of the measurement

The first three measurements were performed on the same 30/50 mesh proppant to be able to determine the gross variance between the measurements. As the reported 20% variance with the API RP 19D standard measurement method can be considered as significant, it was important to determine what accuracy can be reached during the measurements, and in this way, we could validate the accuracy of the later measurements.

Since the API RP 19D standard recommends that permeability values should be determined at the end of each closing pressures (by the application of different flow rates), this method has been used. The driving equation for calculating the permeability has been introduced by [Darcy \(1856\)](#) and can be seen in [Eq. 7-1](#), where the Q is the flow rate in m^3/s , A is the cross-sectional area of the flow in m^2 , k is the permeability in m^2 , ΔP is the total pressure drop in Pa, μ is the dynamic viscosity of the fluid in Pas and L is the length of the sample in m.

$$\frac{Q}{A} = k \frac{\Delta P}{\mu L} \quad (7-1)$$

The result of the three measurements can be seen in [Fig. 7-3](#) where the mean value of the three measurements is illustrated with gross variance of the measurements.

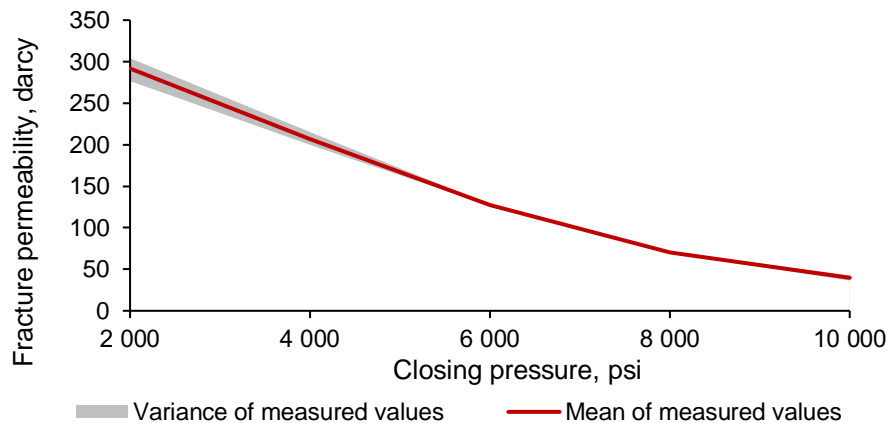


Figure 7-3: Validation of the measurement accuracy on the 30/50 mesh proppant

The gross variance between the measurements has been evaluated by the [Eq. 7-2](#) ([Richard et al., 2019](#)).

$$Gross\ Variance = \frac{\sigma}{\bar{X}} \quad (7-2)$$

Where σ is the standard deviation and \bar{X} is the mean. The statistical comparison of the results is shown in the [Tab. 7-2](#).

Table 7-2: Statistical comparison of the permeability results on the 30/50 mesh proppant

Closure stress <i>psi</i>	Permeability, A sample <i>darcy</i>	Permeability, B sample <i>darcy</i>	Permeability, C sample <i>darcy</i>	Mean Permeability <i>darcy</i>	Standard deviation <i>darcy</i>	Gross Variance %
2,000	304.2	294.4	276.7	291.8	13.9	4.8%
4,000	215.5	205.6	199.5	206.9	8.1	3.9%
6,000	126.6	127.7	128.2	127.5	0.8	0.6%
8,000	71.1	69.2	71.3	70.5	1.2	1.6%
10,000	42.5	36.1	40.7	39.8	3.3	8.3%

From the results, it can be observed that the reproduction of nearly identical permeability values was successful with the measurement method up to 8.3% variance and an average value of 3.9%. These results exceed the results of similar experiments with the API RP 19D method by [Anderson \(2013\)](#) and provides almost the same results as [Richard et al. \(2019\)](#) published in 2019 presenting two different vibration methods. This low variance proved the suitable reproducibility of the measurements and thus ensuring the accuracy of the later measurements on the mixtures.

7.1.2 Mixed proppant measurement results

The mixing of the two proppants was done by 20 m/m% increment, and each proppant-pack was measured with the same approach as the three measurements were on the 30/50 mesh proppant (photos taken on the mixtures before the measurements can be seen in [Appendix AE](#), while photos taken on the samples after the measurements can be seen in [Appendix AF-AU](#)). The results are illustrated in [Fig. 7-4](#) where in the case of the 30/50 mesh proppant, the average value of the three measurements is used (red line on [Fig. 7-3](#)).

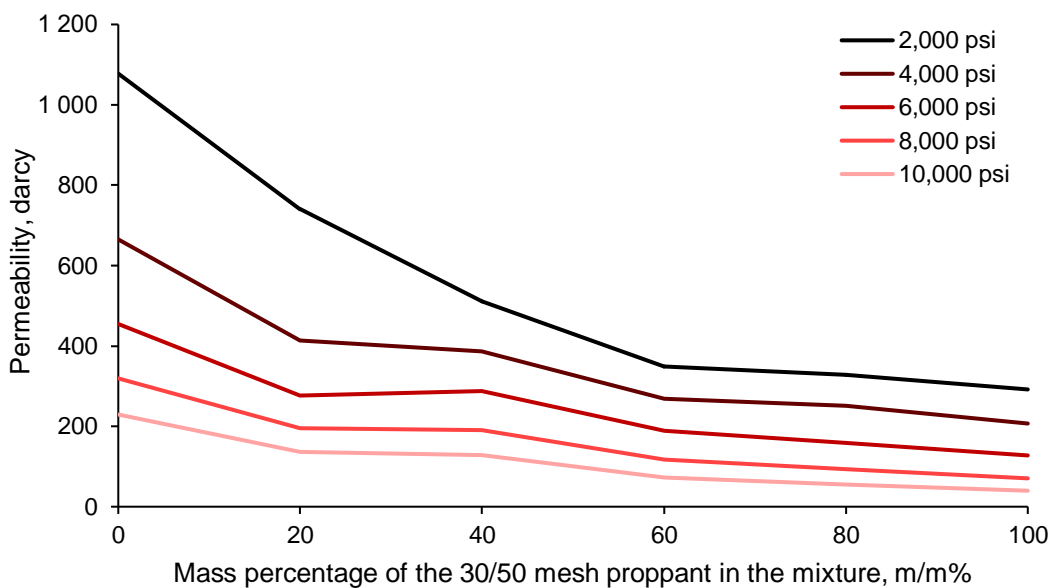


Figure 7-4: Effect of mixing on permeability at different closing pressures

It can be seen from the above presented results that the fracture permeability values are decreasing with increasing closing pressure and also decreasing with decreasing average particle diameter in the sample (larger mass percentage of 30/50 mesh proppant in the mixture results in decreasing average median particle size). The connection between these variables is not linear but rather exponential. It can be concluded from the results that a small amount of smaller diameter particles can significantly deteriorate the larger proppant's performance. In contrast, adding a small amount of larger proppant to a mixture cannot provide significantly better performance. The results of the individual measurements can be seen in [Appendix AV-AZ](#).

7.2 Theoretical Analysis

As the API standard measurement method is a very time-consuming process an equation that can predict the permeability of the proppant-pack under reservoir conditions can be practical. The proppant can be viewed as an unconsolidated, heterogeneous (although well-sorted) granular packing of which one of the main properties is the permeability that it can provide under reservoir conditions. The properties of flow through granular packings have been extensively studied, both theoretically ([Kozeny, 1927](#); [Carman, 1937](#); [Macdonald et al., 1979](#)), numerically ([Martys et al., 1994](#); [Coelho et al., 1997](#); [Zaman and Jalali, 2010](#)), and experimentally ([Loudon 1952](#); [Chapuis 2004](#)). These studies were developed under different conditions than proppants are usually applied. The main difference is that proppants are placed in reservoirs where the pressure and temperature ranges are higher than in the case of the studies mentioned above. These conditions can cause discrepancies in the developed models as the granular materials are prone to deformation, crush, embedment, and corrosion which challenge the application of those models in such conditions. Since proppants (especially particular types of proppants such as ceramic or resin-coated proppants) have distinct properties (e.g., crush resistance; temperature resistance; Young modulus), several studies have been published pronouncedly on proppant behavior ([Mollanouri et al., 2015](#); [Liang et al., 2016](#); [Mittal et al., 2018](#)). There is no literature that comprehensively analyses and evaluates the applicability of different models for flow-through granular packings on proppant packings of different size distributions. The primary purpose of this analysis is to provide a suitable way to compare the available models and offer a model which can be used to describe the proppant-pack permeability under reservoir conditions, providing a suitable alternative instead of the very time-consuming standard measurement methods.

There are two driving mechanisms that have an impact on fracture permeability. One is the effect of viscous shear from the fracture wall, and the other is the viscous drag from the surface of the proppants ([Brinkman, 1949](#)). It can be readily inferred that if the fracture is wider than the viscous drag of the proppant becomes more pronounced, and in case of a narrower fracture or in case the fracture is not propped efficiently, the effect of viscous shear on the wall becomes more prominent. In most of the available theoretical models, the fracture permeability is approximated with the proppant-pack permeability (neglecting the effect of viscous shear from the wall), resulting in that most of the developed models can be inapplicable to the scenario where the effect of viscous shear is considerable ([Teng et al., 2020](#)). Taking into consideration both mechanisms, there will be a transient zone where the effect of both mechanisms is noticeable.

For an unpropped vertical fracture, the fluid flow can be calculated by [Eq. 7-3](#) ([Sutera and Skalak, 1993](#)).

$$q = \frac{w_f^3}{12\mu} h_f \frac{dp}{dL} \quad (7-3)$$

Where q is the volume-flux rate in m^3/s , w_f is the fracture width in m, μ is the dynamic viscosity of the fluid in Pa-s, h_f is the fracture height in m, p is the pressure in Pa, L is the length in m. Using Darcy's law, the flux rate also can be calculated by the [Eq. 7-4](#).

$$q = \frac{k_f}{\mu} w_f h_f \frac{dp}{dL} \quad (7-4)$$

Where k_f is the fracture permeability in m^2 .

Combining [Eq. 7-3](#) and [Eq. 7-4](#) the fracture permeability of an unpropped fracture can be calculated by [Eq. 7-5](#).

$$k_f = \frac{w_f^2}{12\mu} \quad (7-5)$$

In order to visualize the effect in case only viscous drag is considered, an empirical correlation was used which can be seen in [Eq. 7-6](#) ([Krumbein and Monk, 1943](#)).

$$k_f = k_p = 760D^2 e^{(-1.31\sigma_D)} \quad (7-6)$$

Where k_p is the proppant-pack permeability in md, D is the geometric mean grain diameter in mm, σ_D is the standard deviation of the size distribution in -.

Using [Eq. 7-5](#) to determine fracture permeability in case only viscous shear is accounted for, and an empirical correlation represented in [Eq. 7-6](#) that considers only viscous drag from the proppant-pack, the two different mechanisms can be visualized in [Fig. 7-5](#), where the D and σ_D parameters in [Eq. 7-6](#) are 0.4704 mm and 0.0529 mm respectively (based on own measurements on the investigated proppants).

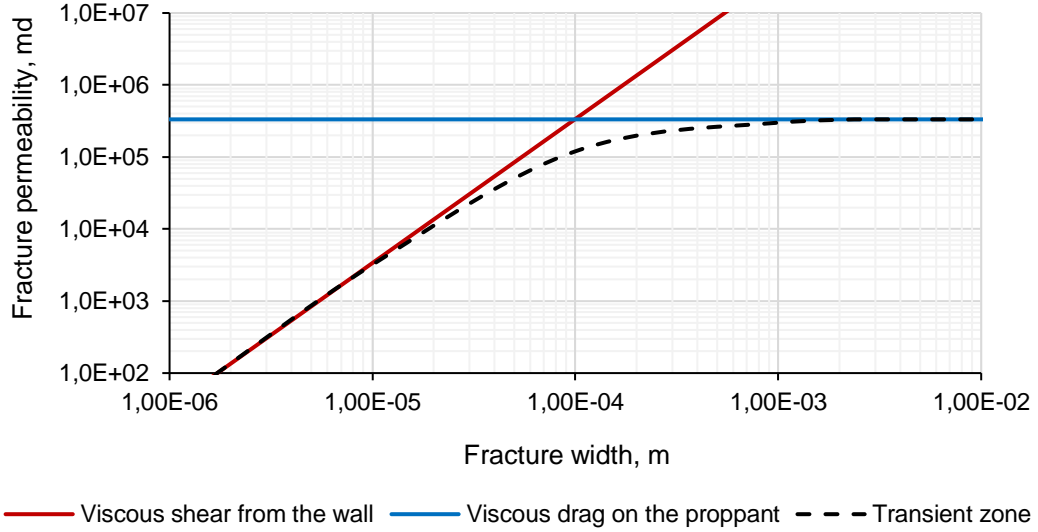


Figure 7-5: Fracture permeability values using [Eq. 7-5](#) and [Eq. 7-6](#) (transient zone is just a visualization)

Since several different models are available that consider only the viscous drag from the proppant-pack, one of the objectives of this study is to compare and analyze them under different scenarios. For this purpose, a combined equation was developed based on the available literature that considers both mechanisms and facilitates the comparison of different proppant-pack permeability models.

As literature on mixed sized proppant can be found sporadically in the literature a model that can forecast the permeability of such systems should be conducive.

7.2.1 Derivation of a new theoretical model

Since a theoretical model should be used that consider both the viscous shear and viscous drag, [Eq. 7-7](#) has been used ([Teng et al., 2020](#)).

$$k_f = k_p \left\{ 1 + \frac{2}{w_f} \left(\frac{v_o}{\frac{k_p \Delta P}{\mu L}} + 1 \right) \sqrt{\frac{k_p}{\phi_p}} \left[csch \left(\sqrt{\frac{\phi_p}{k_p}} w_f \right) - coth \left(\sqrt{\frac{\phi_p}{k_p}} w_f \right) \right] \right\} \quad (7-7)$$

Where k_f is the fracture permeability in m^2 , k_p is the proppant-pack permeability in m^2 , w_f is the fracture width in m, v_o is the flow velocity at fracture walls in m/s (in case laminar flow

the value is equal to 0), μ is the dynamic viscosity of the fluid in Pa-s, ΔP is the pressure difference in Pa, L is the length of the fracture in m, and Φ_p is the proppant pack permeability in m^2 . The model can be used under the following assumptions:

- The fluid is incompressible
- The viscosity of the fluid is constant
- The fluid flow is laminar and in a steady state
- The effect of gravity is neglected
- The proppants are immobile, and the porosity and permeability of the proppant pack are constant

As the slippage on the fracture wall is assumed to be 0 during our measurements the [Eq. 7-7](#) can be reduced to [Eq. 7-8](#).

$$k_f = k_p \left\{ 1 + \frac{2}{w_f} \sqrt{\frac{k_p}{\Phi_p}} \left[\operatorname{csch} \left(\sqrt{\frac{\Phi_p}{k_p}} w_f \right) - \operatorname{coth} \left(\sqrt{\frac{\Phi_p}{k_p}} w_f \right) \right] \right\} \quad (7-8)$$

Several correlations can be found in the literature for the calculation of pressure drop caused by fluid flow through packed beds. These correlations can be utilized to determine the proppant-pack permeability in the [Eq. 7-8](#). Those correlations often accompanied by a so-called friction factor coefficient which is a kind of descriptor of the viscous drag exerted by the granular packings ([Erdim et al., 2015](#)). This coefficient has been modified to a so-called “modified particle friction factor” that can be seen in [Eq. 7-9](#) ([Montillet et al., 2007](#)).

$$f_p = \frac{-\Delta P d_p}{\rho v^2 L} \quad (7-9)$$

Where f_p is the modified particle friction factor in -, d_p is the particle mean diameter in m, ρ is the fluid density in kg/m^3 , v is the fluid velocity based on the empty cross-section of the bed in m/s. This term is often referred to as the “dimensionless pressure drop” ([Eisfeld and Schnitzlein, 2001](#)).

The well-known Darcy’s equation can be used to determine the permeability of a proppant-pack ([Darcy, 1856](#)). The equation shows similarity with the [Eq. 7-9](#) and can be seen in the [Eq. 7-10](#).

$$V = \frac{-\Delta P k_p}{\mu L} \quad (7-10)$$

Combining [Eq. 7-9](#) with [Eq. 7-10](#) an equation can be expressed which allows to substitute the k_p term in the [Eq. 7-8](#). The interrelation can be seen in the [Eq. 7-11](#).

$$f_p = \frac{d_p \mu}{\rho V k_p} \quad (7-11)$$

Utilizing the kinematic viscosity, the equation can be modified to [Eq. 7-12](#). This new equation establishes the relationship between the proppant-pack permeability (k_p) and the modified particle friction factor (f_p).

$$k_p = \frac{d_p v}{v f_p} \quad (7-12)$$

Substituting the [Eq. 7-12](#) into the [Eq. 7-8](#) a final relationship is reached with which the different correlations of modified particle friction factor can be analyzed. The final equation can be seen in the [Eq. 7-13](#).

$$k_f = \left(\frac{d_p v}{v f_p} \right) \left\{ 1 + \frac{2}{w_f} \sqrt{\frac{\left(\frac{d_p v}{v f_p} \right)}{\phi_p}} \left[\operatorname{csch} \left(\sqrt{\frac{\phi_p}{\left(\frac{d_p v}{v f_p} \right)}} w_f \right) - \operatorname{coth} \left(\sqrt{\frac{\phi_p}{\left(\frac{d_p v}{v f_p} \right)}} w_f \right) \right] \right\} \quad (7-13)$$

7.2.1.1 Modified particle friction factor correlations

Numerous correlations are available in the literature. The limiting factors that were used during the investigation is the Reynolds number, modified Reynolds number (two variations) and porosity, valid under the measurement conditions. During the measurements the following ranges have been reached in these parameters, that can be seen in the [Tab. 7-3](#). Calculation of the Reynolds number and modified Reynolds numbers in case of porous media can be calculated by the equations shown in [Appendix BA](#) ([Ergun, 1952](#); [Erdim et al., 2015](#)).

Table 7-3: Boundary conditions during the measurements

		Minimum value	Maximum value
Reynolds number, -	Re	0.08	0.27
Modified Reynolds number, -	Re_m	0.13	0.37
Modified Reynolds number, -	Re_1	0.02	0.06
Porosity, -	Φ_p	0.32	0.39

For the comparison purposes only those modified friction factor correlations were used that satisfy (or nearly satisfy) the boundary conditions and equations without predefined applicable range have also taken into consideration. Thirteen different correlations were selected and the main equations with the applicable ranges are shown in the [Tab. 7-4](#) based on [Erdim et al. \(2015\)](#).

Table 7-4: Modified particle friction factor correlations considered in this study

Author(s)	Modified friction factor	Equation	Applicable range
Carman (Carman, 1937)	$f_p = \left(180 + 2.871 \left(\frac{Re}{1-\Phi_p}\right)^{0.9}\right) \frac{(1-\Phi_p)^2}{\Phi_p^3 Re}$	(7-14)	$0.01 < Re_1 < 10,000$
Rose (Rose, 1945a)	$f_p = \left(\frac{1,000}{Re} + \frac{60}{\sqrt{Re}} + 12\right) h(\Phi_p)$	(7-15)	$0.01 < Re < 10,000$ $0.32 < \Phi_p < 0.9$
Morcom (Morcom, 1946)	$f_p = \left(\frac{784.8}{Re} + 13.73\right) \left(\frac{0.405}{\Phi_p}\right)^3$	(7-16)	$Re < 750$
Rose and Rizk (Rose and Rizk, 1949)	$f_p = \left(\frac{1,000}{Re} + \frac{125}{\sqrt{Re}} + 14\right) h(\Phi_p)$	(7-17)	$0.01 < Re < 10,000$
Leva (Leva, 1949)	$f_p = 2f_m \frac{(1-\Phi_p)^{(3-n)}}{\Phi_p^3}$	(7-18)	$Re < 10,000$
Fahien and Schiver (Fahien and Schiver, 1961)	$f_p = \left(q \frac{f_{1L}}{Re_m} + (1-q) \left(f_2 + \frac{f_{1T}}{Re_m}\right)\right) \frac{(1-\Phi_p)}{\Phi_p^3}$	(7-19)	No data
Tallmadge (Tallmadge, 1970)	$f_p = \left(150 + 4.2 \left(\frac{Re}{1-\Phi_p}\right)^{5/6}\right) \frac{(1-\Phi_p)^2}{\Phi_p^3 Re}$	(7-20)	$0.1 < Re_m < 100,000$
Macdonald et al. (Macdonald et al., 1979)	$f_p = \left(180 + 1.8 \left(\frac{Re}{1-\Phi_p}\right)\right) \frac{(1-\Phi_p)^2}{\Phi_p^3 Re}$	(7-21)	$Re_m < 10,000$
Foscolo et al. (Foscolo et al., 1983)	$f_p = (17.3 + 0.336Re) \frac{(1-\Phi_p)}{\Phi_p^{4.8} Re}$	(7-22)	No data
Meyer and Smith (Meyer and Smith, 1985)	$f_p = \left(90 + 0.462 \left(\frac{Re}{1-\Phi_p}\right)\right) \frac{(1-\Phi_p)^2}{\Phi_p^{4.1} Re}$	(7-23)	$Re_1 < 1,000$
Watanabe; Kurten et al.; Steinour (Watanabe, 1989 ; Kurten et al., 1966 ; Steinour, 1944)	$f_p = 6.25 \left(\frac{21}{Re} + \frac{6}{\sqrt{Re}} + 0.28\right) \frac{(1-\Phi_p)^2}{\Phi_p^3}$	(7-24)	$0.1 < Re < 4,000$
Avontuur and Geldart (Avontuur and Geldart, 1996)	$f_p = \left(141 + 1.52 \left(\frac{Re}{1-\Phi_p}\right)\right) \frac{(1-\Phi_p)^2}{\Phi_p^3 Re}$	(7-25)	$Re_m < 10,000$
Erdim et al. (Erdim et al., 2015)	$f_p = (160 + 2.81Re_m^{0.904}) \frac{(1-\Phi_p)^2}{\Phi_p^3 Re}$	(7-26)	$2 < Re_m < 3,600$

[Carman \(1937\)](#) published a paper where an empirical correlation was fitted on data provided by earlier studies and expressed that [Eq. 7-14](#) described the collected data best. The collected experimental data was based on measurements on glass spheres ([Schriever, 1930](#); [Green and Ampt, 1912](#); [Muskat and Botset, 1931](#)), steel spheres ([Coulson, 1935](#)), lead shot ([Burke and Plummer, 1928](#); [Chalmers et al., 1932](#); [Uchida and Fujita, 1934](#), [Furnas, 1929](#); [Ray and Kreisinger, 1911](#)), and wire spirals, Lessing ring, and porcelain saddles ([Arnould, 1929](#); [Uchida and Fujita, 1934](#); [Mach, 1934](#)).

[Rose \(1945a\)](#) conducted extensive data analyses based on measurements of both his own and other researchers. Data provided by [Burke and Plummer \(1928\)](#), [Bakhmeteff and Feodoroff \(1937\)](#), [Mavis and Wilsey \(1937\)](#), and [Saunders and Ford \(1940\)](#) were used besides his own measurements to illustrate the curve of Resistance Coefficient against the Reynolds Number. He found a correlation that is best suited for the collected data and

considers only the relationship between the Reynolds number and resistance coefficient. In a different study, the $h(\Phi_p)$ porosity correction function was presented in a graphical form (Rose, 1945b), and later the function was extended for higher porosities by Rose and Rizk (1949). To be able to use the graphical representation efficiently in the case of extended calculations, Erdim et al. (2015) developed a curve-fitting polynomial on the porosity correction function which can be seen in Eq. 7-27.

$$h(\Phi_p) = 54.3218\Phi_p^4 - 156.3496\Phi_p^3 + 169.7978\Phi_p^2 - 83.0717\Phi_p + 15.6676 \quad (5-27)$$

Morcom (1946) suggested the two-term equation presented in Eq. 7-16 in which the effect of porosity is accounted for a correction factor of the form $(\Phi_n/\Phi_p)^3$, where Φ_p is the actual porosity of the bed in -, while Φ_n is the porosity under “normal packing conditions” in - (Morcom, 1946). In the case of spherical particles, Morcom (1946) defined the value of Φ_n as equal to 0.405. The “normal packing” was obtained by dropping the particles in the bed, and the packing formed a few meter high column (Morcom, 1946).

Rose and Rizk (1949) proposed a modified version of Eq. 7-15 in the form of Eq. 7-17 and with the application of the porosity correction function. In their paper, they used the same data as in the paper published by Rose (1945a) complemented by their own measurements.

Leva (1949) presented a friction factor correlation in graphical form. The original correlation of the friction factor can be seen in Eq. 7-28 and the relationship between the proposed friction factor and the modified particle friction factor is given in Eq. 7-18.

$$f_m = \frac{-\Delta P d_p}{2\rho V^2 L} \frac{\Phi_p^3}{(1-\Phi_p)^{(3-n)}} \quad (7-28)$$

Since the correlation was provided in graphical form, Erdim et al. (2015) proposed a curve-fitting expression to facilitate its use in the form of Eq. 7-29 and Eq. 7-30.

$$n = \sum_{k=0}^6 B_k Re^k \quad (7-29)$$

$$\log f_m = \sum_{k=0}^5 C_k Re^k \quad (7-30)$$

Where B_k ($k = 0, \dots, 6$) = 7.60657, -19.2986, 21.02695, -10.96663, 3.02928, -0.42867, and 0.02453 and C_k ($k = 0, \dots, 5$) = 1.982535, -1.0218594, 0.0295464, 0.0269893, 0.0024996, and -0.0008754, respectively. Eq. 7-29 is applicable if $Re \geq 11.5$; otherwise $n = 1$.

[Fahien and Schriver \(1961\)](#) tested the Ergun equation ([Ergun, 1952](#)) in the case of data for beds with varying porosities and concluded that the constants in the equation (150 and 1.75) depend on the porosity and developed an alternative correlation by assuming the flow can be turbulent or laminar in different regions of the bed, which can be seen in [Eq. 7-19](#). The expressions of the functions represented in [Eq. 7-19](#) are described from [Eq. 7-31](#) to [Eq. 7-34](#).

$$q = \exp\left(-\frac{\Phi_p^2(1-\Phi_p)}{12.6} Re_m\right) \quad (7-31)$$

$$f_{1L} = \frac{136}{(1-\Phi_p)^{0.38}} \quad (7-32)$$

$$f_{1T} = \frac{29}{(1-\Phi_p)^{1.45} \Phi_p^2} \quad (7-33)$$

$$f_2 = \frac{1.87\Phi_p^{0.75}}{(1-\Phi_p)^{0.26}} \quad (7-34)$$

[Tallmadge \(1970\)](#) claimed that the Ergun equation ([Ergun, 1952](#)) is applicable up to $Re_m = 1,000$ and, by analyzing the data provided by [Wentz and Thodos \(1963\)](#), developed a new empirical correlation which is applicable up to $Re_m = 105$ and can be seen in [Eq. 7-20](#).

[Macdonald et al. \(1979\)](#) proposed a modification on the Ergun equation, and the alternative empirical correlation is applicable in smooth particles. They concluded that the Ergun equation is applicable for engineering purposes, but the term Φ_p^3 should be changed to $\Phi_p^{3.6}$ in order to get a better fit to the data points.

[Foscolo et al. \(1983\)](#) proposed a pressure drop - flow rate correlation that can be applied for both fixed and fluidized beds. It can be inferred that the voidage dependency in [Eq. 7-22](#) differs from that of the Ergun equation.

[Meyer and Smith \(1985\)](#) introduced a correlation that can be used in both consolidated and unconsolidated media. [Eq. 7-23](#) was performed by studying sintered stainless-steel compacts, and originally it contained a roughness term to account for flow through rough media, but this term was eliminated as the current work accounts for relatively smooth materials.

[Watanabe \(1989\)](#) introduced “the drag model” to predict the pressure drop in a porous medium where the total pressure drop can be calculated by the number of spheres in the bed multiplied by the drag force on each sphere multiplied by a porosity function. [Eq. 7-24](#)

is generated by combining a drag coefficient formula for spheres developed by [Kurten et al. \(1966\)](#) with a porosity function developed for fluidized beds by [Steinour \(1944\)](#). It should be noted that [Eq. 7-24](#) was not presented by [Watanabe \(1989\)](#) or [Kurten et al. \(1966\)](#) but by [Erdim et al. \(2015\)](#) by combining Watanabe's "drag model" with one of the drag coefficients expressed by [Kurten et al. \(1966\)](#).

[Avontuur and Geldart \(1996\)](#) proposed [Eq. 7-25](#), the Ergun equation's modification where the two coefficients from 150 and 1.75 were modified to 141 and 1.52.

[Erdim et al. \(2015\)](#) performed an extensive overview and comparison of the different friction factors and based on their own 813 measurements on nine spherical particles (glass balls), [Eq. 7-26](#) was developed, which provides the best fit on their measurements.

The driving parameters for determining the modified particle friction factors from [Eq. 7-14](#) to [Eq. 7-26](#) are the proppant-pack porosity and the Reynolds number (or a modified Reynolds number) valid in the case of porous media. With the utilization of the developed [Eq. 7-13](#) and the correlations presented in [Tab. 7-4](#) the behavior of each model can be analyzed without any measurements. The behavior of each model is illustrated in [Fig. 7-6](#) and [Fig. 7-7](#), where the Φ_p is assumed to be 0.3, ν is assumed to be $9 \times 10^{-7} \text{ m}^2/\text{s}$, V is assumed to be $2 \times 10^{-4} \text{ m/s}$, and d_p is assumed to be $8 \times 10^{-4} \text{ m}$.

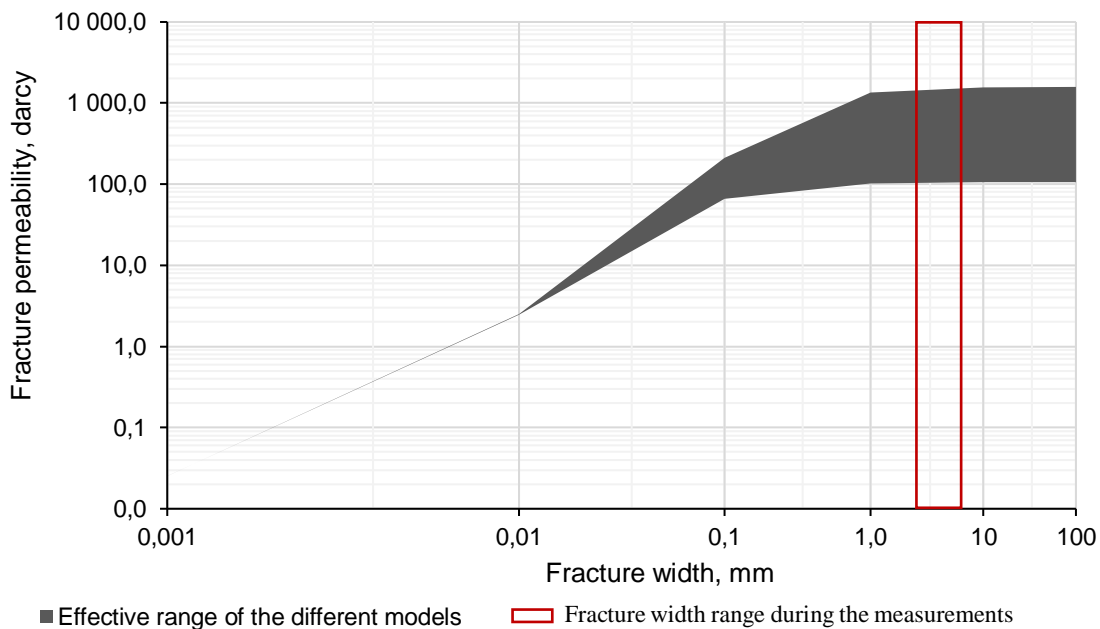


Figure 7-6: Effective range of the different modified particle friction factor models using [Eq. 7-13](#)

It is evident from [Fig. 7-6](#) that the results are highly dependent on the selected modified particle friction model. For better visualization, the effective range can be magnified, and the behavior of each identical model can be interpreted. As one model, namely Leva ([Eq. 7-18](#)), provided significantly higher fracture permeability values, it is eliminated in the later investigation. It can happen as the Reynolds number range during the measurements is lower than 11.5, which causes the value n in [Eq. 7-18](#) to be equal to 1, and it reduces the f_p value and consequently increases the fracture permeability value of [Eq. 7-13](#) - comparing if [Eq. 7-29](#) was used instead of the value 1. [Fig. 7-7](#) shows the behavior of the individual models in the applied fracture width range during the later presented measurements. For better understanding, the axis types are changed from logarithmic to normal intervals in [Fig. 7-7](#).

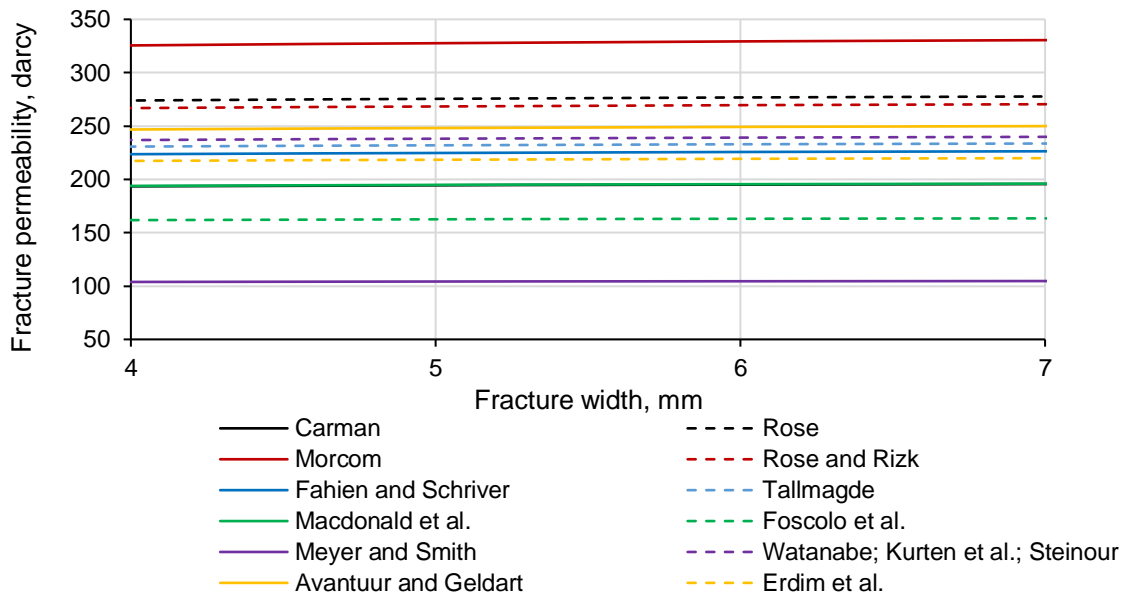


Figure 7-7: Behavior of different modified particle friction factor models in [Eq. 7-13](#)

It can be readily inferred from [Fig. 7-6](#) and [Fig. 7-7](#) that the lines represent the three assumed zones (viscous shear dominated, transient, and viscous drag dominated). The fracture width range that is reached during the measurements is between 4.4 and 6.1 mm, which represents mainly the zone that is dominated by the viscous drag on the proppant particles. Although the viscous drag is dominant in this region, a slight increase in fracture permeability can be seen with increasing fracture width, and also, as the models show different behaviors, measurements were necessary to analyze which model can substitute the time-consuming standard proppant permeability measurement.

7.2.2 Comparisons of the models

Using [Eq. 7-13](#) and the modified particle friction factor correlations presented in [Tab. 7-4](#), the measured fracture permeability values can be compared with the correlation results. As f_p correlations contain the proppant-pack porosity (Φ_p) as a parameter, its values had to be determined. To calculate the porosity of the proppant-pack under different applied closing pressures, two parameters needed to be measured, which are the specific gravity of the proppant particle and the bulk density of the proppant-packs at each applied closing pressure.

7.2.2.1 Specific gravity measurement

Specific gravities of the pure and mixed proppant-packs were determined by the Pentapyc 5200e device, which was detailed earlier (in chapter [7.1](#)). The specific gravity measurements on the proppant-packs were performed at least three times, and the average gross variance between the measurements was 0.013%, calculated by the equation presented by [Richard et al. \(2019\)](#). The result of the specific gravity measurements can be seen in the [Fig. 7-8](#), where the mean values of the measurements are presented with the gross variance of the measurements on each proppant-pack sample.

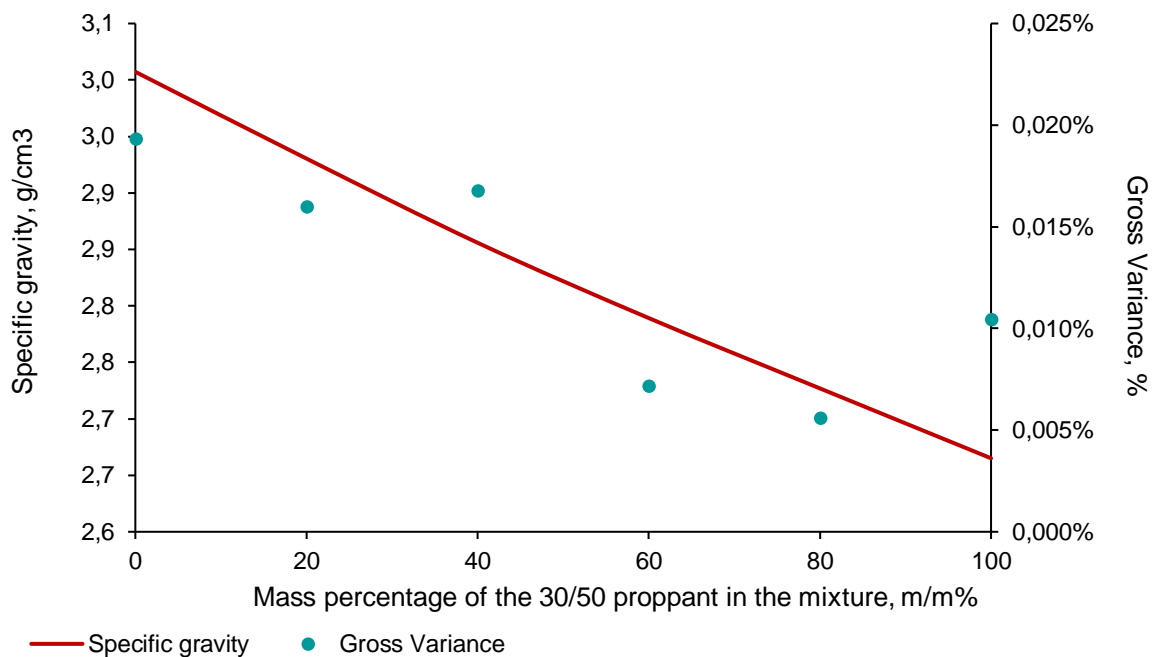


Figure 7-8: Specific gravity of the proppant-packs with the gross variance of the measurements

It can be seen that higher percentage of 30/50 mesh proppant in the mixture resulted lower specific gravity results as the 30/50 mesh proppant is a light-weight ceramic proppant.

7.2.2.2 New bulk density measurement

A new method had to be developed to determine the bulk density of the proppant-pack under different applied closing pressures as no method can be found in the literature for this purpose.

The crush test described in the [API RP 19C \(2008\)](#) was the basis of the bulk density measurement at different closing pressures. A schematic drawing of the measurement equipment is illustrated in [Fig. 7-9](#).

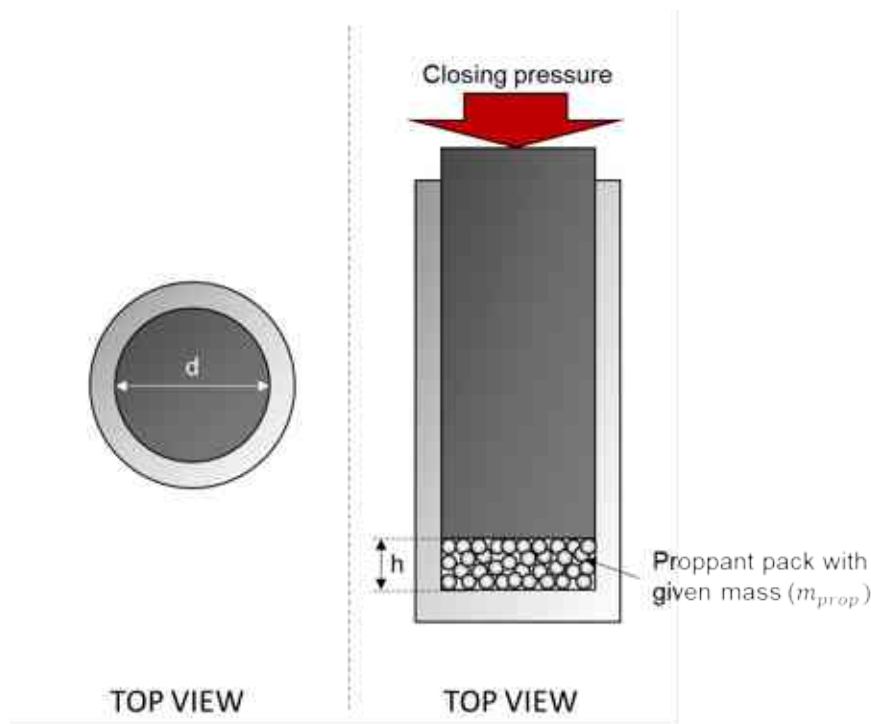


Figure 7-9: Schematic illustration of the crush test apparatus used during the bulk density measurements (not to scale)

Applying an exact mass of proppant in the cell and utilizing a width measurement device during the process described in the [API RP 19C \(2008\)](#), the bulk densities can be easily calculated as the geometry of the cell and piston is well known with [Eq. 7-35](#).

$$\rho_{bulk} = \frac{4m_{propp}}{d^2\pi h} \quad (7-35)$$

Where ρ_{bulk} is the bulk density of the proppant-pack in g/cm^3 , m_{propp} is the mass of the proppant-pack in the cell in gram, d is the diameter of the cell's inner side in cm, h is the height of the proppant-pack in cm. During the measurements, the closing pressures were applied on the sample for two minutes (as described in the API RP 19C), and the proppant-

pack widths were registered (photos taken on the crush test apparatus can be seen in [Appendix BB](#) and on the setup in [Appendix BC](#)). Each measurement has been performed three times to be able to analyze the gross variance of the measurements. The average gross variance that was obtained by the measurements is 4.41%. The result of the bulk density measurements is illustrated in the [Fig. 7-10](#), while the results obtained on each proppant-pack measurement can be seen in [Appendix BD](#).

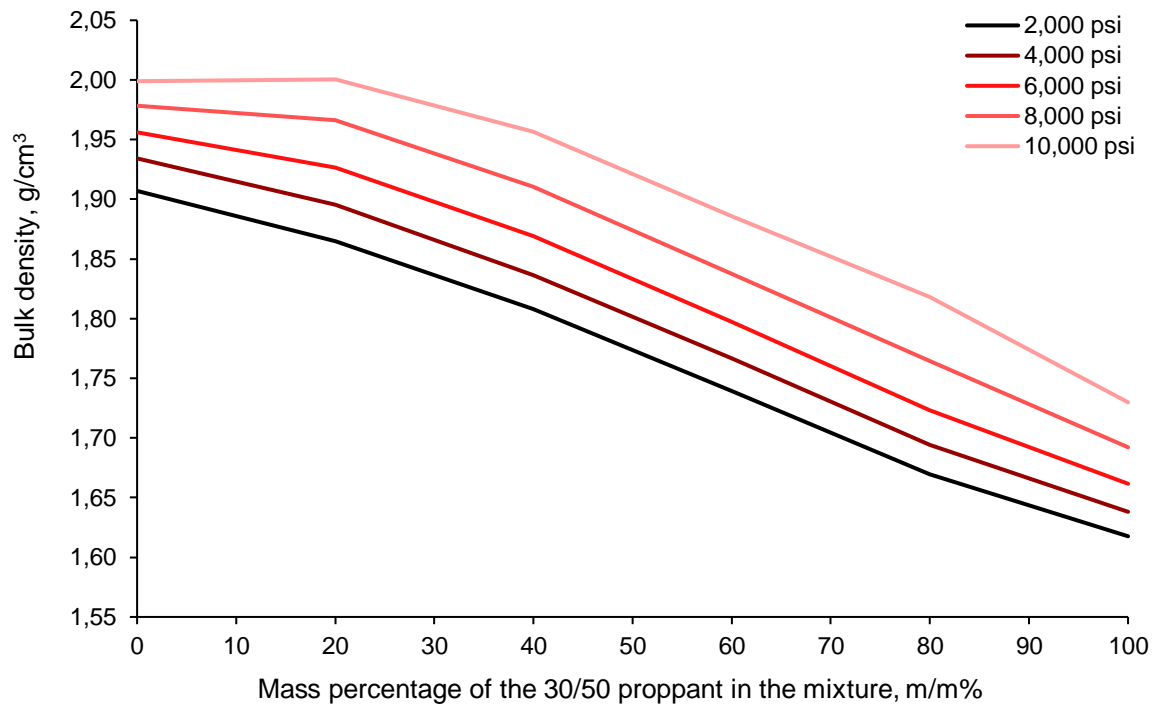


Figure 7-10: Bulk density measurement results at different proppant mixtures and at different closing pressures

The results show that with higher closing pressure the bulk densities are increasing in each case as the proppant-packs become more compact. It is expected that with higher ratio of smaller diameter proppant (30/50 mesh) in the mixture the bulk density should increase as more void is filled by the smaller diameter proppants. As the results show with higher ratio of 30/50 mesh size proppant in the mixture the bulk densities are decreasing, which can be interpreted by the fact that the 30/50 mesh size proppant is a light-weight ceramic proppant and its specific gravity is lower than of the 16/32 mesh size proppant. This effect from the lower specific gravity compensates the effect of the smaller size and the final bulk density results decreasing accordingly.

7.2.2.3 Proppant-pack porosity

As the specific gravities and bulk densities of the proppant-pack mixtures were determined, the porosity of the proppant-pack under different closing pressures can be calculated by [Eq. 7-36](#).

$$\Phi_p = 1 - \frac{\rho_{bulk}}{\rho_{particle}} \quad (7-36)$$

Where ρ_{bulk} is the measured bulk density of the proppant-pack at a given closing pressure in g/cm^3 , and $\rho_{particle}$ is the particle density calculated from the specific gravity measurements in g/cm^3 . The results can be seen in [Fig. 7-11](#).

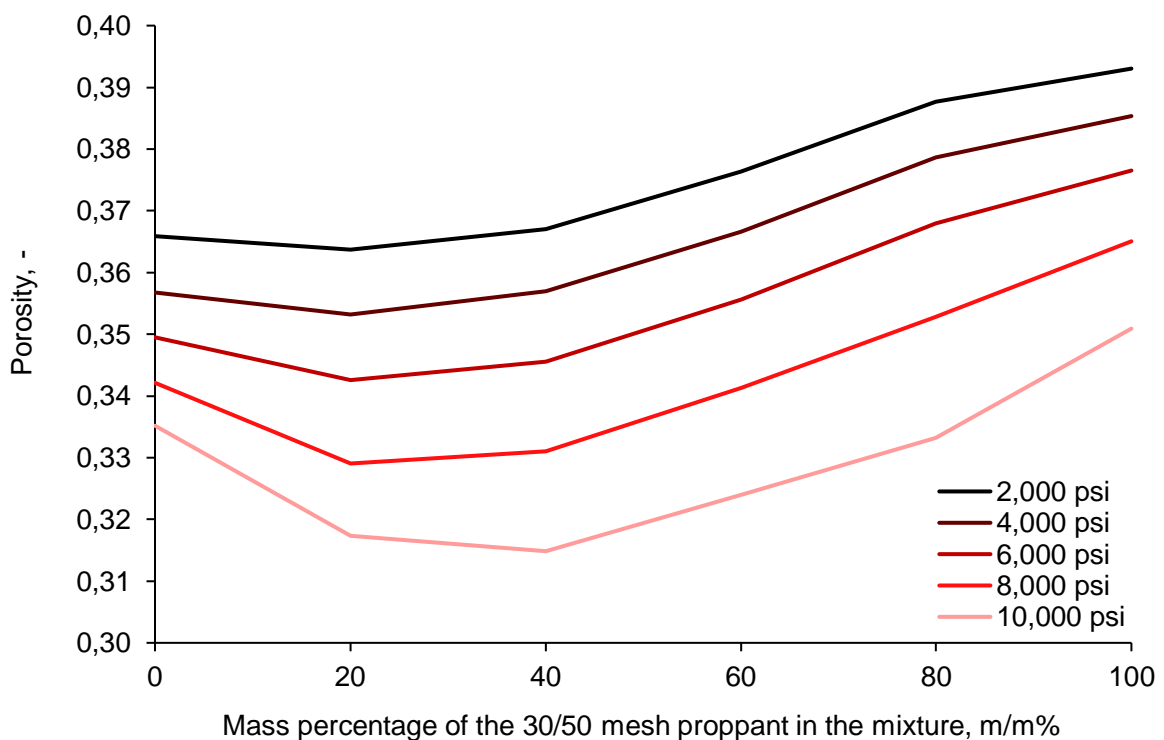


Figure 7-11: Porosity values at different applied closing pressure in case of different mixtures

As the specific gravity of the proppant-pack decreases near linearly with increasing mass percentage of 30/50 mesh proppant in the mixture and the bulk density is following a nearly parabolic decrease with an increasing amount of 30/50 mesh proppant in the mixture, the final porosity results show a decreasing trend until 20-30% of 30/50 mesh proppant is in the mixture and an increasing trend at higher concentrations.

7.2.2.4 Result of the comparison

Since the porosity values of the proppant-pack under different closing pressures were determined, the comparison of the different models could be performed with the application of the developed [Eq. 7-13](#). The summary of the results is illustrated in [Fig. 7-12](#). The average deviation from the measured values is represented with the maximum and minimum deviations. One can observe that the deviations are significantly higher than practicable (practicable range can be considered within 20% variance as [Richard et al. \(2019\)](#) showed). This result will be analyzed further in the following part, where a new model (present work in [Fig. 7-12](#)) is introduced.

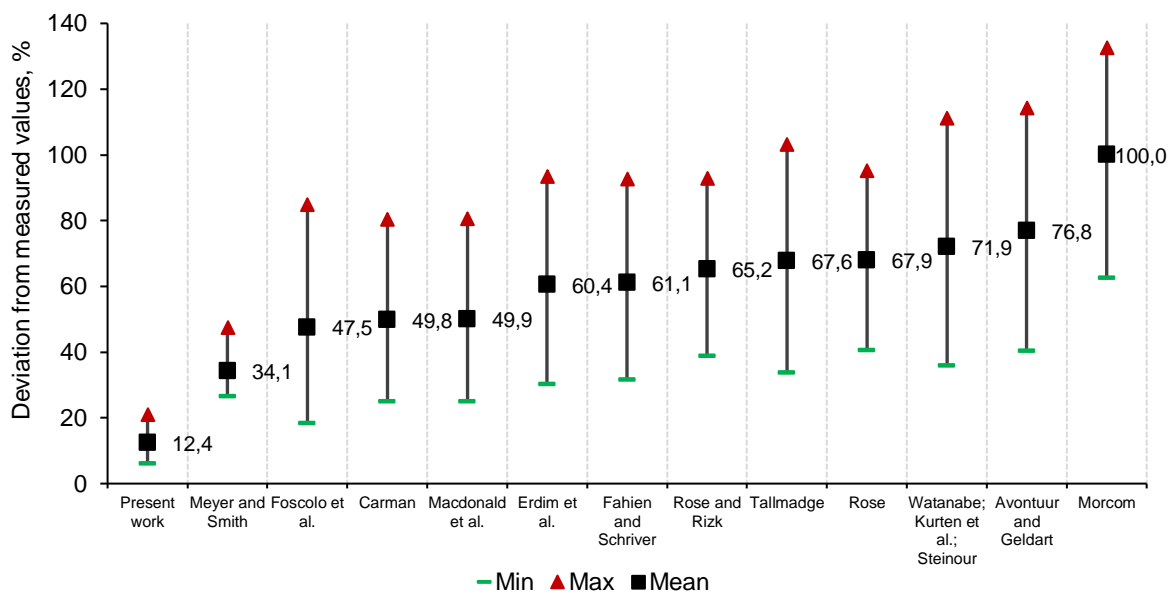


Figure 7-12: Comparison of the calculated and measured fracture permeability values in case of the different models

Combining the investigated models represented in [Tab. 7-4](#) with the developed [Eq. 7-13](#) could not provide satisfactory results that can be considered to be practical. Some apparent facts can explain this result:

- In the case of the models represented in [Tab. 7-4](#) the particles were unconsolidated, where the particles usually can move nearly freely, while during the proppant measurements, the proppant particles were nearly in fixed position.
- In the case of the models represented in [Tab. 7-4](#) there was no applied pressure on the particles, while during the measurements, the particles were under significant pressure, which can cause deformation, crushing, and embedment on the closure

body's surface. These effects can significantly deteriorate the final permeability results ([Liang et al., 2016](#)).

A correction is needed on the available models to overcome these effects and provide a useful correlation.

7.3 Modified Particle Friction Factor Correlation

To obtain a better correlation the [Meyer and Smith \(1985\)](#) correlation was used as a base because it provided the best results (see in [Fig. 7-12](#)). The Generalized Reduced Gradient Method has been used for the optimization which was created by [Lasdon et al. \(1978\)](#) and it is considered to be one of the most prominent approaches for solving nonlinear optimization problems ([Chapra and Canale, 2009](#)). This method requires only that the objective function is differentiable and the main goal is to solve a nonlinear problem dealing with active inequalities ([Maia et al., 2017](#)). The variables are divided into two categories: basic (dependent) and nonbasic (independent). The reduced gradient is then computed in order to determine the minimum. This procedure is repeated until convergence has been achieved ([Venkataraman, 2009](#)). After a GRG optimization on the correlation coefficients the result has still a high gross variance comparing to the measured values. The correlation coefficients on which the optimization was performed can be seen in [Eq. 7-37](#) as the a, b, and c values.

$$f_p = \left(a + b \left(\frac{Re}{1-\Phi_p} \right) \right) \frac{(1-\Phi_p)^2}{\Phi_p^c Re} \quad (7-37)$$

After the optimization, the values of the correlation coefficients are a = 2; b = 0.311; and c = 7.60. With these coefficients the average gross variance of the model is 29.3%, which is although better than values represented in the [Fig. 7-12](#) but still worse than the objective of the approach. The objective is to find a correlation which can predict the measurement values with an average gross variance at maximum 20% as this value is considered to be the average accuracy of the API RP 19D standard measurement method. From the results, it can be inferred that the effect of closing pressure and mixing on the proppant-pack cannot be described efficiently by the Meyer and Smith model. This phenomenon can be seen in [Fig. 7-13](#).

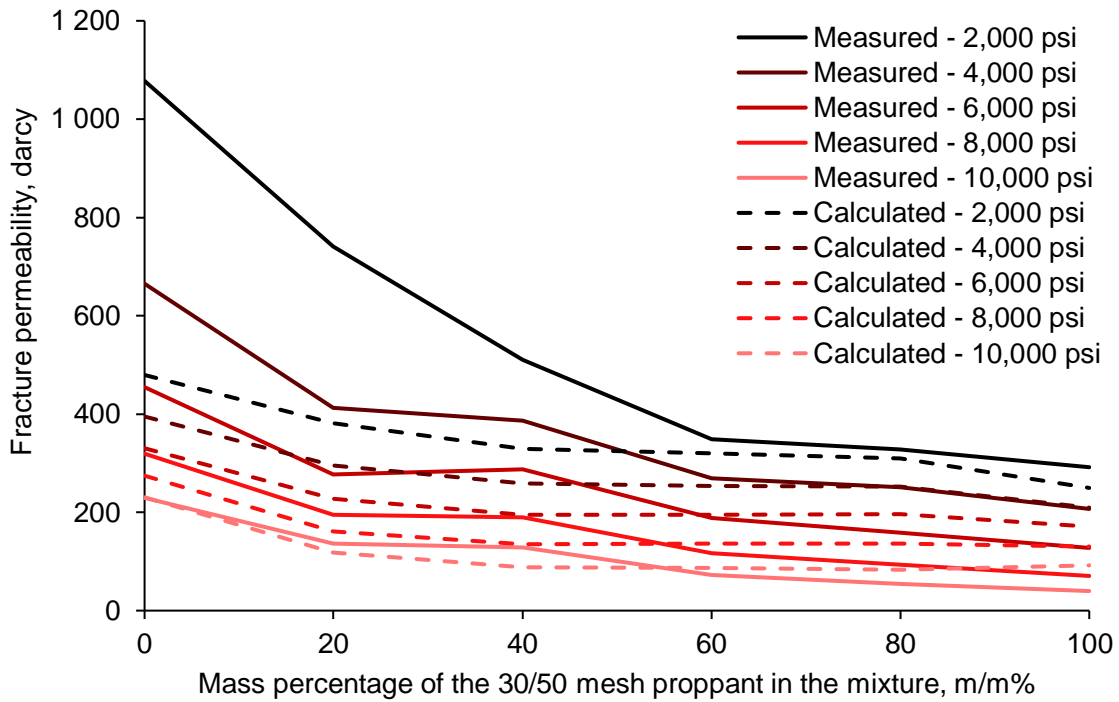


Figure 7-13: Comparison of the results obtained by the modified correlation to the measured fracture permeability values

In the analyses, it is assumed that the closing pressure has an exponential effect on the proppant-pack because the particles under higher closure stresses can suffer more prominent deformation, breakage, and embedment. Modifying the model with the exponential closing pressure term [Eq. 7-38](#) was obtained, on which the previously described GRG optimization was repeated.

$$f_p = e^{\alpha \frac{P_c}{1,000}} \left[\left(a + b \left(\frac{Re}{1-\Phi_p} \right) \right) \frac{(1-\Phi_p)^2}{\Phi_p^c Re} \right] \quad (7-38)$$

Where P_c is the closing pressure in psi, α ; a ; b ; and c are the correlation coefficients in -. During the optimization it was a key priority to modify the coefficients in the Meyer and Smith model as less as possible and utilize simplification in the model if possible. After the optimization, [Eq. 7-39](#) was reached.

$$f_p = e^{0.203 \frac{P_c}{1,000}} \left[\left(542 + 0.462 \left(\frac{Re}{1-\Phi_p} \right) \right) \frac{(1-\Phi_p)^2}{\Phi_p Re} \right] \quad (7-39)$$

Applying [Eq. 7-39](#) on the measurements, the average gross variance of 12.4% can be reached with the highest value of 21.0%. The results are also illustrated in [Fig. 7-14](#).

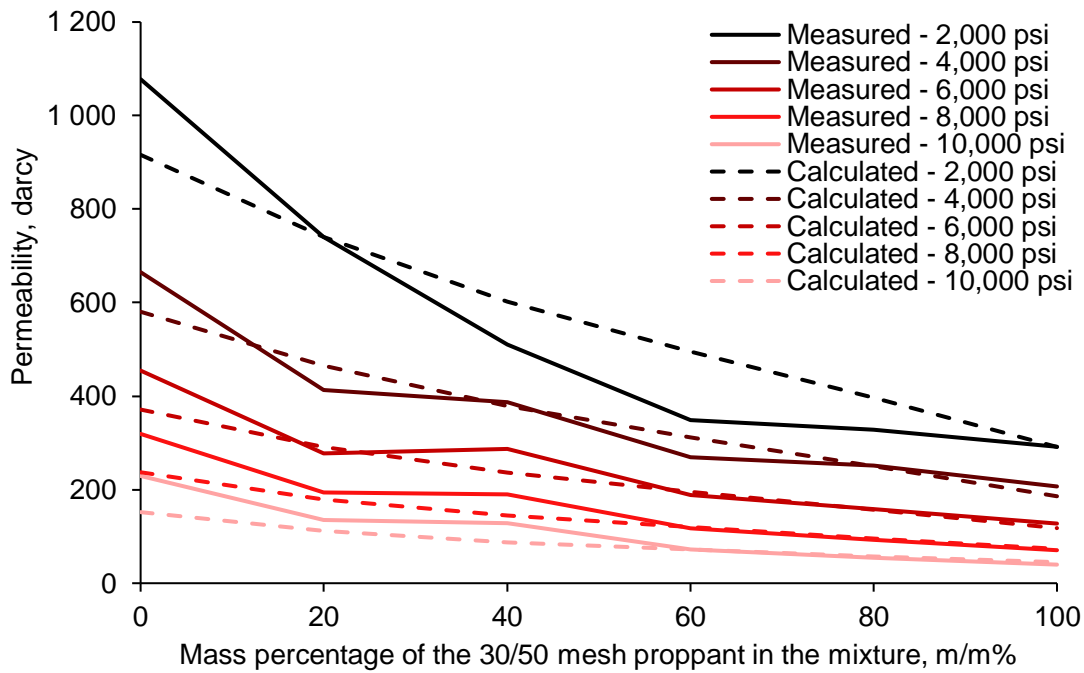


Figure 7-14: Comparison of the present work to the measured fracture permeability values

7.4 Conclusion on the proppant measurement and analysis

As oil and gas reserves are constantly decreasing, the role of intensification methods is getting more prominent. One of the widely used intensification methods is hydraulic fracturing, where during the process, a propping agent is injected into the fracture. Understanding the behavior of the granular propping agent under reservoir conditions is a key objective of several studies. In this study, the utilization of the correlations on unconsolidated, granular materials and their applicability on proppant-packs under reservoir conditions were the main objectives.

A theoretical model was developed which considers the viscous shear from the fracture wall and viscous drag from the surface of proppants and with which the behavior of the different modified particle friction factor correlations can be analyzed. One major result is the developed measurement process with which the proppant-pack porosity can be determined under different closing pressures utilizing the API RP 19C crush test apparatus.

After the analyses, it was obvious that the assessed models could not be used efficiently to determine the proppant behaviors under reservoir conditions, and a closing pressure dependent term was introduced. It can happen as although pressure dependent porosities were used (measured by the proposed new measurement method), but the applied closing pressure has a higher effect on the permeability and the used correlations which assume a

relationship between the porosity plus Reynold's number and the modified particle friction factor cannot describe this effect efficiently. Although the final correlation ([Eq. 7-39](#)) does not perfectly fit the measured values, its applicability can be practical as the API RP 19D standard measurement method can also be reproduced with nearly identical variances. The proposed method can predict the measurement results in an average gross variance of 12.4%. Utilizing the developed semi-analytical model, [Eq. 7-13](#) and the new correlation, [Eq. 7-39](#), the calculated fracture permeability values can be tested to the measured values (both to our measurements and to the technical datasheet). The result of the comparison is illustrated in [Fig. 7-15](#). The calculated results had an average gross variance of 5.5% compared to our measurements and 12.5% to the technical datasheet. These results reinforced the validity of this new approach.

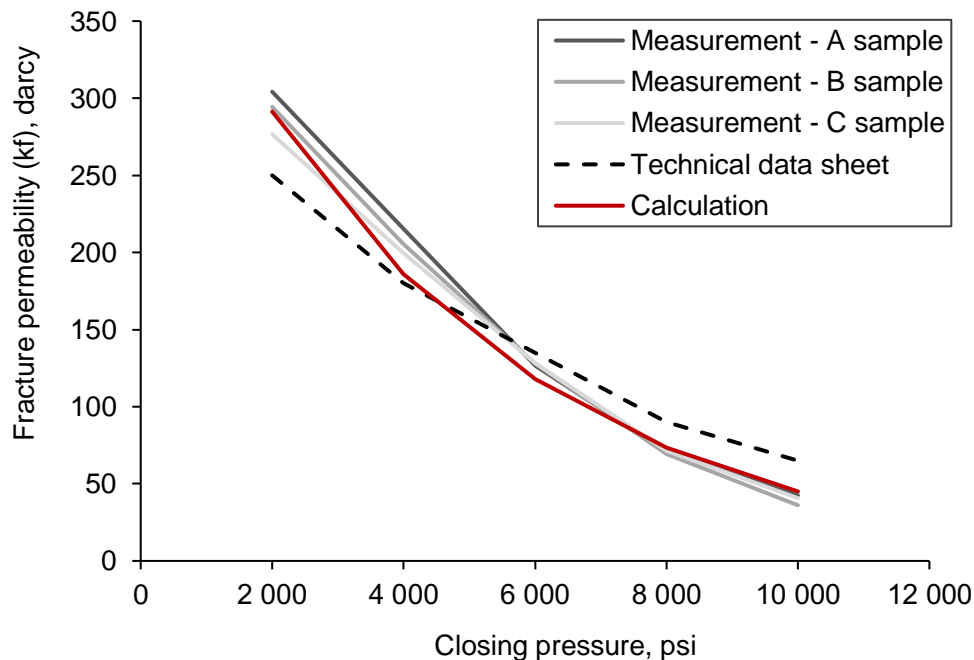


Figure 7-15: Comparison of the measured and calculated fracture permeability values with the 30/50 mesh size proppant

One significant benefit of the proposed measurement procedure and correlation is the less time required to obtain the permeability values than in case of the standard measurement method. The API RP 19D measurement requires nearly two weeks to perform, while performing the proposed bulk density and specific gravity measurements on the samples only require around 1-2 hours. This approach's benefit makes it practical and applicable for later research. It should be mentioned that the closing pressure dependent term in [Eq. 7-39](#) should be tested for different types of proppants in the future to ascertain the value of the coefficient in a broader range.

8 RESULTS

Twenty simulations were carried out with different permeability values of the porous domains. Each simulation was interrupted after 90 days and the curves were fitted to evaluate how it will reach 100 °C outlet temperature in time (this method is represented in chapter [6.3.5](#)). The permeability values were changed from 128 darcy to 455 darcy with equal increments. This minimum and maximum values were chosen as the reservoir pressure is assumed to be 6,000 psi and the corresponding proppant measurements resulted in those values (it can be seen in [Fig. 7-4](#)). The results confirm that the flow can be controlled by changing the permeability values of the different zones in the propped fracture. The results are illustrated in [Fig. 8-1](#) where the abscissa is represented on a logarithmic scale to visualize the difference between the scenarios more efficiently. Each model has an identification number and the permeability values of the zones from the well to the outer parts. Each results are illustrated in [Appendix BE–BI](#) individually with the residual values.

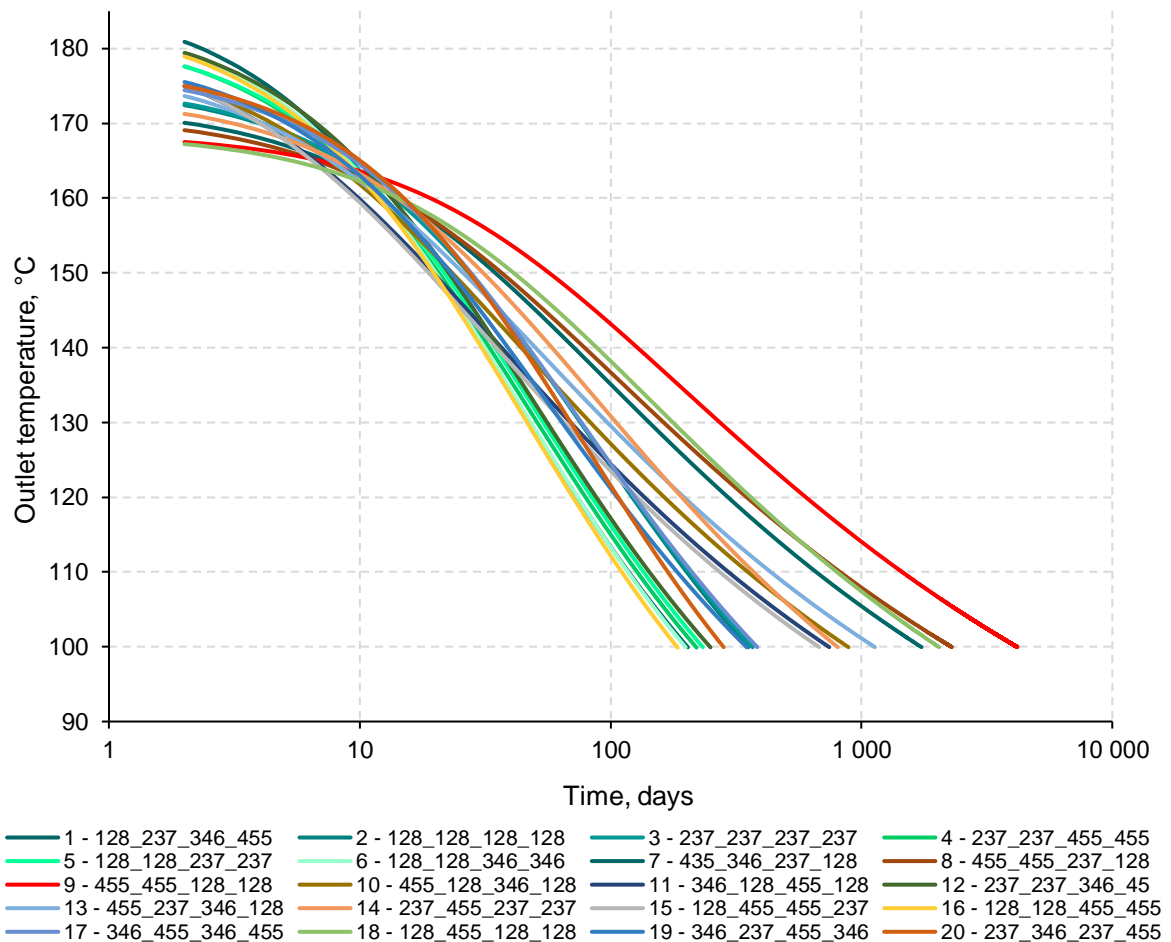


Figure 8-1: Results of the simulations

It can be readily inferred that there are significant differences between the models. The scenario where the zones near the wellbore have higher permeability values, while the outer zones have lower permeability values provided the best results. With this arrangement nearly 20 times better heat recovery can be reached than in case the most unfavorable arrangements. The total power production of each model can be seen in [Fig. 8-2](#), where besides the new EGS model the already detailed model proposed by [Danko et al. \(2018\)](#) has been also added. It can be realized that with the new EGS method significantly better energy production can be realized as with other models. It can happen as the propped fracture does not limit the available rock surface and the flow is controlled in the way to maximize production efficiency.

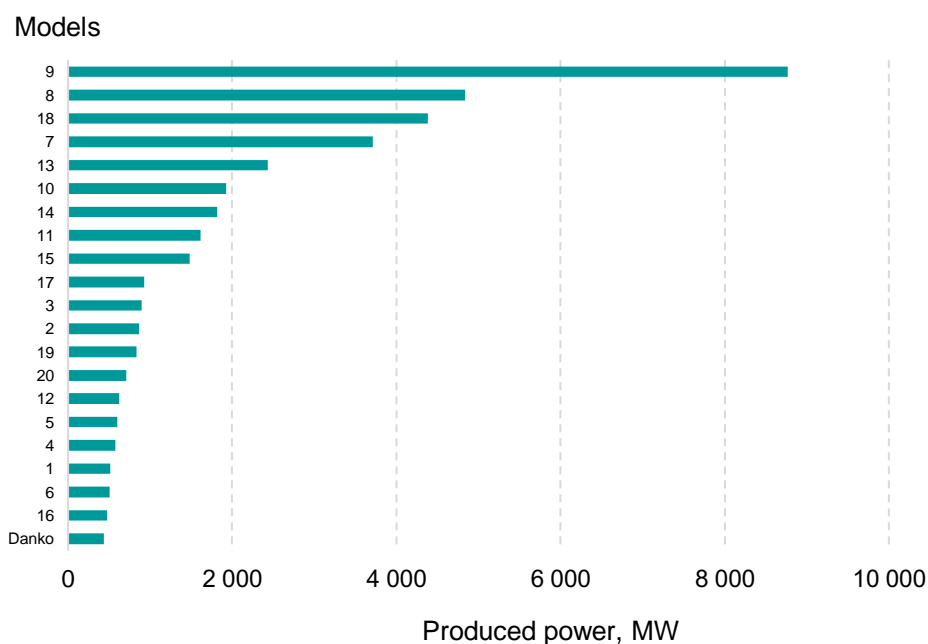


Figure 8-2: Total power production with each model

The power production capacity of the models is significantly different that means selecting the best arrangement can have a significant effect on the project's economics.

One can realize that the starting outlet temperatures are different in each scenario (in [Fig. 8-1](#)), which can occur as the initial fracture temperature was set to be equal with the inlet temperature (60°C). During the initial time of the simulation the temperature of the fluid inside the fracture will be heated up, while the flow is constant. This approach was tested to ensure it does not have a significant effect on the final result. In [Fig. 8-3](#) two scenarios were analyzed with the same arrangement. In the first approach the simulation was done by assuming that the initial fluid temperature in the fracture is 60 °C then it was changed to 180 °C and the simulation was repeated.

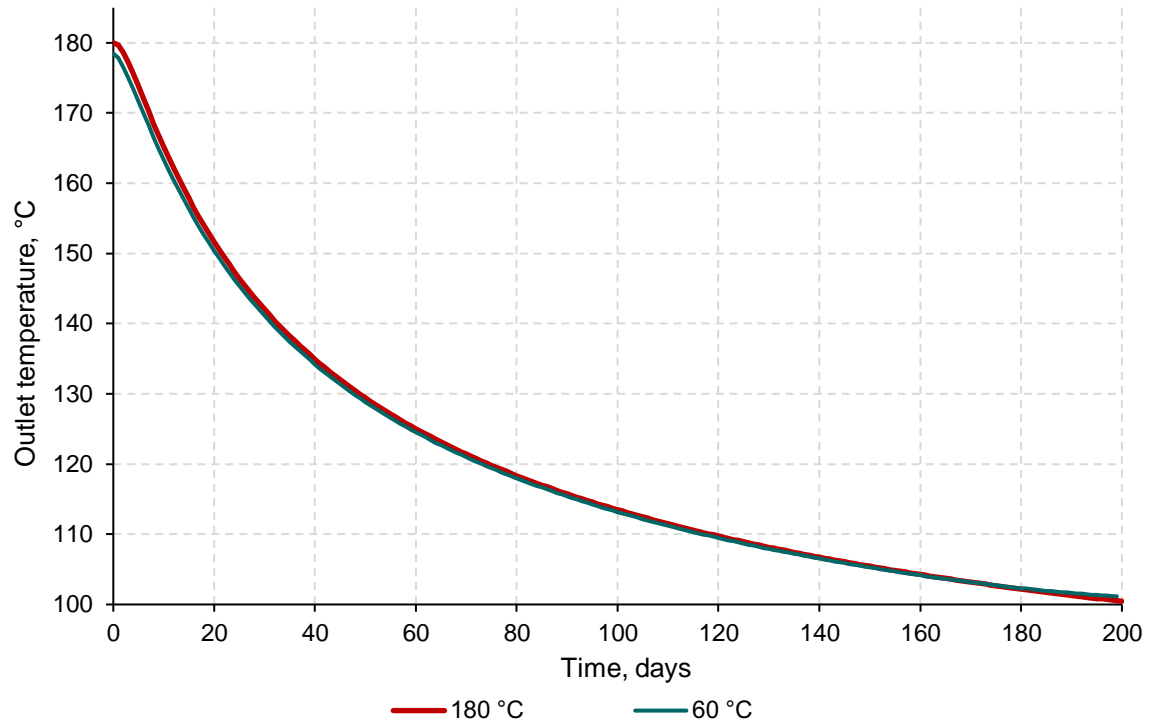


Figure 8-3: Comparing the effect of initial temperature in the fracture

It can be readily inferred that there is no significant difference between the two approaches as the temperatures rapidly equalize and the heat recovery from the reservoir during a 200 days simulation has only 0.8% difference.

With this analyzes it was confirmed that the flow can be controlled by the arrangement of different permeability zones in a propped fracture well. The next step is to find a solution to optimize this arrangement in order to maximize the heat recovery from this type of EGS well.

8.1 Optimization procedure

The optimization procedure in order to maximize heat recovery was done by a response surface analysis (RSA) using multivariate polynomial regression (MPR). This is a regression method that enables describing complex²¹ data. With this approach the basic polynomial equations are extended to multivariable data. These analyses can be used to interpret non-time-series data set. Eighteen datasets were selected for the analyses and two datasets were used to validate the model. The dataset came from the simulation results and

²¹ In this context complex means that there is nonlinear relationship between the data, including interactions among multiple variables.

presented in [Tab. 8-1](#). Here the independent variables are the permeability values of the different zones (k_x), while the dependent variable is the sum of outlet temperature at each timestep. The yellow highlighted datasets are the ones used for validation.

Table 8-1: Dataset for the RSA

Dataset Number	k_1 darcy	k_2 darcy	k_3 darcy	k_4 darcy	Y – Simulation °C
2	128	128	128	128	42,026
3	237	237	237	237	43,539
4	237	237	455	455	26,428
5	128	128	237	237	27,978
6	128	128	346	346	24,043
7	455	346	237	128	192,840
8	455	455	237	128	253,269
9	455	455	128	128	460,689
10	455	128	346	128	99,346
11	346	128	455	128	83,331
12	237	237	346	455	29,923
13	455	237	346	128	125,991
14	237	455	237	237	91,730
15	128	455	455	237	76,089
16	128	128	455	455	22,451
17	346	455	346	455	45,309
18	128	455	128	128	227,180
19	346	237	455	346	40,920
1	128	237	346	455	24,468
20	237	346	237	455	33,996

After the analysis a robust polynomial equation was reached with which the regression model on the 18 dataset was nearly perfect with 0.999 R^2 value. The MPR model is represented in [Eq. 8-1](#).

$$\begin{aligned} \sum T_{out_{pred}}(k_1, k_2, k_3, k_4) = & 7,365 - \frac{3.09746 \times 10^{-9} k_1^3 k_2^3}{\sqrt{k_3} \sqrt{k_4}} + \frac{0.10732 k_1 k_2^3}{k_3 k_4} + \frac{3.5369 k_1 \sqrt{k_2}}{\sqrt{k_3} k_4} + \\ & \frac{19,574 \sqrt{k_1} k_2^3}{k_3 k_4^3} + \frac{1,589 k_3^3}{k_1 k_4^2} + \frac{4.5434 \times 10^{-10} k_2^3 k_3 k_4^3}{k_1^2} \end{aligned} \quad (8-1)$$

If we are implementing this equation to the independent variables the following results can be obtained and the residual values of the fitted data are illustrated in [Appendix BJ-BK](#) with the residual values of the validated value. One can see that the residual values of the validated data do not differ significantly from the residual values of the fitted data, which means that the model predicts data reliably.

Table 8-2: Result of the RSA model

Y - Simulation	Y - Predicted	Residuals, darcy	Residuals, %
42,026	47 720,6	- 5 694,7	11,9%
43,539	49 646,2	- 6 106,9	12,3%
26,428	28 849,6	- 2 421,1	8,4%
27,978	25 131,5	2 846,4	-11,3%
24,043	20 685,8	3 356,8	-16,2%
192,840	194 240,9	- 1 401,0	0,7%
253,269	257 466,7	- 4 197,9	1,6%
460,689	457 448,9	3 239,6	-0,7%
99,346	93 279,0	6 066,9	-6,5%
83,331	85 507,9	- 2 176,8	2,5%
29,923	28 353,7	1 569,5	-5,5%
125,991	124 151,0	1 839,6	-1,5%
91,730	95 627,6	- 3 897,9	4,1%
76,089	76 687,7	- 598,6	0,8%
22,451	20 903,4	1 547,6	-7,4%
45,309	43 588,6	1 720,7	-3,9%
227,180	228 247,2	- 1 066,9	0,5%
40,920	36 549,6	4 370,1	-12,0%
24,468	31 149,2	- 6 681,1	21,4%
33,996	42 664,0	- 8 668,0	20,3%

The deviations are although not neglectable but several more simulations are necessary to reduce their values and as the simulation time is significant (10 days at least) and the behavior of MPR model describes sufficiently the behavior of the simulation, this result was accepted for further analyzes. It is difficult to represent the response surface behavior since 4 independent variables were used. One attempt for visualization is represented in [Fig. 8-4](#), where the independent variables k_1 and k_2 are illustrated as x and y respectively, while the dependent variable is represented with z . The obtained result shows that the best results can be reached if the k_1 and k_2 permeability values are high, while the k_3 and k_4 values are as low as possible.

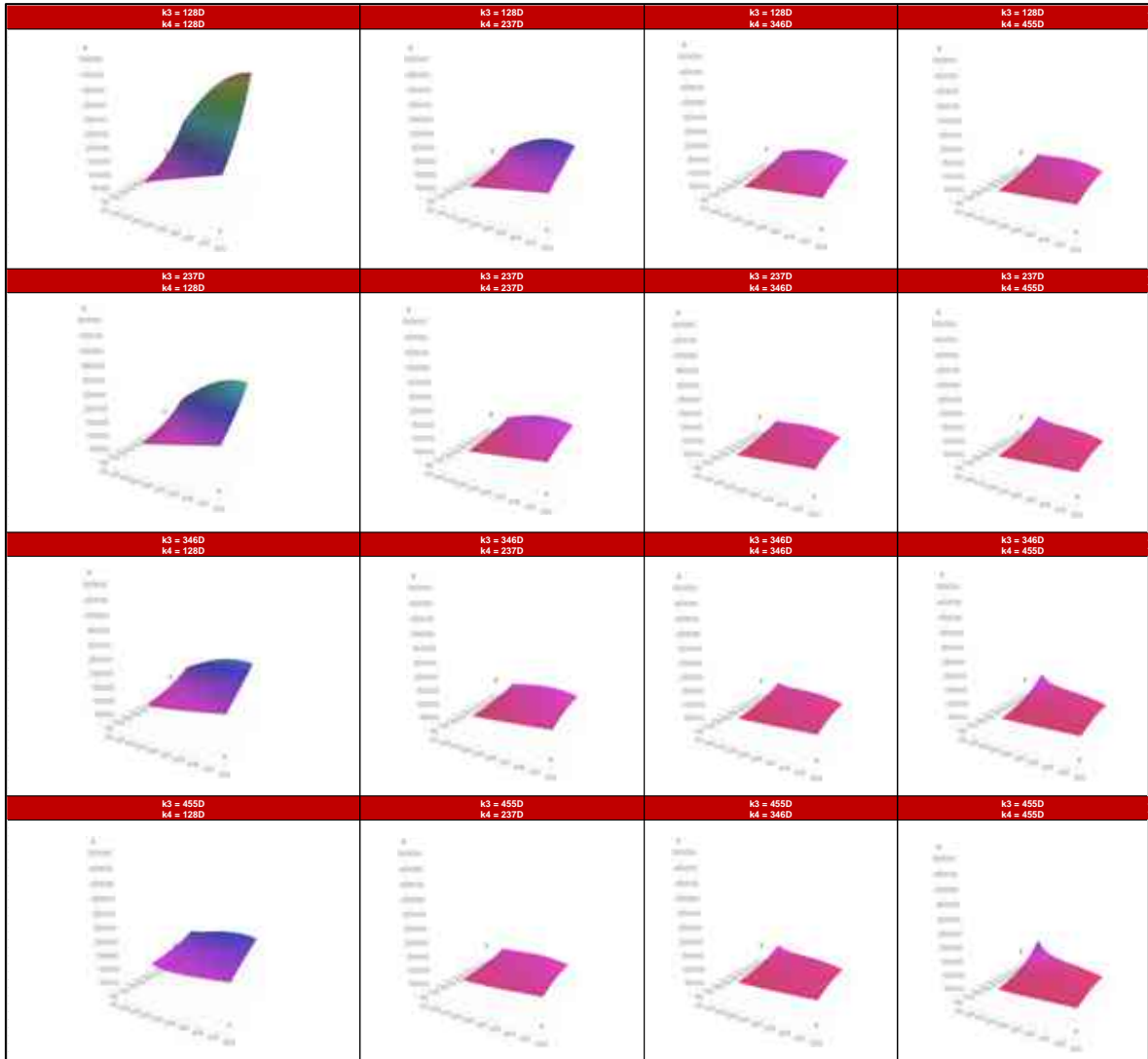


Figure 8-4: Response surface of the analyzed dataset

[Eq. 8-1](#) can be maximized with an optimization method. For this purpose, the already presented evolutionary algorithm was used. After the maximization process the optimum permeability values of each zone where the maximum heat can be produced until the outlet temperature decreased below 100°C are $k_1 = 455$ darcy, $k_2 = 455$ darcy, $k_3 = 128$ darcy, and $k_4 = 128$ darcy.

8.2 Results summary

After the simulations and the optimization, the permeability arrangement that provides the most efficient heat recovery was identified. Utilizing the developed semi-analytical model in chapter 5 the required proppant mixture can be determined under reservoir conditions. For this purpose, [Eq. 7-39](#) and [Eq. 7-13](#) should be solved respectively, where the constants were determined based on the simulation data. As the porosity values should be determined

under reservoir conditions in those equations a response surface equation was applied on the results represented in [Fig. 7-11](#). The equation can be seen in [Eq. 8-2](#), while the response surface is represented in [Appendix BL](#) with the residual values in [Appendix BM](#).

$$\Phi_p(P_c, m_{\%}) = 5.43073m_{\%}^3 - 1.31865 \times 10^{-15}P_c^3\sqrt{m_{\%}} - 0.00000378501P_c - 4.94082 \times 10^{-7}P_c\sqrt{m_{\%}} + 0.00000460117\sqrt{P_c}m_{\%} + 0.372687 - 2.03736 \times 10^{-12}\sqrt{P_c}m_{\%}^6 - \frac{0.0030107m_{\%}}{\sqrt{P_c}} + \frac{0.000120715m_{\%}^6}{P_c^3} \quad (8-2)$$

In this current model the application of the semi-analytical model developed in chapter [7](#) was not necessary since the two extreme permeability values (minimum and maximum) resulted in the best heat recovery. Since these values were measured in case the pure 30/50 mesh proppant and 16/32 mesh proppant respectively under 6,000 psi closing pressure (see in [Fig. 7-11](#)) the corresponding mass percent ratios of the mixtures represented in [Tab. 8-3](#).

Table 8-3: Optimized permeability arrangement and proppant mixture

Zone	Permeability, darcy	Mass percentage of 16/32 proppant, m/m%	Mass percentage of 30/50 proppant, m/m%
#1	455	100	0.0
#2	455	100	0.0
#3	128	0.00	100
#4	128	0.00	100

In different situations the optimization method should be repeated, but the developed methods for the simulations, optimizations, and proppant-pack permeability determination can be utilized to simplify and shorten the process.

To have a comparison the model introduced by [Danko et al. \(2018\)](#) was also built in the simulation where the center area is a non-permeable zone, and the fracture is not filled with proppant material. The comparison of the simulations on the optimized new EGS method and the method offered by [Danko et al. \(2018\)](#) can be visualized in [Fig. 8-5](#), where the upper row contains the results of the new EGS method and the lower row represents the results obtained by the Danko et al. model.

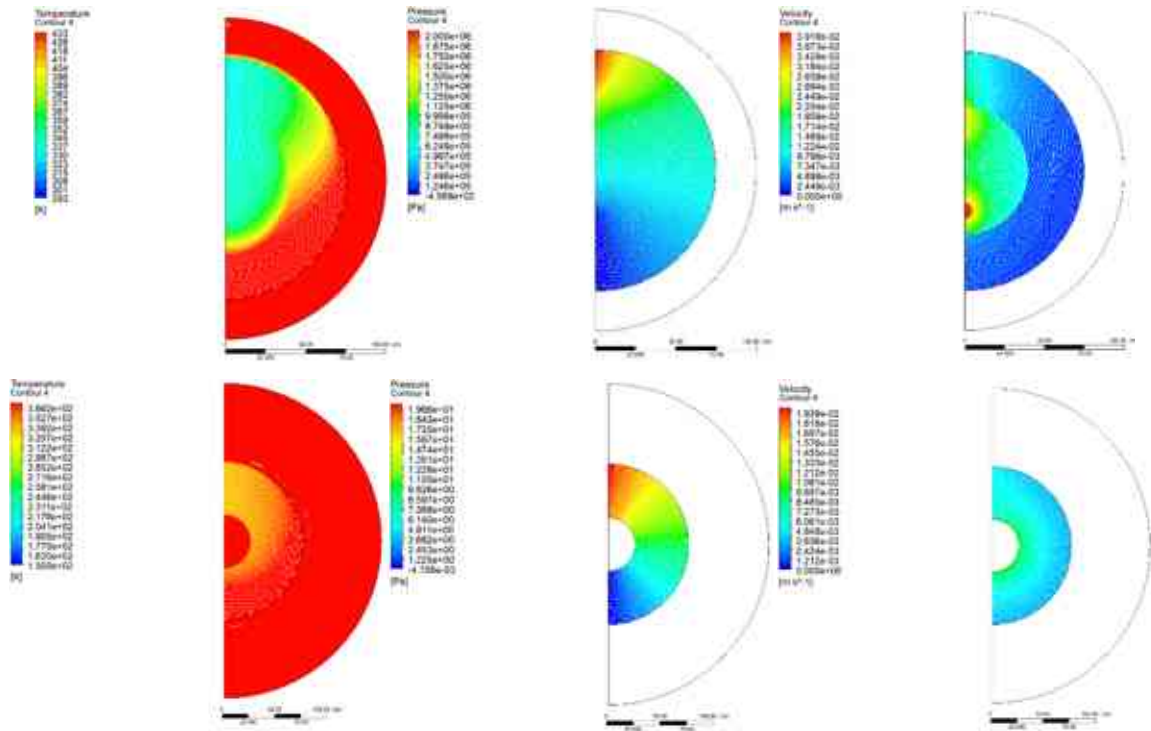


Figure 8-5: Temperature, pressure, and velocity profiles of the optimized new EGS method and the method offered by [Danko et al. \(2018\)](#)

It can be seen at results of the Danko et al. model that the velocities are higher near the wellbore as it was depicted and illustrated in [Appendix M](#). Two basic advantages of the new EGS model can be readily inferred from the results:

1. The whole fracture surface is available for the heat recovery
2. The flow in the whole fracture can be controlled and thus optimized

One not so obvious advantage is that while the propped fracture technology is mature and proved several times in the industry, injecting a non-permeable zone in the fracture while the fracturing fluid is constantly circulated to maintain pressure and keep the fracture open has never been tested in real life.

The result of the comparison is illustrated in [Fig. 8-6](#), where the thermal drawdown is represented in respect to time in the two cases. While with the new EGS technology a very slow drawdown can be reached the thermal power production decrease more significantly in case the “grouted island” model.

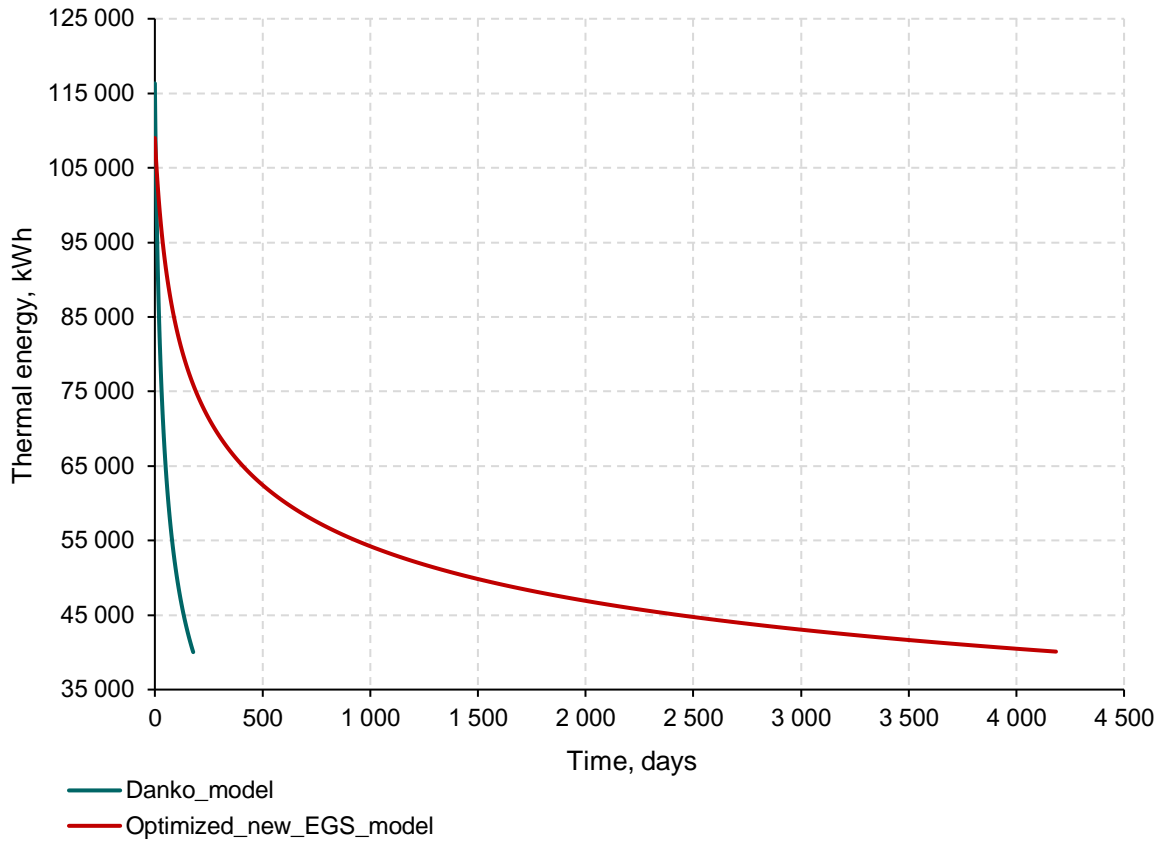


Figure 8-6: Comparison of thermal energy production of the two EGS technology

It can be clearly depicted from the presented results that the proposed new EGS technology has a significant potential and may provide an efficient method in the future to better exploit the geothermal energy resources.

9 SCIENTIFIC ACHIEVEMENTS

Novel scientific results have been found during the research conducted and presented in the Ph. D. Thesis. This chapter summarizes the scientific findings and forms the theses.

9.1 Thesis #1

Proppant can be viewed as an unconsolidated, heterogeneous (in size distribution) although well-sorted granular packing, and the different relationships that can predict the permeability of such systems can be utilized. The pressure drop across a proppant-pack is usually described by the permeability term, while several correlations for granular-packings use the term of modified particle friction factor. In essence these terms try to describe the same phenomenon but the relationship between them was not identified in the literature as other approaches were used. To be able to analyze the different models a **novel relationship was established by the Author between the modified particle friction factor and the proppant-pack permeability** in the form of [Eq 7-12](#).

With the developed relationship ([Eq 7-12](#)) the applicability of the different modified particle friction factor models can be extended. The two main driving mechanism in flow through porous media is the viscous shear from the fracture wall, and the viscous drag from the surface of the proppants. The modified particle friction factor models usually account for the viscous drag from the surface of the proppants and neglect the effect of the apparatus to the system. Complementing an analytical model that considers both mechanisms with the developed relationship ([Eq. 7-12](#)) **a new semi-analytical model was developed by the Author in the form of [Eq. 7-13](#), with which the behavior of different models can be applied on proppant-packs**. The behavior of the different models with the new semi-analytical model clearly accounts for both mechanism as it can be seen in [Fig. 7-6](#).

9.2 Thesis #2

Using [Eq. 7-13](#) and the modified particle friction factor correlations presented in [Tab. 7-4](#), the measured fracture permeability values can be compared with the correlation results. As f_p correlations contain the proppant-pack porosity (Φ_p) as a parameter, its values had to be determined. To calculate the porosity of the proppant-pack under different applied closing pressures, two parameters needed to be measured, which are the specific gravity of the proppant particle and the bulk density of the proppant-packs at each applied closing pressure.

A new method had to be developed to determine the bulk density of the proppant-pack under different applied closing pressures as no method can be found in the literature for this purpose. **A new measurement method was developed by the Author based on the [API RP 19C \(2008\)](#) standard method to determine the bulk density of proppant-packs under different closing pressures** and the schematic representation of the new method can be seen in [Fig. 7-9](#). The results show that with an average 4.41% gross variance the bulk densities can be measured under different closing pressures. With the obtained bulk density values the porosities can be easily determined as it is illustrated in [Fig. 7-11](#).

9.3 Thesis #3

The different modified particle friction factor correlations do not describe the behavior of proppant-pack under reservoir conditions efficiently, as it is shown in [Fig. 7-12](#). This can be interpreted by the following considerations:

- In the case of the models represented in [Tab. 7-4](#) the particles were unconsolidated, where the particles usually can move nearly freely, while during the proppant measurements, the proppant particles were nearly in fixed position.
- In the case of the models represented in [Tab. 7-4](#) there was no applied pressure on the particles, while during the measurements, the particles were under significant pressure, which can cause deformation, crushing, and embedment on the closure body's surface. These effects can significantly deteriorate the final permeability results ([Liang et al., 2016](#)).

A correction was applied on the available models to overcome these effects and provide a new, more effective correlation by implementing a pressure dependent term. The pressure dependent term was considered to be an exponential relationship and [Eq. 7-38](#) was developed to account for this effect. The correlation coefficients were optimized to best fit to the measurement values and **a new modified particle friction factor correlation was developed by the Author which account for the closing pressure that is asserted on the particles in the form of [Eq. 7-39](#)**. With this new correlation the average gross variance of 12.4% can be reached compared to the 34.1%-100% of other correlations. The behavior of this new correlation compared to the measurement values can be seen in [Fig. 7-14](#).

9.4 Thesis #4

An optimization method was developed by the Author with which the time required to simulate the transient heat recovery of the system can be drastically reduced. The

optimization method is based on an evolutionary algorithm and the results show that after around 90 days (simulation time) the remaining exponential curve of the temperature decrease can be estimated under 0.5% deviation as it can be seen in [Fig. 6-27](#). It was tested on 5 different simulation and one detailed example is shown in [Appendix W](#).

9.5 Thesis #5

Most of the EGS methods involve one or more injection and production wells to be implemented. Later studies such as [Kehrer et al. \(2007\)](#) and [Danko et al. \(2018\)](#) offers EGS systems where the injection and production are integrated in one well, thus reducing the cost of the total investment. These methods although have some advantages also have some limitations that promotes the investigation of a novel technology.

It was proven with simulations by the Author that the flow inside a propped fracture can be controlled by creating concentric zones with different permeabilities. Significant differences can be reached in the heat recovery by this method as it is shown in [Fig. 8-1](#).

A new EGS method was proposed by the Author with which a more efficient heat recovery can be reached. In this new method a propped fracture is used where different concentric zones are established. A complex Finite Element Model was established to simulate the new EGS method. The developed 3-dimensional model can be analyzed by a state-of-the-art method where the steady-state simulation is coupled to the transient simulation. This coupling method facilitates to reduce the simulation time, while the model accuracy is not harmed. This could be reached as the fluid flow inside the fracture will reach a steady state after enough time (this can be seen in [Fig. 6-18](#)), while the heat transfer from the reservoir to the fluid is constantly changing as the circulated fluid draws the reservoir temperature down (illustrated in [Fig. 6-20](#)). The validity of the model was proved by several standard measurements, where the results of the simulation showed an excellent match with the measured data, and it can be seen in [Fig. 6-24](#).

An optimization procedure was also established by the Author where the new EGS technology can be optimized in the point of heat recovery. The optimization method is based on a Response Surface Method (RSM) using multivariate polynomial regression (MPR). The results proved that there is an optimal arrangement of the zones' permeability values where the maximum heat recovery can be reached. The RSM optimization method is illustrated in [Fig. 8-3](#), where the dependent variables are the permeability values of the

zones and the independent variable that should be maximized is the sum of outlet temperature values of the different simulations.

10 ACKNOWLEDGEMENT

Conducting a comprehensive research is a complex and demanding task and without support almost impossible to accomplish. In this part, I would like to express my gratitude to all the individuals and groups who helped me through this journey.

First of all, I would like to thank the support of my advisors Dr. Anita Jobbik and Dr. Krisztián Mátyás Baracza who helped me throughout my research and made the resources of the Research Institute of Applied Earth Sciences available to me.

I would like to acknowledge support from GEOCHEM Ltd. and Mecsekérc Plc. For providing me the necessary equipment and tools to conduct measurements.

The research was carried out in the framework of the GINOP-2.3.2-15-2016-00010 “Development of enhanced engineering methods with the aim at utilization of subterranean energy resources” project of the Research Institute of Applied Earth Sciences of the University of Miskolc in the framework of the Széchenyi 2020 Plan. The authors acknowledge support from GEOCHEM Ltd. and Mecsekérc Plc.

Last but not least, I would like to express my appreciation to my Family who are constantly supporting me to this journey, especially my Wife who established a calm and supportive atmosphere during my research.

11 REFERENCES

- Abdollahi, R. & Shadizadeh, S.R.** (2012). *Effect of acid additives on anticorrosive property of henna in regular mud acid*. *Scientia Iranica*, 19(6):1665-1671, <https://doi.org/10.1016/j.scient.2012.09.006>
- Adachi, J., Siebrits, E., Peirce, A. & Desroches, J.** (2007). *Computer simulation of hydraulic fractures*. *International Journal of Rock Mechanics and Mining Science*, 44(05):739-757, <https://doi.org/10.1016/j.ijrmms.2006.11.006>
- Adams, J. & Rowe, C.** (2013). *Differentiating Applications of Hydraulic Fracturing*. *Effective and Sustainable Hydraulic Fracturing*, <https://doi.org/10.5772/56114>
- Agarwal, R.G., Carter, R.D. & Pollock, C.B.** (1979). *Evaluation and Performance Prediction of Low-Permeability Gas Wells Stimulated by Massive Hydraulic Fracturing*. *Journal of Petroleum Technology*, 31(03):362-372, <https://doi.org/10.2118/6838-PA>
- Alberich-Bayarri, A., Moratal, D., Marti-Bonmati, L., Salmeron-Sanchez, M., Valles-Lluch, A., Nieto-Charques, L., & Rieta, J.J.** (2007). *Volume Mesh Generation and Finite Element Analysis of Trabecular Bone Magnetic Resonance Images*. 29th Annual International Conference of the IEEE Engineering in Medicine and Biology Society. <https://doi.org/10.1109/IEMBS.2007.4352612>
- Aldersey-Williams, J. & Rubert, T.** (2019). *Levelised cost of energy – A theoretical justification and critical assessment*. *Energy Policy*, 124:169-179, <https://doi.org/10.1016/j.enpol.2018.10.004>
- An, M., Huang, H., Zhang, F. & Elsworth, D.** (2020). *Effect of slick-water fracturing fluid on the frictional properties of shale reservoir rock gouges*. *Geomechanics and Geophysics for Geo-Energy and Geo-Resources*, 6(28), <https://doi.org/10.1007/s40948-020-00153-1>
- Anderson, R.** (2013). *Performance of Fracturing Products*. US Silica, Chandler, AZ
- Andritsos, N., Karabelas, A. & Koutsoukos, P.** (2002). *Scale Formation in Geothermal Plants*. *International Summer School on Direct Application of Geothermal Energy*, 179–189. Access: https://www.researchgate.net/publication/248390587_SCALE_FORMATION_IN_GEOTHERMAL_PLANTS
- ANSYS** (2011). *ANSYS CFX-Solver Theory Guide*, ANSYS, Inc., Southpointe, 275 Technology Drive, Canonsburg, Release 14.0
- ANSYS** (2019). *ANSYS CFX-Solver Modeling Guide*, ANSYS, Inc., Southpointe, 275 Technology Drive, Canonsburg, Release 15.0
- API RP 19C** (2008). *Measurement of Properties of Proppants Used in Hydraulic Fracturing and Gravel-packing Operations, 1st Edition*. American Petroleum Institute (API)
- API RP 19D** (2008). *Measuring the Long-Term Conductivity of Proppants*, Washington, DC, API
- API RP 61** (1989). *Recommended Practices for Evaluating Short Term Proppant Pack Conductivity*, Washington, DC, API
- Arndt, N.** (2011). *Geothermal Gradient*, In: Gargaud, M. et al. (eds) *Encyclopedia of Astrobiology*, Springer, Berlin, Heidelberg, 662–662. https://doi.org/10.1007/978-3-642-11274-4_643
- Arnould, J.** (1929). *Corps de Remplissage et de Garnissage et Perte de Charge Creers par Leur Empilages*. *Jour. Chimie Ind.*, 21:478-482
- Árpási, M., Lorberer, Á. & Pap, S.** (2000). *High Pressure and Temperature (Geopressured) Geothermal Reservoirs in Hungary*. *Proceedings World Geothermal Congress, 2000, Kyushu – Tohoku, Japan, May 28 – June 10, 2000*, Access: <https://www.geothermal-energy.org/pdf/IGAstandard/WGC/2000/R0868.PDF>
- Ashat, A., Ridwan, R., Judawisastra, L., Situmorang, J., Elfajrie, I., Atmaja, R., Iskandar, C. & Ibrahim, R.** (2019). *CONCEPTUAL MODEL AND NUMERICAL SIMULATION UPDATE OF PATUHA GEOTHERMAL FIELD, WEST JAVA, INDONESIA*. *Proceedings 41st New Zealand Geothermal Workshop, Auckland, New Zealand, 25-27 November, 2019*, Access: https://www.researchgate.net/publication/337885462_CONCEPTUAL_MODEL_AND_NUMERICAL_SIMULATION_UPDATE_OF_PATUHA_GEOTHERMAL_FIELD_WEST_JAVA_INDONESIA

Avontuur, P.P.C. & Geldart, D. (1996). *A quality assessment of the Ergun equation*. The 1996 IChemE Research Event/Second European Conference for Young Researchers 1996, 994-996

Awada, A., Santo, M., Lougheed, D., Xu, D. & Virues, C. (2015). *Is That Interference? A Workflow for Identifying and Analyzing Communication Through Hydraulic Fractures in a Multi-Well Pad*. Paper presented at the SPE/AAPG/SEG Unconventional Resources Technology Conference, San Antonio, Texas, USA, July 2015, <https://doi.org/10.15530/URTEC-2015-2148963>

Axelsson, G., Arnaldsson, A., Ármannsson, H., Árnason, K., Einarsson, G., Franzson, H., Fridriksson, T., Guðmundsson, G., Gylfadóttir, S., Halldórsdóttir, S., Hersir, G.P., Mortensen, A., Thordarson, S., Jóhannesson, S., Bore, C., Karingithi, C., Koech, V., Mbithi, U., Muchemi, G. & Ouma, P. (2013). *UPDATED CONCEPTUAL MODEL AND CAPACITY ESTIMATES FOR THE GREATER OLKARIA GEOTHERMAL SYSTEM, KENYA*. PROCEEDINGS, Thirsty-Eight Workshop on Geothermal Reservoir Engineering, Stanford University, Stanford, California, February 11-13, 2013, SGP-TR-198, Access: https://www.researchgate.net/publication/288324333_UPDATED_CONCEPTUAL_MODEL_AND_CAPACITY_ESTIMATES_FOR_THE_GREATER_OLKARIA_GEOTHERMAL_SYSTEM_KENYA

Azari, V., Al Badi, M., Vazquez, O., Al-Kalbani, M. & Mackay, E. (2020). *Scale Treatment Optimization in Geothermal Wells*. Paper presented at the SPE Europec, Virtual, December 2020, Paper Number: SPE-200565, <https://doi.org/10.2118/200565-ms>

Bakhmeteff, B.A. & Feodoroff, N.V. (1937). *Flow Through Granular Media*. ASME. J. Appl. Mech., 4(3):A97-A104, <https://doi.org/10.1115/1.4008783>

Banks, D. (2012). *An Introduction to Thermogeology: Ground Source Heating and Cooling*. 2nd edition, A John Wiley & Sons, Ltd., Publication, ISBN [978-0-470-67034-7](https://doi.org/10.1002/9781119967034)

Barbier, E. (1997). *Nature and technology of geothermal energy: A review*. Renewable and Sustainable Energy Reviews, 1(1-2):1-69, [https://doi.org/10.1016/s1364-0321\(97\)00001-4](https://doi.org/10.1016/s1364-0321(97)00001-4)

Barbier, E. (2002). *Geothermal Energy Technology and Current Status: an overview*. Renewable and Sustainable Energy Reviews, 6(1-2):3-65, [https://doi.org/10.1016/S1364-0321\(02\)00002-3](https://doi.org/10.1016/S1364-0321(02)00002-3)

Bathia, S.C. (2014). *14 - Geothermal power generation*. Advanced Renewable Energy Systems, Woodhead Publishing India, Editor(s): S.C. Bhatia, 334-388, <https://doi.org/10.1016/B978-1-78242-269-3.50014-0>

Beckers, K.F., Lukawski, M.Z., Anderson, B.J., Moore M.C. & Tester, J. W. (2014). *Levelized costs of electricity and direct-use heat from Enhanced Geothermal Systems*. Journal of Renewable and Sustainable Energy, vol. 6, <https://doi.org/10.1063/1.4865575>

Belyadi, H., Fathi, E. & Belyadi, F. (2019). *Chapter Six - Proppant characteristics and application design*. Editor(s): Hoss Belyadi, Ebrahim Fathi, Fatemeh Belyadi, Hydraulic Fracturing in Unconventional Reservoirs (Second Edition), Gulf Professional Publishing, 71-95, <https://doi.org/10.1016/B978-0-12-817665-8.00006-0>

Bradford, J., McLennan, J., Tiwari, S., Moore J., Podgorney, R., Plummer, M. & Majer, E. (2016). *Application of hydraulic and thermal stimulation techniques at Raft River, Idaho: a DOE enhanced geothermal system demonstration project*. Paper presented at the 50th U.S. Rock Mechanics/Geomechanics Symposium, Houston, Texas, June 2016., Paper Number: [ARMA-2016-858](https://doi.org/10.1016/B978-1-78242-858-8)

Breede, K., Dzebisashvili, K., Liu, X. & Falcone, G. (2013). *A systematic review of enhanced (or engineered) geothermal systems: past, present and future*. Geothermal Energy, 1(4):1-27, <https://doi.org/10.1186/2195-9706-1-4>

Brinkman, H.C. (1949). *A calculation of the viscous force exerted by a flowing fluid on a dense swarm of particles*. Applied Sciences Research, A1:27-34, <https://doi.org/10.1007/BF02120313>

Bronicki, L.Y. (2003). *Geothermal Power Stations*. Editor(s): Robert A. Meyers, Encyclopedia of Physical Science and Technology (Third Edition), Academic Press, 709-718, <https://doi.org/10.1016/B0-12-227410-5/00290-8>

Bronicki, L.Y. (2013). *Geothermal Power Stations*. Reference Module in Earth Systems and Environmental Sciences, Elsevier, <https://doi.org/10.1016/B978-0-12-409548-9.05463-4>

- Bronicki, L.Y.** (2016). *1 - Introduction to geothermal power generation*. Editor(s): Ronald DiPippo, Geothermal Power Generation, Woodhead Publishing, 1-3, <https://doi.org/10.1016/B978-0-08-100337-4.00001-2>
- Brophy, P., Lippmann, M., Dobson, P.F. & Poux, B.** (2010): *The Geysers Geothermal Field Update 1990/2010*. Special Report NO. 20, Geothermal Resources Council, Report Number(s) LBNL-4918E, United States, <https://doi.org/10.2172/1048267>
- Brown, D.W., Duchane, D.V., Heiken, G. & Hriscu, V.T.** (2012). *Mining the earth's heat: hot dry rock geothermal energy*. Springer Berlin Heidelberg, <https://doi.org/10.1007/978-3-540-68910-2>
- Brown, L.R., Flavin, C. & Postel, S.** (1990). *Picturing a Sustainable Society: State of the World, A Worldwatch Institute Report on Progress Toward a Sustainable Society*. New York/London: Norton, pp. 17
- Burke, S.P., & Plummer, W.B.** (1928). *Gas Flow through Packed Columns*. Ind. Eng. Chem., 20(11):1196-1200, <https://doi.org/10.1021/ie50227a025>
- Cao, W.J., Huang, W.B. & Jiang, F.M.** (2016). *A novel-hydraulic-mechanical model for the enhanced geothermal system heat extraction*. International Journal of Heat and Mass Transfer, 100:661-671, <https://doi.org/10.1016/j.ijheatmasstransfer.2016.04.078>
- Carey, M.A., Mondal, S. & Sharma, M.M.** (2015). *Analysis of Water Hammer Signatures for Fracture Diagnostics*. Paper presented at the SPE Annual Technical Conference and Exhibition, Houston, Texas, USA, September 2015, <https://doi.org/10.2118/174866-MS>
- Carman, P.C.** (1937). *Fluid Flow through Granular Beds*. Chemical Engineering Research and Design, 75(Supplement):S32-S48, [https://doi.org/10.1016/S0263-8762\(97\)80003-2](https://doi.org/10.1016/S0263-8762(97)80003-2)
- Chalmers, J., Taliaferro, D.B. & Rawlins, E.L.** (1932). *Flow of Air and Gas through Porous Media*. Transactions of the AIME, 98(01):375-400, <https://doi.org/10.2118/932375-g>
- Chandrasekharam, D. & Bundschuh, J.** (2008). *Low-enthalpy geothermal resources for power generation*. CRC Press Taylor & Francis Group, New York, ISBN: [978-0-415-40168-5](https://doi.org/10.2118/932375-g)
- Chapra, S. & Canale, R.** (2009). *Numerical Methods for Engineers*. sixth ed. McGraw-Hill, New York, NY.
- Chapuis, R.P.** (2004). *Predicting the Saturated Hydraulic Conductivity of Sand and Gravel Using Effective Diameter and Void Ratio*. Canadian Geotechnical Journal, 41(5):787-795, <https://doi.org/10.1139/t04-022>
- Cipolla, C.L. & Mayerhofer, M.** (1998). *Understanding Fracture Performance by Integrating Well Testing & Fracture Modeling*. Paper presented at the SPE Annual Technical Conference and Exhibition, New Orleans, Louisiana, September 1998, <https://doi.org/10.2118/49044-MS>
- Coelho, D., Thovert, J-F. & Adler, P.M.** (1997). *Geometrical and transport properties of random packings of spheres and aspherical particles*. Physical Review E, 55(2):1959-1978, <https://doi.org/10.1103/PhysRevE.55.1959>
- Coulson.** (1935). *The Streamline Flow of Liquids through Beds composed of Spherical Particles*. Univ. of London, Ph.D. thesis
- Covas, J.A. & Gaspar-Cunha, A.** (2009). *Extrusion Scale-up: An Optimization-based Methodology*. International Polymer Processing, 24(1), 67–82. <https://doi.org/10.3139/217.2200>
- Daneshy, A.A.** (1973). *On the Design of Vertical Hydraulic Fractures*. Journal of Petroleum Technology, 25(01):83–97, <https://doi.org/10.2118/3654-PA>
- Danko, G., Bahrami, D., Varga, Gy., Baracza, M.K. & Jobbik, A.** (2018). *Conceptual Study of a Well-Fracture-Well Type Fluid Circulation System for EGS*. PROCEEDINGS, 43rd Workshop on Geothermal Reservoir Engineering, Stanford University, Stanford, California, February 12-14, 2018, [SGP-TR-213](https://doi.org/10.2118/3654-PA)
- Danko, G., Jobbik, A., Baracza, M.K., Varga, G., Kovacs, I. & Wittig, V.** (2020). *Energy potential of a single-fracture, robust, engineered geothermal system*. Geomech. Geophys. Geo-energ. Geour., 6(26), <https://doi.org/10.1007/s40948-020-00149-x>

- Darcy, H.** (1856). *Les fontaines publiques de la ville de Dijon*, Paris, Dalmont
- Dezayes, C., Genter, A. & Valley, B.** (2010). *Structure of the low permeable naturally fractured geothermal reservoir at Soultz*. *Comptes Rendus Geoscience*, 342(7-8):517-530, <https://doi.org/10.1016/j.crte.2009.10.002>
- Dincer, I. & Ezzat, M.F.** (2018). 3.6 *Geothermal Energy Production*. *Comprehensive Energy Systems*, Elsevier, 3:252-303, <https://doi.org/10.1016/B978-0-12-809597-3.00313-8>
- DiPippo, R.** (2016a). 9 - *Elements of thermodynamics, fluid mechanics, and heat transfer applied to geothermal energy conversion systems*. Editor(s): Ronald DiPippo, *Geothermal Power Generation*, Woodhead Publishing, pp. 217-247, <https://doi.org/10.1016/B978-0-08-100337-4.00009-7>
- DiPippo, R.** (2016b). 14 - *Combined and hybrid geothermal power systems*. Editor(s): Ronald DiPippo, *Geothermal Power Generation*, Woodhead Publishing, pp. 391-420, <https://doi.org/10.1016/B978-0-08-100337-4.00014-0>
- DiPippo, R.** (2016c). *The Geysers Dry-Steam Power Plants, Sonoma and Lake Counties, California, USA*. *Geothermal Power Plants*, <https://doi.org/10.1016/B978-0-08-100879-9.00012-4>
- Doonechaly, N.G. & Bruhn, D.F.** (2018). *Effectiveness of the Thermal Stimulation for Deep Geothermal Reservoirs*. *Geophysical Research Abstracts*, volume 20, EGU2018-17090, EGU General Assembly 2018, Access: <https://meetingorganizer.copernicus.org/EGU2018/EGU2018-17090.pdf>
- EIA** (2021a):.1. *Energy Overview*. U.S. Energy Information Administration, Available at: <https://www.eia.gov/totalenergy/data/monthly/pdf/sec1.pdf>, Date of Access: 31.10.2021
- EIA** (2021b). *International Energy Outlook 2021*. U.S. Energy Information Administration, Reference Case, Available at: <https://www.eia.gov/outlooks/ieo/>, Date of Access: 31.10.2021
- Eisfeld, B. & Schnitzlein, K.** (2001). *The influence of confining walls on the pressure drop in packed beds*. *Chemical Engineering Science*, 56:4321-4329, [https://doi.org/10.1016/S0009-2509\(00\)00533-9](https://doi.org/10.1016/S0009-2509(00)00533-9)
- Elders, W.A. & Fridleifsson, G.O.** (2010). *The Science Program of the Iceland Deep Drilling Project (IDDP): a Study of Supercritical Geothermal Resources*. *Proceedings of World Geothermal Congress 2010*, Bali, Indonesia, 25-29 April 2010, Access: https://www.researchgate.net/publication/228556206_The_Science_Program_of_the_Iceland_Deep_Drilling_Project_IDDP_a_study_of_supercritical_geothermal_resources
- Elders, W.A., Fridleifsson, G.O. & Palsson, B.** (2014). *Iceland Deep Drilling Project: The first well, IDDP-1, drilled into magma*. *Geothermics*, 49:1, <https://doi.org/10.1016/j.geothermics.2013.08.012>
- Erdim, E., Akgiray, Ö. & Demir, I.** (2015). *A revisit of pressure drop-flow rate correlations for packed beds of spheres*. *Powder Technologies*, 283:488-504, <https://doi.org/10.1016/j.powtec.2015.06.017>
- Ergun, S.** (1952). *Fluid flow through packed columns*. *Chemical Engineering Progress*, 48:89-94
- Fahien, R.W. & Schriver, C.B.** (1961). *Fundamentals of Transport Phenomena*. Paper presented and Denver meeting of AIChE, in R.W. Fahien (Ed.), McGraw-Hill, New York, 1983 (1961)
- Fanchi, J.R.** (2010). 16 - *Modern Reservoir Management Applications*. Editor(s): John R. Fanchi, *Integrated Reservoir Asset Management*, Gulf Professional Publishing, pp. 279-293, <https://doi.org/10.1016/B978-0-12-382088-4.00016-5>
- Fazal, M.R. & Kamran, M.** (2021). *Chapter 9 - Geothermal energy*. Editor(s): Muhammad Kamran, Muhammad Rayyan Fazal, *Renewable Energy Conversion Systems*, pp. 265-281, <https://doi.org/10.1016/B978-0-12-823538-6.00006-3>
- Foscolo, P.U., Gibilaro, L.G. & Waldram, A.** (1983). *A unified model for particulate expansion of fluidised beds and flow in fixed porous media*. *Chemical Engineering Science*, 38(8):1251-1260, [https://doi.org/10.1016/0009-2509\(83\)80045-1](https://doi.org/10.1016/0009-2509(83)80045-1)
- Fridleifsson, G.O., Albertsson, A. & Elders, W.A.** (2010). *Iceland Deep Drilling Project (IDDP) - 10 Years Later – Still an Opportunity for International Collaboration*. *Proceedings World geothermal Congress 2010*, Bali, Indonesia, 25-29 April 2010, Access:

https://www.researchgate.net/publication/343111483_Geothermal_energy_in_Mexico_update_and_perspectives

Fridleifsson, G.O., Elders, W.A., Zierenberg, R., Fowler, A.P.G., Weisenberg, T., Mesfin, K., Sigurdsson, O., Nielsson, S., Einarsson, G., Oskarsson, F., Gudnason, E. A., Tulinius, H., Hokstad, K., Gilbert, B., Nono, F., Loggia, D., Parat, F., Cichy, S., Escobedo, D. & Mainprice, D. (2020). *The Iceland Deep Drilling Project at Reykjanes: Drilling into the root zone of a black smoker analog*. Journal of Volcanology and Geothermal Research, volume 391, <https://doi.org/10.1016/j.jvolgeores.2018.08.013>

Furnas, C.C. (1929). *Flow of Gases Through Beds of Broken Solids*. Bull. U.S., Bureau of Minerals, Bulletin 307

Gardien, C.J., Pope, G.A. & Hill, A.D. (1996). *Hydraulic Fracture Diagnosis Using Chemical Tracers*. Paper presented at the SPE Annual Technical Conference and Exhibition, Denver, Colorado, October 1996, <https://doi.org/10.2118/36675-MS>

Geertsma, J. & de Klerk, F. (1969). *A rapid method of predicting width and extent of hydraulically induced fractures*. Journal of Petroleum Technology, 21(12):1571–1581, <https://doi.org/10.2118/2458-PA>

Ghassemi, A., Tarasovs, S. & Cheng, A.H.D. (2007). *A 3-D study of the effects of thermomechanical loads on fracture slip in enhanced geothermal reservoirs*. International Journal of Rock Mechanics and Mining Science, 44(8):1132-1148, <https://doi.org/10.1016/j.ijrmms.2007.07.016>

Gischig, V. & Preisig, G. (2015). *Hydro-fracturing versus Hydro-shearing: A Critical Assessment of Two Distinct Reservoir Stimulation Mechanisms*. Proceedings of 13th International Congress of Rock Mechanics, ISRM 2015, May 10-13 2015, Montreal, Canada, <https://doi.org/10.13140/RG.2.1.4924.3041>

Grant, M.A., & Bixley, P.F. (2011). *Chapter 12 - Field Examples*. Geothermal reservoir Engineering (Second Edition), pp. 219-247, <https://doi.org/10.1016/B978-0-12-383880-3.10012-5>

Grant, M.A., Clearwater, J., Quinao, J., Bixley, P.F. & Le Brun, M. (2013). *Thermal Stimulation of Geothermal Wells: A Review of Field Data*. Proceedings, Thirty-Eight Workshop on Geothermal Reservoir Engineering, Stanford University, Stanford, California, February 11-13, 2013, Access: <https://pangea.stanford.edu/ERE/pdf/IGAstandard/SGW/2013/Grant1.pdf>

Green, H. & Ampt, G.A. (1912). *Studies on Soil Physics: Part II — The Permeability of an Ideal Soil to Air and Water*. The Journal of Agricultural Science, 5(01):1-26, <https://doi.org/10.1017/s0021859600001751>

Gui, F., Rahman, K., Moos, D., Vassilellis, G., Li, C., Liu, Q., Zhang, F., Peng, J., Yuan, X. & Zou, G. (2013). *Optimizing Hydraulic Fracturing Treatment Integrating Geomechanical Analysis and Reservoir Simulation for a Fractured Tight Gas Reservoir*. Tarim Basin, China. In A.P. Bunger, J. McLennan, & R. Jeffrey (Eds.), Effective and Sustainable Hydraulic Fracturing. IntechOpen, <https://doi.org/10.5772/56384>

Guo, B., Liu, X. & Tan X. (2017). *Chapter 14 - Hydraulic Fracturing*. Editor(s): Boyun Guo, Xinghui Liu, Xuehao Tan, Petroleum Production Engineering (Second Edition), Gulf Professional Publishing, <https://doi.org/10.1016/B978-0-12-809374-0.00014-3>

Gupta, H. & Roy, S. (2007a). *Chapter 4 – Geothermal Systems and Resources*. Editor(s): Harsh Gupta, Sukanta Roy, Geothermal Energy, An Alternative Resource for the 21st Century, pp. 49-59, Elsevier, <https://doi.org/10.1016/B978-044452875-9/50004-6>

Gupta, H. & Roy, S. (2007b). *The Cerro Prieto Geothermal Field, Mexico*. Geothermal Energy, Chapter 7, pp. 165-197, <https://doi.org/10.1016/b978-044452875-9/50007-1>

Gutiérrez-Negrín, L.C.A., Félix, I.C., Romo-Jones, J.M. & Quijano-León, J.L. (2020). *Geothermal energy in Mexico: update and perspective*. Proceedings World Geothermal Congress 2020, Reykjavik, Iceland, April 26 – May 2, 2020, Access: https://www.researchgate.net/publication/343111483_Geothermal_energy_in_Mexico_update_and_perspectives

- Hammons, T.J.** (2004). *Geothermal Power Generation Worldwide: Global Perspective, Technology, Field Experience, and Research and Development*. Electric Power Components and Systems, 32(5):529–553, <https://doi.org/10.1080/15325000490224076>
- Han, S., Cheng, Y., Gao, Q., Yan, C. & Zhang, J.** (2019). *Numerical study on heat extraction performance of multistage fracturing Enhanced Geothermal System*. Renewable Energy, 149:1214-1226, <https://doi.org/10.1016/j.renene.2019.10.114>
- Hardee, H.C.** (1981). *Convective heat extraction from molten magma*. Journal of Volcanology and Geothermal Research, 10(1-3):175-193, [https://doi.org/10.1016/0377-0273\(81\)90061-5](https://doi.org/10.1016/0377-0273(81)90061-5)
- Harvey, W. & Wallace, K.** (2016). *10 - Flash steam geothermal energy conversion systems: single-, double-, and triple-flash and combined-cycle plants*. Editor(s): Ronald DiPippo, Geothermal Power Generation, Woodhead Publishing, pp. 249-290, <https://doi.org/10.1016/B978-0-08-100337-4.00010-3>
- Hill, A.D. & Schechter, R. S.** (2000). *16 – Fundamentals of Acid Stimulation, Reservoir Stimulation*. Third Edition, Editor(s): Micheal J. Economides and Kenneth G. Nolte, Publisher: Chichester, England; New York: Wiley, Access: https://www.google.com/url?sa=t&rct=j&q=&esrc=s&source=web&cd=&cad=rja&uact=8&ved=2ahUKewi88u3-r30AhVr-yoKHeEqDkQQFnoECAMQAQ&url=https%3A%2F%2Fwww.researchgate.net%2Ffile.PostFileLoader.html%3Fid%3D591b038148954c7bac0eeb2d%26assetKey%3DAS%253A494639238529025%25401494942593011&usq=AOvVaw0bK7EI2Sv0ye9s4E_T15dx
- Hubbert, M.K. & Willis, D.G.** (1957). *Mechanics Of Hydraulic Fracturing*. Trans. 210(01):153–168, <https://doi.org/10.2118/686-G>
- Huenges, E.** (2016). *25 - Enhanced geothermal systems: Review and status of research and development*. Editor(s): Ronald DiPippo, Geothermal Power Generation, Woodhead Publishing, pp. 743-761, <https://doi.org/10.1016/B978-0-08-100337-4.00025-5>
- IEA** (2008). *World Energy Outlook 2008*. International Energy Agency (IEA), IEA Publications, 9, rue de la Fédération, 75739, Paris, CEDEX 15, Printed in France by STEDI MEDIA (612008231P1), ISBN-13 [978 92 64 04560-6](https://doi.org/10.1016/B978-0-08-100337-4.00025-5)
- IEA** (2010). *World Energy Outlook 2010*. International Energy Agency (IEA), IEA Publications, 9, rue de la Fédération, 75739, Paris, CEDEX 15, Printed in France by STEDI MEDIA (61 2010 15 1P1), November 2010, ISBN [978-92-64-08624-1](https://doi.org/10.1016/B978-0-08-100337-4.00025-5)
- IEA** (2012). *World Energy Outlook 2012*. International Energy Agency (IEA), IEA Publications, 9, rue de la Fédération, 75739, Paris, CEDEX 15, Printed in France by Corlet, November 2012, (61 2012 25 1P1), November 2010, ISBN [978 92 64 18084 0](https://doi.org/10.1016/B978-0-08-100337-4.00025-5)
- IEA** (2014). *World Energy Outlook 2014*. International Energy Agency (IEA), IEA Publications, 9, rue de la Fédération, 75739, Paris, CEDEX 15, Printed in France by Corlet, November 2014, (61 2014 03 1P1), ISBN [978 92 64 20804 9](https://doi.org/10.1016/B978-0-08-100337-4.00025-5)
- IEA** (2016). *World Energy Outlook 2016*. International Energy Agency (IEA), IEA Publications, 9, rue de la Fédération, 75739, Paris, CEDEX 15, Layout in France by DESK, November 2016, (612016221E1), ISBN 978-92-64-26495-3, ISSN [2072-5302](https://doi.org/10.1016/B978-0-08-100337-4.00025-5)
- IEA** (2018). *World Energy Outlook 2018*. International Energy Agency (IEA), IEA Publications, Layout in France by DESK, November 2018, (612019191E1), ISBN 9789264306776, ISSN [2072-5302](https://doi.org/10.1016/B978-0-08-100337-4.00025-5)
- IEA** (2020). *World Energy Outlook 2020*. International Energy Agency (IEA), IEA Publications, Typeset in France by IEA, October 2020, ISBN 978-92-64-44923-7, ISSN [2072-5302](https://doi.org/10.1016/B978-0-08-100337-4.00025-5)
- IGA** (2021). *Geothermal Power Database*. International Geothermal Association, Available at: <https://www.geothermal-energy.org/explore/our-databases/geothermal-power-database/>, Date of Access: 01.11.2021
- IRENA** (2021). *Renewable Power Generation Costs in 2020*. International Renewable Energy Agency, Abu Dhabi. [ISBN 978-92-9260-348-9](https://doi.org/10.1016/B978-0-08-100337-4.00025-5)

Ismail, I.B. (2011). *Power Generation Using Nonconventional Renewable Geothermal & Alternative Clean Energy Technologies*. Planet Earth 2011 - Global Warming Challenges and Opportunities for Policy and Practice. <https://doi.org/10.5772/25132>

Ismail, I.B. (2019). *Introductory Chapter: Power Generation Using Geothermal Low-Enthalpy Resources and ORC Technology*. Renewable Geothermal Energy Explorations, <https://doi.org/10.5772/intechopen.84390>

ISO 13503-5. (2006). *Procedures for measuring the long-term conductivity of proppants*. Petroleum and natural gas industries – Completion fluids and materials – Part 5, Geneva, Switzerland, ISO

Jung, R. (2013). *EGS – Goodbye or Back to the Future 95*. Effective and Sustainable Hydraulic Fracturing, Andrew P. Bunker, John McLennan and Rob Jeffrey, IntechOpen, <https://doi.org/10.5772/56458>

Kabeyi, M. (2019). *Geothermal Electricity Generation, Challenges, Opportunities and Recommendations*. International Journal of Advances in Scientific Research and Engineering, 5(8), <https://doi.org/10.31695/IJASRE.2019.33408>

Kalra, S. & Mashuq-un-Nabi (2016). *Study of coronary stent deformation using finite element method*. 11th International Conference on Industrial and Information Systems (ICIIS), Roorkee, India, 2016, pp. 404-407, <https://doi.org/10.1109/ICIINFS.2016.8262974>

Kazemi, H., Yazdjerdi, K., Asadi, A., & Mozafari, M.R. (2020). *Application of genetic and K-means algorithms in clustering Babakoochi Anticline joints north of Shiraz*. Iran, Central European Geology, 63(1), 38-48. <https://doi.org/10.1556/24.2020.00004>

Kehrer, P., Orzol, J., Jung, R., Jatho, R. & Junker, R. (2007). *The GeneSys project – a contribution of GEOZENTRUM Hannover to the development of Enhanced Geothermal Systems (EGS) [Das GeneSys-Projekt – ein Beitrag des GEOZENTRUMs Hannover zur Entwicklung von "Enhanced Geothermal Systems" (EGS)]*. Zeitschrift Der Deutschen Gesellschaft Für Geowissenschaften, 158(1):119–132, <https://doi.org/10.1127/1860-1804/2007/0158-0119>

Khasanov, M.M., Krasnov, V., Musabirov, T. & Mukhamedshin, R. (2009). *Novel Approach to Waterflood Design to Enhance Pattern Performance with Massive Hydraulic Fracturing Applications*. Paper presented at the SPE/EAGE Reservoir Characterization and Simulation Conference, Abu Dhabi, UAE, October 2009. <https://doi.org/10.2118/125750-MS>

Khristianovic, S.A. & Zheltov, Y.P. (1955). *Formation of vertical fractures by means of highly viscous liquid*, In: Proceedings of the fourth world petroleum congress, Rome, pp. 579–86.

King, G.E. & Miskimins, J.L. (2020). *Hydraulic Fracturing: Fundamentals and Advancements – Chapter 1: Introduction*. Editor(s): Jennifer L. Miskimins, Society of Petroleum Engineers, Richardson, Texas, USA, ISBN: [978-1-61399-719-2](https://doi.org/10.1016/j.geothermics.2014.05.014)

Kozeny, J. (1927). *Ueber kapillare Leitung des Wassers im Boden*, Sitzungsber Akad. Wiss., 136(Abt. 2a):271-306

Kozloff, K. L. & Dower, R.C. (1993). *A New Power Base—Renewable Energy Policies for the Nineties and Beyond*. Washington, DC: World Resour. Inst., pp. 196

Kraft, T. & Deichmann, N. (2014). *High-precision relocation and focal mechanism of the injection-induced seismicity at the Basel EGS*. Geothermics, 52:59-73, <https://doi.org/10.1016/j.geothermics.2014.05.014>

Krumbein, W.C. & Monk, G.D. (1943). *Permeability as a Function of Size Parameters of Unconsolidated Sand*. In Transactions of the Society of Petroleum Engineers, 151(1):153-163, <https://doi.org/10.2118/943153-G>

Kundu, A (2017). *Geo-thermal Energy – A Green-lane Towards Sustainability*. Proceedings of the National Conference on Waste to Energy, Carbon Capture and Storage (NCWECCS – 2017), NIT Rourkela, India, 3-5 August 2017, Access: https://www.researchgate.net/publication/320583880_GEO-THERMAL_ENERGY_-_A_GREEN-LANE_TOWARDS_SUSTAINIBILITY

- Kurten, H., Raasch, J. & Rumpf, H.** (1966). *Beschleunigung eines kugelförmigen Feststoffteilchens im Stromungsfeld konstanter Geschwindigkeit*. Chem. Ing. Tech., 38(9):941-948, <https://doi.org/10.1002/cite.330380905>
- Lasdon, L.S., Waren, A.D., Jain, A. & Ratner, M.** (1978). *Design and testing of a generalized reduced gradient code for nonlinear programming*. ACM Trans. Math. Softw. (TOMS), 4(1):34-50, <https://doi.org/10.1145/355769.355773>
- Law, B.E. & Spencer, C.W.** (1993). *Gas in tight reservoirs-an emerging major source of energy*. in David G. Howell (editor), *The Future of Energy Gasses*, US Geological Survey, Professional Paper 1570, pp. 233-252, <https://doi.org/10.3133/pp1570>
- Leong, Y., de longh, J.E., Bähring, S., Tuxen, A.K. & Nielsen, T.B.** (2015). *Estimation of Fracture Volume Between Well Pairs Using Deuterium Tracer*. Paper presented at the SPE Annual Technical Conference and Exhibition, Houston, Texas, USA, September 2015, <https://doi.org/10.2118/174832-MS>
- Leva, M.** (1949). Quoted in: Green, D.W. and Perry, R.H. (Eds.), *Perry's Chemical Engineering Handbook*, Eight edition, Chemical Engineering, 56:115-117, ISBN 10: [0071593136](https://doi.org/10.1002/cite.330380905)
- Li, T., Shiozawa, S. & McClure, M.W.** (2016). *Thermal breakthrough calculations to optimize design of a multiple-stage Enhanced Geothermal System*. Geothermics, 64:455-465, <https://doi.org/10.1016/j.geothermics.2016.06.015>
- Liang, F., Sayed, M., Al-Muntasheri, G.A. & Chang, F.F.** (2015). *Overview of Existing Proppant Technologies and Challenges*. Society of Petroleum Engineers, <https://doi.org/10.2118/172763-MS>
- Liang, F., Sayed, M., Al-Muntasheri, G.A., Chang, F.F. & Li, L.** (2016). *A comprehensive review on proppant technologies*. Petroleum. 2(1):26-39, <https://doi.org/10.1016/j.petlm.2015.11.001>
- Loudon, A.G.** (1952). *The Computation of Permeability from Simple Soil Tests*. Géotechnique, 3(4):165-183, <https://doi.org/10.1680/geot.1952.3.4.165>
- Lu, S.M.** (2018). *A global review of enhanced geothermal system (EGS)*. Renewable and Sustainable Energy Reviews, 81(2):2902-2921, <https://doi.org/10.1016/j.rser.2017.06.097>
- Lund, W.J. & Toth, A.N.** (2021). *Direct utilization of geothermal energy 2020 worldwide review*. Geothermics, volume 90, <https://doi.org/10.1016/j.geothermics.2020.101915>
- Maad, M.M.** (2016). *Genetic Algorithm Optimization by Natural Selection*. computer science <https://doi.org/10.13140/RG.2.2.23758.18246>
- Macdonald, L.F., El-Sayed, M.S., Mow, K. & Dullien, F.A.L.** (1979). *Flow through Porous Media-the Ergun Equation Revisited*, Ind. Eng. Chem. Fundamen., 18(3)199-208, <https://doi.org/10.1021/i160071a001>
- Mach, E.** (1934). *Druckverluste und Belastungsgrenzen von Füllkörpersäulen*. Dechema Monographien, 49-56(6):38-55
- Mack, M.G. & Dowell, S.** (2000). *Mechanics of Hydraulic Fracturing, Reservoir Stimulation*. Third Edition, Editor(s): Micheal J. Economides and Kenneth G. Nolte, Publisher: Chichester, England; New York: Wiley, Access: https://www.google.com/url?sa=t&rct=j&q=&esrc=s&source=web&cd=&cad=rja&uact=8&ved=2ahUKewi88u3-r30AhVr-yoKHeEqDkQQFnoECAMQAQ&url=https%3A%2F%2Fwww.researchgate.net%2Ffile.PostFileLoader.html%3Fid%3D591b038148954c7bac0eeb2d%26assetKey%3DAS%253A494639238529025%25401494942593011&usq=AOvVaw0bK7EI2Sv0ye9s4E_T15dx
- Maia, A., Ferreira, E., Oliveira, M.C., Menezes, L.F. & Andrade-Campos, A.** (2017). *Numerical optimization strategies for springback compensation in sheet metal forming*, Computational Methods and Production Engineering, pp. 51-82, <https://doi.org/10.1016/b978-0-85709-481-0.00003-3>
- Mao, S., Siddhamshetty, P., Zhang, Z., Yu, W., Chun, T., Kwon, J.S. & Kan W.** (2021). *Impact of Proppant Pumping Schedule on Well Production for Slickwater Fracturing*. SPE Journal, 26(01): 342-358, <https://doi.org/10.2118/204235-PA>

- Martínez, E.L., Jaimes, R., Gomez, J.L. & Filho, R.M.** (2012). *CFD Simulation of Three-Dimensional Multiphase Flow in a Rotating Packed Bed*, Editor(s): Ian David Lockhart Bogle, Michael Fairweather, Computer Aided Chemical Engineering, Elsevier, 30:1158-1162. <https://doi.org/10.1016/B978-0-444-59520-1.50090-7>
- Martys, N.S., Torquato, S. & Bentz, D.P.** (1994). *Universal scaling of fluid permeability for sphere packings*. Physical Review E, 50(1):403-408, <https://doi.org/10.1103/physreve.50.403>
- Mavis, F.T. & Wilsey, E.F.** (1937). *University of Iowa Study Bulletin No. 7*
- Mayerhofer, M.J., Lolon, E.P., Youngblood, J.E., & Heinze, J.R.** (2006). *Integration of Microseismic Fracture Mapping Results With Numerical Fracture Network Production Modeling in the Barnett Shale*. Paper presented at the SPE Annual Technical Conference and Exhibition, San Antonio, Texas, USA, September 2006, <https://doi.org/10.2118/102103-MS>
- McDaniel, R.R. & Willingham, R.J.** (1978). *The effect of various proppants and proppant mixtures on fracture permeability*. Paper presented at the SPE Annual Fall Technical Conference and Exhibition, Houston, Texas, October 1978, <https://doi.org/10.2118/7573-MS>
- Meyer, B.A. & Smith, D.W.** (1985). *Flow through porous media: comparison of consolidated and unconsolidated materials*. Industrial and Engineering Chemistry Fundamentals, 24(3):360-368, <https://doi.org/10.1021/i100019a013>
- Mines, G.** (2016). *13 - Binary geothermal energy conversion systems: basic Rankine, dualepressure, and dualefluid cycles*. Editor(s): Ronald DiPippo, Geothermal Power Generation, Woodhead Publishing, pp. 353-389, <https://doi.org/10.1016/B978-0-08-100337-4.00013-9>
- Mittal, A., Rai, C.S. & Sondergeld, C.H.** (2018). *Proppant-Conductivity Testing Under Simulated Reservoir Conditions: Impact of Crushing, Embedment, and Diagenesis on Long-Term Production in Shales*. SPE Journal, 23(04):1304-1315, <https://doi.org/10.2118/191124-PA>
- Mock, J.E., Tester, J.W. & Wright, P.M.** (1997). *GEOHERMAL ENERGY FROM THE EARTH: Its Potential Impact as an Environmentally Sustainable Resource*. Annual Review of Energy and the Environment, 22(1):305–356. <https://doi.org/10.1146/annurev.energy.22.1.305>
- Mollanouri, M.M., Nia, F.S. & Jessen, K.** (2015). *Conductivity of Proppant-Packs under Variable Stress Conditions: An Integrated 3D Discrete Element and Lattice Boltzman Method Approach*. Paper presented at the SPE Western Regional Meeting, Garden Grove, California, USA, April 2015. <https://doi.org/10.2118/174046-MS>
- Mondejar, M.E. & Chamorro, C.R.** (2017). *Geothermal Power Technologies*. Encyclopedia of Sustainable Technologies, Editor(s): Martin A. Abraham, Elsevier, pp. 51-61, <https://doi.org/10.1016/B978-0-12-409548-9.10095-8>
- Montillet, A., Akkari, E. & Comiti, J.** (2007). *About a correlating equation for predicting pressure drops through packed beds of spheres in a large range of Reynoldss numbers*. Chemical Engineering and Processing: Process Intensification, 46(4):329-333, <https://doi.org/10.1016/j.cep.2006.07.002>
- Morcom, A.R.** (1946). *Fluid flow through granular materials*. Joint meeting of the Institution of Chemical Engineers with the Chemical Engineering Group, Apartments of the Geological Society, Burlington House, London, pp. 30-43
- Moya Rojas, P.** (2016). *23 - Central and South America: Significant but constrained potential for geothermal power generation*. Geothermal Power Generation, Woodhead Publishing, Editor(s): Ronald DiPippo, pp. 667-715, <https://doi.org/10.1016/B978-0-08-100337-4>
- Muskat, M. & Botset, H.G.** (1931). *Flow of Gas Through Porous Materials*. Physics, 1(1):27–47, <https://doi.org/10.1063/1.1744983>
- Muther, T., Khan, M.J., Chachar, M.H. & Aziz, H.** (2020). *A Study on designing appropriate hydraulic fracturing treatment with proper material selection and optimized fracture half-length in tight multilayered formation sequence*. SN Appl. Sci. 2:886, <https://doi.org/10.1007/s42452-020-2729-9>
- Nordgren, R.P.** (1972). *Propagation of a Vertical Hydraulic Fracture*. SPE Journal, 12(04):306–314, <https://doi.org/10.2118/3009-PA>

- Oikawa, Y., Tenma, N., Tsutomu, Y., Karasawa, H., Egawa, Y. & Yamauchi, T.** (2021). *Heat Extraction Experiment at Hijiori Test Site*. Proceedings, Twenty-Sixth Workshop on Geothermal Reservoir Engineering, Stanford University, Stanford, California, January 29-31, 2001, SGP-TR-168, Access: https://www.researchgate.net/publication/265269408_HEAT_EXTRACTION_EXPERIMENT_AT_HIJIORI_TEST_SITE
- Olasolo, P., Juarez, M.C., Morales, M.P., D'Amico, S. & Liarte, I.A.** (2016). *Enhanced geothermal systems (EGS): A review*. Renewable and Sustainable Energy Reviews, pp. 133-144, <https://doi.org/10.1016/j.rser.2015.11.031>
- Orzol, J., Jatho, R., Jung, R., Kehrer, P. & Tischner, T.** (2004). *The GeneSys project - Development of concepts for the extraction of heat from tight sedimentary rocks*. Zeitschrift für Angewandte Geologie. 50:17-23.
- Orzol, J., Jung, R., Jatho, R., Tischner, T. & Kehrer, P.** (2005): *The GeneSys-Project: Extraction of geothermal heat from tight sandstones*. Proceedings World Geothermal Congress, Antalya, Turkey, 24-29. April 2005.
- Owusu, P.A. & Asumadu-Sarkodie, S.** (2016). *A review of renewable energy sources, sustainability issues and climate change mitigation*. Cogent Engineering, 3(1), <https://doi.org/10.1080/23311916.2016.1167990>
- Pálsson, B., Holmgeirsson, S., Gudmundsson, A., Boasson, H.A., Ingasson, K., Sverisson, H. & Thorhallsson, S.** (2014). *Drilling of the well IDPP-1*. Geothermics, 49:23-30, <https://doi.org/10.1016/j.geothermics.2013.08.010>
- Panwar, N.L., Kaushik, S.C. & Kothari, S.** (2011). *Role of renewable energy sources in environmental protection: A review*. Renewable and Sustainable Energy Reviews, 15(3):1513-1524, <https://doi.org/10.1016/j.rser.2010.11.037>
- Patel, P.S., Robart, C.J., Ruegamer, M. & Yang, A.** (2014). *Analysis of US Hydraulic Fracturing Fluid System and Proppant Trends*. Paper presented at the SPE Hydraulic Fracturing Technology Conference, The Woodlands, Texas, USA, February 2014, <https://doi.org/10.2118/168645-MS>
- Pedlosky, J.** (1987). *Geophysical fluid dynamics*. Springer. pp. 10-13- ISBN [978-0-387-96387-7](https://doi.org/10.1007/978-0-387-96387-7)
- Penny G.S.** (1987). *An Evaluation of the Effects of Environmental Conditions and Fracturing Fluids Upon the Long-Term Conductivity of Proppants*. Paper presented at the SPE Annual Technical Conference and Exhibition, Dallas, Texas, September 1987, <https://doi.org/10.2118/16900-MS>
- Perkins, T.K. & Kern, L.R.** (1961). *Widths of Hydraulic Fractures*. Journal of Petroleum Technology, 13(09):937-949, <https://doi.org/10.2118/89-PA>
- Peter-Borie, M., Loschetter, A., Blaisonneau, A., Tran, V.H., Gaucher, E., Sigurdsson, O., Fridleifsson, G.O., Damy, P.C., Lous, M.L. & Tulinius, H.** (2019). *Thermal stimulation of the deep geothermal wells: insights from the H2020- DEEPEGS project*. European Geothermal Congress 2019, Den Haag, The Netherlands, 11-14 June 2019, Access: https://www.researchgate.net/publication/351123925_Thermal_stimulation_of_the_deep_geothermal_wells_insights_from_the_H2020-DEEPEGS_project
- Phair, K.** (2016). *Direct steam geothermal energy conversion system*. Editor(s): Ronald DiPippo, Geothermal Power Generation, Woodhead Publishing, pp. 291-319, <https://doi.org/10.1016/B978-0-08-100337-4.00011-5>
- Portier, S., Vuataz, F.D., Nami, P., Sanjuan, B. & Gérard, A.** (2009). *Chemical stimulation techniques for geothermal wells: experiments on the three-well EGS system at Soultz-sous-Forêts, France*. Geothermics, 38(4):349-359, <https://doi.org/10.1016/j.geothermics.2009.07.001>
- Rapp, B.E.** (2023). *Chapter 32 - Finite element method*. Editor(s): Bastian E. Rapp, In Micro and Nano Technologies, Microfluidics (Second Edition), Elsevier, pp. 701-725, <https://doi.org/10.1016/B978-0-12-824022-9.00052-8>.
- Ray, W.T. & Kreisinger, H.** (1911). *Significance of Drafts in Steam-Boiler Practice*. Department of the Interior, Bureau of Mines, Bulletin 21 (Reprint of United States Geological Survey Bulletin 367)

REN (2021). *Renewables 2021 Global Status Report*. (Paris: REN21 Secretariat), ISBN: [978-3-948393-03-8](https://doi.org/10.1016/S0376-7361(08)70504-1)

Richard, S., Schrader, S., Schrader, R. & Ereaux, B. (2019). *Improved Methods of Measuring Proppant Conductivity*. Paper presented at the SPE Western Regional Meeting, San Jose, California, USA, April 2019., <https://doi.org/10.2118/195368-MS>

Ritchie, H. & Roser, M. (2020). *Energy*, Available at: <https://ourworldindata.org/energy>, Date of Access: 31.10.2021

Robertson, J.O. & Chilingarian, G.V. (1989). *Chapter 5 Acidizing Oilwells*. Developments in Petroleum Science, Editor(s): G.V. Chilingarian, J.O. Robertson, S. Kumar, Elsevier, 19(B), [https://doi.org/10.1016/S0376-7361\(08\)70504-1](https://doi.org/10.1016/S0376-7361(08)70504-1)

Rose, H.E. (1945a). *On the Resistance Coefficient–Reynolds Number Relationship for Fluid Flow through a Bed of Granular Material*. ARCHIVE: Proceedings of the Institution of Mechanical Engineers 1847-1982 (vols. 1-196), 153:154-168, https://doi.org/10.1243/PIME_PROC_1945_153_020_02

Rose, H.E. (1945b). *An Investigation into the Laws of Flow of Fluids through Beds of Granular Materials*. Proceedings of the Institution of Mechanical Engineers, 153(1):141–148, https://doi.org/10.1243/pime_proc_1945_153_01

Rose, H.E. & Rizk, A.M.A. (1949). *Further Researches in Fluid Flow through Beds of Granular Material*. ARCHIVE: Proceedings of the Institution of Mechanical Engineers 1847-1982 (vols. 1-196), 160:493-511, https://doi.org/10.1243/PIME_PROC_1949_160_047_02

Rose, P., Hickman, S., McCulloch, J., Davatzes, N., Moore, J., Kovac, K., Adams, M., Mella, M., Wannamaker, P., Julian, B., Foulger, G., Swenson, D., Gosavi, S., Bhat, A., Richards-Dinger, K., Monastero, F., Weidler, R., Baisch, S., Ghassemi, A. & Mégel, T. (2012): *Final Report: Creation of an Enhanced Geothermal System through Hydraulic and Thermal Stimulation*, DE-FC07-01ID14186, Energy and Geoscience Institute at the University of Utah, Access: https://www.researchgate.net/publication/262415657_Final_Report_Creation_of_an_Enhanced_Geothermal_System_through_Hydraulic_and_Thermal_Stimulation

Salah, M., Gabry, M. & El-Sabae, M. (2017). *Evaluation of Multistage Fracturing Stimulation Horizontal Well Completion Methods in Western Desert*. Egypt., <https://doi.org/10.2118/183785-MS>

Salameh, Z. (2014). *Chapter 5 – Emerging Renewable Energy Sources*. Editor(s): Ziyad Salameh, Renewable Energy System Design, Academic Press, pp. 299-371, <https://doi.org/10.1016/B978-0-12-374991-8.00005-2>

Santilano, A., Trumpy, E., Gola, G., Donato, A., Scrocca, D., Ferrarini, F., Brozzetti, F., de Nardis, R., Lavecchia, G. & Manzella, A. (2019). *A Methodology for Assessing the Favourability of Geopressured-Geothermal Systems in Sedimentary Basin Plays: A Case Study in Abruzzo (Italy)*. Geofluids, 2019:1-28, <https://doi.org/10.1155/2019/4503943>

Saunders, O.A. & Ford, H. (1940). *Heat transfer in the flow of gas through a bed of solid particles*. J. Iron Steel inst., 141:291-316

Schmidt, D., Russell, R.P.E., Brandon, W., Statoil, Terry, P. & Kullman, J. (2014). *Performance of Mixed Proppant Sizes*. Paper presented at the SPE Hydraulic Fracturing Technology Conference, The Woodlands, Texas, USA, February 2014., <https://doi.org/10.2118/168629-MS>

Schriever, W. (1930). *Law of Flow for the Passage of a Gas-free Liquid through a Spherical-grain Sand*. Transactions of the AIME, 86(01):329–336, <https://doi.org/10.2118/930329-g>

Scott, M.P., Johnson, R.L., Datey, A., Vandeborn, C. & Woodroof, R.A. (2010). *Evaluating Hydraulic Fracture Geometry from Sonic Anisotropy and Radioactive Tracer Logs*. Paper presented at the SPE Asia Pacific Oil and Gas Conference and Exhibition, Brisbane, Queensland, Australia, October 2010, <https://doi.org/10.2118/133059-MS>

Seth, P., Manchanda, R., Kumar, A. & Sharma, M. (2018). *Estimating Hydraulic Fracture Geometry by Analyzing the Pressure Interference Between Fractured Horizontal Wells*. Paper presented at the SPE Annual Technical Conference and Exhibition, Dallas, Texas, USA, September 2018, <https://doi.org/10.2118/191492-MS>

- Seth, P., Shrivastava, K., Kumar, A. & Sharma, M.** (2019). *Pressure Interference Between Fractured Horizontal Wells: Impact of Complex Fracture Growth on Offset Well Pressure Measurements*. Paper presented at the 53rd U.S. Rock Mechanics/Geomechanics Symposium, New York City, New York, June 2019, Paper Number: [ARMA-2019-1827](#)
- Sharma, V., Sircar, A. & Gupta, A.** (2018). *Hydraulic Fracturing Design and 3D Modeling: A Case Study from Cambay Shale and Eagleford Shale*. *Multiscale and Multidisciplinary Modeling, Experiment and Design*, 2:1-13, <https://doi.org/10.1007/s41939-018-0014-z>
- Shen, W.Z.** (2019). *Wind Turbine Aerodynamics*. MDPI – Applied Sciences, Editor(s): Wen Zhong Shen, Basel, Switzerland, <https://doi.org/10.3390/books978-3-03921-525-6>
- Smith, I.K.** (2016). *12 - Total flow and other systems involving two-phase expansion*. Editor(s): Ronald DiPippo, *Geothermal Power Generation*, Woodhead Publishing, pp. 321-351, <https://doi.org/10.1016/B978-0-08-100337-4.00012-7>
- Smith, M.B. & Hannah, R.R.** (1996). *High-Permeability Fracturing: The Evolution of a Technology*. *Journal of Petroleum Technology*, 48(7):628-633, <https://doi.org/10.2118/27984-JPT>
- Soelaiman, T.A.F.** (2016). *7 – Geothermal Energy*. Editor(s): Muhammad H. Rashid, *Electric Renewable Energy Systems*, Academic Press, pp. 114-139, <https://doi.org/10.1016/B978-0-12-804448-3.00007-4>
- Speight, J.G.** (2016). *Handbook of hydraulic fracturing*. Published by John Wiley & Sons, Inc., Hoboken, New Jersey, ISBN 10: [1119225108](#)
- Steinour, H.H.** (1944). *Rate of sedimentation. Nonflocculated suspensions of uniform spheres*. *Industrial and Engineering Chemistry*, 36(7):618-624, <https://doi.org/10.1021/ie50415a005>
- Stopa, J., Wojnarowski, P. & Janiga, D.** (2014). *Integrated model of hydraulic fracturing and hydrocarbon production*, *AGH Drilling Oil Gas*, 31(1):49-57, <https://doi.org/10.7494/drill.2014.31.1.49>
- Sutera, S.P. & Skalak, R.** (1993). *The History of Poiseuille's Law*. *Annual Review of Fluid Mechanics*, 25:1-19, <https://doi.org/10.1146/annurev.fl.25.010193.000245>
- Szabó, N.P. & Dobróka, M.** (2017). *Exploratory Factor Analysis of Wireline Logs Using a Float-Encoded Genetic Algorithm*. *Mathematical Geosciences*, 50(3), 317–335. <https://doi.org/10.1007/s11004-017-9714-x>
- Tallmadge, J.A.** (1970). *Packed bed pressure drop – an extension to higher Reynolds numbers*. *AIChE Journal*, 16:1092-1093, <https://doi.org/10.1002/aic.690160639>
- Teng, B., Huazhou, L. & Yu, H.** (2020). *A Novel Analytical Fracture-Permeability Model Dependent on Both Fracture Width and Proppant-Pack Properties*. *SPE Journal*, 25(06):3031-3050, <https://doi.org/10.2118/201093-PA>
- Thain, I.A. & Carey, B.** (2009). *Fifty years of geothermal power generation at Wairakei*. *Geothermics*, 38(1):48-63, <https://doi.org/10.1016/j.geothermics.2008.12.004>
- Thomas, R.L. & Morgenthaler, L.N.** (2000). *13 – Introduction to Matrix Treatments*. *Reservoir Stimulation*, Third Edition, Editor(s): Micheal J. Economides and Kenneth G. Nolte, Publisher: Chichester, England; New York: Wiley, Access: https://www.google.com/url?sa=t&rct=j&q=&esrc=s&source=web&cd=&cad=rja&uact=8&ved=2ahUKewi88u3-r30AhVr-yoKHeEqDkQQFnoECAMQAQ&url=https%3A%2F%2Fwww.researchgate.net%2Ffile/PostFileLoader.html%3Ffid%3D591b038148954c7bac0eeb2d%26assetKey%3DAS%253A494639238529025%25401494942593011&usq=AOvVaw0bK7EI2Sv0ye9s4E_T15dx
- Tischner, T., Evers, H., Hauswirth, H.K., Jatho, R., Kosinowski, M. & Sulzbacher, H.** (2010). *New Concepts for Extracting Geothermal Energy from One Well: The GeneSys-Project*. *Proceedings World Geothermal Congress 2010, Bali, Indonesia, 25-29 April 2010*, Access: <https://www.geothermal-energy.org/pdf/IGAstandard/WGC/2010/2272.pdf>
- Tu, J., Yeon, G., & Liu C.** (2018). *Chapter 4 - CFD Mesh Generation: A Practical Guideline*. *Computational Fluid Dynamics (Third Edition)*, Editor(s): Jiyuan Tu, Guan-Heng Yeoh, Chaoqun Liu, Pages 125-154, <https://doi.org/10.1016/B978-0-08-101127-0.00004-0>

- Uchida, S. & Fujita, S.** (1934). *Pressure drop through dry packed column*. Journal of the Society of Chemical Industry, Japan, Supplemental Binding, 37(11):724B-733B, https://doi.org/10.1246/nikkashi1898.37.Supplement_704B
- Venkataraman, P.** (2009). *Applied Optimization With MATLAB Programming*. John Wiley & Sons, New York, NY.
- Wang, Y., Cui, Y., & Yang, C.** (2011). *Hybrid regularization methods for seismic reflectivity inversion*. Int J Geomath 2, 87–112. <https://doi.org/10.1007/s13137-011-0014-1>
- Warpinski, R.N., Sullivan, R.B., Uhl, J.E., Waltman, C.K. & Machovoie, S.R.** (2005). *Improved microseismic fracture mapping using perforation timing measurements for velocity calibration*. SPE Journal, 10(01):14–23. <https://doi.org/10.2118/84488-PA>
- Watanabe, H.** (1989). *Drag Coefficient and voidage function on fluid flow through granular packed beds*. Int. J. Eng. Fluid Mech., 2:93-108
- Weijers, L. & de Pater, H.** (2019). *Chapter 4 – Hydraulic Fracture Modeling*. Hydraulic Fracturing Fundamentals and Advancements, Editor in chief: Jennifer L. Miskimins, Society of Petroleum Engineers, Richardson, Texas, USA, pp. 75-142, <https://doi.org/10.2118/9781613997192-04>
- Wentz, C.A. & Thodos, G.** (1963). *Pressure drops in the flow of gases through packed and distended beds of spherical particles*. AIChE Journal, 9(1):81–84, <https://doi.org/10.1002/aic.690090118>
- White, D.E., Muffler, L.J.P. & Truesdell, A.H.** (1971). *Vapor-dominated hydrothermal systems compared with hot-water systems*. Economic Geology, 66(1):75-97, <https://doi.org/10.2113/gsecongeo.66.1.75>
- Wright, C.A., Davis, E.J., Golich, G.M., Ward, J.F., Demetrius, S.L., Minner, W.A. & Weijers, L.** (1998). *Downhole Tiltmeter Fracture Mapping: Finally Measuring Hydraulic Fracture Dimensions*. Paper presented at the SPE Western Regional Meeting, Bakersfield, California, May 1998, <https://doi.org/10.2118/46194-MS>
- Wu, H., Gao, S., Wang, R., & Ding, M.** (2017). *A global approach to multi-axis swept mesh generation*. Procedia Engineering, 203, 414–426. <https://doi.org/10.1016/j.proeng.2017.09.817>
- Zaman, E. & Jalali, P.** (2010). *On hydraulic permeability of random packs of monodisperse spheres: Direct flow simulations versus correlations*. Physica A: Statistical Mechanics and Its Applications, 389(2):205-214, <https://doi.org/10.1016/j.physa.2009.09.030>
- Zarrouk, S.J. & Moon, H.** (2014). *Efficiency of geothermal power plants: A worldwide review*. Geothermics, 51:142-153, <https://doi.org/10.1016/j.geothermics.2013.11.001>

12 THE AUTHOR'S MAIN SCIENTIFIC PUBLICATIONS

12.1 Publications

Jobbik, A., Lengyel, T. & Pusztai, P. (2015). *Összetett matematikai modell hidraulikus rétegrepszítés optimalizálására*. Műszaki Földtudományi Közlemények, University of Miskolc, Miskolc, 85(1):97-105, ISSN [2063-5508](#)

Pusztai, P. & Lengyel, T. (2015). *A hidraulikus rétegrepszítés gazdasági optimalizációja*. Diáktudomány: A Miskolci Egyetem Tudományos Diákköri Munkáiból, University of Miskolc, Miskolc, 8:38-43, ISSN [2062-0721](#)

Lengyel, T., Pusztai, P. & Jobbik, A. (2016). *An Innovative Method for Hydraulic Fracturing Optimization*. Proceedings of the 4th International Scientific Conference on Advances in Mechanical Engineering (ISCAME 2016), University of Debrecen Faculty of Engineering, Debrecen, pp. 302-307, ISBN [978-963-473-944-9](#)

Pusztai, P. & Jobbik, A. (2017). *Micro- És Nanométerű Pórusterekben Történő Gázáramlás Vizsgálata*. Műszaki Tudomány Az Észak-Kelet Magyarországi Régióban, Elektronikus Műszaki füzetek, Debreceni Akadémiai Bizottság Műszaki Szakbizottsága, Nyíregyháza, pp. 435-442, ISBN [978-963-706-435-7](#)

Pusztai, P. & Jobbik, A. (2017). *Rendkívül kis pórusterekben történő gázáramlások vizsgálata*. Műszaki Földtudományi Közlemények, University of Miskolc, Miskolc, Volume 86(2):131-140, ISSN [2063-5508](#)

Pusztai, P. (2017). *Palagázban történő áramlások áttekintése és alkalmazása egy magyarországi ultra magas nyomású és hőmérsékletű (UHPHT) tároló magmintáin keresztül*. Diáktudomány: A Miskolci Egyetem Tudományos Diákköri Munkáiból, University of Miskolc, Miskolc, 10:31-38, ISSN [2062-0721](#)

Pusztai, P. & Jobbik, A. (2018). *A New, Extended Material Balance Equation for Investigation of Different Gas Flow Models*. Tavasz Szél 2018 Konferencia = Spring Wind 2018: Konferenciakötet I., Association of Hungarian PHD and DLA Students, Budapest, 1:359-368, <https://doi.org/10.23715/TSZ.2018.1>

Pusztai, P. & Jobbik, A. (2019). *Modeling Natural Gas Flow Behaviors in Unconventional, UHPHT Reservoirs with Nanoporous Media*. 13th International Conference on Heat Engines and Environmental Protection Proceedings, BME Department of Energy Engineering, Budapest, pp. 125-131, ISBN 978-963-420-907-2

Pusztai, P. & Koroncz, P. (2021). *Modified Approach for Proppant Conductivity Measurement*. Geosciences and Engineering, Miskolc University Press., Miskolc, 9(14):43–59, ISSN [2063-6997](#)

Pusztai, P. & Jobbik, A. (2021). *Investigation of gas flow models in case of micro and nano pore size reservoirs*. Geosciences and Engineering, Miskolc University Press., Miskolc, 9(14):96–115, ISSN [2063-6997](#)

Pusztai, P. (2022): *A New Method for Determining Propped Fracture Permeability*. Abstract Book of the International Congress on Geomathematics in Earth- & Environmental Sciences, and the 22nd Hungarian Geomathematical Congress, Publisher: Pécs Regional Committee of the Hungarian Academy of Sciences, ISBN: [978-963-7068-14-0](#)

Pusztai, P., Koroncz, P., Kuncz, M., Jobbik, A. & Fedor, F. (2023). *Semi-analytical approach to the determination of fracture permeability*. Int J Geomath **14**, 16. <https://doi.org/10.1007/s13137-023-00227-8>

12.2 Conferences

Pusztai, P., Lengyel T. & Jobbik, A. (2015). *Hidraulikus rétegrepesztés optimalizálása*. ENERGOExpo Nemzetközi Energetikai Szakkiállítás és Konferencia, Debrecen

Pusztai, P. & Jobbik, A. (2017). *Micro- És Nanoméretű Pórusterekben Történő Gázáramlás Vizsgálata*. Műszaki Tudomány az Észak-kelet Magyarországi Régióban, Nyíregyháza

Pusztai, P. & Jobbik, A. (2017). *Modeling Natural Gas Flow Behaviors in Unconventional, UHPHT Reservoirs with Nanoporous Media*. 13th International Heat Engines and Environment Protection Conference, Budapest

Pusztai, P. & Jobbik, A. (2017). *Investigation of gas flow models in case of micro and nano pore size reservoirs*. PULSE - Új kutatási irányok a földi energiaforrások hasznosításához kapcsolódóan” című szakmai tudományos konferencia, Miskolc

Pusztai, P. & Jobbik, A. (2017). *Investigation of Gas Flow Models in case of Tight Reservoirs*. XXXI. Nemzetközi Olaj- és Gázipari Konferencia, Siófok

Pusztai, P. & Jobbik, A. (2018). *A New, Extended Material Balance Equation for Investigation of Different Gas Flow Models*. Tavaszi Szél 2018 Nemzetközi Multidiszciplináris Konferencia, Győr

Pusztai, P. (2022). *A New Method for Determining Propped Fracture Permeability*. International Congress on Geomathematics in Earth- & Environmental Sciences, and the 22nd Hungarian Geomathematical Congress, Pécs

Pusztai, P. (2022). *Laboratory developments supporting thermal water reinjection technologies 2. Proppant qualification, fracture conductivity measurements*. GINOP-2.2.1-15-2017-00102 "Development of a well completion technology for sustainable and cost-effective reinjection of thermal water", Closing Conference, Pécs

13 ANNEXES

13.1 Appendix A



Figure 13-1: Aerial view of Stillwater combined power plant ([DiPippo, 2016c](#))

13.2 Appendix B

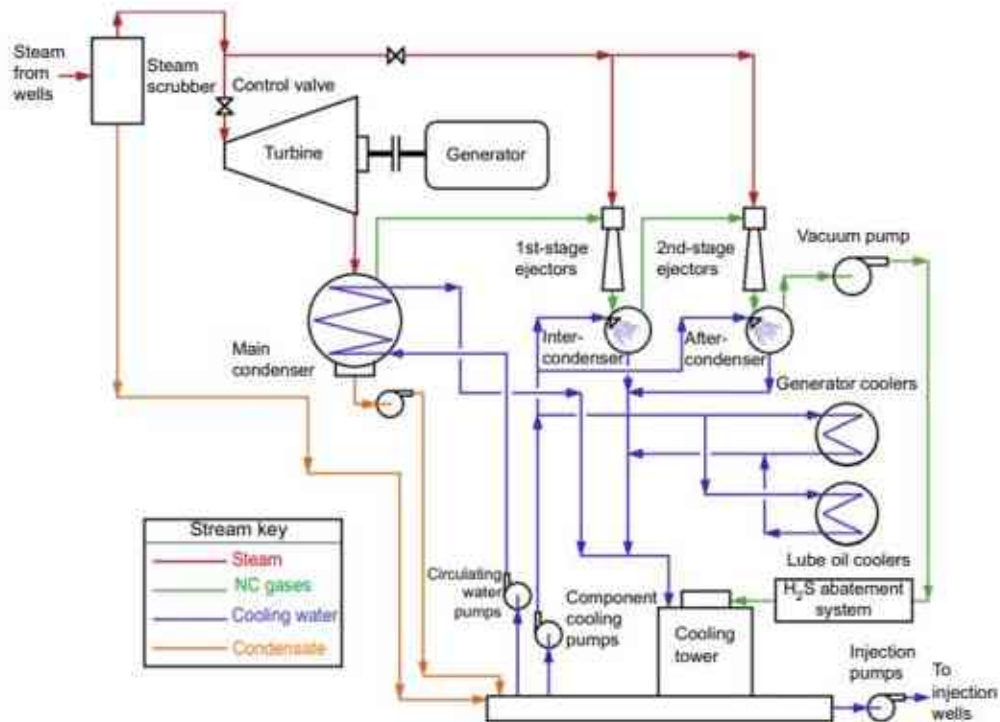


Figure 13-2: Direct steam schematic example, with surface condenser (Phair, 2016)

13.3 Appendix C

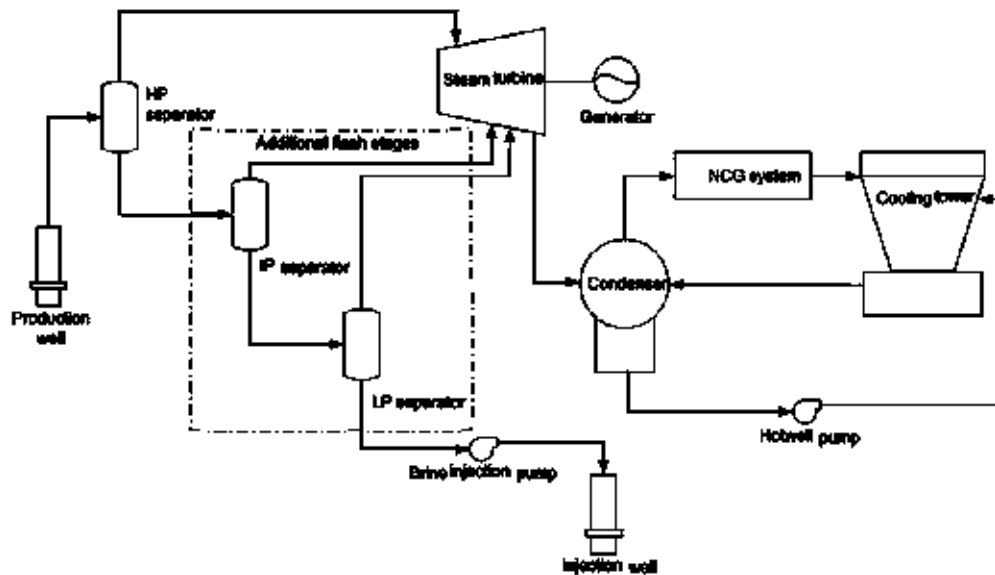


Figure 13-3: Flash plant schematic example, showing potential for second and third flash stages (Harvey and Wallace, 2016)

13.4 Appendix D

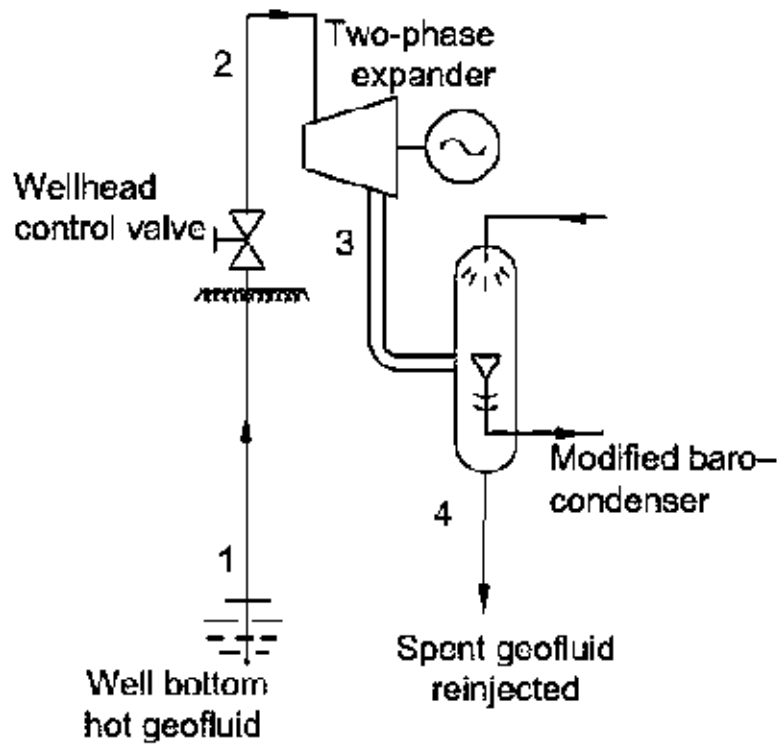


Figure 13-4: Total flow schematic example ([Smith, 2016](#))

13.5 Appendix E

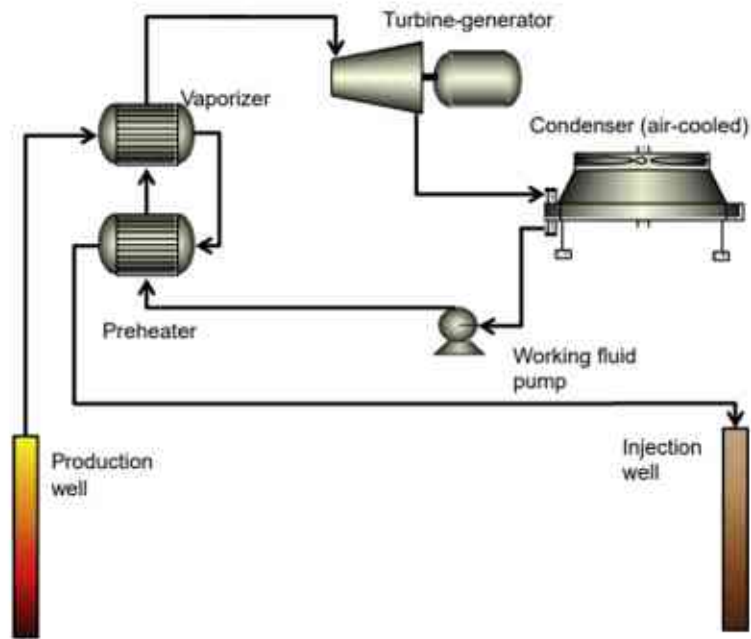


Figure 13-5: Basic binary cycle schematic example with air-cooled condenser ([Mines, 2016](#))

13.6 Appendix F

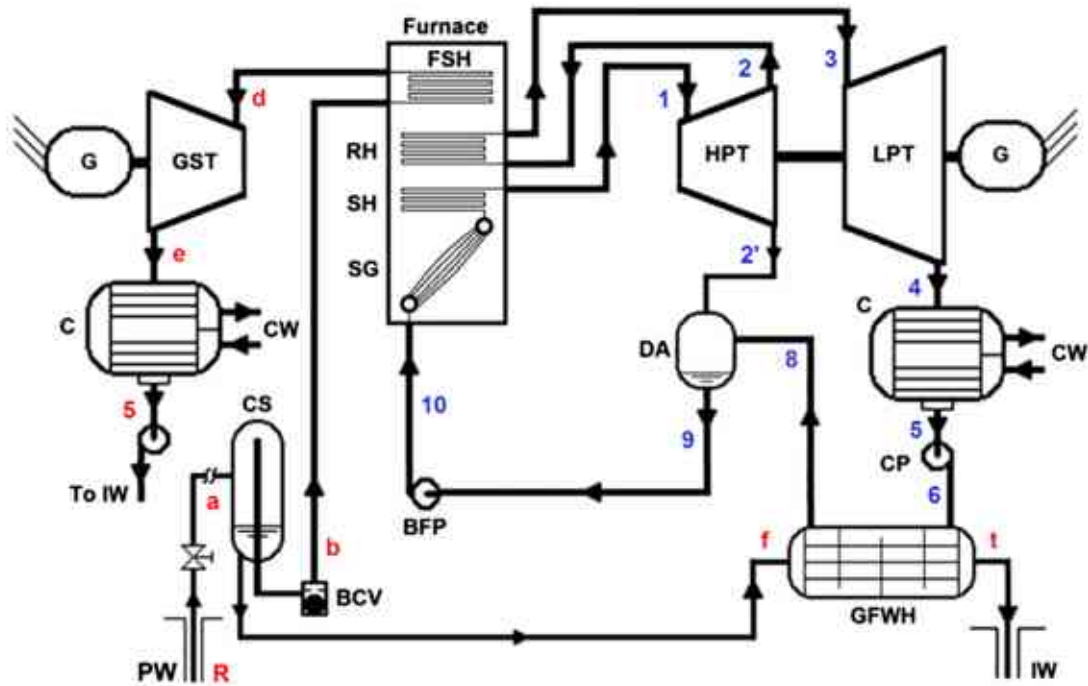


Figure 13-6: Compound fossil-geothermal hybrid schematic example (DiPippo, 2016b)

13.7 Appendix G

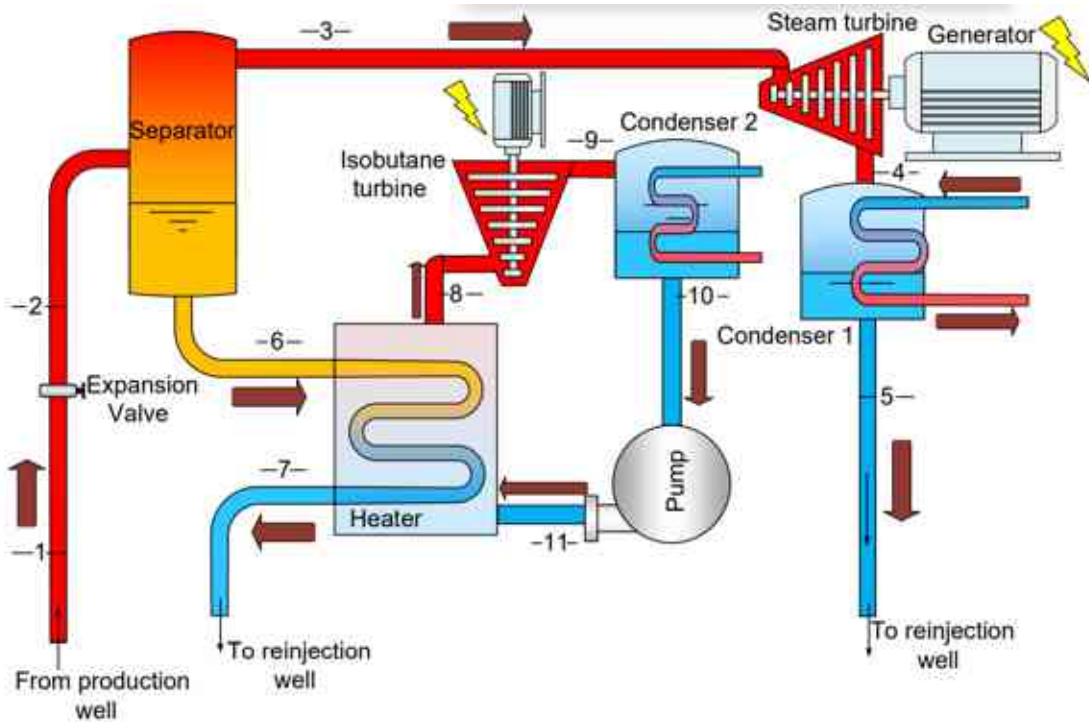


Figure 13-7: Hybrid (single flash – binary) geothermal power plant schematic example (Dincer and Ezzat, 2018)

13.8 Appendix H

Table 13-1: Chemical analysis of waters associated with vapor-dominated and liquid-dominated geothermal systems (2/1)

Name	1/ The Geysers	2/ The Geysers	3/ GS-7	4/ Spring 8	5/ Mud Volcano	6/ Mud Volcano	7/ Y-11 Mud Volcano
Location	Calif.	Calif.	Steamboat, Nev.	Steamboat, Nev.	Yellowstone, Wyo.	Yellowstone, Wyo.	Yellowstone, Wyo.
Water type	HCO ₃ -SO ₄	Acid-sulfate	HCO ₃ -SO ₄	Cl-HCO ₃	Acid-sulfate	HCO ₃ -SO ₄	HCO ₃ -SO ₄
System type	Vapor-dom.	Vapor-dom.	Vapor-dom.	Hot water	Vapor-dom.	Vapor-dom.	Vapor-dom.
SiO ₂	66	225	14	293	540	215	
Al		14		0.5	146		
Fe		63		0.05	17		
Mn		1.4		0.05			
As				2.7			
Ca	58	47	6.3	5.0	14	28.7	28
Mg	108	281	0	0.8	11	16.4	0.5
Na	18	12	9.3	653	16	74.3	105
K	6	5	4.5	71	17	47.5	12.6
Li			0	7.6		0.2	0.18
NH ₄	111	1 400		<1	26	0.2	3.2
H		9.5			43		
HCO ₃	176	0	21	305		298	258
CO ₃	--	--	--	--	--	--	
SO ₄	766	5 710	24	100	3 149	65.3	74
Cl	1.5	0.5	0.5	865	Tr.	13.5	9.6
Fe			0	1.8	1	2.0	
Br				0.2			
NO ₃			Tr.	--			0.2
B	15	3.1	1.3	49		0.6	0.1
H ₂ S	0	--	2.4	4.7	0		
Total reported	1330	7 770	83	2 360	3 980	761.7	491.4
pH	neutral	1.8±	6.5	7.9	Strong acid	7	8.5(?)
Temperature, °C	100	Boiling?	161	89.2	65	58.5	131.7

([White et al., 1971](#))

13.9 Appendix I

Table 13-2: Chemical analysis of waters associated with vapor-dominated and liquid-dominated geothermal systems (2/2)

	8/	9/	10/	11/	12/	13/
Name	Norris Basin	Norris Basin	Well 4	Well 5	Carboli A,	Mud Volcano
Location	Yellowstone, Wyo.	Yellowstone, Wyo.	Wairakei, N.Z.	Wairakei, N.Z.	Italy	Matsukawa, Japan
Water type	Cl (HCO ₃)	Acid-sulfate	Cl	HCO ₃ -SO ₄	SO ₄ HCO ₃ (Cl)	SO ₄ (HCO ₃)
System type	Hot water	Hot water	Hot water	Vapor-dom. (?)	Hot water	Vapor-dom. (?)
SiO ₂	529	109	386	191		635
Al		2.4			Trace	29
Fe		0.8			Trace	508
Mn						
As	3.1					
Ca	5.8	2.2	26	12		
Mg	0.2	0	<0.1	1.7	5.0	8.7
Na	439	2	1 130	230	56.6	264
K	74	3	146	17	32	144
Li	8.4		12	1.2		
NH ₄	0.1	30	0.9	0.2	19	
H		14				
HCO ₃	27	--	35	670	89.7	37
CO ₃	--	--	0(?)			
SO ₄	38	758	35	11	137.4	1 780
Cl	744	15	1 930	2.7	42.6	0.12
Fe	4.9		6.2	3.7		
Br	0.1					
NO ₃	--					
B	12	6.9	26	0.5	13.9	61.2
H ₂ S	0		1.1	0		Trace
Total reported	1 890	943	3 750	1 140	396.2	3 478.9
pH	7.5	1.97	8.6	6.7		4.9
Temperature, °C	84.5	90	228±	High	~300	~240

(White et al., 1971)

13.10 Appendix J

Table 13-3: Status of global Enhanced Geothermal Systems

Site name	Development period	Country	Reservoir lithology	Development attribution	Important feature
Fenton Hill	1974 - 1995	United States	Granite	Greenfield	The world's first EGS site, and there were 60 kW binary power system demonstrations.
Rosemanowes	1977 - 1991	United Kingdom	Granite	Greenfield	Laid the foundation of EGS development for the followed Eden and Redruth in the United Kingdom.
Hijiori	1981 - 1986	Japan	Granodiorite	Greenfield	Japan's first EGS site, and there were 130 kW binary power system demonstrations
Fjallbacka	1984 - 1989	Sweden	Granite	Greenfield	500 m deep shallow EGS site, applicable as a heat pump greenhouse.
Ogachi	1989 - 2001	Japan	Granodiorite	Greenfield	Combined with CO ₂ sequestration and CO ₂ -EGS test.
Basel	2005 - 2006	Switzerland	Granite	Greenfield	Tests were suspended due to earthquake, and the EGS relevant specifications were introduced.
Insheim	2008 - present	Germany	Granite	Greenfield	Power plant of 4 MWe is constructed in commercial grade.
Landau	2004 - present	Germany	Granite	Greenfield	2.9 MWe/3 MWt power plant, in commercial grade, and in conjunction with greenhouse.
Groß Schönebeck	2007 - present	Germany	Sandstone / conglomerate	Greenfield	Hydraulic fracturing process is in progress, and three units of a total installed capacity of 1 MWe operated in binary power generation cycles have been built in the site
Soultz	1987 - present	France	Granite	Greenfield	The first commercial-scale EGS power plant in France with installed capacity of 1.5 MWe.
KiGam at Pohang	2010 - present	South Korea	Granodiorite	Greenfield	1.5 MWe-targeted demonstration plant, site test in progress
Habanero	2003 - present	Australia	Granite	Greenfield	1 MWe demonstration plant is in operation, targeting for 40 MWe in the first phase, and the overall objective is 450 MWe.
Paralana	2005 - present	Australia	Sedimentary / metamorphic	Greenfield	Targeting for 3.75 MWe power plant, and fluid cycle test in progress
Newberry	2009 - present	United States	Marl, quartz porphyry, granite	Greenfield	1. Hydraulic fracture and fluid circulation had been completed in 2013. 2. Use of the thermo-degradable zonal isolation materials (TZIM) to shorten the hydraulic fracturing process
The Geysers	2009 - present	United States	Metasandstone	Near field	1. 5 MW demonstration plant in progress. 2. Urban wastewater reinjection to the reservoir to increase capacity. 3. Use the method of cold crack to create fractures in the surrounding of wells
Raft River	2009 - present	United States	Granite	Near field	1. 5 MWe EGS demonstrated plants are targeted by 2020, and the flow rate is at least 20 kg/s per well. 2. The method of cold crack is used to create fractures in the surrounding of wells.
Brandys Hot Spring	2008 - present	United States	Rhyolite, metamorphic substrate	In field	Use of the existing geothermal wells to increase capacity, and the establishment of 2–3 MWe EGS power plant in commercial-scale is targeted.
Desert Peak	2002 - present	United States	Metamorphic tuff	In field	1. The establishment of a 1.7 MWe power plant in commercial-scale was scheduled at end of 2013. 2. Mix the cold cracking, shear, chemical and other hydraulic fracturing technologies.

(Lu, 2018)

13.11 Appendix K

Table 13-4: Results of chemical treatment in selected geothermal fields

Geothermal field	Chemical agent used	Number of treated wells	Injectivity index before and after the chemical treatment ($\text{kg s}^{-1} \text{bar}^{-1}$)
Bacman, Philippines	HCl-HF	2	0.68 - 3.01 0.99 - 1.40
Leyte, Philippines	HCl-HF	3	3.01 - 5.84 0.68 - 1.77 1.52 - 10.80
Tiwi, Philippines	HCl-HF	1	2.52 - 11.34
Mindanao, Philippines	HCl-HF	1	Successful
Salak, Indonesia	HCl-HF	1	4.70 - 12.10
Berlin, El Salvador	HCl-HF	5	1.60 - 7.60 1.40 - 8.60 0.20 - 1.98 0.90 - 3.40 1.65 - 4.67
Las Tres Virgenes, Mexico	HCl-HF	2	0.8 - 2.0 1.2 - 3.7
Los Azufres, Mexico	HCl-HF	1	3.3 - 9.1
Beowawe, USA	HCl-HF	1	Successful
The Geysers, USA	HCl-HF	1	No effect
Coso, USA	HCL and NTA	30	24 wells successful
Larderello, Italy	HCl-HF	5	11 - 54 4 - 25 1.5 - 18 Successful 11 - 54
Fenton Hill, USA	Na_2CO_3	1	About 1000 kg of quartz were dissolved and removed from the reservoir but no impedance reduction resulted.
Fjallbacka, Sweden	HCl-HF	1	Efficiency of acid injection in returning rock particles (Portier et al., 2009)

13.12 Appendix L

Table 13-5: Different multistage fracturing projects in deviated or horizontal wells

Country	Project (Development period)	Well name	Depth, m	Temperature, °C	Well type	Completion method
Australia	Paralana (2005–present)	Paralana-2	4,003	180 – 200	deviated	perforated casing
Germany	Groß Schönebeck (2007–present)	GrSk-4	4,400	> 150	deviated	zonal isolation materials
USA	Newberry (2009–present)	NWG 55-29	3,067	331	nearly horizontal	zonal isolation
China	Qiabuqia (2007–present)	GR-1	3,600	> 180	horizontal	perforated casing

([Han et al., 2019](#))

13.13 Appendix M

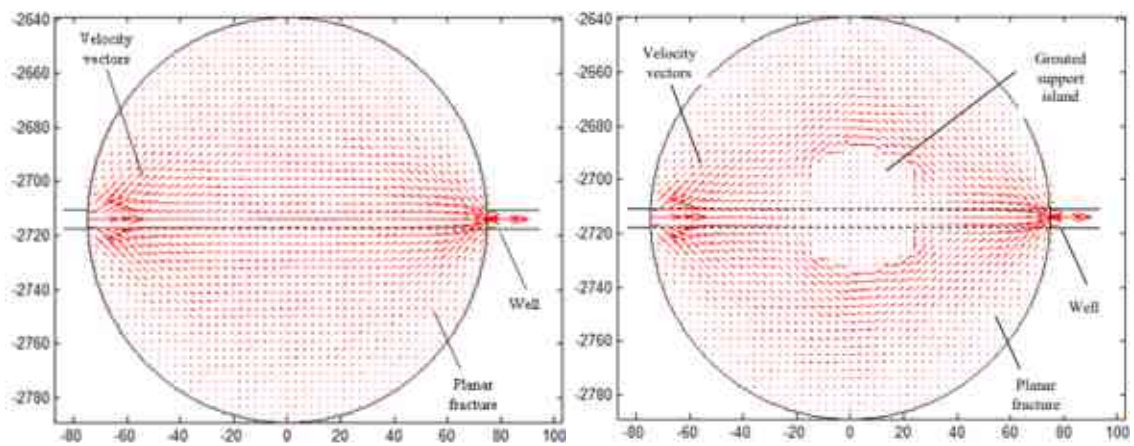


Figure 13-8: Flow profiles in a single-well EGS model with and without a flow control mechanism ([Danko et al., 2018](#))

13.14 Appendix N

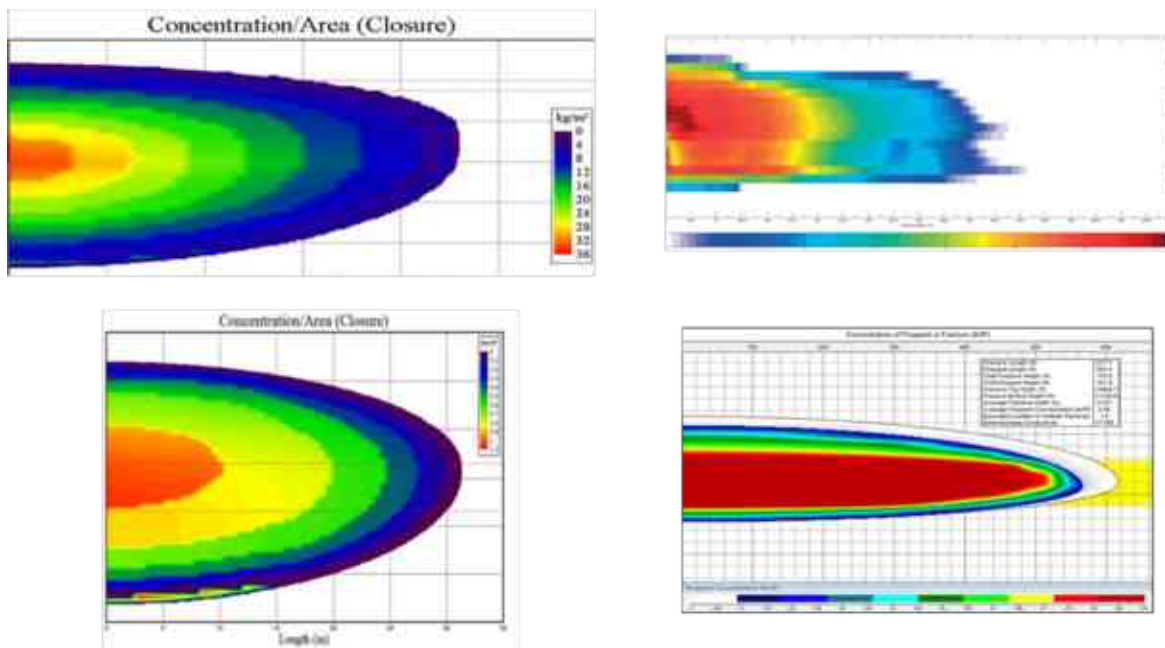


Figure 13-9: Different zones of proppant concentrations in the fractures based on studies (upper left by [Gui et al. \(2013\)](#), upper right by [Stopa et al. \(2014\)](#), bottom left by [Sharma et al. \(2018\)](#), bottom right by [Muther et al. \(2020\)](#))

13.15 Appendix O

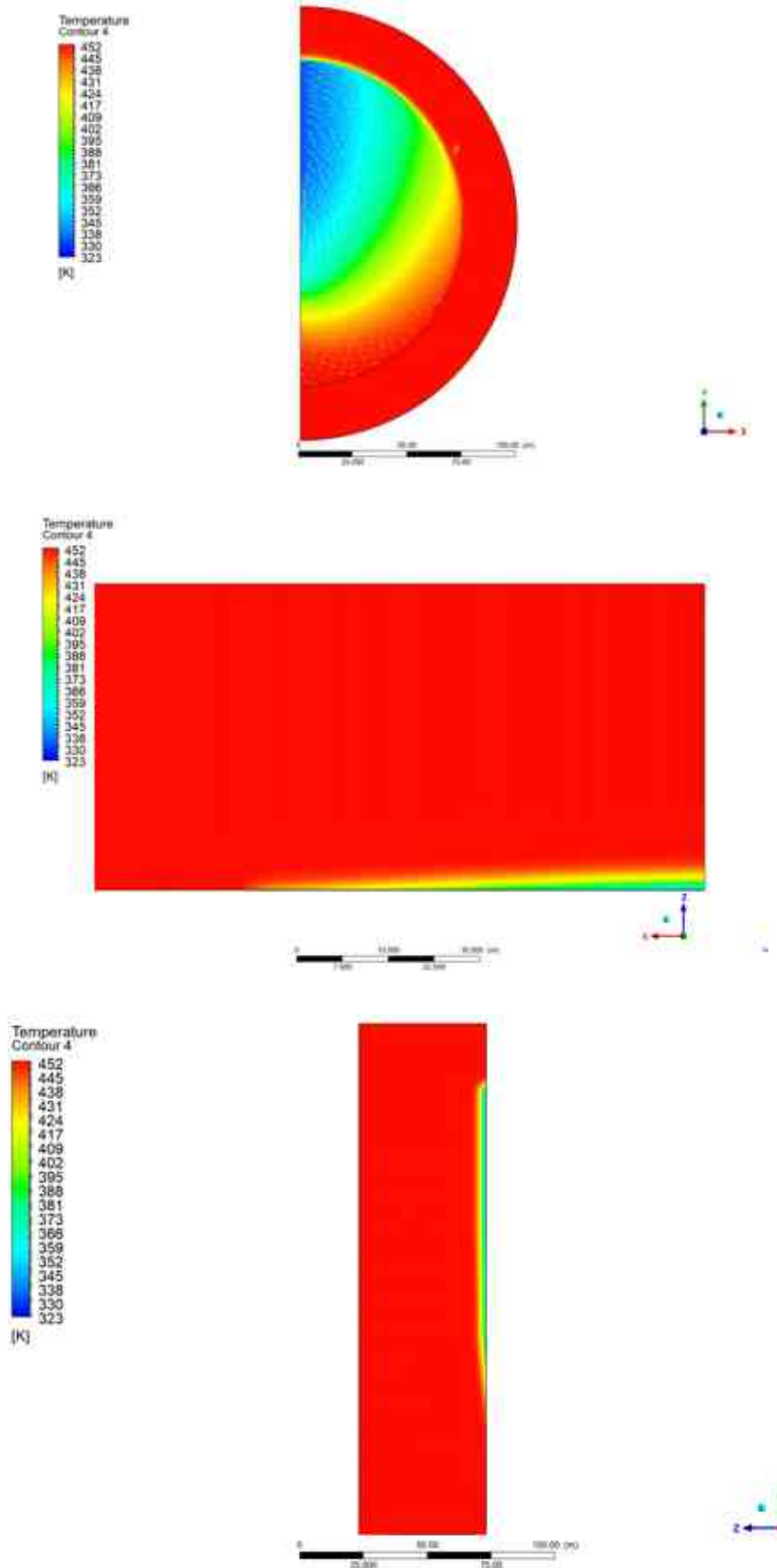


Figure 13-10: Heat profile after the simulation in the X-Y, X-Z, and Y-Z axis

13.16 Appendix P

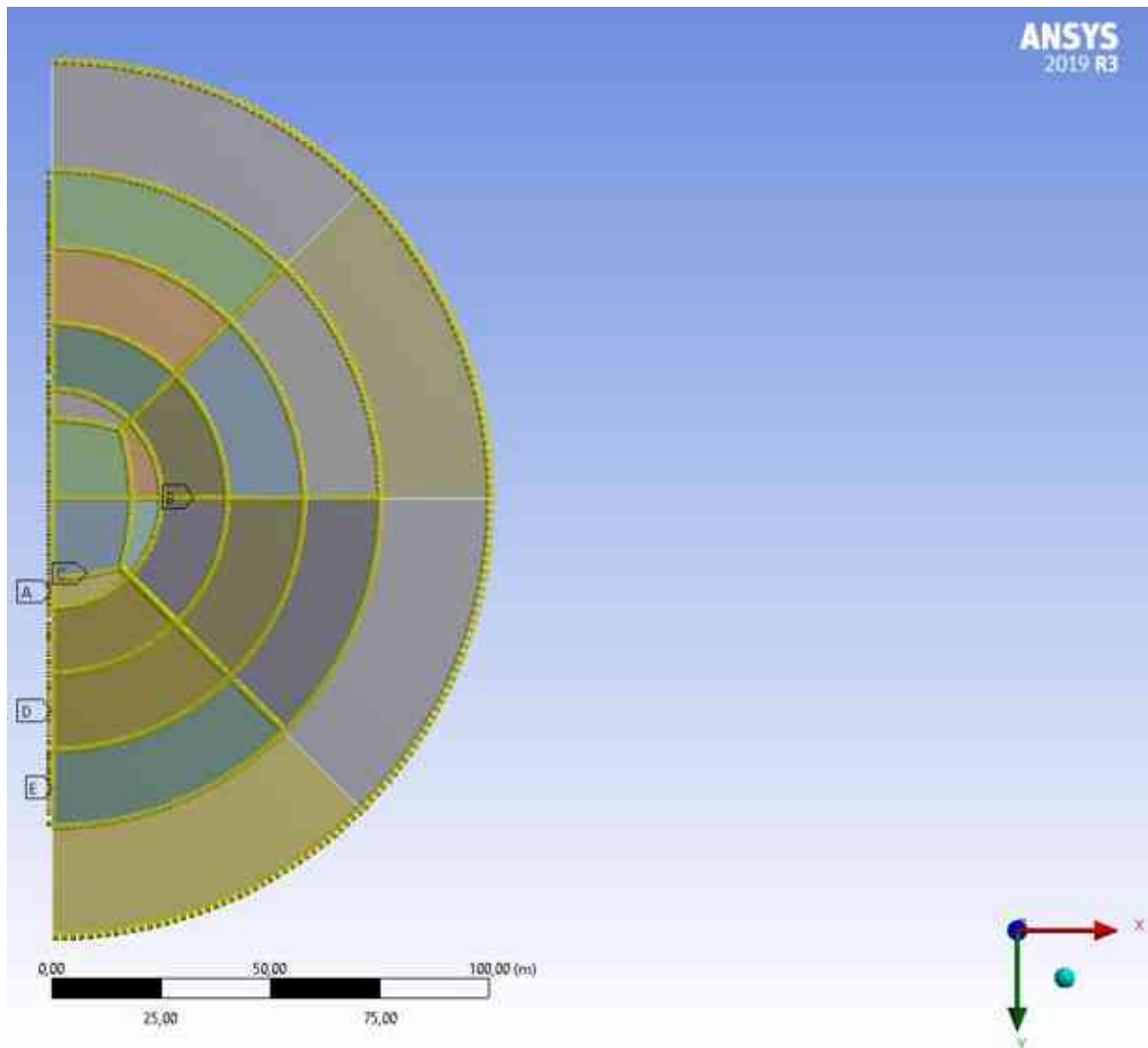


Figure 13-11: Edge-sizing during the meshing procedure

13.17 Appendix Q

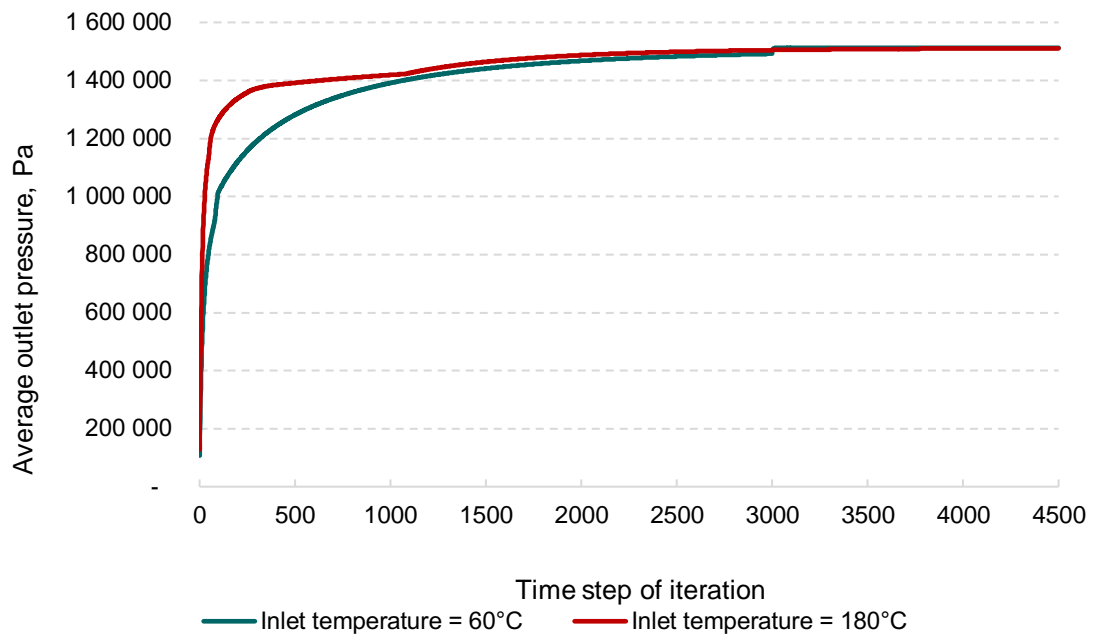


Figure 13-12: Average outlet pressure during the steady-state simulation

13.18 Appendix R

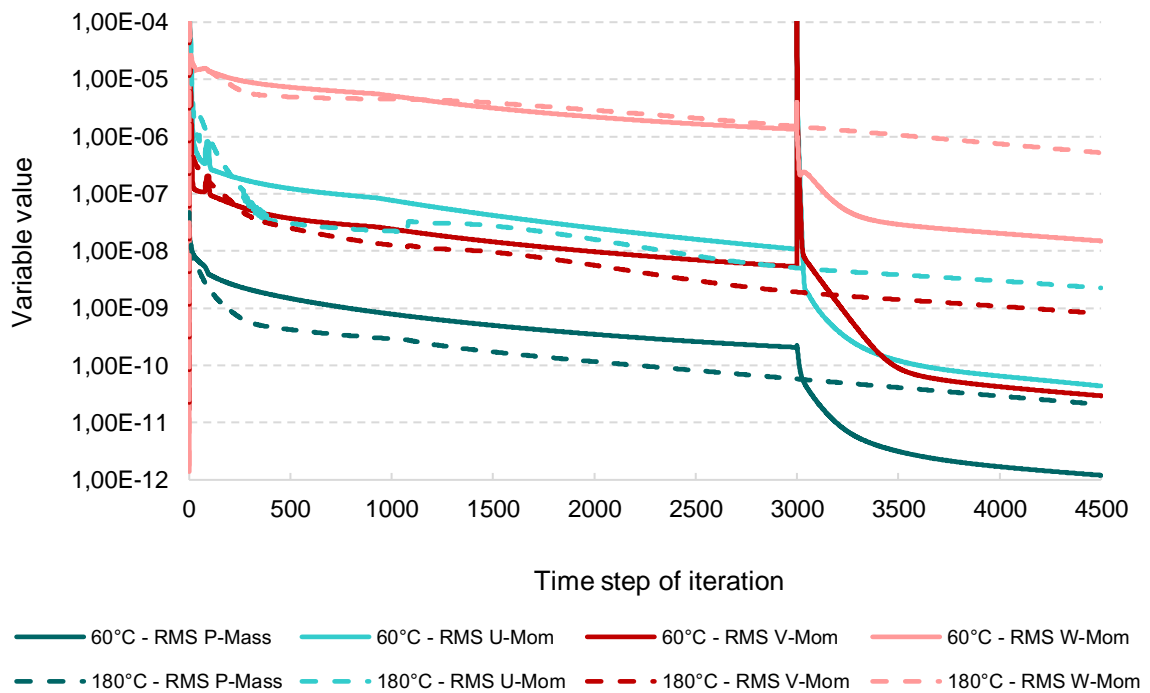


Figure 13-13: Residuals during steady-state simulation

13.19 Appendix S

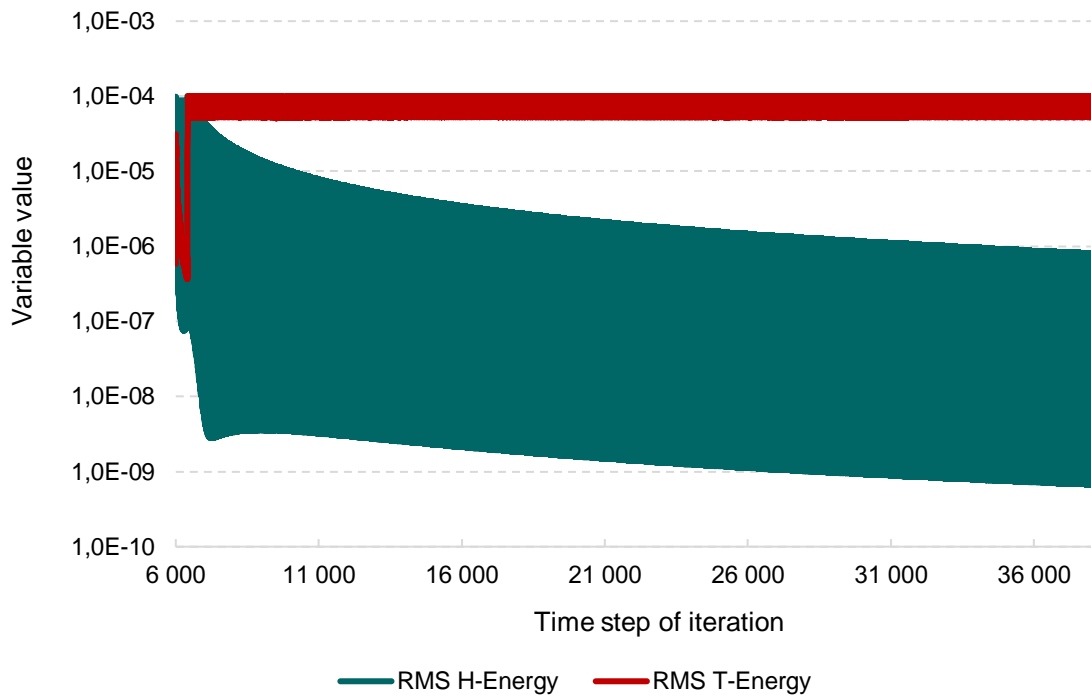


Figure 13-14: Residuals during transient simulation

13.20 Appendix T

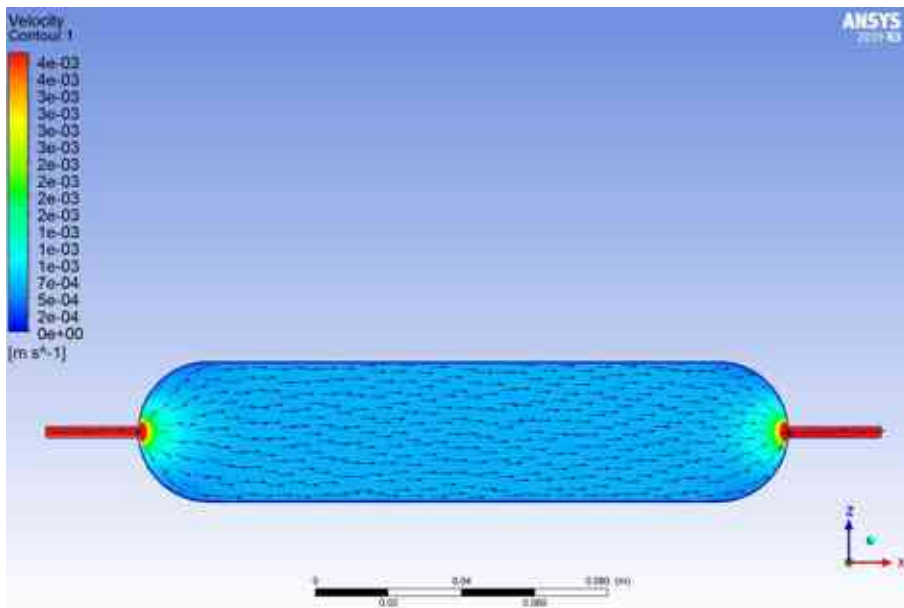


Figure 13-15: Velocity profile of the validation model

13.21 Appendix U

16/32:30/50 - 1000																
	Δpcor [measured]		Q	Q	Wp _{eff}	Cell width	A	viscosity	Length	Average Permeability [measured]	Permeabilities [measured]	Porosities [measured]	Measured		Variance	
	Pa	Δpcor [simulated] Pa	ml/min	m ³ /s	mm	mm	m ²	Pas	m	Darcy	Darcy	-	Q/A	dp/(nu-L)	Perm [LINEST]	Variance
2.000	14.86	14.75	2.0	3.3E-08	5.733	38.35	0.00022	0.00094	0.127		1230.34		1.5E-04	124.864		
	19.44	19.25	2.4	4.0E-08	5.728	38.35	0.00022	0.00094	0.127		1129.28	0.366	1.8E-04	163.374		
	24.72	24.50	2.8	4.7E-08	5.728	38.35	0.00022	0.00094	0.127	1077.7	1036.21		2.1E-04	207.718	1077.7	0.46%
4.000	28.08	28.00	3.2	5.3E-08	5.731	38.35	0.00022	0.00094	0.127		1042.34		2.4E-04	235.905		
	26.15	26.00	2.0	3.3E-08	5.543	38.35	0.00021	0.00094	0.127		725.05		1.6E-04	219.747		
	33.59	33.50	2.4	4.0E-08	5.539	38.35	0.00021	0.00094	0.127	665.1	676.05	0.357	1.9E-04	282.224	665.1	0.42%
6.000	40.14	40.00	2.8	4.7E-08	5.529	38.35	0.00021	0.00094	0.127		661.30		2.2E-04	337.251		
	47.18	46.75	3.2	5.3E-08	5.516	38.35	0.00021	0.00094	0.127		644.44		2.5E-04	396.407		
	40.83	40.50	2.0	3.3E-08	5.284	38.35	0.00020	0.00094	0.127	454.6	485.83		1.6E-04	343.086		
8.000	51.92	51.75	2.4	4.0E-08	5.281	38.35	0.00020	0.00094	0.127		458.71	0.350	2.0E-04	436.263		
	60.90	60.50	2.8	4.7E-08	5.273	38.35	0.00020	0.00094	0.127		456.96		2.3E-04	511.666	454.6	0.43%
	72.22	71.75	3.2	5.3E-08	5.267	38.35	0.00020	0.00094	0.127		440.89		2.6E-04	606.818		
10.000	62.95	62.75	2.0	3.3E-08	5.125	38.35	0.00020	0.00094	0.127		324.92		1.7E-04	528.901		
	76.92	76.50	2.4	4.0E-08	5.125	38.35	0.00020	0.00094	0.127	319.3	319.08	0.342	2.0E-04	646.315		
	89.74	89.25	2.8	4.7E-08	5.125	38.35	0.00020	0.00094	0.127		319.07		2.4E-04	754.034	319.3	0.37%
10.000	103.10	102.50	3.2	5.3E-08	5.125	38.35	0.00020	0.00094	0.127		317.43		2.7E-04	866.216		
	93.33	92.75	2.0	3.3E-08	5.044	38.35	0.00019	0.00094	0.127	229.3	222.67		1.7E-04	784.196		
	106.79	106.25	2.4	4.0E-08	5.044	38.35	0.00019	0.00094	0.127		233.52	0.335	2.1E-04	897.301		
10.000	125.51	124.75	2.8	4.7E-08	5.044	38.35	0.00019	0.00094	0.127		231.81		2.4E-04	1,054.571	229.3	0.36%
	145.83	145.25	3.2	5.3E-08	5.044	38.35	0.00019	0.00094	0.127		228.01		2.8E-04	1,220.405	229.3	0.36%

Figure 13-16: Validation results I.

13.22 Appendix V

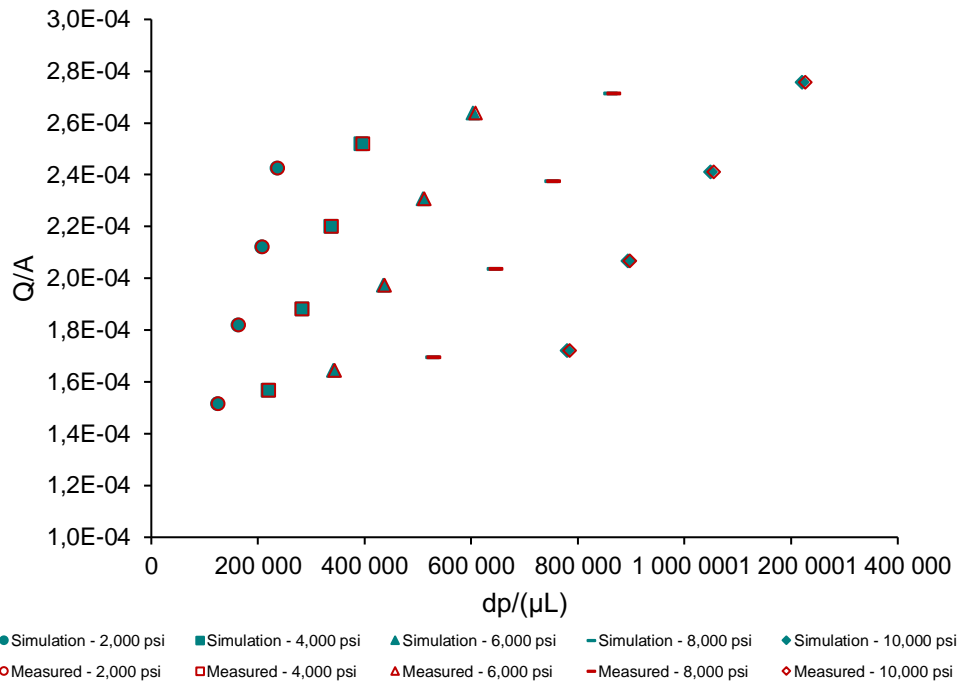


Figure 13-17: Validation results II.

13.23 Appendix W

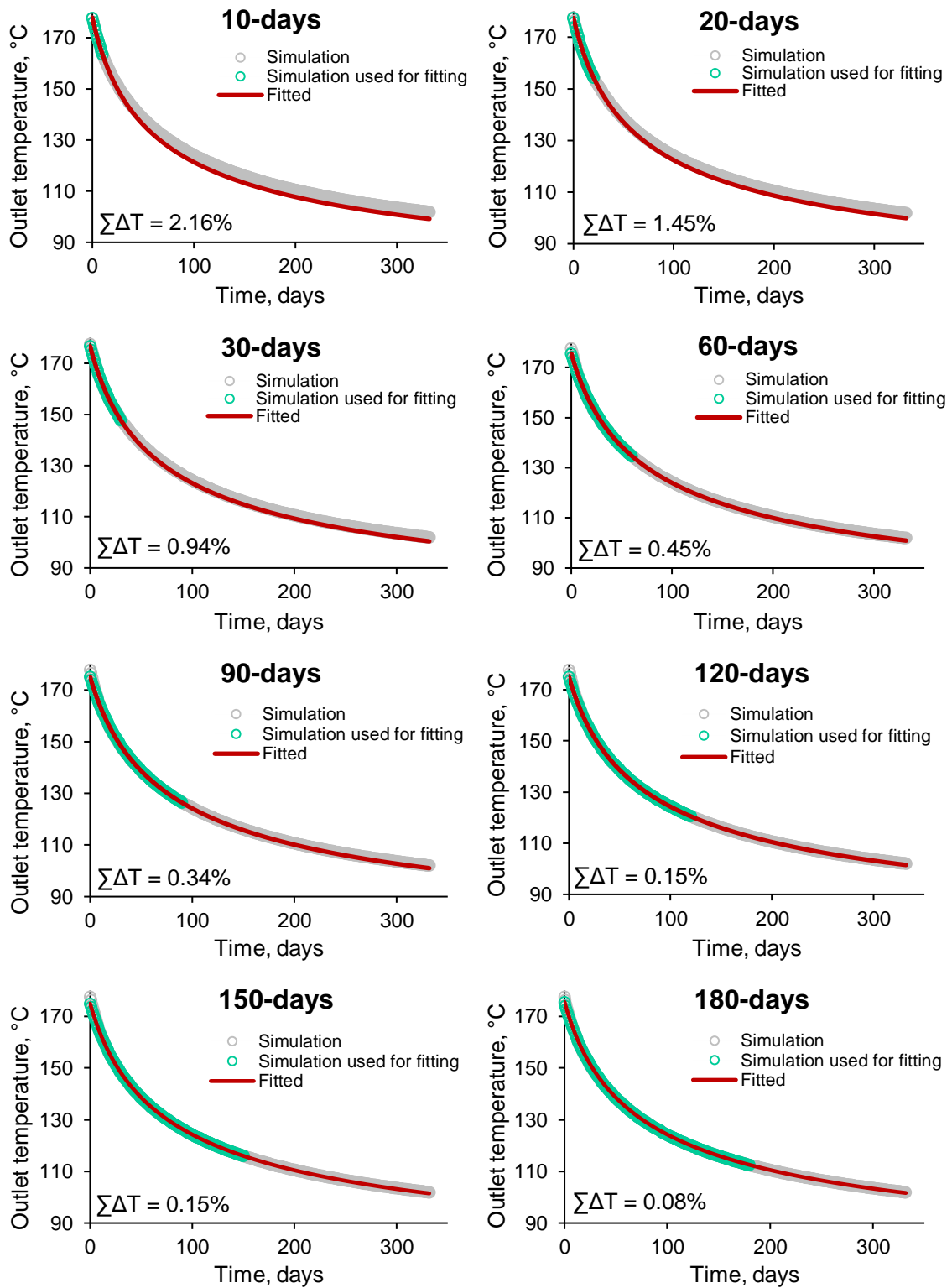


Figure 13-18: Fitting results based on different simulation time in case the fracture permeability in the zones is 128 Darcy with the difference in the sum temperatures ($\Sigma\Delta T$) of the simulated and the fitted data

13.24 Appendix X



Figure 13-19: Equipment used during the measurements

13.25 Appendix Y

TECHNICAL DATA SHEET

CARBOECONOPROP


Low-density ceramic proppant

Features

- Bulk density and specific gravity similar to frac sand
- Chemically inert
- Available in three standard sizes—20/40, 30/50 and 40/70

Benefits

- Developed for largest well concentration
- Cost-effective alternative for resin-coated sand
- Will not react with fracturing fluid crosslinkers and breakers
- High conductivity for increased production



Ideally suited for moderate-depth natural gas wells

Both the bulk density and specific gravity of CARBOECONOPROP®, a low-density ceramic proppant, are similar to frac sand, yet its high conductivity makes it more cost-effective than resin-coated sand proppant. CARBOECONOPROP is non-reactive to fracturing fluid crosslinkers and breakers.

Long-term conductivity

Reference conductivity, md-ft @ 250°F

Closure stress (psi)	2 lb./ft. ³ 20/40	2 lb./ft. ³ 30/50	2 lb./ft. ³ 40/70
2,000	6,300	4,950	2,250
4,000	5,300	3,500	1,660
6,000	4,300	2,550	1,270
8,000	3,300	1,600	870
10,000	2,300	975	555

Reference permeability, Darcies @ 250°F

Closure stress (psi)	2 lb./ft. ³ 20/40	2 lb./ft. ³ 30/50	2 lb./ft. ³ 40/70
2,000	340	220	135
4,000	300	180	100
6,000	230	140	80
8,000	150	90	60
10,000	85	65	35

Reference conductivity and permeability are measured with a single phase fluid under laminar flow conditions in accordance with API RP 19EX. In an actual fracture, the effective conductivity will be much lower due to non-Darcy and multiphase flow effects. For more information, please refer to SPE Paper #106301 - "Determining Realistic Fracture Conductivity and Understanding its Impact on Well Performance - Theory and Field Examples."

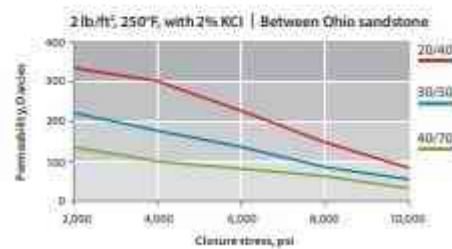
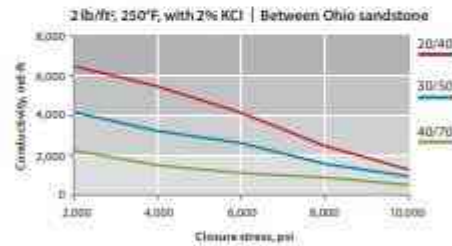


Figure 13-20: Technical data sheet of the 30/50 mesh proppant used during the measurements (2/1)

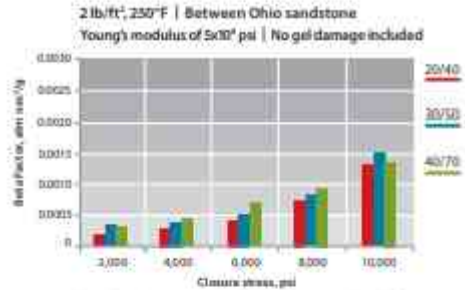
13.26 Appendix Z

CARBOECONOPROP

Low-density ceramic proppant

Beta factors

Closure stress (psi)	Beta factor (atm sec ² /g)		
	20/40	30/50	40/70
2,000	0.00024	0.00025	0.00034
4,000	0.00029	0.00040	0.00046
6,000	0.00043	0.00050	0.00070
8,000	0.00075	0.00080	0.00092
10,000	0.00129	0.00150	0.00121



Beta factor data reported by Siles-Lab Consortium, Profit Feb 2012.

Physical and chemical properties

Typical sieve analysis (weight % retained)

U.S. Mesh (mesh)	Micros	20/40	30/50	40/70
-16+20 mesh	1180+850	5		
20+30 mesh	850+600	60	3	
50+40 mesh	610+425	35	79	5
40+50 mesh	425+300		17	72
50+70 mesh	300+212		1	22
70 mesh	212			1
Median particle diameter (microns)		635	473	312
API/ISO crush test	@5,000 psi	1.0	0.8	0.4
% by weight fines generated	@1,500 psi	5.2	2.8	2.0

Sizing requirements: A minimum of 90% of the tested sample should fall between the designated sieve sizes. These specifications meet the recommended practices as detailed in API RP 53C.

Typical additional properties

Roundness	0.9	Apparent specific gravity	2.70
Sphericity	0.9	Absolute volume (gal/lb)	0.044
Bulk density (lb/ft ³) (g/cm ³)	16 1.56	Solubility in 12.5 HCl/14F acid [% weight loss]	1.7

All data represents typical values.

Talk to CARBO to find out how we can help you enhance your production.

carboceramics.com

© 2012 CARBO Ceramics, Inc. All Rights Reserved. 3307_3/12

CARBO
Production. Enhanced.

Figure 13-21: Technical data sheet of the 30/50 mesh proppant used during the measurements (2/2)

13.27 Appendix AA



Figure 13-22: Pentapyc 5200e device used for specific gravity measurements

13.28 Appendix AB



Figure 13-23: API RP 19C measurement device used for bulk density measurements

13.29 Appendix AC



Figure 13-24: Occhio Zephyr ESR 2 equipment used during proppant size distribution, sphericity and roundness measurements

13.30 Appendix AD

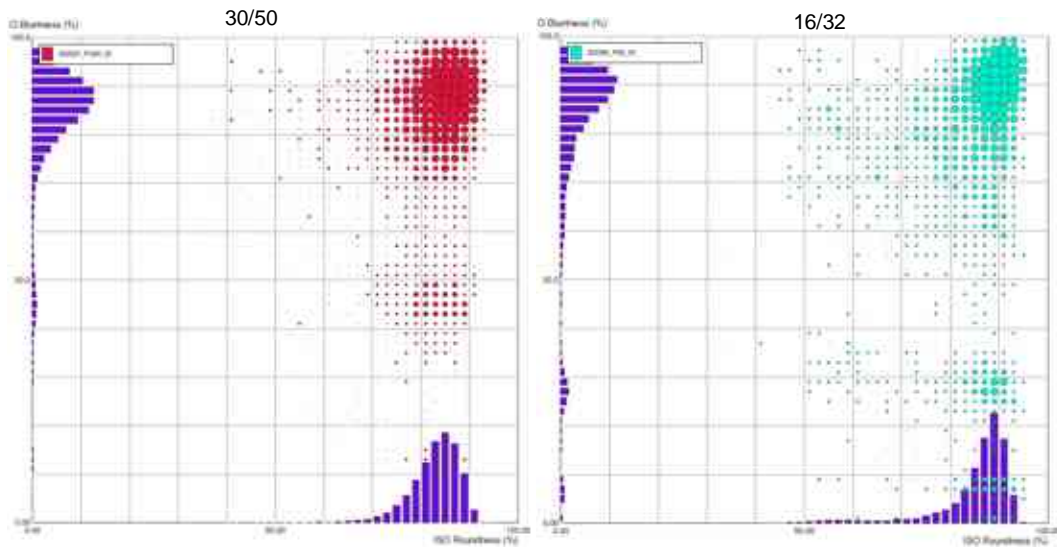


Figure 13-25: Roundness and sphericity values of the 30/50 and 16/32 mesh proppants

13.31 Appendix AE



Figure 13-26: Pure and mixed proppant samples – before measurement

13.32 Appendix AF



Figure 13-27: 16/32 mesh proppant – sample after measurement 2/1

13.33 Appendix AG



Figure 13-28: 16/32 mesh proppant – sample after measurement 2/2

13.34 Appendix AH

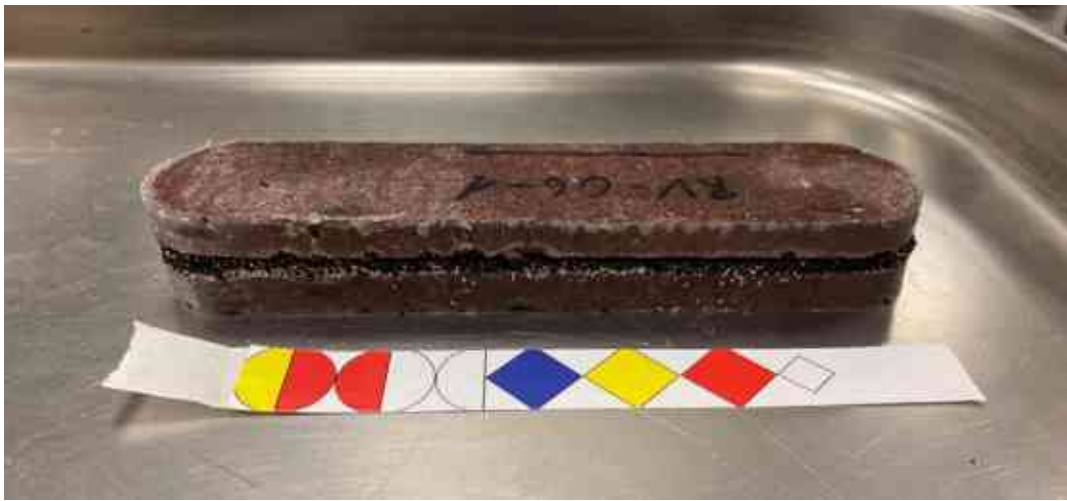


Figure 13-29: 80:20 mixture of 16/32:30/50 mesh proppants – sample after measurement
2/1

13.35 Appendix AI



Figure 13-30: 80:20 mixture of 16/32:30/50 mesh proppants – sample after measurement
2/2

13.36 Appendix AJ

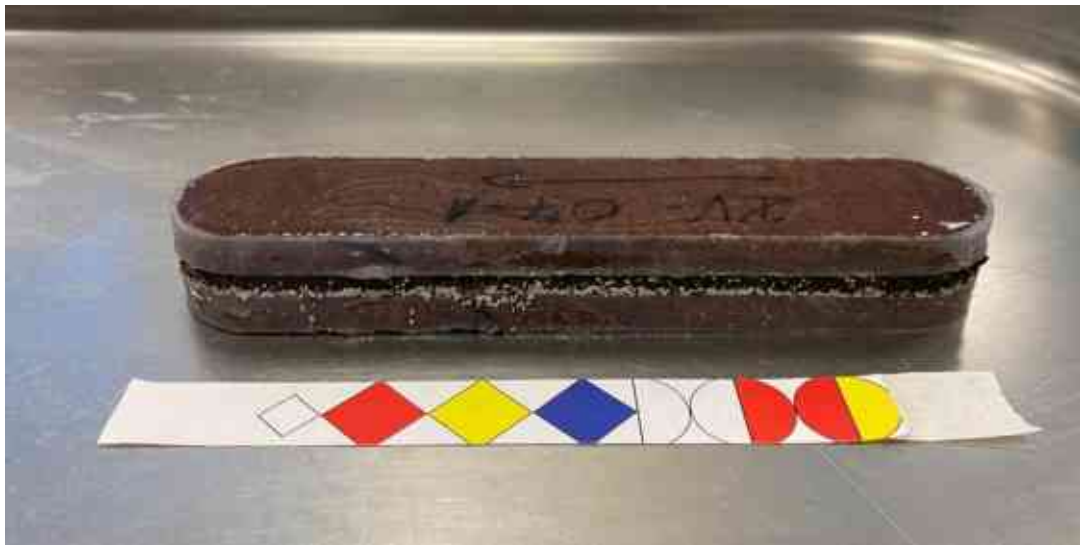


Figure 13-31: 60:40 mixture of 16/32:30/50 mesh proppants – sample after measurement
2/1

13.37 Appendix AK

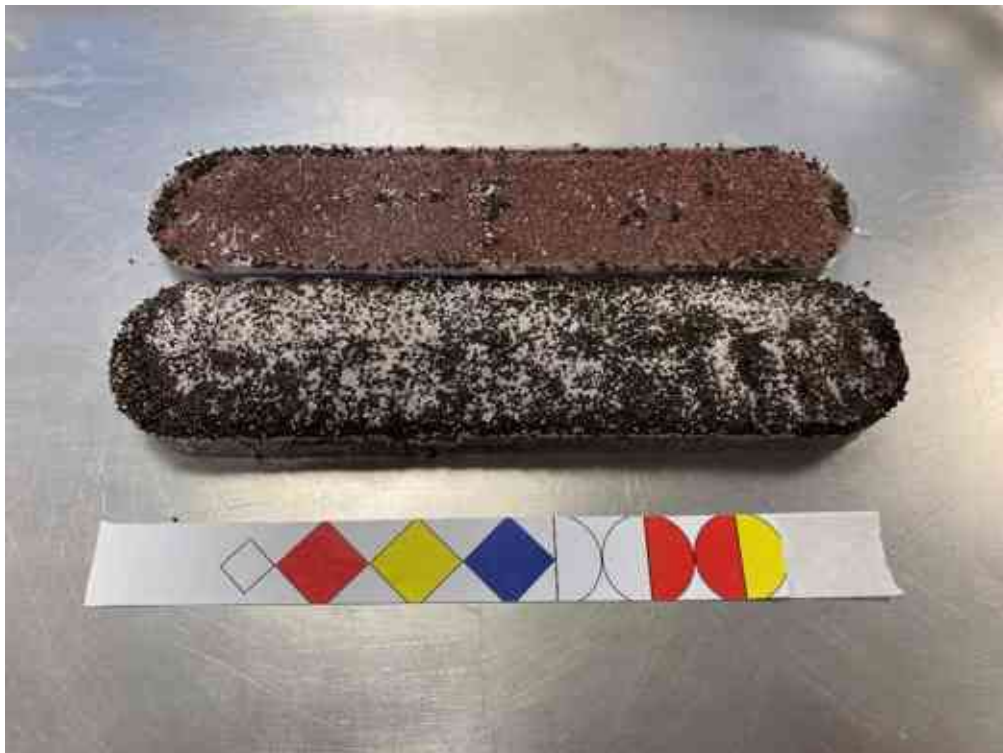


Figure 13-32: 60:40 mixture of 16/32:30/50 mesh proppants – sample after measurement
2/2

13.38 Appendix AL

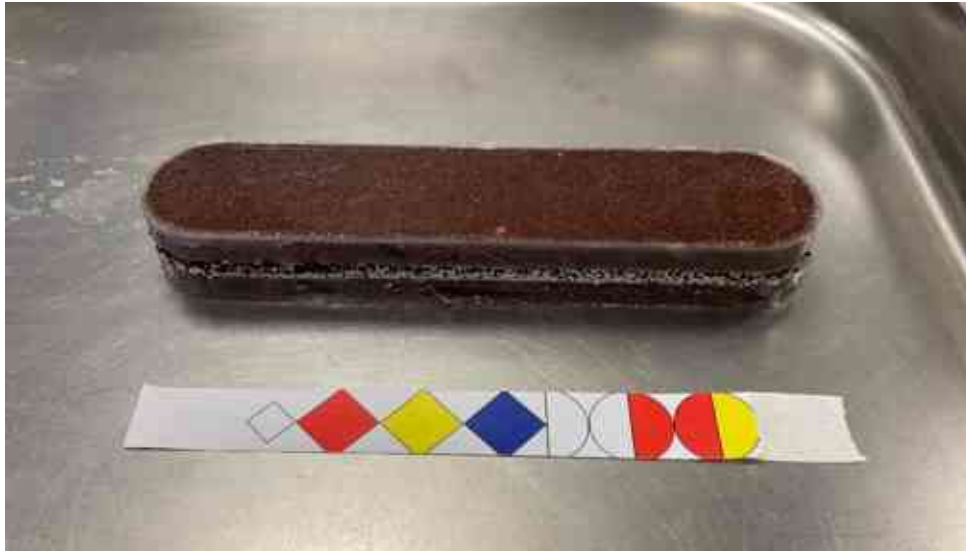


Figure 13-33: 40:60 mixture of 16/32:30/50 mesh proppants – sample after measurement
2/1

13.39 Appendix AM



Figure 13-34: 40:60 mixture of 16/32:30/50 mesh proppants – sample after measurement
2/2

13.40 Appendix AN

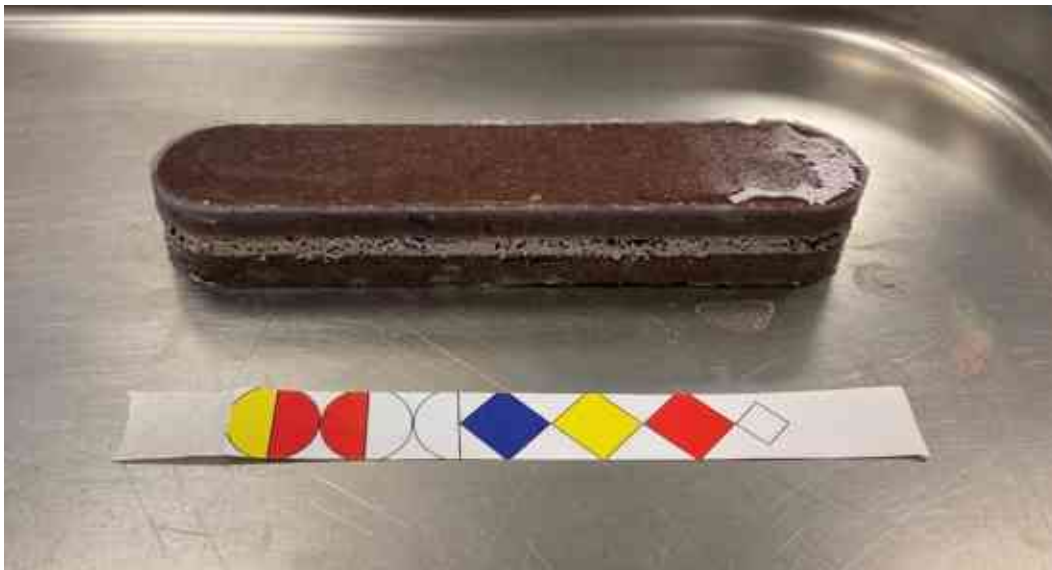


Figure 13-35: 20:80 mixture of 16/32:30/50 mesh proppants – sample after measurement
2/1

13.41 Appendix AO



Figure 13-36: 20:80 mixture of 16/32:30/50 mesh proppants – sample after measurement
2/2

13.42 Appendix AP

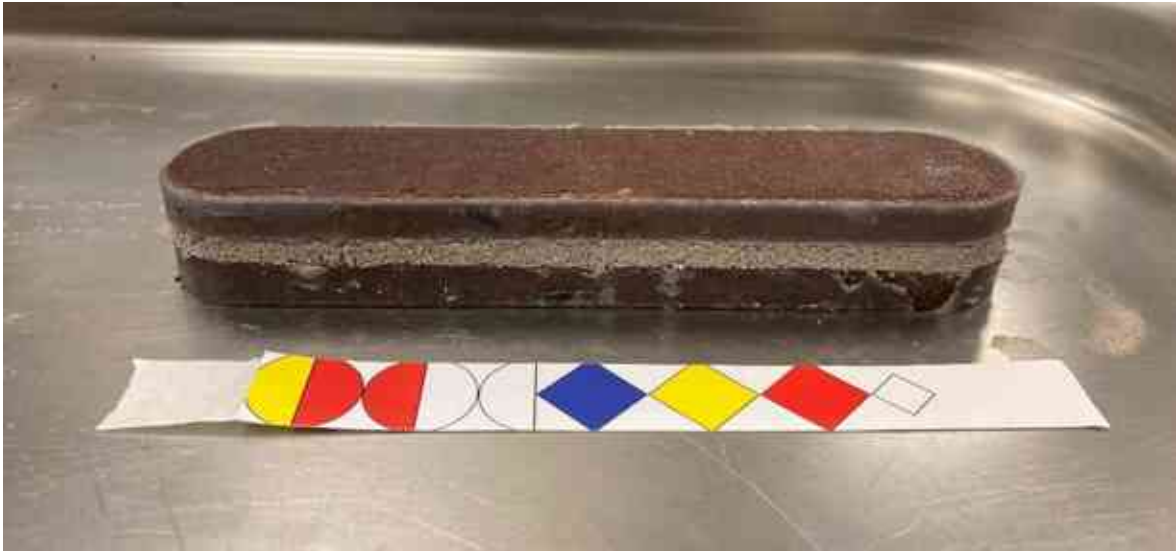


Figure 13-37: 30/50 mesh proppant – A sample after measurement 2/1

13.43 Appendix AQ

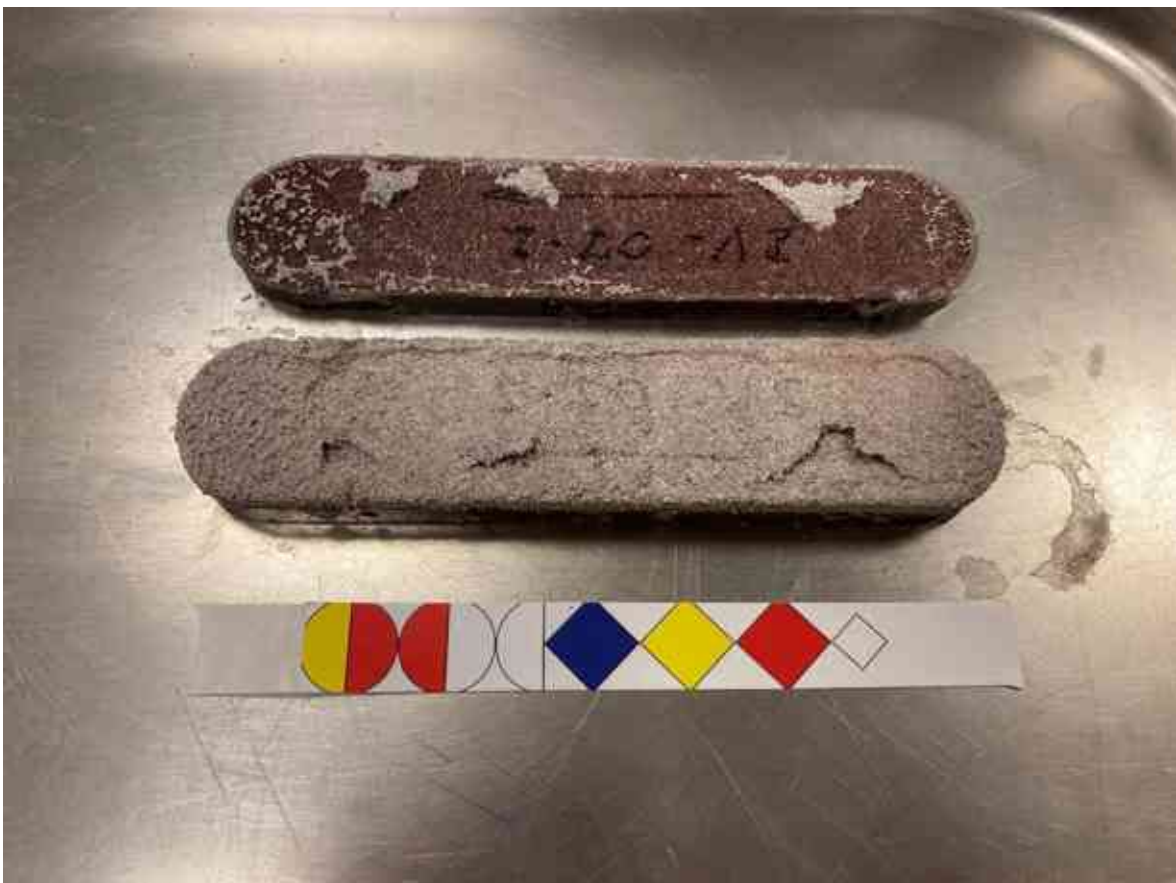


Figure 13-38: 30/50 mesh proppant – A sample after measurement 2/2

13.44 Appendix AR



Figure 13-39: 30/50 mesh proppant – B sample after measurement 2/1

13.45 Appendix AS



Figure 13-40: 30/50 mesh proppant – B sample after measurement 2/2

13.46 Appendix AT



Figure 13-41: 30/50 mesh proppant – C sample after measurement 2/1

13.47 Appendix AU



Figure 13-42: 30/50 mesh proppant – C sample after measurement 2/2

13.48 Appendix AV

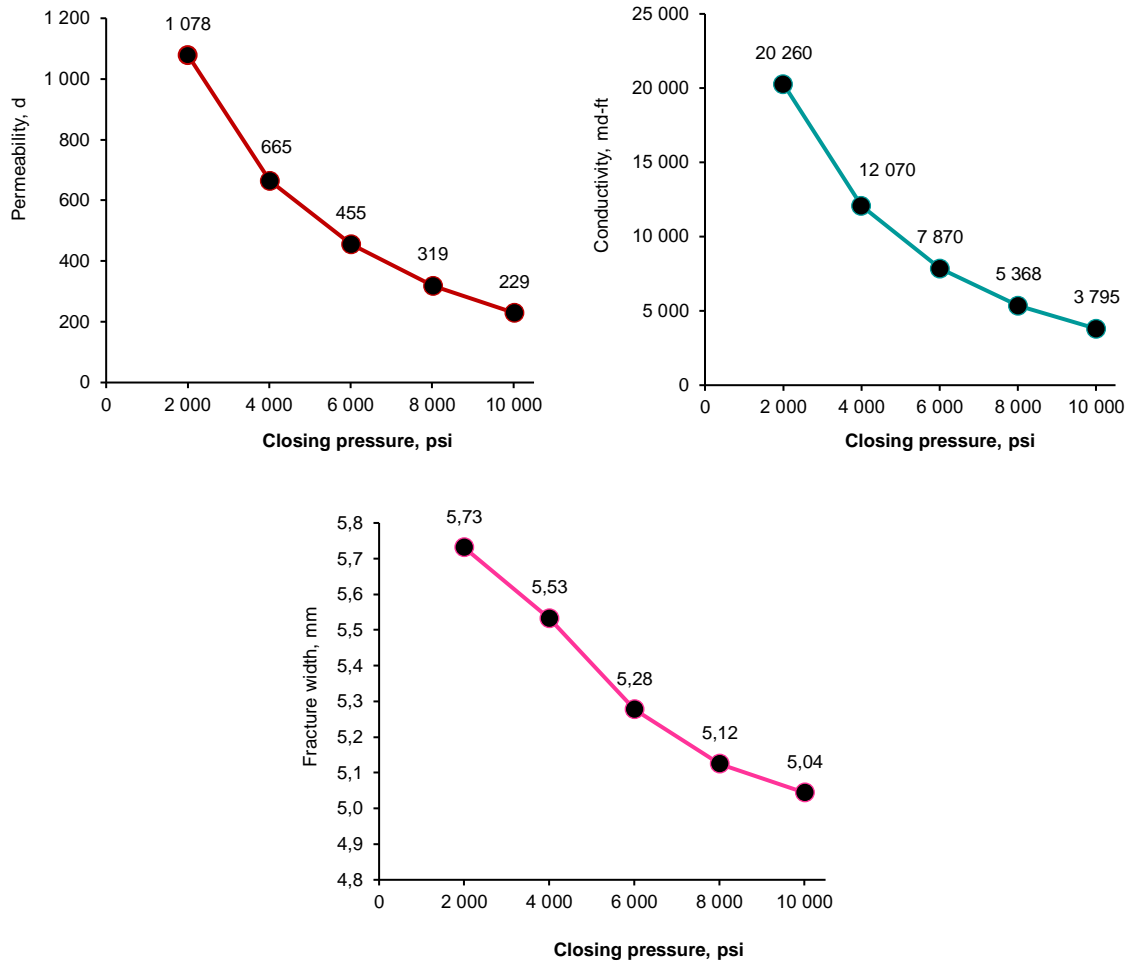


Figure 13-43: Permeability, conductivity and fracture width results in case of the 16/32 mesh proppant at different closing pressures

13.49 Appendix AW

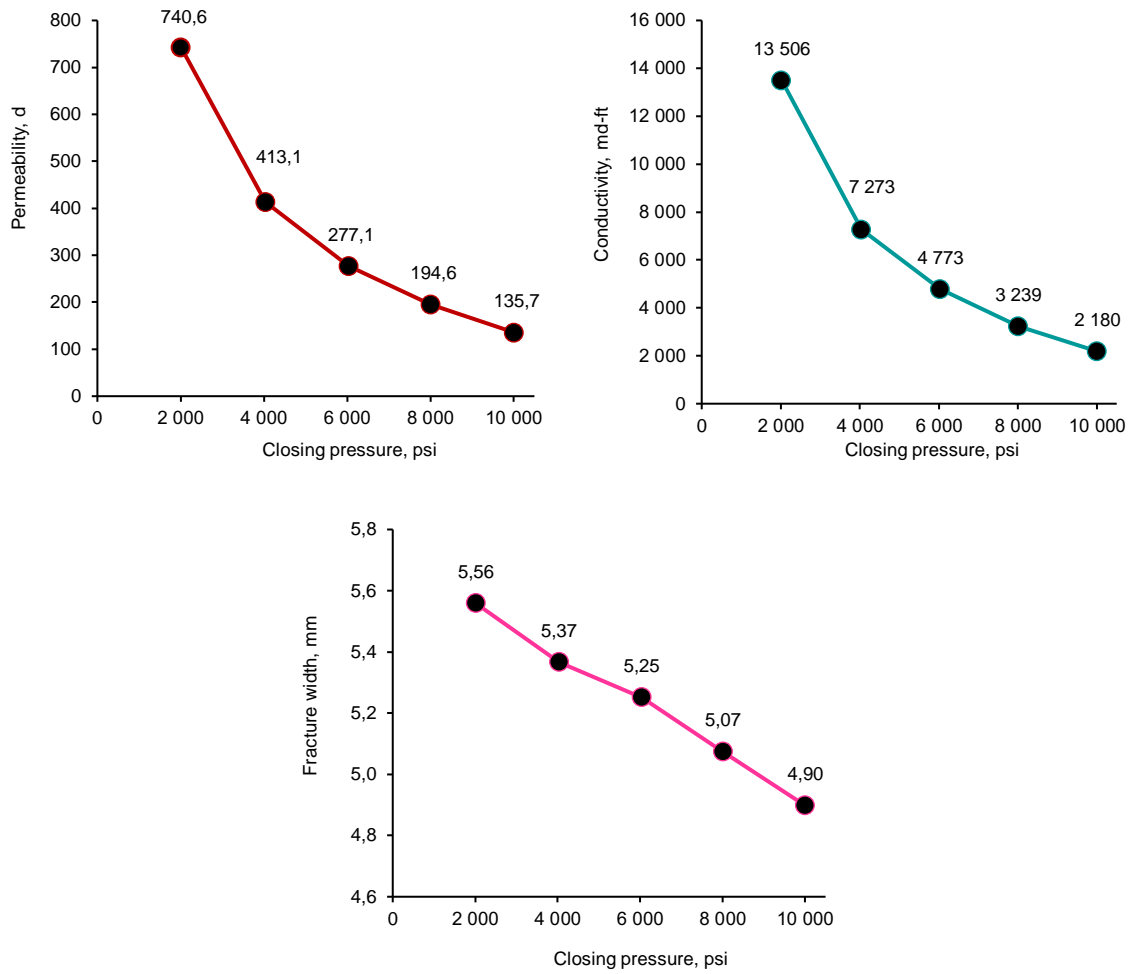


Figure 13-44: Permeability, conductivity and fracture width results in case of the 80:20 m/m% mixture of 16/32 and 30/50 mesh proppant at different closing pressures

13.50 Appendix AX

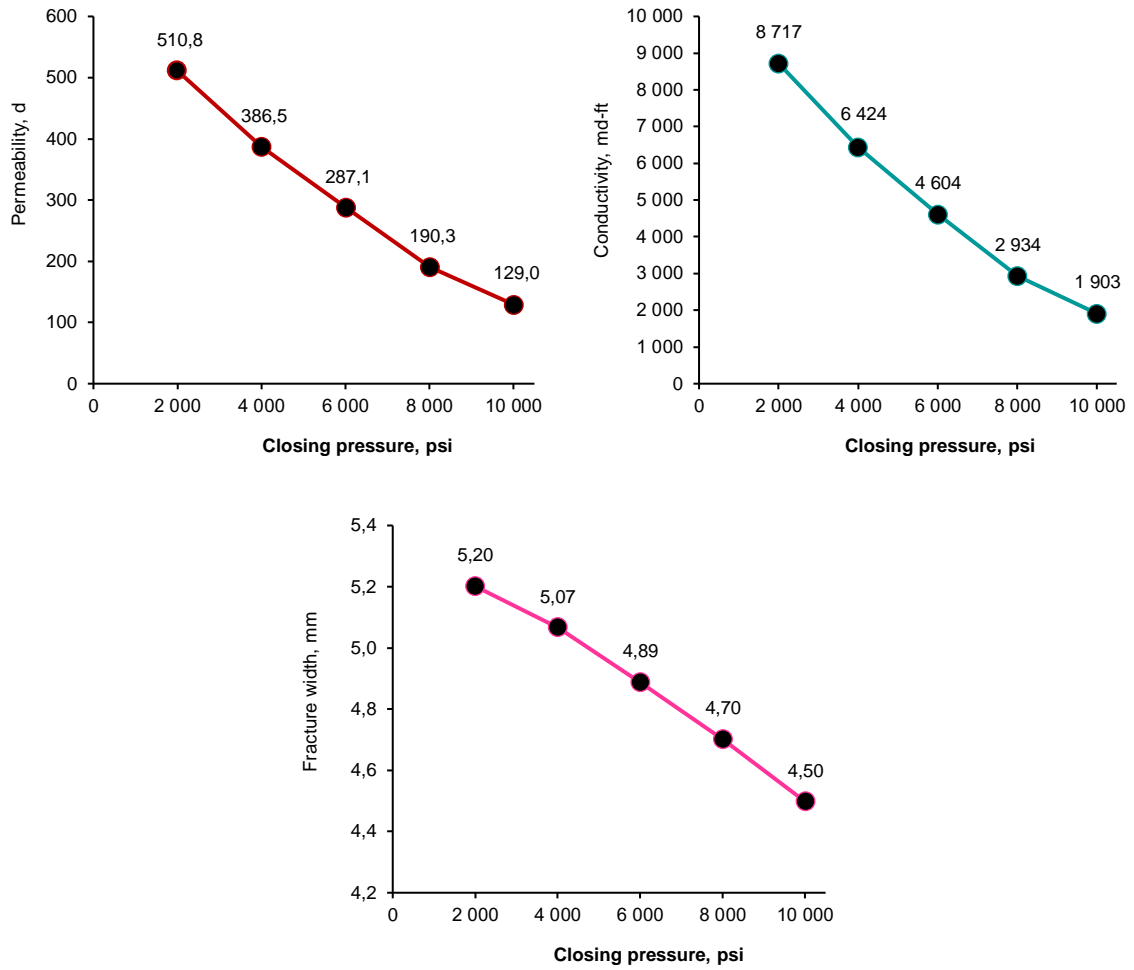


Figure 13-45: Permeability, conductivity and fracture width results in case of the 60:40 m/m% mixture of 16/32 and 30/50 mesh proppant at different closing pressures

13.51 Appendix AY

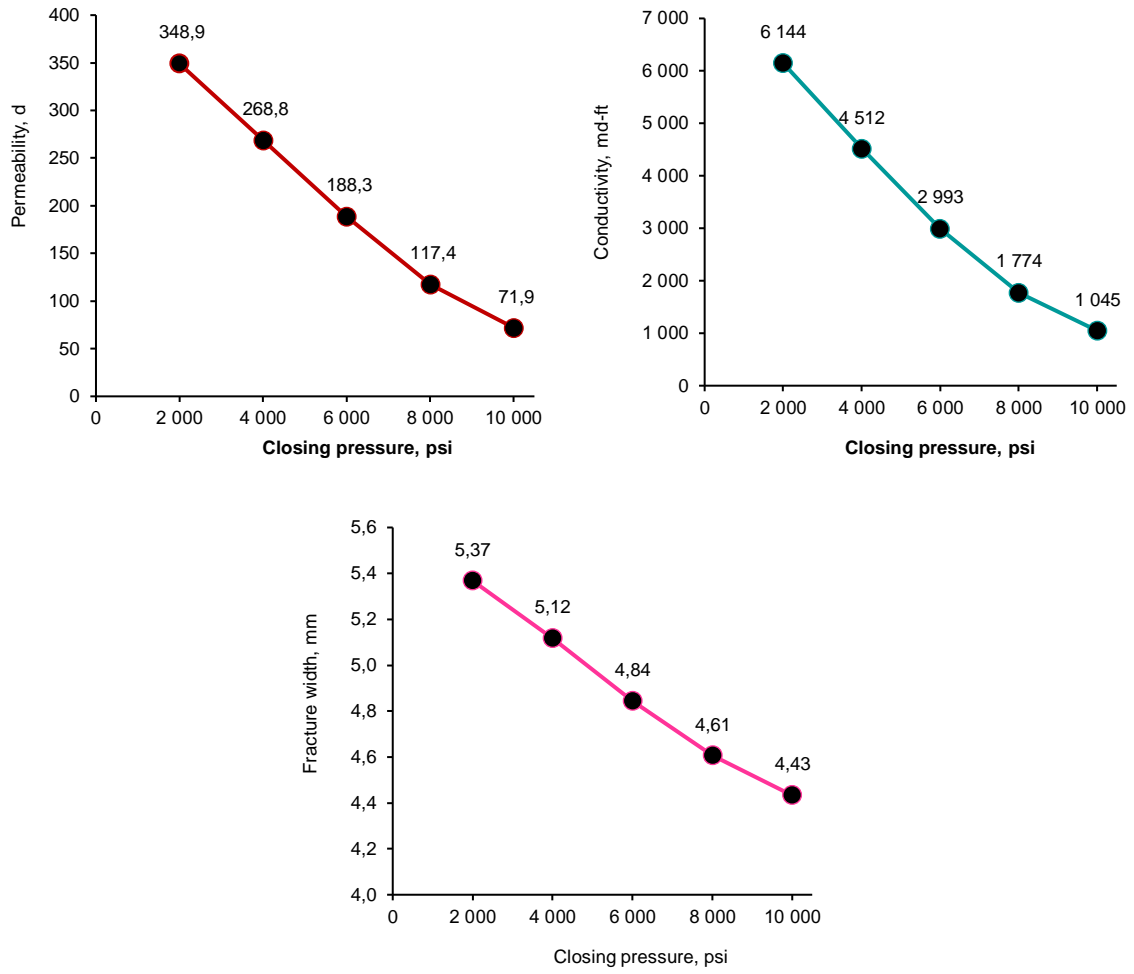


Figure 13-46: Permeability, conductivity and fracture width results in case of the 40:60 m/m% mixture of 16/32 and 30/50 mesh proppant at different closing pressures

13.52 Appendix AZ

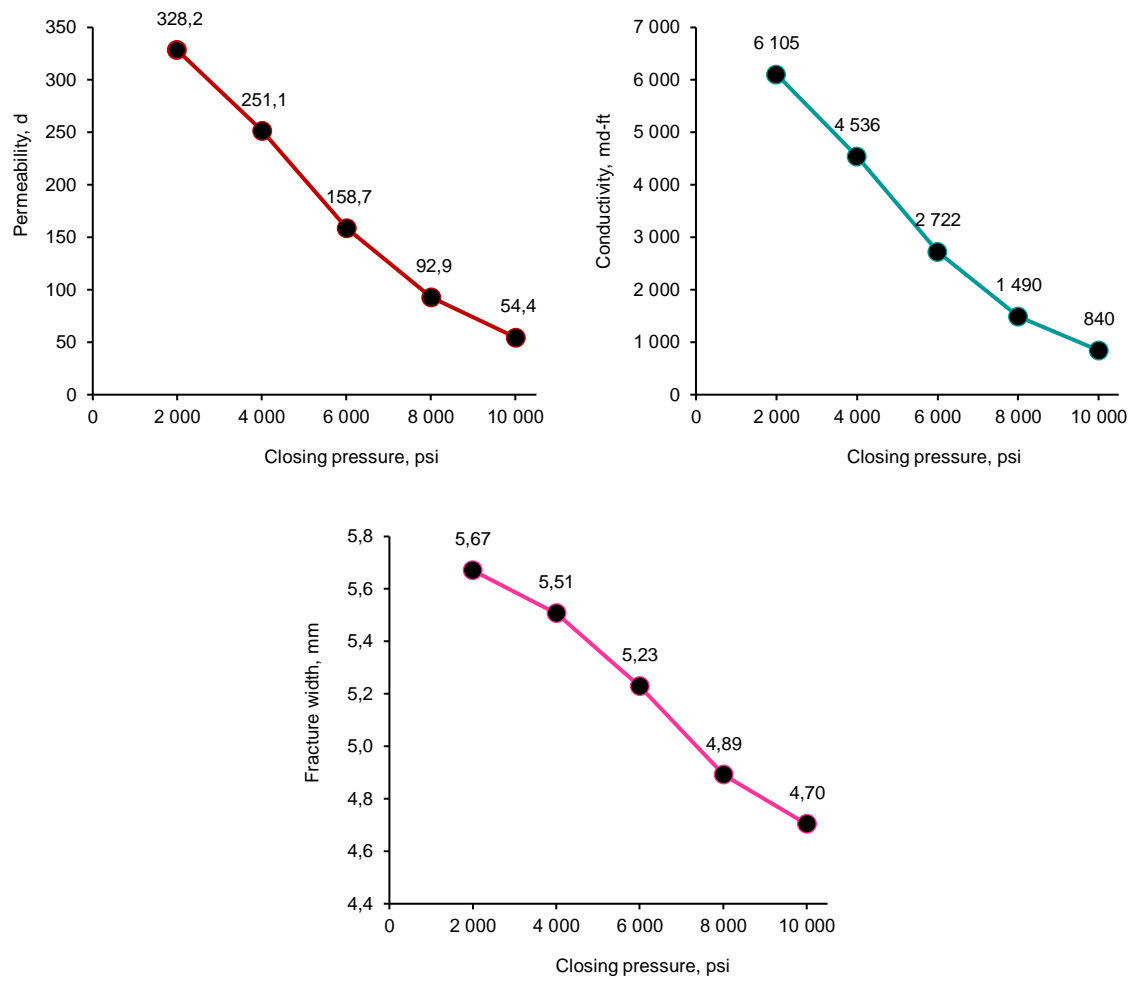


Figure 13-47: Permeability, conductivity and fracture width results in case of the 20:80 m/m% mixture of 16/32 and 30/50 mesh proppant at different closing pressures

13.53 Appendix BA

$$Re = \frac{d_p \rho v}{\mu} \quad (13-1)$$

$$Re_m = \frac{Re}{(1-\Phi_p)} \quad (13-2)$$

$$Re_1 = \frac{Re}{6(1-\Phi_p)} \quad (13-3)$$

13.54 Appendix BB



Figure 13-48: API RP 19C crush test apparatus used for bulk density measurements

13.55 Appendix BC



Figure 13-49: Bulk density measurement setup

13.56 Appendix BD

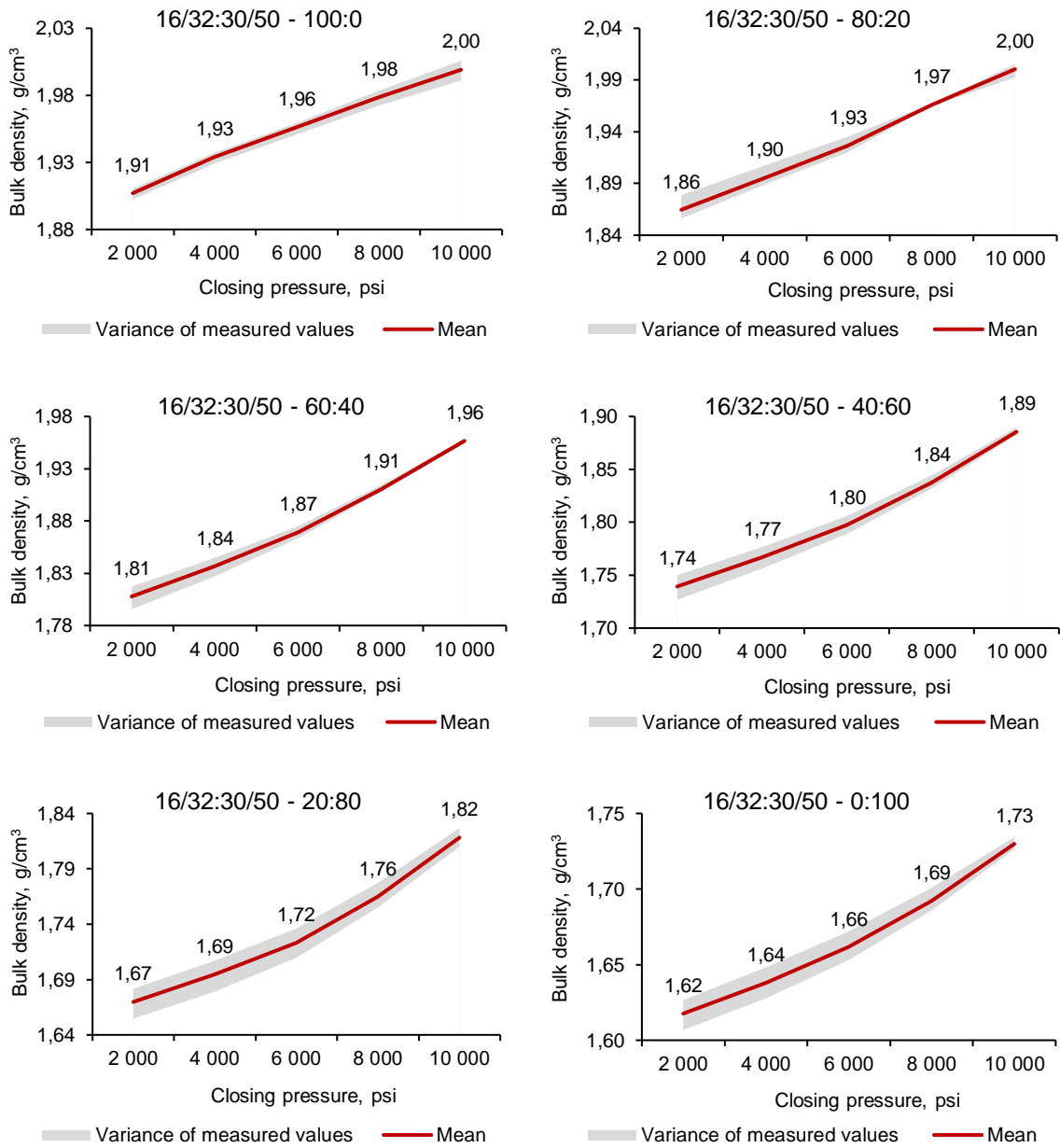


Figure 13-50: Bulk density measurement results on the proppant-pack mixtures

13.57 Appendix BE

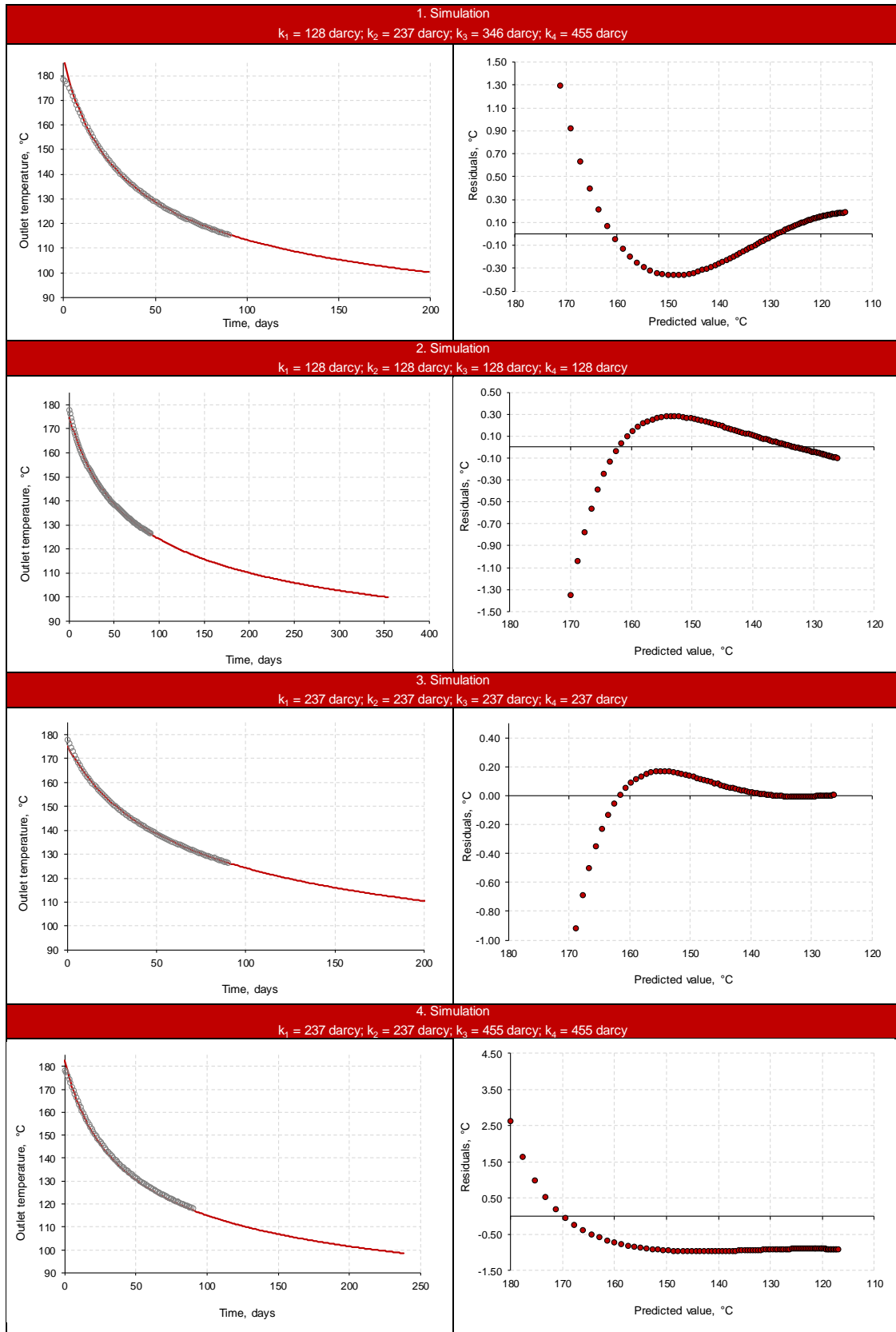


Figure 13-51: Simulation results I.

13.58 Appendix BF

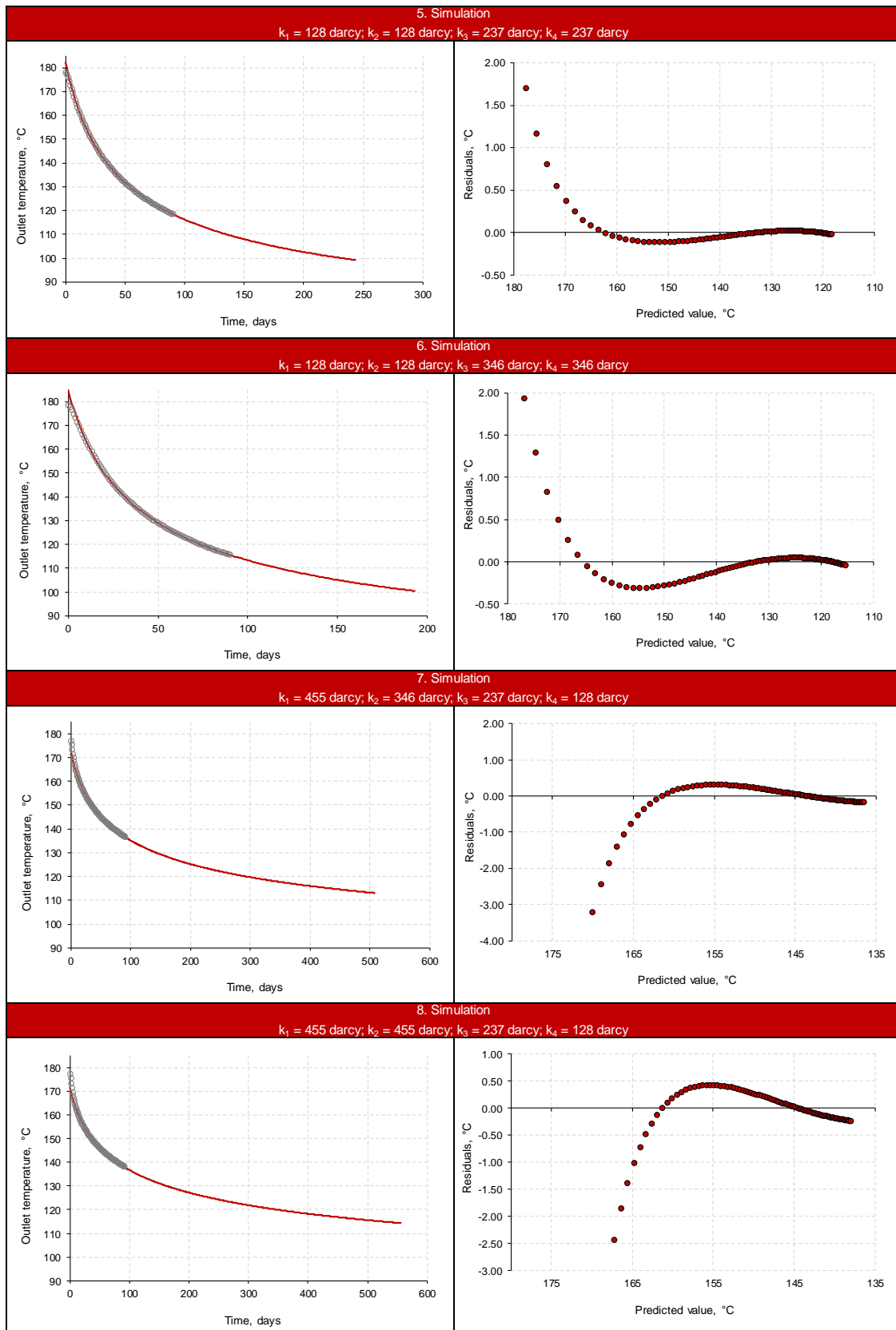


Figure 13-52: Simulation results II.

13.59 Appendix BG

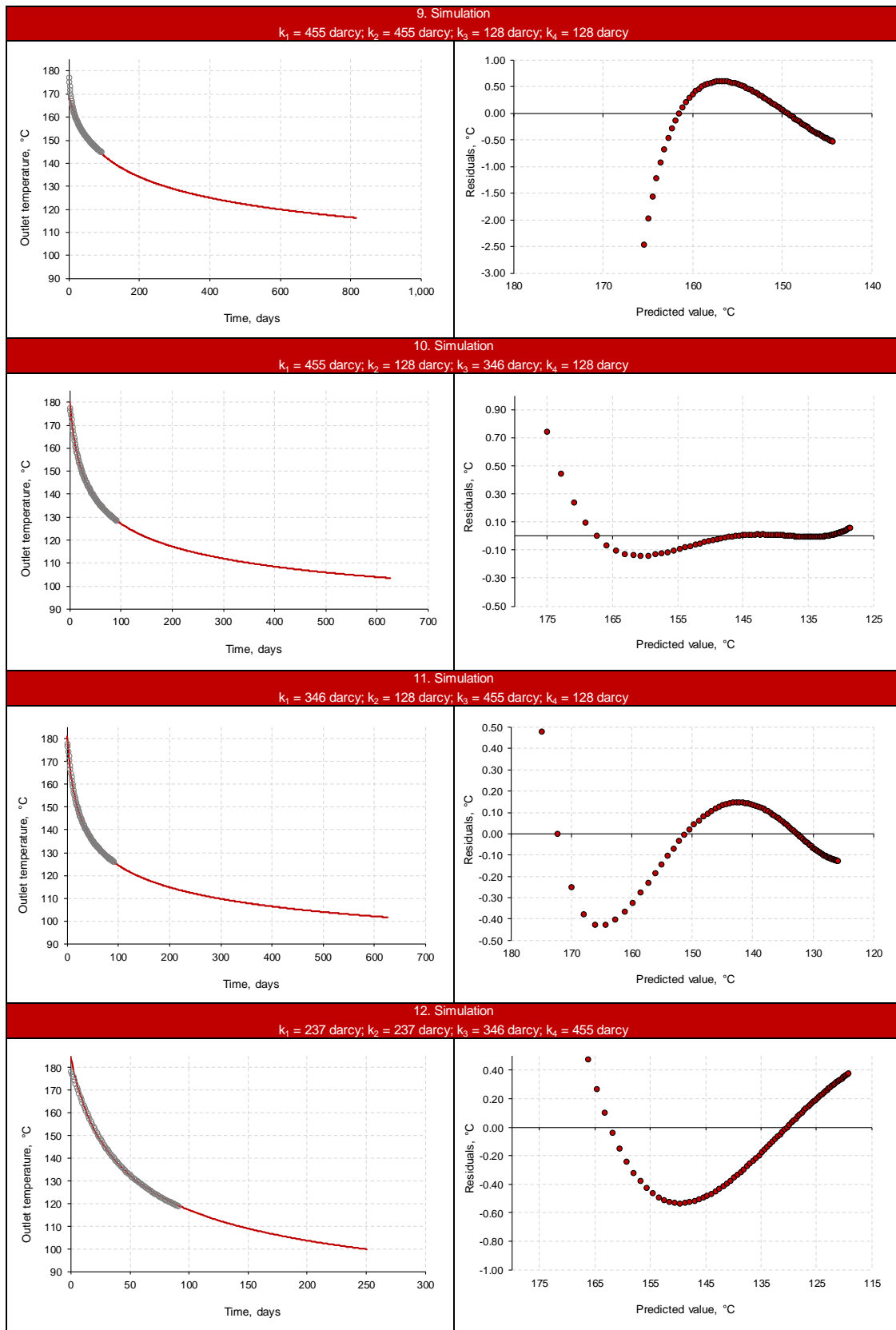


Figure 13-53: Simulation results III.

13.60 Appendix BH

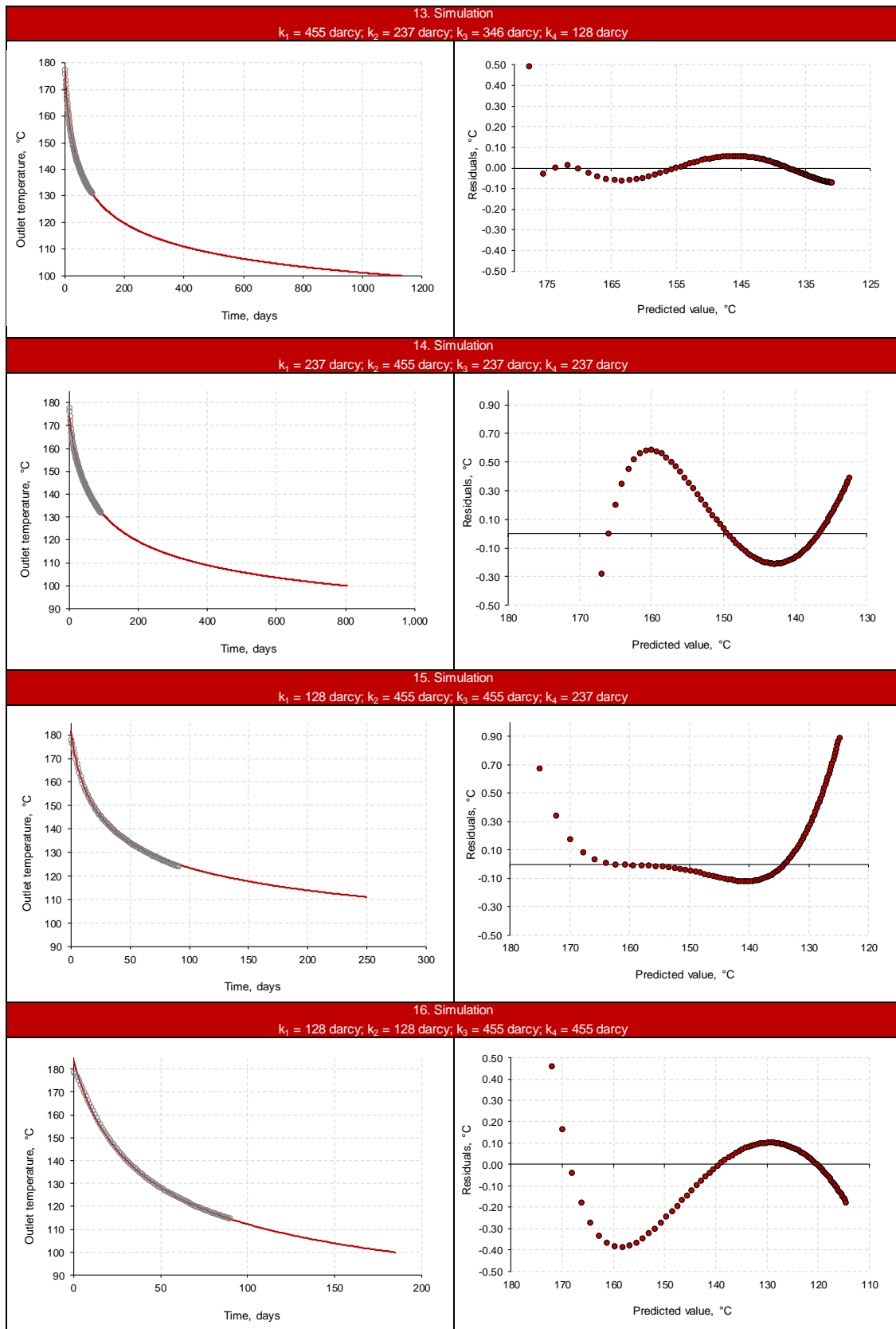


Figure 13-54: Simulation results IV.

13.61 Appendix BI

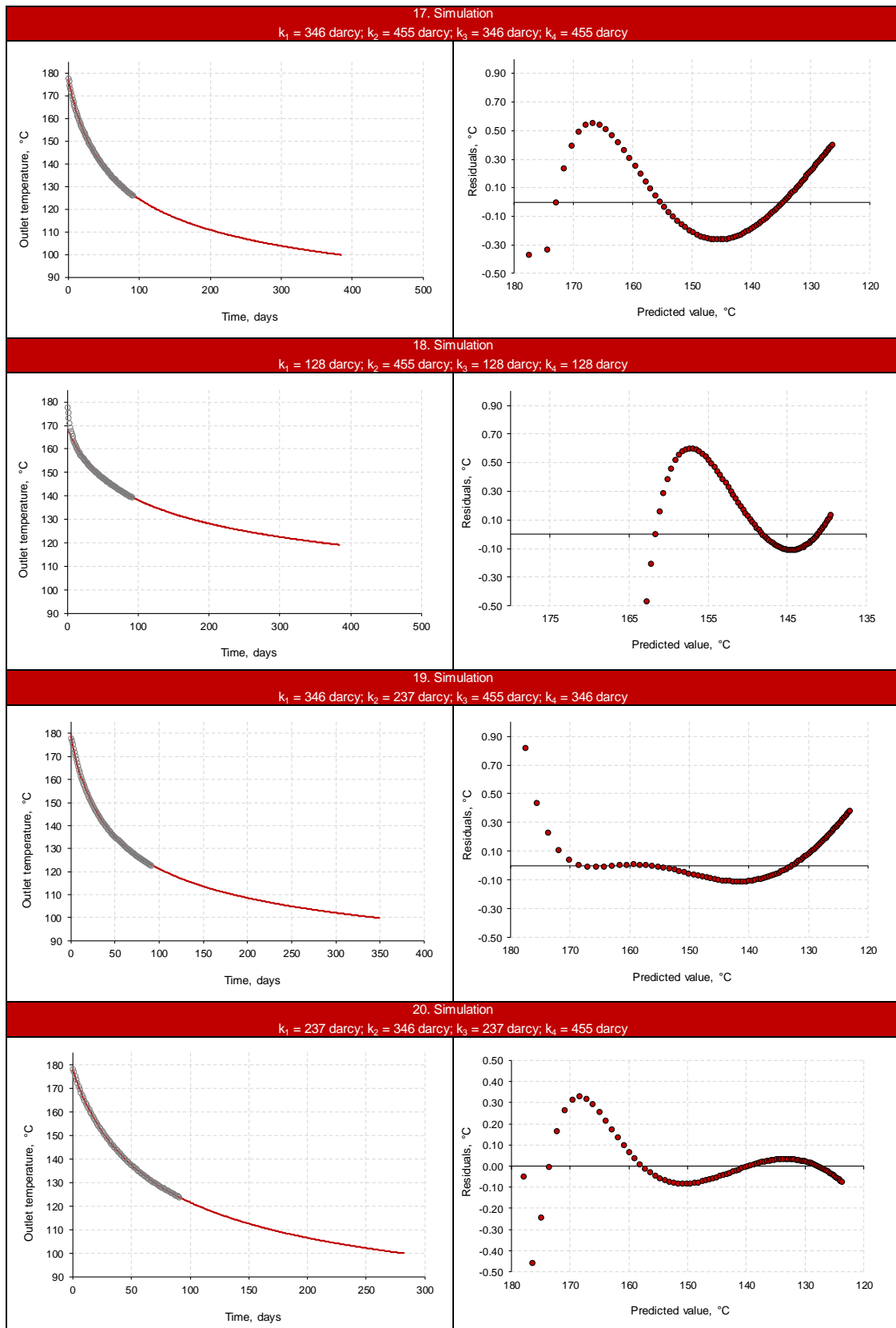


Figure 13-55: Simulation results V.

13.62 Appendix BJ

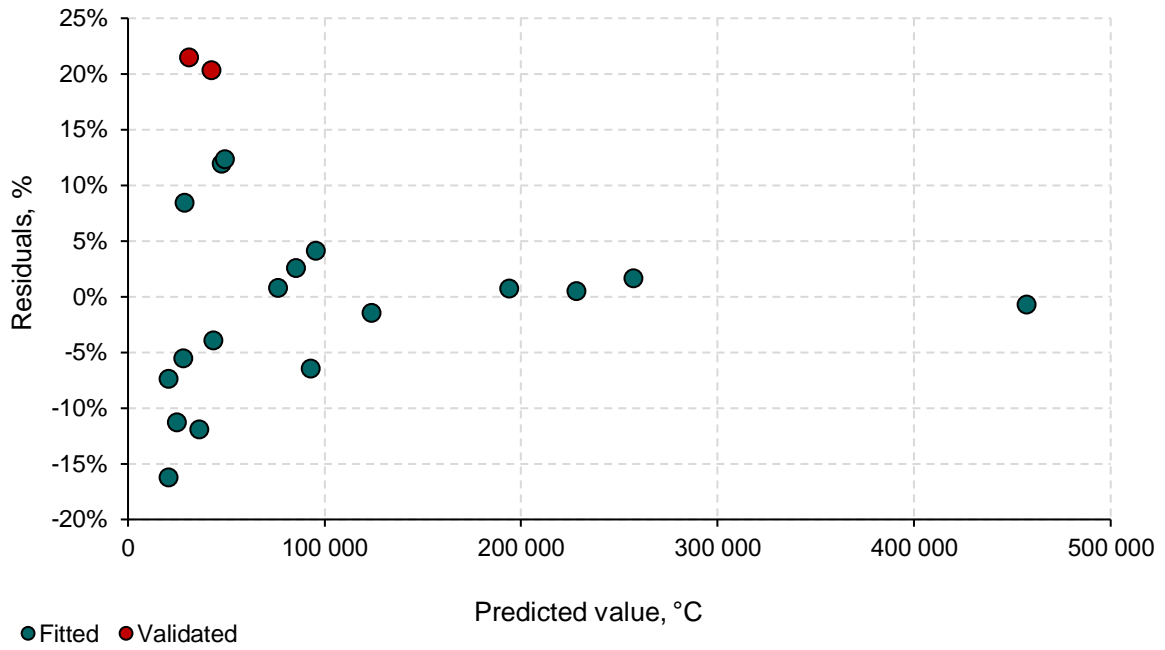


Figure 13-56: Residuals of the RSA model I.

13.63 Appendix BK

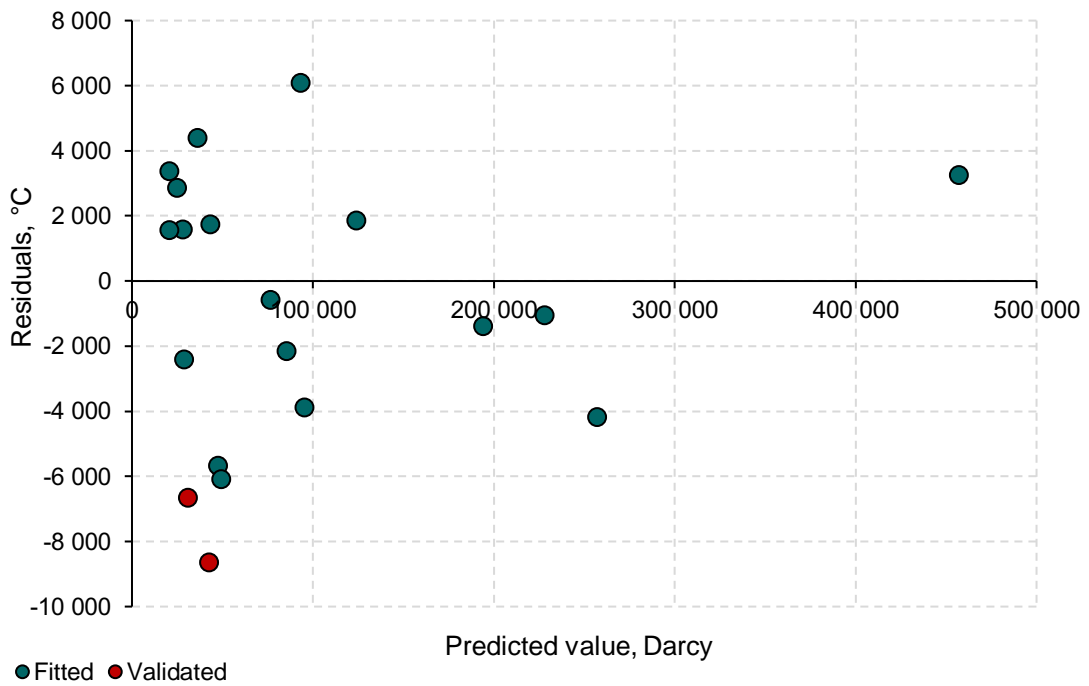


Figure 13-57: Residuals of the RSA model II.

13.64 Appendix BL

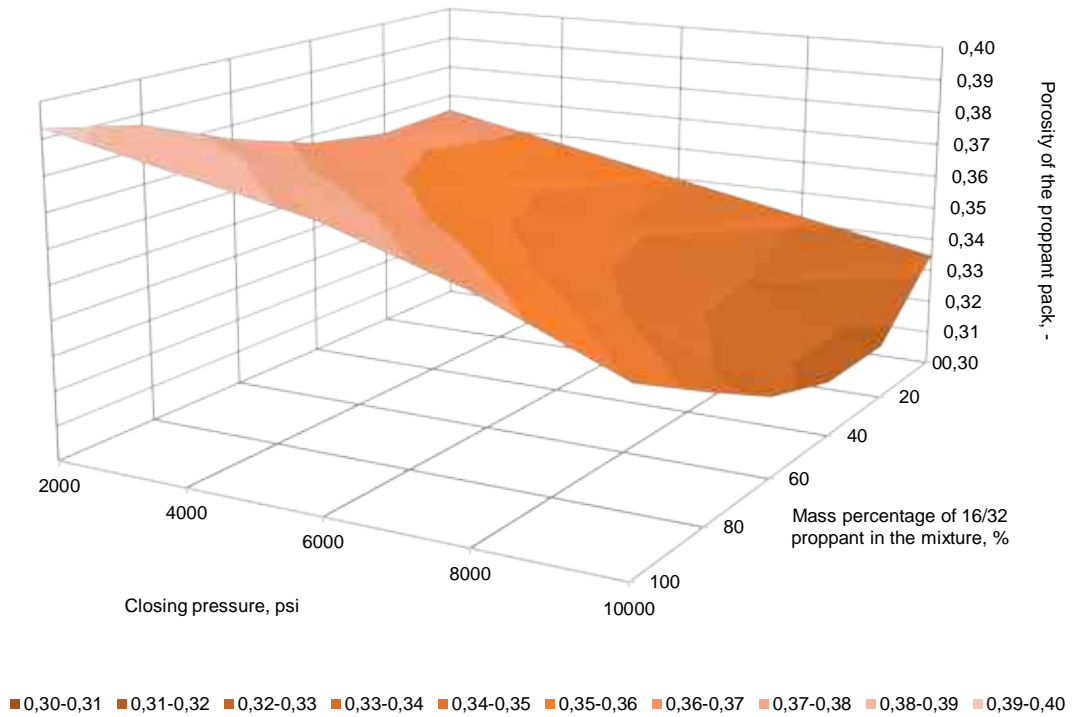


Figure 13-58: Response surface of the porosity values

13.65 Appendix BM

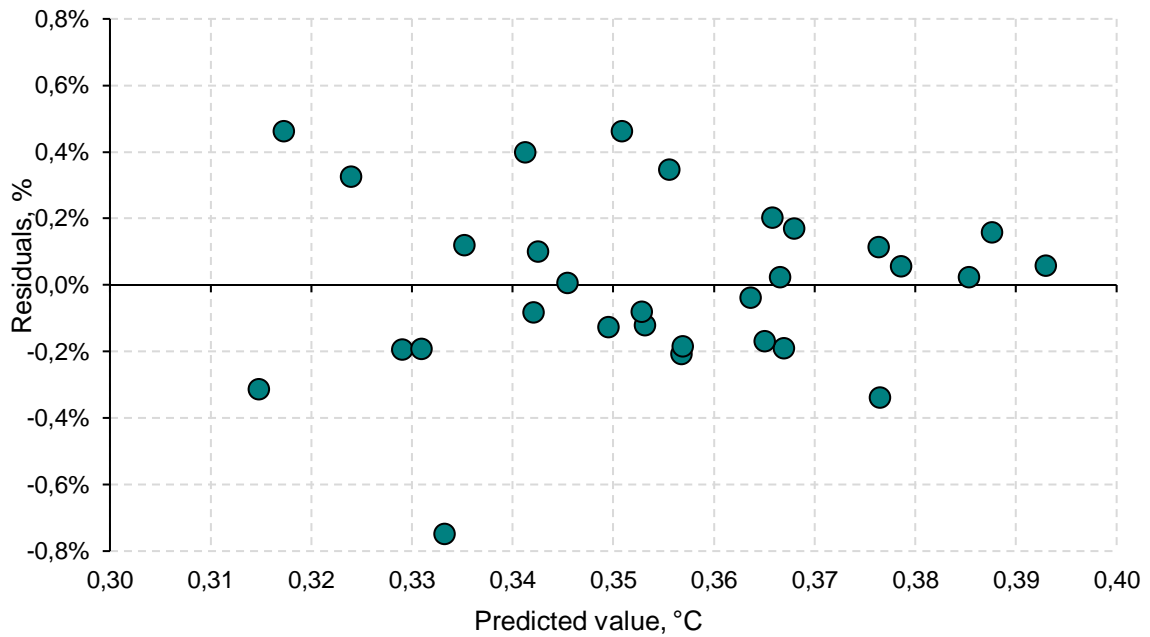


Figure 13-59: Residuals of the porosity RSM

13.66 Appendix BN

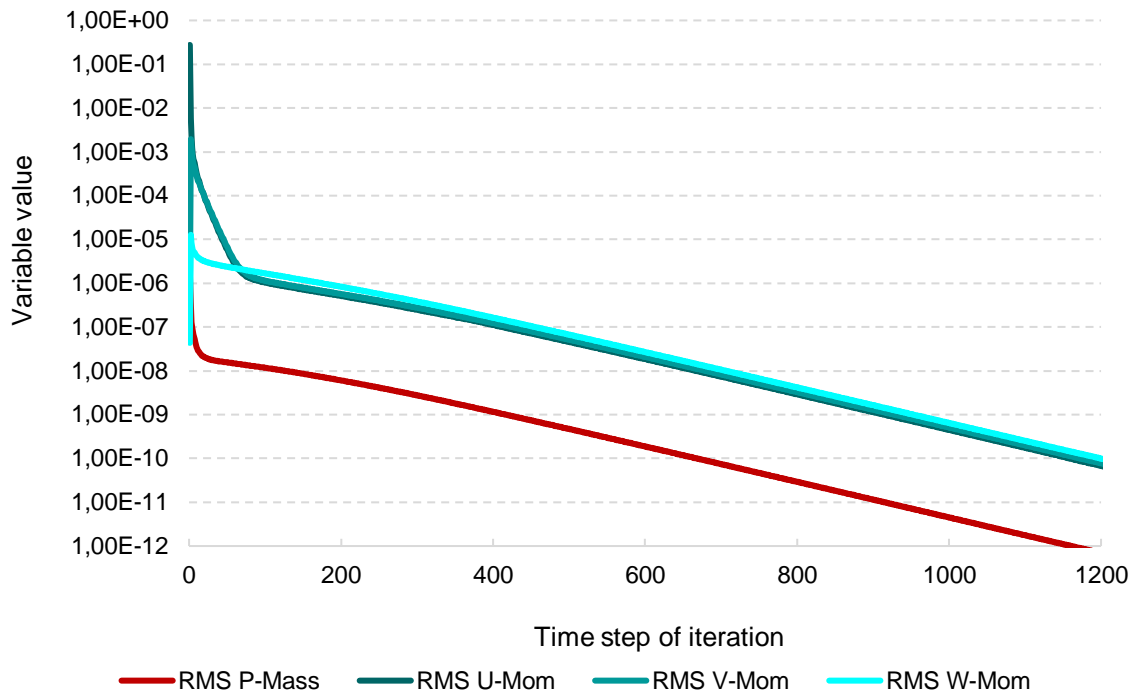


Figure 13-60: Convergence of the Danko model

13.67 Appendix BO

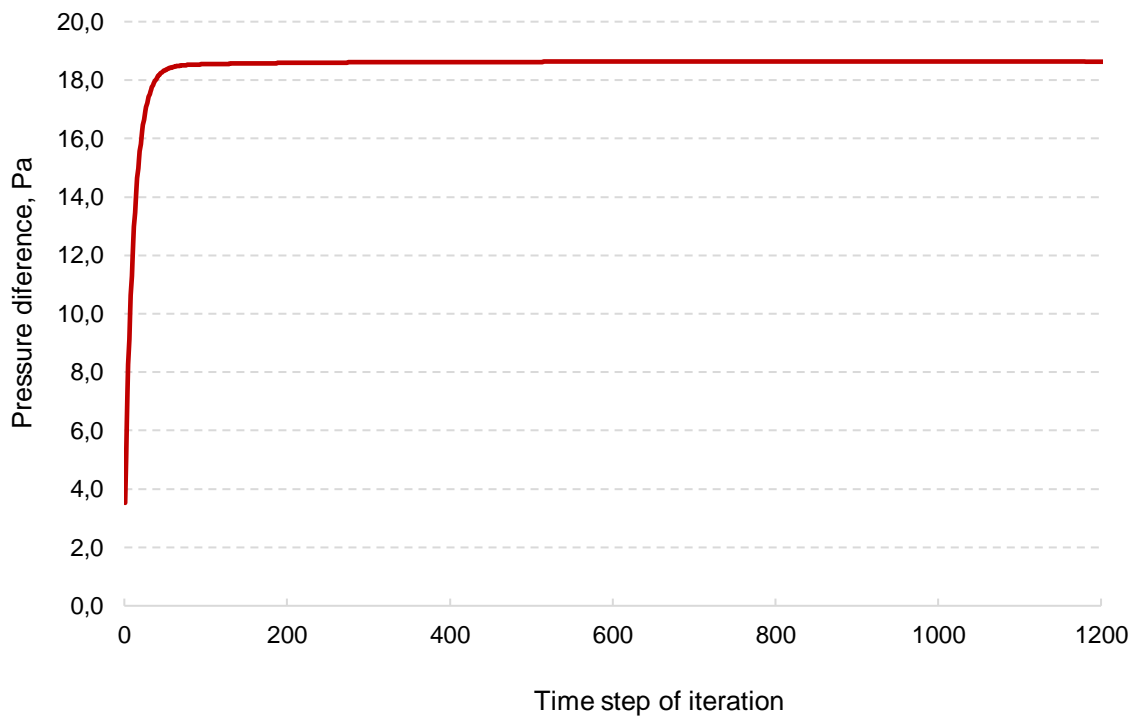


Figure 13-61: Convergence of pressure difference of the Danko model

14 LIST OF ANNEXES

13.1	Appendix A.....	IV
13.2	Appendix B.....	V
13.3	Appendix C	V
13.4	Appendix D	VI
13.5	Appendix E.....	VI
13.6	Appendix F.....	VII
13.7	Appendix G	VII
13.8	Appendix H	VIII
13.9	Appendix I.....	IX
13.10	Appendix J.....	X
13.11	Appendix K.....	XI
13.12	Appendix L.....	XII
13.13	Appendix M.....	XII
13.14	Appendix N	XIII
13.15	Appendix O	XIV
13.16	Appendix P.....	XV
13.17	Appendix Q	XVI
13.18	Appendix R	XVI
13.19	Appendix S.....	XVII
13.20	Appendix T.....	XVII
13.21	Appendix U	XVIII
13.22	Appendix V.....	XIX
13.23	Appendix W.....	XX
13.24	Appendix X.....	XXI
13.25	Appendix Y.....	XXII
13.26	Appendix Z.....	XXIII
13.27	Appendix AA	XXIV

13.28	Appendix AB	XXV
13.29	Appendix AC	XXV
13.30	Appendix AD	XXVI
13.31	Appendix AE	XXVI
13.32	Appendix AF.....	XXVII
13.33	Appendix AG.....	XXVII
13.34	Appendix AH	XXVIII
13.35	Appendix AI.....	XXVIII
13.36	Appendix AJ.....	XXIX
13.37	Appendix AK	XXIX
13.38	Appendix AL.....	XXX
13.39	Appendix AM.....	XXX
13.40	Appendix AN	XXXI
13.41	Appendix AO	XXXI
13.42	Appendix AP	XXXII
13.43	Appendix AQ.....	XXXII
13.44	Appendix AR	XXXIII
13.45	Appendix AS	XXXIII
13.46	Appendix AT.....	XXXIV
13.47	Appendix AU	XXXIV
13.48	Appendix AV	XXXV
13.49	Appendix AW	XXXVI
13.50	Appendix AX	XXXVII
13.51	Appendix AY	XXXVIII
13.52	Appendix AZ.....	XXXIX
13.53	Appendix BA	XL
13.54	Appendix BB	XL
13.55	Appendix BC	XLI
13.56	Appendix BD	XLII

13.57	Appendix BE	XLIII
13.58	Appendix BF.....	XLIV
13.59	Appendix BG.....	XLV
13.60	Appendix BH	XLVI
13.61	Appendix BI.....	XLVII
13.62	Appendix BJ.....	XLVIII
13.63	Appendix BK	XLVIII
13.64	Appendix BL.....	XLIX
13.65	Appendix BM.....	XLIX
13.66	Appendix BN	L
13.67	Appendix BO.....	L